

Sheffield Hallam University

The reduction of magnetite and lean magnetite sinters.

HARRINGTON, M. J.

Available from the Sheffield Hallam University Research Archive (SHURA) at:

<http://shura.shu.ac.uk/20166/>

A Sheffield Hallam University thesis

This thesis is protected by copyright which belongs to the author.

The content must not be changed in any way or sold commercially in any format or medium without the formal permission of the author.

When referring to this work, full bibliographic details including the author, title, awarding institution and date of the thesis must be given.

Please visit <http://shura.shu.ac.uk/20166/> and <http://shura.shu.ac.uk/information.html> for further details about copyright and re-use permissions.

SHEFFIELD S1 1WB

74.20624 669.000000000
7 4 2 0 6 2 4 0 1 1



HARRINGTON, M.J.
THE REDUCTION OF MAGNETITE A
NO LEAN MAGNETITE SINTERS.

**SHEFFIELD POLYTECHNIC
LIBRARY SERVICE**

MAIN LIBRARY

~~19 NOV 75~~

~~ADDRESS~~

Sheffield City Polytechnic Library

REFERENCE ONLY

Books must be returned promptly, or renewed, on
or before the last date stamped above.

FAILURE TO DO SO WILL INCUR FINES

PL/17

ProQuest Number: 10699994

All rights reserved

INFORMATION TO ALL USERS

The quality of this reproduction is dependent upon the quality of the copy submitted.

In the unlikely event that the author did not send a complete manuscript and there are missing pages, these will be noted. Also, if material had to be removed, a note will indicate the deletion.



ProQuest 10699994

Published by ProQuest LLC (2017). Copyright of the Dissertation is held by the Author.

All rights reserved.

This work is protected against unauthorized copying under Title 17, United States Code
Microform Edition © ProQuest LLC.

ProQuest LLC.
789 East Eisenhower Parkway
P.O. Box 1346
Ann Arbor, MI 48106 – 1346

64792

THE REDUCTION OF MAGNETITE AND
LEAN MAGNETITE SINTEREDS

A thesis submitted in candidature for the degree of
Doctor of Philosophy of the Council for National
Academic Awards.

November, 1972



74-20624

Details of Complementary Academic Studies

- | | | |
|-------|--|---------|
| (i) | 1967/68 Advanced course of lectures on Ferrous Process Metallurgy* | 60 hr |
| (ii) | 1967/68 A Tutorial course in Mathematics, and a short course on Fortram programming* | 60 hr |
| (iii) | 1968 Easter School in Chemical Thermodynamics at Royal School of Mines | 10 days |
| (iv) | 1968-69 Special course in Quantitative Metallography* | 20 hr |
| (v) | 1969-70 Special course: Modern Aspects of Iron and Steelmaking* | 28 hr |
| (vi) | 1969-70 Special course: Thermodynamics and kinetics of metallurgical processes* | 32 hr |

* Sheffield Polytechnic

Declaration

I hereby declare that the work described herein is the result of my own investigations excepting where due reference has been made to other work.

This thesis is not being and has not been submitted in candidature elsewhere for any other degree.

Signed:

CONTENTS

Synopsis

Acknowledgements

<u>Chapter</u>	<u>Section</u>		<u>Page</u>
		<u>REVIEW OF PREVIOUS WORK</u>	1
1	1.1.	Reduction of Iron Oxides	1
	1.1.1.	Equilibrium	1
	1.1.2.	Crystal Structure	1
	1.1.2.1.	Hematite	1
	1.1.2.2.	Magnetite	1
	1.1.2.3.	Wustite	2
	1.1.3.	Theories of Reduction	2
	1.1.3.1.		2
	1.1.3.2.	Kinetics	6
	1.2.	<u>Factors Affecting Reduction</u>	7
	1.2.1.	Temperature	7
	1.2.2.	Porosity	8
	1.2.3.	Reduction Cracking	10
	1.2.4.	Constitution	12
	1.2.5.	Effect of Impurities	13
	1.2.6.	Influence of Matrix	15
	1.3.	<u>Mechanisms of Reduction</u>	17
	1.3.1.	Gaseous Diffusion	18
	1.3.2.	Chemical Reaction	20
	1.3.3.	Solid State Diffusion	23
	1.4.	<u>Laws of Reduction</u>	27
	1.4.1.	Diffusion through the Gaseous Boundary Layer	27

<u>Chapter</u>	<u>Section</u>	<u>Page</u>
	1.4.2.	Solid State Diffusion through Solids 28
	1.4.3.	Gaseous Diffusion through Solids 30
	1.4.4.	Chemically Controlled Reaction Rate 31
	1.4.5.	Combined Reduction Laws 34
	1.4.6.	Conclusions 36
	1.5.	<u>Reduction of Magnetite</u> 37
	1.5.1.	General 37
	1.5.2.	Reduction Rate Minima 40
	1.6.	<u>Constitution and Reducibility of Sinter</u> 42
	1.6.1.	Constitution 42
	1.6.2.	Reducibility 43
	1.6.3.	Thermal and Oxidation Treatment 46
2		<u>EXPERIMENTAL DETAILS</u> 49
	2.1.	<u>Introduction</u> 49
	2.1.1.	Magnetite Samples 49
	2.1.2.	Sinter Samples 50
	2.1.3.	Oxidised Sinter Pellets 51
	2.1.4.	Thermally Treated Sinter 51
	2.2.	<u>Equipment</u> 53
	2.2.1.	The Glass Spring Balance 53
	2.2.1.1.	Temperature Control 54
	2.2.1.2.	Calibration of the Glass Springs 54
	2.2.2.	Stanton Massflow Thermogravimetric Balance 55
	2.2.2.1.	Weighing Operations 55
	2.2.2.2.	Temperature Control 56
	2.3.	<u>Gas Purification</u> 57
	2.4.	<u>Critical Gas Flow Rate</u> 57
	2.5.	<u>Preliminary Tests</u> 57

<u>Chapter</u>	<u>Section</u>	<u>Page</u>
	2.5.1. Blank Tests	57
	2.5.2. Test Series	58
	2.6. <u>Metallographic Preparation</u>	59
	2.6.1. Mounting	59
	2.6.2. Microscopic Examination and Photography	59
	2.7. <u>X-ray Diffraction</u>	60
	2.8. <u>Electron Probe Micro Analysis</u>	60
	2.9. <u>Porosity Determinations</u>	60
	2.10. <u>Naphthalene Sublimation Experiments</u>	61
	2.10.1. Introduction	61
	2.10.2. Technique	61
	2.10.3. Sample Preparation	62
	2.10.4. Temperative Measurement	62
	<u>DETERMINATION OF MASS TRANSFER</u>	
	<u>CHARACTERISTICS</u>	63
	3.1. <u>Introduction</u>	63
	3.1.1. Technique	63
	3.1.2. Diffusion Coefficient $D_{H_2-H_2O}$	65
	3.2. <u>Discussion of Mass Transfer Results</u>	67
	3.2.1. Determination of A	67
	3.2.2. Diffusion Coefficient $D_{H_2-C_{10}H_8}$	67
	3.2.3. Determination of B and n	68
	3.2.4. Determination of Mass Transfer Coefficients	69
	3.2.5. Effect of Mass Transfer Coefficient on Reaction Rate	69
	3.3. <u>Conclusions</u>	71

<u>Chapter</u>	<u>Section</u>	<u>Page</u>
4	<u>MATHEMATICAL TREATMENT</u>	73
	4.1. <u>Individual Laws</u>	73
	4.2. <u>Combined Laws</u>	74
5	<u>REDUCTION OF MAGNETITES</u>	79
	5.1. <u>Introduction</u>	79
	5.2. <u>Effect of Temperature</u>	79
	5.3. <u>Rate Maxima and Minima</u>	80
	5.4. <u>Metallography of Reduced Magnetite</u>	81
	5.4.1. Unreduced Magnetite Samples	81
	5.4.2. Reduced Magnetite Samples	81
	5.4.2.1. Series 1 (spring balance)	81
	5.4.2.1.1. Reduction Rate Minimum 650°C	81
	5.4.2.1.2. Reduction Rate Maximum 750°C	83
	5.4.2.1.3. Reduction Rate Minimum 900°C	85
	5.4.2.2. Series 2 (spring balance)	86
	5.4.2.2.1. Reduction Rate Maximum 550°C	86
	5.4.2.2.2. Reduction Rate Minimum 900°C	86
	5.4.2.3. Series 2 (Stanton balance)	87
	5.4.2.3.1. Reduction Rate Minimum 650°C	87
	5.5. <u>Porosities</u>	89
	5.6. <u>Apparent Activation Energies</u>	90
	5.7. <u>Mathematical Treatment</u>	91
	5.8. <u>Discussion</u>	95
	5.8.1. Introduction	95
	5.8.2. Discussion	95
6	<u>REDUCTION OF A.F. SINTER PELLETS</u>	102
	6.1. <u>Introduction</u>	102
	6.2. <u>Effect of Reduction Temperature and</u> <u>Thermal and Oxidation Treatments on Reduction</u> <u>Rates</u>	102

<u>Chapter</u>	<u>Section</u>	<u>Page</u>
	6.2.1. Effect of Temperature	102
	6.2.2. Effect of Oxidation	103
	6.2.3. Effect of Thermal Treatment	103
	6.3. <u>Metallography of Reduced Sinters</u>	104
	6.3.1. Unreduced Sinter Pellets	104
	6.3.2. Reduced Sinter Pellets	104
	6.3.2.1. Untreated Sinter Pellets	104
	6.3.2.2. Oxidised Sinter Pellets	105
	6.3.2.3. Thermally Treated Sinter Pellets	106
	6.4. <u>Porosities</u>	106
	6.5. <u>Apparent Activation Energies</u>	106
	6.6. <u>Mathematical Treatment</u>	108
	6.6.1. Untreated Sinter Pellets	108
	6.6.2. Oxidised Sinter Pellets	110
	6.6.3. Thermally Treated Sinter Pellets	111
	6.7. <u>Discussion</u>	112
7	<u>GENERAL DISCUSSION</u>	117
	REFERENCES	
	NOMENCLATURE	
	APPENDIX I	
	TABLES	
	FIGURES AND MICROGRAPHS	

SYNOPSIS

The problems encountered in attempting to determine the rate controlling step in the reduction of magnetite and sinters to iron are revealed by a survey of the pertinent literature.

On the basis of previous work supplemented by the investigations reported in this thesis the probable sequence of rate controlling steps has been determined.

Exhaustive metallographic and mathematical studies have been carried out on the hydrogen reduction of magnetite and lean magnetite sinter samples reduced in thermal balances.

The existence of rate minima at 650°C and 900°C in the reduction of magnetite has been shown by metallographic techniques.

Additionally the extent of chemical reaction and mass transport control has been shown by mathematical studies.

Similarly the extent of chemical and transport control in sinter reduction has been shown metallographically and mathematically.

The effect of thermal treatment in oxidising and inert atmospheres has been shown. The improvement in reaction rates as a result of particular thermal treatments has been displayed.

ACKNOWLEDGEMENTS

The work was carried out in the Department of Metallurgy, Sheffield Polytechnic, and thanks are due to Mr D Thacker, the former Head and Dr A W D Hills the present Head of Department for provision of laboratory facilities and helpful advice. Thanks are also due to the Sheffield Education Authority for the financial support of a Research Assistantship.

The author is particularly indebted to Mr T J J Smith (Director of Studies) and Dr B C Blakey (Industrial Supervisor) for the many stimulating discussions and helpful advice.

The willing assistance given by many members of the academic staff particularly Mr R H Parker and Dr G Briggs is gratefully acknowledged. As is the help and assistance given by Mr G Farnsworth and his technical staff.

Finally thanks are due to the Appleby-Frodingham Works of the Scunthorpe Group BSC for the provision of samples.

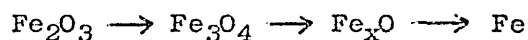
1.1. REDUCTION OF IRON OXIDES

1.1.1. Equilibrium

Four possible phases may exist ⁽²⁴⁾ during the reduction of hematite to iron. (Figure 1.)

- (i) hematite (two forms α -Fe₂O₃ and maghemite γ -Fe₂O₃)
- (ii) magnetite (Fe₃O₄)
- (iii) wustite (Fe_xO)
- (iv) iron (Fe)

The wustite phase is a solid solution which is unstable below 570°C. At this temperature wustite undergoes a eutectoid decomposition to α - iron and magnetite. Above 570°C, hematite should follow a four phase sequence of reduction to metallic iron:



1.1.2. Crystal Structure

1.1.2.1. Hematite: may exist in two forms with different lattices

- (i) α -Fe₂O₃ is a rhombohedral corundum type (a = 5.42 Å, x = 55° 14). The oxygen ions are arranged in a close-packed hexagonal lattice with two thirds of the octahedral interstices occupied by Fe³⁺ ions. The oxide has a small oxygen deficit due to oxygen vacancies.
- (ii) γ -Fe₂O₃ has a structure similar to that of magnetite, viz: a cubic spinel (a = 8.32Å) there is an average of 21½ Fe³⁺ ions per unit cell. It can be obtained by low temperature oxidation of magnetite.

1.1.2.2. Magnetite has a cubic spinel lattice (a = 8.38Å) with a close packed cubic lattice of O²⁻ ions with Fe²⁺ and Fe³⁺ ions at the interstices. 8 Fe³⁺ and 8 Fe²⁺ ions are in tetrahedral positions. There is a slight reduction in lattice parameter

as oxygen content increases indicating the presence of cation vacancies. The magnetite lattice is similar to the wustite lattice.

1.1.2.3. Wustite has a cubic lattice of the sodium chloride type. It is a close packed oxygen lattice with iron ions at the octahedral interstices. The deviation from stoichiometry of the wustite is due to the 5% to 11% of iron ion vacancies. Electrical neutrality is maintained by Fe^{3+} ions.

1.1.3. Theories of Reduction

1.1.3.1. The reduction of iron oxides is a complex heterogeneous process involving three major and distinct stages.

- (i) transport of reactants to the oxide.
- (ii) chemical reaction at the interface.
- (iii) transport of products away from the oxide.

With sinters the situation is further complicated by the introduction of a matrix through which transport of reactants and products to and from the oxides must occur.

The several stages of reduction have been illustrated diagrammatically by using modified versions of the Hauffe diagram (26,29) (Figure 2), the Heubler diagram (106, 107) (Figure 3) and by a spherical model (Figure 4).

The possible reduction steps can be summarised as follows:

- (i) transport of reactant and product gases across a stagnant boundary layer.
- (ii) transport of reactant and product gases across a matrix.
- (iii) product shell penetration of reductant and product gases.
- (iv) chemical reaction at the iron - iron oxide interface.
- (v) diffusion of iron ions through the wustite layer.

- (vi) reaction between iron ions and magnetite at the wustite - magnetite interface.
- (vii) diffusion of Fe^{3+} ions through the magnetite layer.
- (viii) reaction between Fe^{3+} and hematite at the magnetite hematite interface.
- (ix) diffusion of O^{2-} ions through the hematite core.

Any one of the above steps could be rate controlling for the reduction of iron oxide. It is therefore, useful at this stage to briefly discuss the mechanisms involved:

Step (i) The effective boundary layer is a function of the bulk gas flow rate and can be determined from Fick's laws of diffusion.

It can be seen that:

$$\delta_e = \frac{C_s - C_g}{\left(\frac{\partial c}{\partial r} \right)_{r=0}} \quad (1) \quad \begin{array}{l} C_s = \text{gas composition at surface} \\ C_g = \text{bulk gas composition} \\ \frac{\partial c}{\partial r} = \text{concentration gradient} \end{array}$$

from Fick's law for streamline flow

$$J = -D \left(\frac{\partial c}{\partial r} \right)_{x=0} + u_x C \quad (2) \quad J_x - \text{is the flux of diffusing substance.}$$

and $J = \frac{D (C_s - C_g)}{\delta_e} \quad (3) \quad \delta_e - \text{is effective boundary layer.}$

Thus the flux of material across the boundary layer is inversely proportional to the boundary layer depth. As the gas flow rate is increased so δ_e becomes small and the effective resistance to gas diffusion becomes small.

Step (ii) There is little information regarding the transport of gases across a matrix, although it has been (68, 87) shown that the more crystalline the matrix the more easily gases may pass through it.

Step (iii) In general, gaseous diffusion across a porous iron layer involves both reactant and product gases.

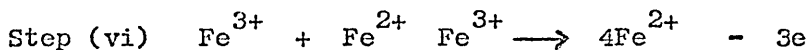
Porosity may be induced in the iron layer, by physical cracking due to pressure build up of product gas inside the product layer. (29) The porosity may also be induced as a result of a phase volume change or by the diffusion of vacancies to form pores.

Step (iv) $\text{Fe}_x\text{O} + \text{H}_2 \rightarrow \text{H}_2\text{O} + x\text{Fe}$

This reaction has been shown to be slower than the magnetite to wustite stage and has been termed the rate controlling step. McKewan (77 - 81) holds strongly to this point of view and with the support of other workers has shown the rate of reaction to be proportional to the surface area of the receding reaction interface and the partial pressure of the reducing gas. Other workers (43, 129, 105) have shown that a linearly contracting interface is not exclusive to surface reaction control mechanisms.

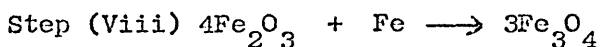
Step (v) involves the diffusion of iron ions across a wustite layer. The ease of iron ion diffusion is a result of the 5% to 11% of iron ion vacancies in the wustite lattice. The value of the self diffusion coefficient of iron ions in wustite is of the order 2.7×10^{-9} and 8.2×10^{-8} cm^2/sec . between 700°C and 900°C with an activation energy for the process of 124 K.J./mol (29K cal/mol) (49). Diffusion coefficients of this order have been indicated by other workers (75, 26, 28, 30) similarly activation energies of the same order. The variation in the diffusion coefficient with temperature was attributed to vacancies. Some workers (74, 26, 28, 30, 118, 139) consider that iron ion diffusion in wustite is rate controlling.

Sandwiches of iron and magnetite have been used (28, 82) showing that the growth of wustite is a parabolic function of time indicating diffusion control. The rate constant can be increased by the introduction of impurity cations (74, 82, 67, 25). Khalafalla (67) considered that this was due to the increase in lattice strain caused by the cation.



This reduction of magnetite to wustite is crystallographically reversible and has not been considered rate - controlling.

Step (vii) Involves the diffusion of ions through the magnetite layer. Himmel et. al (49) have shown that this is the inward diffusion of iron ions.



occurs at the magnetite - hematite interface. A crystallographic phase change from α - Fe_2O_3 to Fe_3O_4 occurs. Edstrom (27) shows that such a change causes lattice strain and imperfections giving an enhanced reduction rate.

Step (ix) Is the diffusion of oxygen ions through the hematite lattice to the hematite - magnetite interface. There exist a small number of oxygen ion vacancies. Davies et. al. (25) have shown that the interface is continued by O^{2-} diffusion through the hematite lattice. Kingery (137) has given the activation energy for ion motion in hematite to be 126 - 167 K.J./mol (30 - 40K. cal/mol). Himmel et. al. (49) have shown that the energy required for self diffusion of iron ions in hematite is 470 K.J./mol (110 K. cal/mol) with a diffusion coefficient of 1.0×10^{-13} to 4.0×10^{-9} $mm^2/sec.$ from $950^\circ C$ to $1250^\circ C.$

1.1.3.2. Kinetics

The progress of reduction may also be considered from the kinetic theories developed for homogenous gas reactions. The driving force for such a reaction is considered as the difference between the free energies of the initial and final states.

The absolute reaction rate theory developed by Eyring considers that a rate process is characterised by an initial state which passes, by continuous change, to a final state. There is a high energy surface which acts as a barrier between the initial and final states. The critical state at the minimum energy position on the energy barrier is the activated complex.

The reaction rate constant for the formation of the activated complex is:

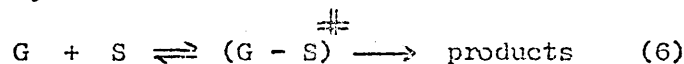
$$k_r = \frac{(k_b T)}{(h)} \cdot e^{\frac{\Delta S^\ddagger}{R}} \cdot e^{-\frac{\Delta H^\ddagger}{RT}} \quad (4)$$

A more usual form of the equation is that suggested by Arrhenius.

$$k_r = A_0 e^{-E/RT} \quad (5)$$

where A is the frequency factor and E is the activation energy or temperature coefficient for the reaction. The value of E can indicate the controlling mechanism for reduction. A low value is commensurate with gaseous diffusion control, a high value with solid state-diffusion control and an intermediate value with chemical reaction control.

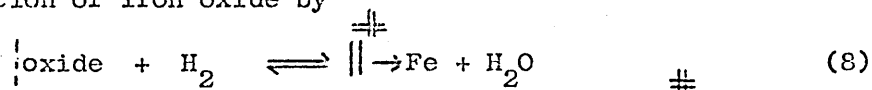
McKewan⁽⁸¹⁾ has used this method of analysis in order to study the mechanism of reduction. He considered that the reaction could be described by



and that the rate equation was

$$\frac{d(\text{product})}{dt} = c_g c_s k_r = c_g c_s \left(\frac{k_B T}{h} \right) e^{-\Delta E^\ddagger / RT} \quad (7)$$

The energy path for the transition between one set of initial and final states is shown in figure 5. The first energy barrier resulting from the activated state for gaseous adsorption on the reaction site. The highest energy level is the activated state for the reduction reaction itself. Quets et. al. (99, 100) also considered the formation of an activated complex and represented the reduction of iron oxide by



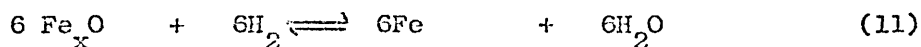
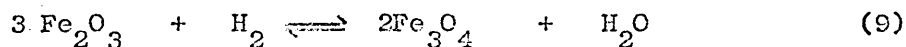
where $\left\{ \begin{array}{l} \text{oxide} \\ | \end{array} \right.$ represents the oxide surface and $\left\| \begin{array}{l} \text{---} \\ \text{---} \end{array} \right\|$ an activated complex, the concentration of which limits the rate of reaction.

The possible mechanisms of reduction have been outlined in this section. They will be more fully considered in section 1.3.

1.2. Factors Affecting Reduction:

1.2.1. Temperature

The reduction of iron oxide by hydrogen is the net result of two or more gas-solid reactions. Above 570°C., the reduction sequence may be represented as follows:



on summation:



The equation may be represented by the general form:



It is generally known that increasing the temperature at which a reaction occurs, frequently causes a marked increase in the rate of reduction. For a simple reaction the rate may be illustrated

by Eyrings' absolute rate theory. (See section 1.1.3.2.).

This is simply described by the Arrhenius equation (Equation

5). Many workers have, in fact, shown that during both hematite (19,26,50,51) and magnetite (76, 85, 99, 100, 112, 113, 125, 120)

reduction there is a fall off in reaction rate as temperature

increases. This gives rise to the existence of rate maxima and

minima. Other workers (77 - 81, 47, 131) have reported a sharp

change in activation energy rather than local rate minima. The

existence of these rate maxima and minima have been said to be due

(86) to changes in micro-porosity (50), sintering and recrystall-

isation, changes in magnitude of the thermodynamic driving force

(23), reduction of water permeability (50), the formation of

protective product layers (26) and changes in the dimensions of

the wustite lattice (139). (The rate minima phenomena will be

discussed in the section on magnetite reduction.)

The reduction of iron oxides is a complex physical and chemical

process. It may be seen that if rate of reduction changes signi-

ficantly with a change in temperature, then it is probable that the

controlling mechanism may change with differing, intermediate degrees

of contribution over the range of temperatures considered.

1.2.2. Porosity

Maximum porosity in a polycrystalline material may be said to

occur when each individual grain is separated from its neighbour.

Thus each grain will have a reducing atmosphere over a finite depth

of penetration. In this case a well-defined macro interface will

not occur. Each individual grain may be reduced in a topochemical

manner. Selective reduction may also occur as a result of unevenness

in porosity. Feinman (33) considered the maximum reduction rate to

occur when all the oxide sites were reached by the reductant. As

porosity increases so the number of sites available for reduction increases. Instead of a sharp interface a volume will undergo reaction. There is a greater surface for reaction in porous materials than in dense materials.

If the reaction occurs topochemically at all points then McKewan's linearly contracting interface law ⁽⁷⁷⁾ can operate. Gray and Henderson ⁽⁴²⁾ point out that with dense oxides, there are only thin intermediate layers. Thus for oxygen removal the interface must recede.

In general it may be said that an increase in initial porosity reduces impedance to gaseous diffusion and increases reduction rates ^(80, 59, 64). Where there is little or no porosity, then gas diffusion may become rate controlling ⁽⁶⁾, Joseph ⁽⁵⁹⁾ has shown that the time for 90% reduction is proportional to the reciprocal of % porosity. Where matrix slags are present, then the matrix porosity can be of major importance. Barner ⁽⁷⁾ points out that porosity is only important when the reaction rate is not controlled by the gas flow rate.

It is generally known that, in addition to the initial porosity of an oxide, there is also an induced porosity caused by the process of reduction.

Wustite formed from hematite is more porous than that formed from magnetite ^(27, 34, 99, 129). This is thought to be a result of the transformation from a hexagonal to a cubic lattice causing lattice imperfections which act as vacancy sinks causing the formation of pores.

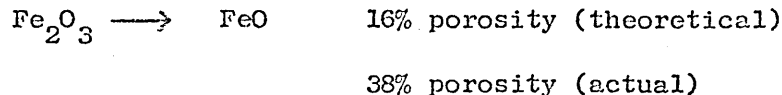
Wustite formed from magnetite should have a porosity of 14% (Pilling-Bedworth ratio = 0.86) ⁽¹²⁹⁾. It has been shown ⁽³⁴⁾ that a 15% lattice misfit can be accommodated before porosity results.

Pore size increases with time and temperature, and molecular rather than Knudsen diffusion occurs (129, 27).

Induced porosity on reduction is a feature of the process and the size, shape and nature of the pores are a function of the initial form of the oxide, the temperature of reduction and the reductant. Where pores do not form there is, in general, a falling off in reduction rate.

1.2.3. Reduction Cracking

Joseph (59) considers that cracking induced by reduction can greatly affect reduction rates. He points out that a high initial porosity may not be so effective in enhancing reduction rates as a high susceptibility to reduction cracking. Large external volume changes occur on reduction (27) especially with gases which have a high reducing potential. This causes more porosity than specific volume changes would suggest.



At temperatures of less than 600°C a cracked finely porous iron product results.

It is considered that (27, 133, 52) the cracking of the product could be due to a pressure build up of the product gas inside the reduced layer eventually causing bursting of the layer. Themelis and Gauvin (120) point out that where a change of structure is involved, then the product should be irregular in density with fissures and cracks.

Brill - Edwards and Samuel (8) consider that reduction cracking is a result of magnetite growth on reduction causing dilation parallel to its growth plane. The magnetite extends across a grain boundary contacting the adjacent grain. The grain boundaries are forced

apart causing a grain boundary crack. This effect may occur within the grain. Tensile stresses operate in the hematite and compressive stresses operate in the magnetite. The rate of magnetite propagation increases with temperature reducing the amount of compensatory contraction such that there will be a decrease in the apparent density of hematite with temperature. At less than 700°C circumferential contraction occurs causing radial cracks. At high temperatures there is a continual creation of new hematite interfaces causing enhanced reduction, whereas, at low temperatures the cracks occur in the magnetite and do not directly affect the reduction rate. Less severe lattice stresses result on reduction to wustite, some stress relief being possible due to wustite plasticity.

The results are consistent with Beeton's ⁽⁶⁾ work which shows that hematite disintegration occurs before 20% reduction.

Stone and Daniell ⁽¹¹⁴⁾ have shown that susceptibility to reduction cracking of hematite increased as the prior sintering temperature was increased above 1300°C. This was associated with the hematite-magnetite transition which occurs at 1450°C. Different cooling rates were thought to alter the cracking tendency. Low density compacts were found to be reduced without damage, presumably due to the stresses being more easily accommodated. This was supported by controlled cracking tests ⁽¹¹⁵⁾ which showed that shrinkage occurred least in the most cracked compacts.

Pepper and Daniell ^(45, 96) found that slag bonded hematites had a lower compressive strength than direct bonded hematites allowing intercrystalline cracking to occur more easily. This allowed easy reduction at high temperatures but was insufficient to overcome the slag barrier at low temperatures. The maximum expansion was found to occur in the hematite → magnetite reduction with a minimum

occurring at 800°C. to 900°C. With direct bonded hematites the expansion occurred over the hematite → wustite stage. The incidence and extent of reduction cracking was found to decrease with decreasing hydrogen partial pressure.

Brill-Edwards (9) showed that there was an improvement in the strength of compacts with both silicate and ferrite slags. However, silicates caused a loss of reducibility. Barrie (10) considered that strength improvement only occurred with up to 15% slag and agreed with Beeton (6) that the majority of breakdown occurred during the first 15% to 20% reduction.

The strength of both hematite and magnetite was shown (92) to be proportional to the reciprocal degree of reduction by carbon monoxide at 970°C.

Most of the investigation into reduction cracking has been carried out on hematites. It indicates that reduction cracking results from stresses created between the initial oxide and the product phase. Prior thermal treatments and the addition of a suitable slag have been shown to significantly affect the reduction cracking characteristics.

1.2.4. Constitution

The state of oxidation of a ferruginous material and the introduction of a matrix to an iron oxide can materially affect reduction characteristics.

Edstrom (31) has pointed out the superior reducibility of hematite compared with magnetite and shows that a small degree of oxidation can significantly affect the rate of reduction. Oxidised magnetite was shown to give very similar reduction rates to natural hematite.

Low temperature oxidation of magnetite results in the formation of the magnetic γ -Fe₂O₃, maghemite (127, 11, 21). Ball et al (11, 21)

consider that oxidation of magnetite to α - hematite always takes place via maghemite and that the first stage of oxidation is complete when a layer of γ - hematite is formed.

Differences in oxidation behaviour of magnetite have been attributed (11, 37) to differences in specific surface area.

Smercek (117) indicates that thermal decomposition of oxidised magnetite can occur with the addition of slag forming compounds.

1.2.5. Effect of Impurities

Metal oxide systems which are subject to reduction reactions have two types of impurity:

(a) foreign atoms in the metal oxide lattice in

(i) the parent lattice

(ii) substitutional sites

(iii) interstitial sites.

(b) excess or deficiency of metal or oxygen ions on deviation from stoichiometry.

Both types of defect can produce the same sort of electronic and lattice defects.

Lattice defects are vacant lattice sites or interstitial ions and quasi-free electrons or positive holes. Their production or elimination is proportional to the concentration of the appropriate impurity.

Wustite is a metal deficit semi-conductor with Schottky holes and electron holes. Previously it was considered that only the octahedral sites were occupied with two ferric ions for each vacancy to preserve electrical neutrality. Roth (101) showed the existence of tetrahedral cations and suggested that since any octahedral site in the cubic close packed oxygen lattice is separated from one another by a tetrahedral site. This is equivalent to suggesting that if one of the two octahedral sites is to be vacant then the remaining cation

prefers to enter a position in the energy saddle between them. The tetrahedral site, because of its smaller size, will be occupied by a ferric ion. If the unit defects are grouped it is considered that the energy of the defect is reduced and a structure identical to that of magnetite is produced. This may be considered as a sub-nucleus of magnetite. Because of the presence of cation vacancies Wagner considers (132) that the metal-oxygen ratio is always less than the stoichiometric ratio. The first stage of reduction is the filling of cation vacancies and the removal of higher valence cations. Where there are interstitial cations and quasi-free electrons, the first stage of reduction is an increase in the concentration of cations and vacancies.

Several workers (53, 82, 83, 74) have studied the effect of impurity cations on reduction. In general it was found that the addition of soluble trivalent cations increased the reduction rates. This was suggested to be due to an increase in the number of vacant lattice sites in wustite. Khalafalla and Weston (67) showed that increasing the number of vacancies increased the reduction rate to a maximum and then reduced it. The increase in reduction rate was found to be directly proportional to the atomic volume and the electronic charge of the impurity cation.

Other workers (118, 119, 38) have investigated the effect of additions of small amounts of slag-forming constituents. Strangway et. al (119) showed that these have a detrimental effect on hematite reduction and attributed this to the formation of a protective product e.g. fayalite, magnesio-wustite, magnesio-ferrite, $\text{FeO} \cdot \text{Al}_2\text{O}_3$. The rate minimum which occurs during the reduction of magnetite was shown to be removed by the addition of oxides whose cation radii were greatly different from the iron ion radius thus distorting the wustite lattice allowing more easy solid state diffusion. They

later show (118) that calcium carbonate can improve hematite reduction by enhancing initial and reduction induced porosity. Egeubaev et.al. (38) considered that promoters forming spinel type compounds dissolve in magnetite and improve reducibility.

1.2.6. Influence of Matrix

In addition to the effect of state of oxidation of the iron oxides and the effect of impurities on their reduction, there is present in all commercial iron bearing materials a matrix, the amount and constitution of which has a major affect upon reducibility. The effect of the matrix on reduction cracking, has been discussed previously.

Matrices comprise, in general, crystalline silicates, silicate glasses containing iron oxides and calcium ferrites. The amounts of each phase vary with the basicity of the matrix. Other minor constituents are also possible in iron ore agglomerates, including: monticellite ($\text{CaO} \cdot \text{MgO} \cdot \text{SiO}_2$), ferro-monticellite ($\text{Ca} \cdot \text{Fe} \cdot \text{SiO}_4$), pyroxene ($\text{Ca} \cdot \text{Fe} \cdot \text{Mg} \cdot \text{Si}_2\text{O}_6$), iron gehlenite ($\text{Ca}_2\text{Fe} \cdot \text{Al} \cdot \text{Si}_2\text{O}_7$), vitreous calcium-alumino silicates with dissolved iron ($x\text{Fe}_2\text{O}_3 \cdot y\text{SiO}_2 \cdot z\text{Al}_2\text{O}_3 \cdot 5\text{CaO}$; $x + y + z = 12$), olivine ($\text{Ca}_x\text{Fe}_{2-x}\text{SiO}_4$) all of which are considered to be poorly reducible.

The proportion of fayalite present normally increases, in sinter, as the amount of coke increases. Between 1150°C . and 1250°C . (87) the reaction between quartz and wustite begins to form fayalite and glass. The greater part of the silica is bound up as the ortho-silicate. Fayalite (135, 102) and ferro-monticellite (54) have been shown to be poorly reducible and are not now common constituents of modern sinters.

The addition of lime causes the formation of ferrites and several workers have shown the existence of different ferrites (10, 54, 88, 69)

The existence of the many different matrix minerals has led

several workers (102, 88, 69, 10) to study them in terms of reducibility.

Rueckl (102) showed that, up to 50% reduction, ferrites reduced following McKewan's advancing interface law. He considered that the controlling step for the reduction is the reaction at the iron-ferrite interface. It was pointed out in the discussion (102) that several interfaces were possible and that, unless the interfaces were co-incidental it was unlikely that McKewan's (77) law would be followed. Rueckl considered that the interfaces advanced at a constant distance apart, with the iron-wustite interface preceding the iron-ferrite interface and that the value for the interfacial penetration was, in fact, an average value.

Temperature also plays a part in mineral formation (13, 87). Ferrites and silicates were said to form between 1050°C. and 1200°C. Between 1250°C. and 1350°C. the mono-calcium was unstable and decomposed forming calcium olivines. They concluded that, although the more basic the matrix, the more ferrites were formed, irreducible olivines and monticellite were formed simultaneously. An increase in magnesia content reduced the amount of ferrite and caused the formation of magnesia olivines, pyroxene and monticellite. They also showed (88) that the effect of alumina varied with concentration. 7% alumina formed brown-millerite and lowered reducibility whereas 12% alumina increased the proportion of ferrites by increasing the surface tension of the melt, lowering viscosity thus facilitating oxidation. Investigators (43, 69, 88, 102) are substantially in agreement with respect to the comparative reducibilities of ferrites and silicates. In general ferrites with a high CaO : Fe₂O₃ ratio were least reducible of the ferrites. A decrease in the amount of glassy phase (88, 69) improved reducibility.

Fitton and Goldring⁽³⁵⁾ considered that a specific matrix constitution could be achieved by heat treatment. They showed that the rate of oxidation varies with temperature. At less than 1200°C the melt develops more slowly causing rapid oxidation. At above 1250°C. the melt develops rapidly, slowing down oxidation. Lime in the matrix reduces the dissociation temperature of hematite. Alumina reduces the degree of oxidation in silicate melts. Ferrites can be encouraged to appear in matrices by the use of free lime and a slow melt formation. The strength of a matrix can be improved by the interpenetrative nature of the prismatic, crystalline ferrites. Silicates also affect strength of sinters.

Bonding can be helped by chemical attack of the matrix⁽²²⁾ forming an intermediate junction compound and also lime diffusion could cause similar continuity. The improved reducibility of a re-oxidised sinter has been associated⁽¹⁰⁷⁾ with the diffusion of calcium ions into the ferruginous grain forming a duplex structure.

Ferrite concentration can be increased⁽¹²⁾ by steam injection in the ignition hood. Short times and fast cooling produce olivines and long times and slow cooling produce pyroxenes⁽⁸⁸⁾.

It is very apparent that the composition of the matrix and its physical nature has a large influence on the reduction of iron oxide agglomerates. Compositional and thermal treatments and their control, therefore, play an important part in the improvement of agglomerate reducibilities.

1.3 Mechanisms of Reduction

Much of the work carried out on the reduction of iron oxides has been an attempt to elucidate the controlling mechanisms of reduction.

More than one mechanism may be operative during reduction.

Three main controlling mechanisms are usually considered:

- (i) gaseous diffusion
- (ii) chemical reaction
- (iii) solid state diffusion

1.3.1. Gaseous Diffusion

Both reactant and product gases diffuse into and out of a partially reduced oxide sample. Diffusion of the species through the boundary layer and the product layer will occur.

Resistance to gaseous diffusion, by the boundary layer, may be reduced to a minimum by increasing the flow rate of the reactant gas to a value above the critical flow rate. Thus gaseous diffusion across the product layer may be considered separately.

During the reduction of iron oxides by hydrogen, an equal number of moles of water vapour are formed as moles of hydrogen consumed. The counter-diffusion of hydrogen and water vapour can be considered as equi-molar. Gaseous diffusion is not expected to be an activated reaction and would follow a temperature dependent form of Fick's law:

$$J = \frac{D \cdot dc}{dr} \quad (14)$$

$$\text{and } N = \frac{-D \cdot A \cdot S \cdot P (C_g - C_e)}{R \cdot T \cdot \Delta x} \quad \text{moles/sec./cm}^2 \quad (15)$$

Other workers (108, 92, 64, 44, 4, 111, 66) have considered the equi-molar counter diffusion of gases and have obtained similar equations such that the rate of transport is a linear function of the concentration differences. Schurman et.al. (111) point out that diffusion increases only slowly with temperature and would thus tend to become more rate controlling at higher temperatures.

Warner (130) points out that, by consideration of Fick's law, solid state diffusion across the wustite layer cannot account for layer thickness. This indicates that gas molecules are the species

diffusing through pores within the product phase. Warner (130) also considered that gaseous diffusion occurs by molecular diffusion. Hindrance to gaseous diffusion depends on the size and nature of the pores (4).

Investigators (130, 4, 111) have given low values for the apparent activation energy of 4.0 - 17.0 K.J./Mol (1 - 4 k.cal/mol) which are of the same order as the heat for diffusion. This would indicate that gaseous diffusion may be rate controlling.

It is considered (4) that magnetite reduction between 600°C. and 900°C. is controlled by the outward diffusion of water molecules.

The most decisive test for gaseous diffusion control is considered (130) to be keeping the hydrogen concentration constant and vary the total pressures. If there is a significant difference between the rates of reduction at different partial pressures of hydrogen, then it is unlikely that an interfacial reaction would be rate controlling.

Up to 1 atmosphere the reaction rate (78, 80) has been shown to be proportional to the hydrogen partial pressure and at high pressures the reduction rate reached a maximum. McKewan explained this in terms of a reaction mechanism involving an equilibrium adsorption step with the reaction interface sparsely occupied by hydrogen at low pressures and fully saturated at high pressures, and evaluated the entropy and enthalpy of adsorption as - 5.3e.u. and -14 K.J./mol (3.3K.cal./mol.). The entropy value is much too low to account for the change between a gas phase and a highly adsorbed layer. The enthalpy value is too low for the heat of adsorption and is in fact of the same order as the heat diffusion. McKewan explains the values as being consistent with van der Waals type of adsorption which is highly unlikely at temperatures above 500°C. (1)

The apparent activation energy was shown ⁽¹³⁰⁾ to be: 63K.J./mol (15 K.cal) at less than 500°C. and 17 K.J./mol (4K.cal/mol) above 500°C. This indicated a change from predominantly chemical reaction control to predominantly gaseous diffusion control.

Hansen et. al. ⁽⁴⁴⁾ consider that if gaseous diffusion is controlling the reaction sites must be close together and close to the exterior edge of the interface where the reductant is available. Thus the interface will be narrow and well defined. As other steps become significant the interface becomes ill defined and reaction occurs at scattered sites.

Equimolar gaseous diffusion has been shown to be a rate-controlling process in reduction systems. Values of the apparent activation energies and of the diffusion coefficient would indicate whether or not gaseous diffusion is contributing significantly to the reduction process.

1.3.2. Chemical Reaction:

The chemical theory developed for homogenous gas reactions has supplied the principles used in analysing the chemical reaction at the phase boundary. The driving force for the overall reaction is the difference in free energies between the initial and final states.

The absolute reaction rate theory was developed by Eyring and states that a rate process is characterised by an initial state which passes continually to a final state. There is an energy barrier between the initial and final states. The lowest energy path over the barrier is the probable path for the reaction. The critical state at the maximum energy position on this path is termed the activated complex.

McKewan ^(77 - 81) used the absolute reaction rate theory to interpret his results. He expressed the rate of a reaction taking

place on a surface as:

$$R_o = K_o (\prod_i C_i) \cdot K' \quad (16)$$

$$K' = K \frac{k_b T}{h} e^{-\Delta H^\ddagger/RT} e^{\Delta S^\ddagger/R} \quad (17)$$

$$[\prod_i C_i] = [H_2] \quad (18)$$

$$\text{therefore } R_o = K_o \cdot \frac{k_b T}{h} \cdot [H_2] e^{-\Delta H^\ddagger/RT} e^{\Delta S^\ddagger/R} \quad (19)$$

K_o - includes no. of active sites, surface roughness
adsorption term, (temp. dependant) conversion factors.

$[\prod_i C_i]$ product of concentrations

K' - specific reaction rate

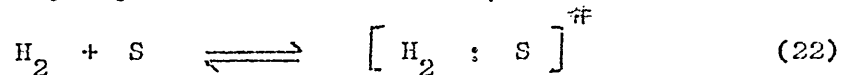
$K = 1$, transmission coefficient

A plot of $\ln R_o$ v $1/T^\circ K$ yielded a straight line with a break
at $570^\circ C$. Values R_o were obtained:

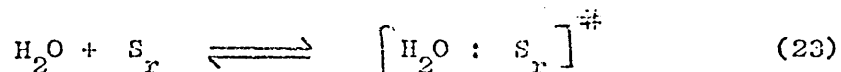
$$R_o = 7.32T [H_2] e^{-64.0/RT} \quad (\text{S.I. units}) \quad 570^\circ C. \quad (20)$$

$$R_o = 9.12T [H_2] e^{-62.0/RT} \quad (\text{S.I. units}) \quad 570^\circ C. \quad (21)$$

A mechanism was suggested involving the chemisorption of hydrogen
on active sites at the oxide-metal interface which is consistent with
the apparent activation energies and the first order rate dependence
on $[H_2]$. An alternative would be the collision of hydrogen mole-
cules with an active oxide surface. The forward reaction was the
reaction of hydrogen with an active site, S to form activated complex.

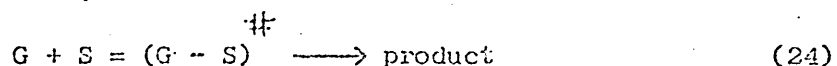


and similarly on desorption r - reacted.



Reaction on a sparsely occupied surface was said to occur with
site poisoning by water vapour due to an oxidising reaction.

In general:



McKewan considered that as the reduction rate was proportional to the hydrogen partial pressure then interfacial reaction was controlling. Warner ⁽¹³⁰⁾ points out that this is also possible with a mixed control reaction and that a 6% error in the data would make separation impossible. He also showed that if the interfacial process is based on the calculated interfacial gas composition then the activation enthalpy would be 63 K.J./mol (15 K.cal/mol) and entropy 28 - 33 e.u. which is characteristic of a simple chemical reaction with a solid surface site. This opposes McKewan's values which indicate the unsound theory of Van der Waal's adsorption. Warner points out that if the interfacial gas composition was the same as the bulk gas phase composition as required by interfacial reaction control, the reduction rates would be 100 times faster. In addition the enthalpy and entropy values are insensitive to reaction rates which indicate that agreements in value do not mean agreement in mechanism.

Quets et.al. ^(99, 100) also used the absolute reaction rate theory and considered the mechanism to involve the formation of vacancies followed by steady state vacancy diffusion and iron ion diffusion. Support for an ion vacancy mechanism was given by the existence of wustite below 570^oC. where the wustite formed a protective layer the reaction was said to be controlled by the concentration of hydrogen in the gas phase and the cation concentration in the wustite which is in turn controlled by the equilibrium between magnetite and wustite at the magnetite - wustite interface.

Auto catalysis may be operative especially during the early stages of reduction ⁽¹²⁰⁾. A rate minimum which has been shown to occur at 11% reduction (stoichiometrically no hematite left) and

low temperatures may be due to the wustite or iron molecules reacting immediately with hematite to form magnetite, so that wustite or iron cannot appear until all the hematite is reacted. At high temperatures, however, all the oxides have been shown to co-exist. An induction period had been reported which may be due to the initiation of the reaction at active sites from which it spreads out until all the surface is covered. Reduction then continues inwards. Autocatalysis may thus be only observed if the induction period can be recorded, i.e. at low temperatures.

The linearly advancing interface was first noted by Stalhane and Malmberg and developed by McKewan. They also pointed out that an autocatalytic reaction operating beyond the induction period should give rise to a linear rate law.

In general the theories involve either the interaction between the reducing gas and an active site at the interface or the chainlike reaction between reactant and product.

1.3.3. Solid State Diffusion

Several workers have considered the solid state diffusion of ions in the reduction process.

Roth (101) suggested there were two diffusing entities in wustite:

- (i) a single electron hole, responsible for electrical transport, with a high mobility, and
- (ii) the ferric ion in a tetrahedral position between octahedral vacancies and responsible for mass transport.

Moran (82) suggested from this a diffusion sequence

- (i) the tetrahedral ferric ion passes into the octahedral vacancy in the direction dictated by the concentration gradient.

(ii) the electron deficit passes to the ferrous ion adjoining the vacancy on the 'downstream' side i.e. in the direction indicated by the electrical potential gradient.

(iii) the ferric ion now moves to one of the tetrahedral sites adjoining it in the direction set by the concentration gradient.

Wagner⁽¹³²⁾ considered that in the first stages of reduction there is an increase in the metal:oxygen ratio which is due to the filling of cation vacancies and decreasing the number of cations in the higher valence states. After an induction period the oxide phase will become supersaturated with respect to the metal. Since the reductant acts at the surface Wagner suggests that surface supersaturation will be greater than in the bulk oxide phase and nuclei will form at the surface. In the vicinity of the nuclei supersaturation will sharply decrease and cation and electron diffusion to the metal-oxide interface will occur. Eventually anions may migrate and no further nuclei will occur. Wagner disregarded the possibility of anion migration and of breakdown in growth of the primary nuclei.

The following stages are considered ^(26, 27, 31) to occur during reduction (similar to Wagner):

- (i) breakdown of oxygen lattice and formation of iron phase at the wustite-iron phase boundary (or wustite-iron-gas boundary of iron phase porous or cracked.)
- (ii) diffusion of iron across the wustite layer to magnetite
- (iii) migration of iron into the magnetite at the magnetite wustite phase boundary during the formation of the wustite phase and without any considerable change in the oxygen lattice.

- (iv) diffusion across a dense magnetite layer
- (v) phase boundary reaction hematite \rightarrow magnetite, accompanied by transformation of the oxygen lattice from hexagonal to cubic close packed.

High rate constants have been obtained ⁽³¹⁾ indicating high ionic mobilities in the wustite lattice. The activation energy was shown to be 140 K.J./mol (33K.cal/mol.). Gellner and Richardson ⁽⁴¹⁾ also proposed the diffusion of excess iron atom through vacant sites in the wustite and considered that the process would have an activation energy of the order 210 K.J./mol. (50K.cal/mol.)

A schematic diagram for the oxidation process was proposed by Hauffe and modified by Edstrom ⁽²⁶⁾ for carbon monoxide reduction. A further modification for hydrogen reduction has been made and the diagram shown in figure 2.

Due to the crystal structure difference between hematite and magnetite, control by transport processes, in this case, is unlikely to be significant. The effect of impurity cations on reduction of ⁽⁸³⁾ magnetite has been studied and it is proposed that the reduction followed steps similar to those shown earlier ^(132, 27, 26, 31). Diffusion through wustite was said to be ⁽⁸³⁾ significant between 600°C. and 900°C. Above 900°C. the reaction at the hydrogen-wustite interface was thought to be controlling.

Annealing of oxides, before reduction, enhanced reduction rates ⁽⁴⁸⁾ due to an equilibration of surface defects caused by adsorbed oxygen diffusing into the oxide. This would operate on the positive holes to a greater extent than on the slower moving vacant cation sites. This was further shown by chromic ion doping which reduced positive hole concentration and increased vacant cation sites thus enhancing reduction. Fensham ⁽³²⁾ showed that increasing numbers of positive

holes increased the reduction rates for nickel oxide. The increasing numbers of positive holes suggested that acceptor holes for positive holes were adsorption centres in the pre-nucleation stages of reduction. Hauffe's work shows that vacant lattice sites become more important in the later stages.

The chemical diffusion coefficients between 900°C. and 1100°C. for the reduction of wustite were up to forty times that for the diffusion of iron in wustite (74). The rate of vacancy diffusion decreased with increased vacancy concentration, and upon doping with a trivalent ion. This contrasts with work by Birchenall et. al. (25, 49) who showed that the self diffusion of iron in wustite increased with increased vacancy concentration. Engell (36) shows, using Birchenall's results, that vacancy diffusion at 800°C. decreased with increased vacancy concentration. Analysis of the kinetics showed that the diffusion process and not the phase boundary reaction was rate controlling. The activation energies for vacancy diffusion were found to be:

100 - 160 K.J./mol. which compares with

120 K.J./mol. given for self-diffusion of iron in wustite (49).

Landler and Komarek (75) found a similar reliance of the chemical diffusion coefficient on vacancy concentration. The activation energy for self diffusion of iron in wustite was found to be 150 K.J./mol. (36 K.cal/mol.) Kinetically the reduction of wustite was found to follow a combined surface plus solid state diffusion reaction.

There is no doubt that iron ions or cation vacancies diffuse through an oxide layer, probably under the driving force of a concentration gradient of vacant lattice sites.

The mechanism of solid state diffusion can be fully or partly rate-controlling depending on the reduction conditions. Usually where there is a protective layer of product either of wustite or iron, then solid-

state diffusion becomes significant.

1.4 Laws of Reduction

The heterogeneous reduction of iron oxides may be considered to involve three basic processes:

- (i) diffusion of reactant and product gases through a boundary layer.
- (ii) diffusion of reactant and product gas and ions through the particle.
- (iii) the chemical reaction at the interface.

1.4.1. Diffusion through the gaseous boundary layer.

If diffusion through the boundary layer is the slow step involved in the reaction, then it is reasonable to assume that the chemical reaction should replenish the product gas molecules at the surface of the particle as fast as diffusion can remove them.

By increasing the flow rate, the influence of the boundary layer can be minimised. Many workers (26, 78, 105, 120, 125) have shown that the rate of reduction depends on the gas flow rate up to a critical value. Above this value no appreciable influence on reduction is observed. It has been assumed that above this value the mass transfer coefficient is sufficiently large so as to ensure that boundary layer diffusion is not controlling. The use of the Ranz equation, according to Warner (130), shows that from

$$\text{Nu} = 2.0 + 0.6 (\text{Re})^{0.5} (\text{Sc})^{0.33} \quad (25)$$

the range of Reynolds numbers employed to establish the 'critical' gas flow is unlikely to affect the gas film mass transfer coefficient. The establishment of critical gas velocity is said to ensure only that the system is not suffering from reducing gas starvation (42, 130).

Increasing the Reynolds number from 1 to 2, i.e. doubling the

gas velocity would increase the mass transfer coefficient by only 15% (43, 105).

Kostelov and Rostovtsev (61) show that for a Reynolds number of 1 the resistance of the boundary layer can contribute 12% to 15% of the total resistance and 5% to 6% at a Reynolds number of 20.

The gas flow rate has an effect on the reduction rate up to a critical flow rate. It has been considered that the critical flow rate is due to the removal of boundary layer resistance. However, other workers consider that flow rate does not greatly influence the mass transfer coefficient and consider that the critical flow rate prevents reducing gas starvation. Flow rates in excess of the 'critical' flow rate have been used in the present work. It may be considered that the resistance effect of the boundary layer is small if the flow rate is above the 'critical' flow rate and any effect would be incorporated in the product layer resistance.

1.4.2. Solid State Diffusion through Solids

When material transport is the rate controlling process it is necessary to add another term to the time and space co-ordinates. This term is the diffusion coefficient of the migrating species.

On considering a reaction between two solid materials with a planar surface, the reactants have to diffuse across a product layer as the reaction proceeds. If the process is uni-directional the rate of growth of the product layer is:

$$\frac{dy}{dt} = D \cdot \frac{k}{y} \tag{26}$$

on integration

$$y^2 = 2k \cdot D \cdot t + c \tag{27}$$

for $y = 0$ when $t = 0$

$$y^2 = 2k D \cdot t = k t \tag{28}$$

Equation (28) is the well known parabolic law. Jander ⁽⁵⁸⁾ applied the parabolic law developed for planar interface reactions to solid state diffusion in powdered compacts. He made several geometric assumptions.

- (i) a coherent product layer is formed
- (ii) bulk diffusion is uni-directional
- (iii) product volume : reactant volume ratio is unity and also
- (iv) the diffusion coefficient of the species transformed is not a function of time. He then applied a sphericity factor to the parabolic rate law such that:

$$y = r_o \cdot \left[1 - (1 - x)^{1/3} \right] \quad (29)$$

and combined equations (28) and (29) to give:

$$\frac{2k D t}{r_o^2} = \left[1 - (1 - x)^{1/3} \right]^2 \quad (30)$$

Equation (30) is the Jander equation relating the fraction of reaction completed to time, for spherical particles.

Other workers ^(62, 63, 121, 136) have modified the Jander equation after considering the validity of his assumptions. Ginstling and Brounshtein ⁽³⁹⁾ considered that Janders ⁽⁵⁸⁾ basic assumption of a parabolic rate law was invalid. They indicate that the parabolic law assumed the reaction surface area remains constant. This is not true for spherical particles where the area of the reacting surface decreases with time. They discarded the parabolic law in favour of Barrer's ⁽³⁾ equation for steady state heat transfer through a spherical shell. They considered that the rate of change of unreacted volume was analagous to the flux of heat diffusing through a spherical shell such that:

$$\frac{2k D t}{r_o^2} = 1 - \frac{2x}{3} - (1 - x)^{2/3} \quad (31)$$

Several modifications of equation (31) can be made. Carter et.al. (17, 126) took into account differences in volume between the product layer and the consumed reactant. This is difficult to apply owing to the lack of high temperature density data.

The volume correction is only significant where the product volume : reactant volume ratio is greater than 2. (40)

Edstrom (26 - 30) considered that, qualitatively, a solid state diffusion mechanism was operative in the reduction of iron oxides. Other workers (31, 82, 83) also support this view.

1.4.3. Gaseous Diffusion through Solids

Resistance to mass transfer across the boundary layer can be reduced by the provision of a rapid gas flow rate around the sample. This ensures that there is no build-up of product gas at the sample surface. Above this critical velocity reduction can be controlled by gaseous diffusion. Bogdandy and Janke (4) show from activation energy values of 13k.J/mol (3.2 k.cal/mol) that gaseous diffusion was controlling since the value compared closely with calculated values for the heat of diffusion (2).

The rate of evolution of water vapour from the pellet should equal the velocity at which the reaction front progresses.

The respective rates can be equated (4) to give

$$\frac{d R_x}{d \theta} = \frac{3 \epsilon_r^D v \eta ([H_2O]_e - [H_2O])}{(1 - \epsilon) \omega r_o^2 [(1 - R_x)^{1/3} - 1]} \quad (32)$$

In equation (32) the labyrinth factor represents the amount of hinderance to diffusion through pores, and increases with reduction. Factors such as density, porosity, size and shape affect the labyrinth factor.

Until 1962 only a few workers (4, 64, 65) had eliminated the effect of boundary layer diffusion before considering gaseous diffusion

through the porous sample. Work carried out on fixed beds is limited by the introduction of boundary layer diffusion due to variation in flow rates around particles through the bed. However, Tenenbaum and Joseph in 1939 (122) indicated that reduction was affected by gaseous diffusion. Udy and Lorig (125) on reduction of single pieces of magnetite considered that the continuous growth of the metallic layer could inhibit gaseous diffusion.

Several workers (125, 130 44) have derived equations or terms of mixed equations to describe the effect of gaseous diffusion which is similar to that which may be derived from Fick's Law such that:

$$N = \frac{D \cdot A_m (P_a - P_e)}{R.T. [(r_o - r) + \delta_o]} \quad (33)$$

Similarly Warner (130) used a term in his mixed control equation when studying the effect of pressure on hematite reduction which was of the same form.

$$\text{rate} = \frac{D_{AB}}{R.T. \Delta x} (P_{g,H_a} - P_{e,H_a}) \quad (34)$$

Olsson and McKewan (92) also considered diffusion across the boundary layer, diffusion through the porous sample, and diffusion between the inner sample surface and the wustite granules. The first and third steps are combined in a mass transfer coefficient k_c :

$$J = \frac{C_g - C_e}{\frac{1}{k_c} + \frac{\Delta x}{D_{\text{eff}}}} \quad (35)$$

Manning and Philbrook (84) showed that if shell diffusion resistance overshadows both boundary layer diffusion and chemical reaction the diffusion model has a curvilinear time dependence:

$$\frac{t}{t_c} = 1 - 3 \left(\frac{x_i}{x_o} \right) + 2 \left(\frac{x_i}{x_o} \right)^3 = 1 - 3 (1 - R_x)^{2/3} + 2(1 - R_x) \quad (36)$$

1.4.4. Chemically Controlled Reaction Rate

According to Laidler (70) when a discontinuous product phase

occurs the rate determining step may be the chemical process occurring at the phase boundary. In such cases the rate is determined by the surface area available for reaction. These processes are termed topochemical.

Contracting volume, kinetic models can be used to describe the phase boundary control of reduction:

$$- \frac{dV_t}{dt} = kS \quad (37)$$

$$(1 - x) = \frac{V_t}{V_o} = \frac{\frac{4}{3} \pi r_t^3}{\frac{4}{3} \pi r_o^3} \quad (38)$$

$$\frac{d(1 - x)}{dt} = \frac{kA_t}{V_t} \quad (39)$$

therefore: $\frac{dx}{dt} = \frac{3k}{r_o} (1-x)^{2/3}$ (40)

for $x = 0$ when $t = 0$
 $kt = 1 - (1 - x)^{1/3}$ (41)

For phase boundary reaction control a significant feature is the linear rate of advance of the reacting interface. Many workers (77 - 81, 99, 100, 131, 47, 123) have used the phase boundary model developed above and have considered that linearly advancing interface indicates chemical reaction control. McKewan (77 - 81) included a particle size term in the equation. Hansen (45) et.al. has used the concept of a linearly advancing interface to develop a reducibility index. Bicknese and Clark (5) found that the law was not particle size dependent as did McKewan. All the workers note a deviation from linearity in the final stages of reduction.

Approximate linear growth is also consistent with a mixed control mechanism (129). Also in a reaction controlled by heat and mass transfer, the interface can appear to move at a constant rate (43).

Some authors (71, 94, 125) have assumed that the reduction of iron oxides is a first order reaction:



$$-\frac{dc}{dt} = kc \quad (43)$$

therefore: $\ln c = -kt$ (44)

and $c = C_0 e^{-k(t-t_0)}$ (45)

thus the concentration of reactant decreases exponentially with time. Smith ⁽¹⁰⁶⁾ has also used this law. The law is however, of the same form as that developed by Themelis and Gauvin ⁽¹²⁰⁾ for control by unsteady state diffusion. Thus if the data follows an exponential law it does not necessarily indicate a first order reaction. A first order reaction is, in fact, valid only for homogenous reactions where all parts of the system are reacting by the same amount at the same time. It can, however, approximate to a reduction situation.

In general there are three mathematical models to describe the limits for mechanisms of reduction. Themelis and Gauvin ⁽¹²⁰⁾ have summarised previous work and proposed the most suitable models for diffusion controlled reaction:

from Fick's laws

$$\frac{\partial c}{\partial t} = D_v \left[\frac{\partial^2 c}{\partial r^2} + \frac{(2)}{(r)} \left(\frac{\partial c}{\partial r} \right) \right] \quad (46)$$

The solution of this equation for fractional reduction is:

$$R_x = \frac{Q}{Q_\infty} = 1 - \frac{6}{\pi^2} \sum_{n=1}^{\infty} \frac{1}{n^2} e^{-4D_v n^2 \pi^2 t / d_p^2} \quad (47)$$

Neglecting all values for the series, of $n > 1$

$$R_x = 1 - \frac{6}{\pi^2} e^{-kt} \quad (48)$$

therefore $\ln(1 - R_x) = \text{constant} - \left(\frac{4D_v \pi^2}{d_p^2} \right) \cdot t$ (49)

This is valid for all reduction systems controlled by any diffusion phenomena through the body of the sphere. The time required for different sizes of spheres to obtain the same degree of reduction

should be proportional to the square of the diameters.

Several workers have used more than one law in an attempt to elucidate the controlling mechanism. Smith (106, 107) used four possible laws: the first order reaction law, the parabolic diffusion law, the linearly contracting interface law and the zero order law. By examination it was found that the best fit was afforded by the exponential law. Themelis and Gauvin (120) show that this law approximates to a diffusion law. Second best fits could be made by the parabolic diffusion law and then the surface reaction law. No single law fitted the data exactly.

Manning and Philbrook (84) and Levenspiel (72) also suggest that more than one law may apply.

Levenspiel (72) indicated that the different laws, and thus control mechanisms, were easily separable. Spitzer et.al. (105) considered that this was not easily carried out. Warner (129) showed that a greater than 6% error in the data precluded the possibility of distinguishing between a surface reaction law and a mixed control law.

1.4.5. Combined Reduction Laws

It can be seen from previous consideration of single step reduction models, that in all models considered, there is either a deviation from agreement with the law considered or there is a theoretical consideration why such a law, on its own, is not sufficiently rigorous to fully describe the reduction reaction.

It can be considered that the contribution or resistance to reduction of each mechanism may not be insignificant.

Themelis and Gauvin (120, 123) combined chemical reaction with diffusion laws:

$$1 - R_x = C_1 e^{-\left(D \pi^2 / r_0^2 + k \right) / t} \quad (50)$$

such that when $k \gg D \pi^2 / r_o^2$ then the chemical reaction is predominant and when $k \ll D \pi^2 / r_o^2$ then diffusion control is predominant.

Cox and Ross (18) showed that the McKewan (77) relationship operated only within a limited temperature range and that a parabolic relationship was otherwise valid.

Lu (73) considered that both chemical reaction and diffusion resistances to reduction were significant and developed a two-step model.

A modified form is:

$$\frac{r_o c_g t}{\rho_o} = \frac{r_o (r_o - r_i)}{k_1} + \frac{1}{6 D_{eff}} (r_o + 2r_i - 3r_o r_i^2) \quad (51)$$

A composite model has been derived (108) in an attempt to simulate the blast furnace.

Warner also (120) considered that the reduction reaction was a function of gaseous diffusion and chemical reaction control. He developed his two step model by considering the reduction of a hematite sphere, the rate of mass transfer across the boundary and each of the product layers being equal to the rate of reaction at the interface.

Seth and Ross (109) also derived a two-step model by considering chemical reaction and diffusion terms. The equation was similar to that derived by Lu (73). Seth and Ross (110) successfully applied their equation to their data and the data of other workers.

Spitzer et.al. (105) considered that none of the individual transport and reaction resistances can be neglected in the development of a physically significant model. A three-step model was developed which included a boundary layer resistance which is constant for constant gas flow and product shell and chemical reaction resistances. Spitzer (105) further showed that his combined equation could be used successfully and a linearly advancing interface be observed.

Other workers have also used multi-step models in order to explain reduction mechanisms.

1.4.6. Conclusions

It can be seen that there are, in general, three limiting laws for reduction. These are firstly surface boundary layer diffusion which, some workers consider, should not be ignored. However, it is apparent that above a 'critical' gas flow rate its effect on reduction rate is negligible. It is also constant with constant flow rates. Secondly bulk diffusion for which equations for both iron ion diffusion and counter diffusion of product and reactant gases have been developed. Molecular diffusion or Knudsen diffusion has been supported by several workers. The parabolic diffusion law has been used to follow ionic diffusion which many workers consider plays a part.

The diffusion equation as developed by Themelis and Gauvin can be used to describe both gaseous and ionic diffusion.

Thirdly surface reaction control has been proposed by many workers, notably McKewan.

It is now accepted that a single limiting case cannot adequately describe the reduction of iron oxides. Because of this both two-and-three-step models have been proposed. In two-step models the resistance due to diffusion across a boundary layer is usually omitted. This is justified by the operation of the tests above a 'critical' gas flow rate such that the flow rate no longer affects reduction rate. The critical flow rate at least ensures that reductant gas starvation does not occur and that the boundary layer resistance is constant and can be incorporated into product layer resistance becoming less significant as the product layer increases. Warner⁽¹³⁰⁾ and Hills⁽⁴³⁾ both consider that mass transfer across the boundary layer is significant at all times.

In three-step models all limiting cases are included although the bulk diffusion term is usually specific for gaseous diffusion.

In the present work four limiting cases are considered initially two are later omitted and a two-step model is considered adequate.

1.5 REDUCTION OF MAGNETITE:

1.5.1. General

Iron oxide reduction is a complex process.

Above 570°C. the reduction of magnetite involves the steps magnetite \rightarrow wustite \rightarrow iron.

Previous work indicates ⁽¹²⁰⁾ that solid reactions propagate in such a way that the reaction interface remains nearly parallel to the crystal face from which it originates. The crystallographic reversibility of magnetite \rightleftharpoons wustite and wustite \rightleftharpoons iron has been shown by Bujnor et.al. When oxide and product axes are parallel then a smooth product will result.

Reduction of magnetite by hydrogen has been shown ⁽¹¹²⁾ to commence at 325°C. and a metallised shell advanced from the outside to the centre with time. The increased resistance to outward diffusion of water vapour by the product layer was considered to be due to the increased product layer thickness. The reduction in interfacial surface area was thought to a contributing factor.

They also showed ⁽¹¹²⁾ that the thermodynamic potential for reduction increased with temperature for both magnetite and wustite reduction. The initial reduction rates also increased regularly indicating the importance of the thermodynamic driving force. Product pressure increased behind the iron film and these pressures were shown to be capable of disrupting the iron film formed, allowing reduction to continue. Edstrom ⁽²⁷⁾ also considered the iron film to act as a semi-permeable membrane and gas pressure build up to burst the film.

Huebler (52) showed that the pressure build up due to hydrogen reduction was insufficient to cause bursting. Bursting was only possible with carbon monoxide reduction.

The faster rate of reduction of hematite compared with magnetite was due to the earlier and more extensive pore formation in the reaction product (27).

The reduction rate has been shown (79, 80, 99, 100) to follow McKewan's relationship.

As a result of this the reaction was thought to be controlled at the iron-iron oxide interface.

The reduction mechanism is thought to involve the adsorption of hydrogen on the surface prior to reduction. Quets et.al. also considered the control to be at the oxide surface by the formation of oxygen anion vacancies accompanied with vacancy diffusion and iron ion diffusion.

The protective nature of the wustite formed on the reduction of magnetite above 570°C. has also been pointed out (99, 100). The solid state reduction of magnetite has been shown (31) to follow a parabolic relationship with time indicating control by mass transport across a dense wustite layer.

Edstrom (29) considered the mechanism of reduction to follow the stages:

- (i) break down of oxygen lattice and formation of iron.
- (ii) diffusion of iron across wustite to magnetite
- (iii) migration of iron into magnetite.

The influence of addition of foreign cations has been used (83) to propose a similar reduction mechanism. Their results indicated that some interface reaction control was also evident. Interface reaction control became predominant above 900°C. The contribution

of diffusion control was most apparent where there was a large amount of retained wustite and a diffuse interface.

Broadbent (15) and Goth (138) have shown that the porosity increases with degree of reduction. Broadbent associated an increase in temperature coefficient with a decrease in pore formation. Pores were said to be formed by the condensation of vacancies at the iron-iron oxide interface. They become isolated as the interface advances. The rate controlling mechanisms were shown to be mixed, varying from complete diffusion control at lower temperatures to probably chemical control at higher temperatures.

Goth also considered that a mixed control mechanism operated with the rate of diffusion controlling in the initial stages of reduction with surface reaction control becoming significant in later stages.

Beeton (6) showed the temperature coefficient for reduction of magnetite to be 59K.J./mol (14K.cal/mol) which applied both above and below a break in the reducibility curve at 620°C. This was in agreement with McKewan's results and indicated interface reaction control.

Warner (129) showed that the evidence of a linear reduction rate, a first order relation between hydrogen partial pressure and rate, and penetration rate independent of diameter can be exhibited by mixed control mechanisms as well as being typical of chemical control. He showed that even a small amount of scatter in the experimental points can preclude differentiation between chemical and mixed control.

Hills (43) also considers that the linearly contracting interface of chemically controlled topochemical reactions are similar to those for transport controlled topochemical reactions.

It can be seen that there is conflicting evidence regarding the controlling mechanism for the reduction of magnetite by hydrogen.

Solid state diffusion (27, 52, 31, 29) gaseous diffusion (112, 125),

surface reaction control (79, 80, 99, 100) and mixed control (83, 15, 138, 129, 43) have all received support.

1.5.2. Reduction Rate Minima

The reduction of magnetite is characterised by the existence of reduction rate minima which have been reported (76, 85, 99, 100) at temperatures above 570°C. This phenomena has also been reported during hematite reduction (112, 113, 50).

The phenomena has variously been explained by changes in ore microporosity (50), by sintering and recrystallisation (112, 90), by changes in the magnitude of the thermodynamic driving force (23), and by the reduction of water vapour permeability in iron (50). Edstrom (26) explains the rates as due to the formation of a protective layer of wustite impeding diffusion.

Several workers (79, 80, 47, 131) have reported a break in the temperature coefficient rather than a rate minimum.

Specht and Zappffe (112) found a rate minimum to occur between 700°C. and 800°C. above 40% reduction. Because there was no maximum or minimum on their free energy plots they concluded that it was a result of sintering or recrystallisation of the product layer.

The rate minimum above 600°C. has been attributed (140) to the formation of continuous layers of wustite.

Edstrom (29) showed metallographically that the rate minimum was associated with the formation of a dense wustite layer. He also showed a discontinuity at 900°C. which was attributed to the $\alpha - \gamma$ transition at 910°C.

Strangway et.al. (118, 119) showed a rate minimum to occur at 600°C. to 700°C. A mixed control mechanism was postulated for the temperature range over which the rate minimum occurred. Metallographically no iron shells were seen and the minimum was associated with

retained wustite.

X-ray studies showed that the iron:oxygen ratio is at a minimum in the unreacted grains. This corresponds to the maximum vacancy concentration which would tend to decrease the amount of iron ion diffusion. They also showed that the lattice spacing in the unreacted wustite was at equilibrium with iron at the wustite-iron interface at all temperatures. This was not the case at the magnetite-wustite interface where the spacing was always larger than at equilibrium. This would enhance iron ion diffusion. The contradiction was not explained. The temperature coefficient for the rate minimum temperature range was 164 K.J./mol (41K. cal/mol) which also indicated iron ion diffusion control.

Later work ⁽¹³⁹⁾ showed a temperature coefficient of 65 K.J./mol (16.3 K.cal/mol) for 10% reduction and 41 K.J./mol (10.3 K.cal/mol) for 80% reduction indicating interfacial and gaseous diffusion control respectively. A plot of the data using Seth and Ross's combined rate equation yielded a straight line.

X-ray diffraction showed the rate minimum to be associated with a minimum value for the wustite lattice spacings.

Quets ⁽⁹⁹⁾ et.al. show a deviation in their Arrhenius plots at the $\alpha - \gamma$ transition temperature indicating that reduction was structure-sensitive. This they claimed did not support the postulated interface reaction control. Although the adsorption step in chemical reaction may be structure sensitive.

Broadbent ⁽¹⁵⁾ associated rate minima at 700°C. to 750°C. and 900°C. with the formation of dense wustite. Micrographs, however, show that a dense shell of iron surrounds the wustite grains at 900°C. Goth ⁽¹³⁸⁾ also attributed the rate minimum at 900°C. to

retention of dense wustite. He also observed retained wustite surrounded by dense iron shells.

Bitsianes and Joseph ⁽¹⁶⁾ also showed an exaggerated degree of wustite retention on reducing magnetite by hydrogen. This was associated with a falling off in reduction rate between 650°C. and 900°C. after 40% reduction.

It is very apparent, from a search of the literature, that there is considerable doubt as to the rate controlling mechanisms of magnetite reduction and to the reasons for the occurrence of rate minima.

1.6 Constitution and Reducibility of Sinter

The addition of impurities to pure iron oxides and the presence of naturally occurring impurities can materially affect the reduction rates.

1.6.1. Constitution:

Hancart et.al. ⁽⁵⁶⁾ indicated the presence of three major phases in sinter matrices. These were:

- (i) silico-ferrite of calcium and alumina (S.F.C.A.)
- (ii) iron-calcium alumina-silicate; similar to iron gehlenite
- (iii) vitreous gangue.

The S.F.C.A. phase was shown to greatly influence sinter cohesion. S.F.C.A. formation was favoured by increasing the formation temperature. Above 1200°C. it decomposes to give magnetite.

Mazanek and Jasienska ⁽⁸⁸⁾ showed that the addition of 12% alumina forms calcium-alumino-ferrite which is highly reducible. Low percentage additions of alumina form the irreducible brown-millerite.

Harbord and Goldring ⁽⁵⁵⁾ considered that the constitution and micro-structure of sinters was dependent on the characteristics of the ore feed and conditions imposed during the sintering process.

They showed the primary constituents of a lean magnetite sinter similar to the one used in the present work to comprise hematite, magnetite, wustite calcium ferrites, quartz, lime, melilite (a solid solution of $2\text{CaO} \cdot \text{MgO} \cdot 2\text{SiO}_2$ and $2 \text{CaO} \cdot \text{Al}_2\text{O}_3 \cdot \text{SiO}_2$), β - dicalcium silicate ($2\text{CaO} \cdot \text{SiO}_2$), glass and olivines (solid solution of $2\text{CaO} \cdot \text{MgO} \cdot 2\text{SiO}_2$ and $2 \text{CaO} \cdot \text{Al}_2\text{O}_3 \cdot \text{SiO}_2$), β - dicalcium $\text{CaO} \cdot \text{FeO} \cdot \text{SiO}_2$, $2\text{FeO} \cdot \text{SiO}_2$ and $2\text{MgO} \cdot \text{SiO}_2$).

The magnetite was formed most commonly by recrystallisation from the melt to form euhedral crystals. The wustite occurred as fernleaf dendrites hematite formed by oxidation of the magnetite and proceeded along the octahedral planes in the magnetite. Maghemite was not observed. The exact composition of the ferrites was difficult to determine because of cation replacement by other similar cations.

Post solidification reactions were considered to be relatively unimportant due to their inhibition by the silicate matrix.

1.6.2. Reducibility

Strangway and Ross (118) added between 7% and 10% of calcium carbonate to ferric oxide and found that reduction rates by hydrogen, between 600°C . and 1000°C ., increased. The improvement was attributed to an increase in porosity, to more easily dissociated wustite and to the promotion of induced porosity on reduction. The McKewan relationship applied throughout and Seth and Ross's mixed control equation did not apply. This indicated that the interface reaction was rate-controlling. However, porosity changes and their effect on instantaneous interfacial area were ignored.

The addition of 1% potassium oxide enhanced reduction rate by greatly distorting the magnetite lattice. (38)

Work has also been carried out on the properties of minerals which make up a sinter matrix,

Sinter reducibility, A, depends on the mineralogy. Coheur (22) attempted to quantify this by putting:

$$A = \frac{a \text{ Fe}_2\text{O}_3 + c \text{ SFCA}}{\text{Fe}} \quad (52)$$

Mazanek and Jasienska (88) showed that since the heat of formation of mono-calcium ferrite was more negative than it should form more easily than di-calcium ferrite. The mono-calcium ferrite dissociated at 1080°C. in the presence of silica. The di-calcium ferrite did not dissociate up to 1200°C. The greater ease of dissociation of the mono-calcium ferrite indicates that it should be more easily reducible.

An order of precedence for reducibility has been established (64, 87). The mono-calcium ferrite was found to reduce more easily than the di-calcium ferrite. The relatively high reducibility of ferrites compared with silicates was a noticeable feature.

Rueckl (102) agreed with this and also showed the reduction of ferrites to follow McKewan's relationship indicating control at the iron-ferrite interface.

The reduction of ferrite passes through several stages (20), Bruner (14) disagreed with Rueckl (102) and showed that the reduction of ferrites became retarded in the later stages. He pointed out that mono-calcium diferrite and mono-calcium ferrite reduce at the same rate in the later stages although, the porosity of the product layer in the mono-calcium di-ferrite was greater. This was a result of the porosity in the mono-calcium ferrite being concentrated at the interface boundary thus 'laying bare' the reaction surface and enhancing reduction. Pore size and distribution is, therefore, highly significant.

Barrie et.al. (10) indicated that mono-calcium ferrite was more easily reduced than di-calcium ferrite.

Pokhvisnev, et.al. (97, 98) considered that maximum cracking occurred on sinter reduction when hematite \rightarrow magnetite. They also showed that reduction of sinters first occurred at the surface and adjacent to straight through pores. Reduction commenced in the hematite regions where there was little unfused gangue or silicate. Idiomorphic magnetite crystals surrounded by silicate were reduced last. The first metallic iron to appear was in the form of globules both on the surface and inside the grain. The regions grew and coalesced forming a continuous white strip enclosing residues of glass or a dispersed mixture of metallic iron and oxides. Where there was little glass there was little cracking of the matrix.

Richardson (104) followed the reduction of lean magnetite sinters by hydrogen between 650°C. and 1010°C. Cracking of the grains was shown to occur during reduction. The cracking tendency increased with increasing temperature. Hickling (57) reduced the same material using carbon monoxide. Values of the temperature coefficients were found to be similar, in each case, for the reduction stage magnetite \rightarrow wustite.

			ref.
magnetite	\rightarrow wustite	$E = 63\text{K.J./mol (15K.cal/mol)}$	(15)
		$E = 90\text{K.J./mol (21.5 " ")}$	(16)
wustite	\rightarrow iron	$E = 36\text{K.J./mol (9 " ")}$	(15)
		$E = 88\text{K.J./mol (22 " ")}$	(16)

Hickling (57) showed a linearly advancing interface for all stages of reduction and all temperatures. The reduction was considered to be controlled at the reaction interface.

Smith et.al. (106) reduced lean magnetite sinters by carbon monoxide between 800°C. and 1000°C. They found that the reducibility increased with temperature. The surface reaction law was found to be supported by the variation of rate as $d^{-0.72}$ to $d^{-0.90}$ (compared with

McKewan's $R \propto d^{1.0}$) and a low value of the activation energy of 57 - 80K.J./mol (13.5 - 20K.cal/mol). However, diffusion and exponential relationships also gave a good agreement and the zoning effect after short times may be indicative of the control exerted by carbon monoxide diffusion through the matrix. Smith ⁽¹⁰⁶⁾ considered that reduction involved three simultaneous processes:

- (i) adsorption of carbon monoxide and migration through the matrix by diffusion and/or migration through capillaries in the matrix.
- (ii) reduction of outer ferruginous grains controlled by the surface reaction law.
- (iii) interference with mixed control by micro-cracking.

Jervis ⁽⁶⁰⁾ reduced lean magnetite sinters with a lime-silica ratio of 1 : 1 and a varying wustite content. Reduction was found to increase between 600°C. and 900°C. A close agreement with the exponential law was found in the early stages of reduction. In the later stages the phase boundary law was operative. Little metallographic evidence of topochemical reduction was found.

1.6.3. Thermal and Oxidation Treatment

Kissin and Litvinova ⁽⁶⁹⁾ and Mazenek and Jasienska ⁽⁶⁷⁾ have shown that sinter reducibility increases as the amount of glassy phase decreases.

Pokhvisnev et.al. ⁽⁹⁸⁾ and Vegman ⁽¹²⁸⁾ have confirmed that devitrification improves reducibility. Optimum temperatures of 1050°C to 1080°C. ⁽⁹⁸⁾ and 1050°C. to 1100°C. ⁽¹²⁸⁾ have been shown to give maximum devitrification. Other Russian work has been reported ⁽⁹⁸⁾ which confirms that heat treatment in an oxidising atmosphere between 900°C. and 1100°C. can improve sinter properties. A reduction in glass volume occurs which is said to increase porosity. Oxidation

of magnetite to the more reducible hematite also occurs.

Ferrite enrichment can be induced ⁽¹²⁾ by the addition of steam to the ignition hood. Water cooling has also been reported ⁽¹⁰³⁾ to improve reducibility.

Bojarski et.al. ⁽¹³⁾ have treated siderite concentrates at 1100°C. to 1250°C. in an oxidising atmosphere. Up to 1150°C. mono-calcium diferrite is formed which then dissociates into hematite and calcium silicate. The ferrite confers good reducibility but poor strength on the concentrate. Satisfactory reducibility and strength are obtained when the silicate forms and acts as a binder.

Control of firing conditions can control mineralogical composition ⁽³⁵⁾.

Oxidation of the magnetite grain in sinter transforms it to the more easily reducible hematite. However, Vasyntinsku and Volgai ⁽²⁷⁾ and Ball et.al. ⁽¹¹⁾ have shown that maghemite (γ - Fe_2O_3) occurs as an intermediate phase. The maghemite becomes stable at temperatures between 500°C. to 700°C. and 300°C. to 800°C. for pure and impure magnetites respectively.

Smith ^(106, 107) investigated the effect of the state of oxidation of lean sinters and confirmed that the more highly oxidised material was more reducible. This was associated with the presence of highly oxidised minerals and a higher matrix permeability. Marked improvements, in reducibility were obtained by high temperature (>1020°C.) sinter re-oxidation. Low temperature re-treatments were shown to be ineffective.

Although reducibility work carried out on sinters has mainly taken place on sinter beds in order to decide on its Blast furnace suitability little serious work has been carried out on determining the reduction mechanisms involved in the sinter piece. There is little

agreement between the work that has been carried out.

Oxidation and thermal treatment is well-established as an improving treatment but little attempt has been made to separate the thermal effect from the oxidation effect. Almost no work has been carried out in the low temperature region (i.e. less than devitrification temperatures) in order to decide whether such treatments are also useful.

CHAPTER 2

EXPERIMENTAL DETAILS

2.1. INTRODUCTION

The purpose of kinetic studies can be to determine the rate of reduction as a function of:

- (i) factors peculiar to the solid sample in its initial state, i.e. chemical composition, micrographic structure, porosity, shape and size;
- (ii) factors peculiar to the gas, i.e. total pressure P, and composition on contact with the sample;
- (iii) and temperature. Physical changes imposed by thermal treatment are also possible.

In the present work both magnetite and lean magnetite sinters have been investigated. In general, factors peculiar to the solid sample and peculiar to the gas have been kept constant. Mineralogical changes have been imposed on the sinter by means of oxidation. The major variable has been that of temperature.

2.1.1. Magnetite samples

Single pieces of naturally occurring Kiruna magnetite were selected within a weight range of 1150 ± 50 mg. (The standard deviation was calculated by normal statistical techniques using the arithmetic mean

$$\bar{x} \text{ and } \sigma = \sqrt{\frac{\sum (x - \bar{x})^2}{n - 1}}$$

The total porosity of the material was $< 4\%$ determined by means of a simple mercury displacement method. (Section 2.9.).

The shape of the samples was similar in all cases and approximated most closely to a sphere of nominal dia. 8 mm.

The composition of the magnetite was:

Fe _{TOT}	Fe ³⁺	SiO ₂	MnO	Al ₂ O ₃	CaO	MgO	P ₂ O ₅	CO ₂
66.8	22.1	3.50	0.29	1.55	0.45	0.95	0.70	0.55

Metallographically the magnetite consisted of dense equi-axed grains with isolated blocks of impurity. (Figure 6). Some of the samples had a blocky magnetite structure with cracks along the cleavage planes. (Figure 7). No apparent change in structure was observed when the magnetite was heated in argon to 1250°C and then furnace cooled. Samples of magnetite were reduced in hydrogen isothermally at temperatures between 400°C and 1100°C.

2.1.2. Sinter Samples

Samples of sinter were taken from the Seraphim sinter plant at the Appleby-Frodingham Works (Scunthorpe Group) of the British Steel Corporation.

The $-\frac{1}{2}'' + \frac{1}{4}''$ fraction was selected from the sample taken from the bunker discharge stream. The selected fraction was crushed, ground to -200 mesh and reconstituted into pellets by means of a disc pelletiser using water as a binder. The pellets were sintered for four hours at 1180°C in a pure argon atmosphere. The pellets weighed 340 ± 40 mg and had nominal diameters of 8mm and a porosity of $11 \pm 1.4\%$.

Prior to sintering the structure was typical of lean Scunthorpe Group Seraphim sinter. The micrographs (Figures 8, 9) show euhedral magnetite grains in a mainly silicate matrix, with some wustite dendrites (Figure 8) together with very small amounts of free iron. Some hematite associated with ferrite laths could be seen where the sinter was more highly oxidised. (Figure 9).

On sintering the composite nature of the structure disappeared. The wustite and ferrites became assimilated into the matrix and the hematite into the magnetite. (Figure 10). The grains were dense and there was some indication of a slight compositional variation

across them. (Figure 11). The pores were, in general, fairly evenly distributed (Figure 12), although in some cases they had become joined. (Figure 13).

The ex-works composition of the sinter was:

Fe _{TOT}	Fe ²⁺	CaO	SiO ₂	Al ₂ O ₂	MgO	MnO	S	K ₂ O	Na ₂ O	C	°oxid
38.70	11.90	18.6	14.7	7.03	2.40	1.07	1.68	0.56	0.20	0.05	89.7

A check analysis was carried out which confirmed the ex-works analysis.

2.1.3. Oxidised Sinter Pellets

Sinter pellets were fully oxidised at 500°C, 750°C and 1000°C in a steam of oxygen and then reduced in hydrogen at 800°C. The samples were fully oxidised. The (O/Fe) atomic ratio was increased from 1.35 to > 1.5. The porosity showed little or no change when oxidised at 750°C and 1000°C. However, oxidation at 500°C results in an actual porosity increase of 4.6 ± 1.5%. The pellet surfaces when oxidised at 500°C became flaky and in some cases shelled off.

The oxidation of the magnetite grains, at 750°C and 1000°C, to hematite could be clearly seen metallographically. (Figure 65a). Some oxidation of the matrix had also occurred. At 500°C although the pellet weight change indicated full oxidation to hematite there was little difference in the state of oxidation metallographically, (Figure 66) and the samples were magnetic. It was considered that the magnetite had oxidised to maghemite (γ -Fe₂O₃), which forms easily at low oxidation temperatures of the order of 500°C. (11) There is no optical difference between magnetite and maghemite. The physical break-up of the pellet shell could be seen clearly.

2.1.4. Thermally Treated Sinter

Sinter pellets were heat treated in argon at temperatures between 500°C and 1000°C. An optimum temperature for reducibility

improvement was found to occur at 750°C. At this temperature heat treatments were carried out for different combinations of heating and cooling rates.

TABLE 1

POROSITY %

	TEMPERATURE °C	BEFORE	AFTER	CHANGE
	500	11.3	10.5	-0.8
	650	11.7	10.9	-0.8
	750	10.8	10.9	+0.1
	850	10.8	9.6	-1.2
	1000	11.9	10.8	-1.1
INITIAL HEATING RATE (750°C)	INITIAL COOLING RATE (750°C)			
SH	SC	10.8	10.9	+0.1
FH	FC	11.2	10.2	-1.0
SH	FC	9.5	9.5	0
FH	SC	9.8	9.8	0

SH = .64°C/sec - slow heating

FC = gas quenched - fast cooling

SC = .24°C/sec - slow cooling

FH = plunged into hot zone - fast heating

Slight decreases in porosity were observed after heat treatment except at 750°C where a very slight increase was recorded. Similarly no change in, or a slight decrease in, porosity was noted when the heating and cooling rates were varied at 750°C. Excepting those which were heated at .64°C/sec and cooled at .24°C/sec where a very slight porosity increase was recorded. There was little variation in pellet diameters before and after thermal treatment.

2.2. Equipment

The principal methods of following reduction are:

- (i) microscopic examination of a section of the oxide sample, after cooling, from various stages of reduction.
- (ii) determination of the loss in weight of an oxide sample.

The first method reveals the evolution of the sample structure and discloses the distribution of residual oxygen between the different phases. The second method allows precision balances to be used.

In the present work the metallographic and the loss-in-weight methods were used in conjunction.

2.2.1. The Glass Spring Balance

The reduction apparatus shown in Figure 14, consisted of a glass tube (V) in which was suspended a pyrex glass spring (G) of internal diameter 19mm with 0.4 turns/mm and a filament diameter of .36mm. Hooks were formed at the ends of the springs by means of a very fine gas flame (provided by a drawn out glass jet). The ends of the spring were held such that, on softening, the hooks were formed by the end loops falling into the required position under their own weight. For improved accuracy the springs were annealed under load for 24 hours at 200°C.

Attached to the end of the spring was a 1mm diameter silica extension rod (E) and sample holder (S) of nickel gauze. The weight of the holder was adjusted before the commencement of each test so that it was within 2mm of the indicating thermocouple sheath. The tests were carried out in a refractory tube (R) heated by the electrical resistance furnace (F).

The changes in weight of the assembly were determined by measuring the change in position of the tip of the extension rod (E) by means of the cathetometer (M) which could be read to .05mm.

2.2.1.1. Temperature Control

Initially the furnace constant temperature zone (hot zone) was restricted to 25mm. The control thermocouple (C) was positioned on the furnace windings at the hot zone position. Control of temperature was carried out to $\pm 5^{\circ}\text{C}$ at 1000°C by means of a Kent Guardsman controller. A six-point recorder from the measuring Pt/Pt - 13% Rh thermocouple (T) recorded the hot zone temperature with similar accuracy.

Subsequently a new furnace was contour wound using Super-Kanthal to give a constant temperature zone of 40mm. The control was carried out by a solid state proportional temperature controller (SIRECT MARK II) manufactured by C.N.S. Instruments Ltd.

The temperature setting control consists of a fifty-turn slide wire potentiometer which was calibrated with the furnace and the platinum resistance thermometer so that the required sample temperature could be easily selected. The control was better than $\pm 0.2^{\circ}\text{C}$ at 1000°C . The initial heating rate was $37^{\circ}\text{C}/\text{min}$ and the initial cooling rate from 1000°C was $18^{\circ}\text{C}/\text{min}$

A continuous balance potentiometer recorder was used in conjunction with this controller. The recorder was the Elektronik 194 Recorder manufactured by Honeywell. By means of an off-set zero facility the sample temperature could be measured with a high degree of accuracy.

2.2.1.2. Calibration of the Glass Springs

The glass tube was removed from the reduction apparatus and clamped in a draught-free laboratory. The glass spring, extension rod and specimen holder were suspended vertically from the hook. The contraction of the glass spring was noted, after removal of known weights from the specimen holder, using a cathetometer to sight onto the tip of the extension rod and measuring its change of position.

Details of the calibration of two springs are given in Figures 15 and 16 which show the load-extension curves to be linear over the whole weight range used for the reduction tests. The spring constants were 13.9mg/mm and 21.3mg/mm respectively. The less sensitive spring could measure a weight loss of better than 1mg for the smallest contraction measurable by the cathetometer. For a sample weight of 1150mg the reduction of magnetite could be measured to better than $\pm 0.3\%$. Full extension of the spring did not occur until 20 minutes had elapsed after applying the load. This period was, therefore, allowed to elapse before commencing measurements.

To confirm that the spring calibration when assembled in the reduction apparatus, remained the same as when determined in the prior calibration, the total weight loss calculated from the calibration constants of the spring was compared with the actual total weight loss determined by an accurate analytical balance. A good agreement was obtained: the measured values being always within 5% of the actual values with a mean agreement of $\pm 1.19\%$. The method was considered to be very satisfactory for the determination of reduction rates.

2.2.2. Stanton Massflow Thermogravimetric Balance

The reduction work carried out on the sinter samples was done by means of the automatic recording balance, model MF-H5 manufactured by Stanton Instruments Ltd. (Figures 17, 18, 19).

2.2.2.1. Weighing Operations

The thermobalance is not a suitable instrument for ordinary direct weighing operations. The balance records weight change and, for isothermal measurements, buoyancy effects may be ignored.

The maximum sample weight is limited by the amount of weight

loss the balance is capable of recording; i.e. 200mgs in this case although the capacity of the balance is 2×10^4 mg. The weight loss can be read to ± 0.1 mg. Thus for a sample of magnetite 0.7 g in weight this sensitivity represents a reduction of better than $\pm 0.05\%$. The maximum rate of weight change which can easily be recorded is 100 mg/min.

The weighing instrument is a precision air-damped analytical balance. There are no mechanical contacts on either beam and the weight change is transmitted directly to the recorder by the capacity follower system.

2.2.2.2. Temperature Control

The furnace tube is a closed-ended 50 mm diameter mullite sheath. A refractory plug is placed over the sheath to reduce convective heat losses.

The maximum temperature possible on the platinum-rhodium bifilar wound furnace is 1350°C . The temperature increases at $6^\circ\text{C}/\text{min}$. Furnace control is achieved by the use of automatic relays actuated by a geared synchronous motor driven cam. A smooth linear temperature rise is achieved.

The recording thermocouples are set in series connection and their combined millivolt output is recorded. The output from the thermocouples is applied to a moving coil millivoltmeter on which the indicating arm has been replaced by a vane which acts as one plate of a variable sensing condenser. The other plate is a vane attached to a follower arm mounted co-axially with the moving coil vane and is arranged to move in the same arc. The follower vane is mechanically coupled to the recorder pen shaft which records in accordance with the movement of the moving coil meter.

The recording thermo-couple is an integrated sheathed thermo-couple of Pt/Pt - 10% Rh. It is not possible to calibrate this thermocouple by placing a potentiometer in parallel with it. Calibration was carried out by means of a fine Pt/Pt - 13% Rh thermo-couple. The recorder operated to better than $\pm 2^{\circ}\text{C}$. Schematic diagrams of the weighing and temperature recording operations are shown in Figures 17, 18, 19.

2.3. Gas Purification

High purity argon was used to flush the reaction chamber in each balance during heating and cooling. Hydrogen was used as the reducing agent, any moisture present being removed by a two-stage drying system consisting of anhydrous magnesium perchlorate followed by a 3.175 mm Molecular sieve type 54 (aluminium calcium silicate). The gas flow rates were regulated by means of Rotameters. (Figure 20).

The gas was allowed to enter the furnace from the top in the spring balance in order to minimise buoyancy effects.

2.4. Critical Gas Flow Rate

In order to determine the critical gas flow rate samples of magnetite were reduced in each balance by the same amount at 1100°C rate which was later confirmed as the temperature for maximum reduction rates. No increase in reduction rate was observed at gas flow rates in excess of .08 litres/second of hydrogen. (Figure 21). A .17 litre/sec flow of gas was, therefore, considered adequate for both the spring balance and the mass flow balance.

2.5. Preliminary Tests

A small number of tests were carried out in order to determine the accuracy of the weight loss methods of determining reduction rates.

2.5.1. Blank Tests

Blank runs were carried out on both the spring balance and the Massflow balance using a Nickel ball to simulate the sample.

The initial balance positions were noted. A flow of argon of .17 litre/sec was admitted into each reaction chamber and the temperatures were allowed to reach and stabilize at 1000°C. The argon was then replaced by hydrogen flowing at .17 litre/sec.

A small amount of turbulence occurred initially, on each balance, as the gas change over was effected. This lasted for less than 60 sec.

In the case of the spring balance no change in the position of the glass spring was noted at any stage during the blank run.

In the case of the Massflow balance an apparent increase in weight was noted as the temperature increased. This was due to buoyancy effects which can be neglected when determining weight changes at isothermal test temperatures. There was no change in the cold blank weights as determined before and after the test sequence.

Subsequent tests were carried out using a magnetite sample in the case of the spring balance and a sinter sample in the case of the Massflow balance. Agreements between recorded weights and weights measured by means of an analytical balance were within $\pm 6\%$ and $\pm 5\%$ respectively.

2.5.2. Test Series

Following the preliminary checks for accuracy a series of tests were carried out in order to determine the reduction behaviour of almost pure magnetite and lean magnetite sinter. This was done by reducing samples of magnetite at temperatures between 400°C and 1000°C, and by reducing sinter pellets between 700°C and 1100°C. The effect of oxidation and thermal treatment of the sinter pellets was investigated by reducing samples which had been oxidised at 500°C, 750°C and 1000°C and samples which had been heat treated in argon at temperatures between 500°C and 1000°C. The effect of varying heating and cooling rates on sinter pellets at 750°C was also investigated.

2.7. X-ray Diffraction

The various sinter pellets heat treated under argon at 750°C (for the various heating and cooling rates) were ground to a fine powder and X-ray diffraction techniques using a Philip's set were employed in order to investigate any crystallographic changes which might have occurred.

A Co - K α target was used with an iron filter. The current used was 10 mA with 32 KV. A Straumanns film set up in a Debye-Scherrer camera was used. The negatives obtained were compared with each other.

2.8. Electron Probe Micro Analysis

Selected samples were prepared for electron probe micro-analysis. A layer of carbon was vacuum deposited onto the polished surface of the samples. They were then subjected to the electron beam; the emitted X-rays being analysed by the SEMZA Electron Probe micro-analyser manufactured by A.E.I.

2.9. Porosity Determinations

The porosities were measured by comparing the apparent density of the samples with their true densities as measured by the specific gravity bottle technique.

The apparent densities were measured by the liquid displacement method. Mercury was used as the liquid and a porosity balance was constructed as shown in Figure 22. The instrument operates on the principle of a hydrometer. The piano-wire frame was weighted such that the marker just touched the surface of the mercury when there was no sample in position. With the sample in position weights were loaded on to the pan until the increased upthrust was balanced and the pointer again touched the mercury surface.

The calculation was:

$$\frac{W_1 + W_2}{D} = V$$

W_1 = Sample weight

W_2 = weight to overcome increased upthrust

$\frac{W_1}{V}$ = apparent density

$$\left(\frac{\text{True density} - \text{apparent density}}{\text{true density}} \right) \cdot 100 = \text{porosity \%}$$

The true density of the magnetite was found to be 5.12 kg/l and of the sinter 3.68 kg/l.

The accuracy of the porosity balance was checked using a steel ball of known density in place of the oxide sample. A good agreement was found.

2.10. Naphthalene Sublimation Experiments

2.10.1. Introduction

In order to determine the value of the mass transfer coefficient to an oxide sphere in a flowing stream of reducing gas it is necessary to simulate this transfer in a non-reducing situation, i.e. where effects due to chemical reaction and product layer diffusion are non-existent.

2.10.2. Technique

A material which sublimates at such a rate that its weight loss, in a reasonably short time, can be measured accurately, is required.

Naphthalene ($C_{10}H_8$) or camphor may be used for this purpose.

Naphthalene was used in this work.

The $C_{10}H_8$ spheres were placed in the two different balances and the weight losses at different gas flow rates were determined.

2.10.3. Sample Preparation

Naphthalene was heated in a glass beaker until just molten, i.e. 80 - 82°C. The C₁₀H₈ was then cast into spheres.

The mould was made by casting a thermoplastic compound around 8mm dia. ballbearings, splitting the mould and removing the ball bearings. The C₁₀H₈ was cast around fine suspension wire.

Casting several spheres together ensures that the spheres are cast at the same temperature. This is to avoid changes in crystal structure from sphere to sphere which can affect sublimation rates.

Similarly casting temperature should be as close to the melting point of C₁₀H₈ as possible. Careful handling of the spheres is necessary due to their friable nature.

2.10.4. Temperature Measurement

The vapour pressure of naphthalene is calculated from

$$\log_{10} \text{V.P. (C}_{10}\text{H}_8) = \frac{-0.05223 \times 71.401}{^{\circ}\text{K}} + 11.450 \text{ mmHg}$$

A change in temperature of 2°C from 25°C to 27°C can change the vapour pressure of C₁₀H₈ from .087 mm Hg to .105 mm Hg. It is therefore, essential that the temperature be measured accurately.

It should be noted that at temperatures greater than 40°C the sublimation of C₁₀H₈ is so rapid that the sphere may disappear and a final weight determination is not possible in such a case.

CHAPTER 3

DETERMINATION OF MASS TRANSFER CHARACTERISTICS

3.1. Introduction

The mass transfer coefficient to a spherical compact is given by an equation of the form:

$$Sh = A + B (Re)^n (Sc)^{1/3} \quad (53)$$

$$\text{where } Sh = \frac{\alpha d}{D_g} \quad (54)$$

Where equation (53) can be derived by application of the Chilton-Colborn analogy between heat and mass transfer to the Ranz heat transfer relationship.

$$Nu = 2.0 + 0.60 (Re)^{1/2} (Pr)^{1/3} \quad (55)$$

3.1.1. Technique

In order to determine accurately the mass transfer coefficient to a sphere positioned in a stream of gas in a tube it was necessary to determine those values of A and B in equation (53) which are specific to the tube-particle geometry involved in this work. The values of A and B cannot be determined directly from the results of the reduction experiments. It was necessary to model the reduction system by replacing the oxide sphere with a sphere of a volatile material which sublimed at a rate such that its loss in weight in a flowing gas stream, at room temperature, could be measured accurately over a reasonable time period. Naphthalene ($C_{10}H_8$) which has a high vapour pressure, and sublimes rapidly at room temperature, was selected as being suitable for this purpose.

Measurement of mass transfer coefficients by the sublimation of naphthalene in an air stream was first used by Winding and Cheyney⁽¹⁴¹⁾ in the study of heat transfer to a tube bank, and has since been used extensively.⁽¹⁴²⁾ Most recently Campbell⁽¹⁴³⁾

has used the technique in order to determine mass transfer coefficients in reduction systems.

The weight loss of naphthalene can be measured accurately over a short time period. The Reynolds (Re) and the Schmidt (Sc) dimensionless numbers (equation 53) are characteristics of the physical dimensions of the system and of the flowing gas stream.

By calculating Re and Sc and by measuring the specific weight loss of the naphthalene spheres at different hydrogen flow rates then the mass transfer coefficient of $C_{10}H_8$ from a sphere, in each of the balances can be determined.

The values of the constants A, B and n in equation (53), can then be calculated. These values can be substituted in equation (53) and a new mass transfer coefficient for the transfer of hydrogen across a $H_2 - H_2O$ boundary layer to an oxide sphere can be calculated for each of the two balances used in this work.

Reynolds Number

$$Re = \frac{V \cdot d}{\gamma_{H_2}} \quad (56)$$

where $V = \frac{\text{flow rate}}{A^1 - a} \quad \text{cm. sec}^{-1} \quad (57)$

Schmidt Number

$$Sc = \frac{\gamma_{H_2}}{D_{H_2 - C_{10}H_8}} \quad \begin{matrix} \gamma_{H_2} \text{ varies with} \\ \text{temperature (152)} \\ \text{(Figure 23)} \end{matrix} \quad (58)$$

Mass Transfer Coefficient

$$\alpha_{C_{10}H_8} = \frac{\dot{n} \cdot R \cdot T}{S \cdot V_{p \text{ eff}}} \quad \text{cm. sec}^{-1} \quad (59)$$

where $\dot{n} = \frac{w}{t \times 60 \times M_{C_{10}H_8}} \quad \text{g. sec}^{-1} \text{ mol}^{-1} \quad (60)$

$$S = \pi d^2 \quad (61)$$

$$V.P_{\text{eff}} = (V.P_{\text{C}_{10}\text{H}_8} - V.P_{\text{C}_{10}\text{H}_8, \text{exit}}) \text{ atmos} \quad (62)$$

$$\text{Where } V.P_{\text{C}_{10}\text{H}_8} = \text{antilog} \left[\frac{-0.05223X}{T} + Y \right] \cdot \frac{1 \text{ atmos}}{760} \quad (63)$$

$$\text{and } V.P_{\text{C}_{10}\text{H}_8, \text{exit}} = \frac{P \cdot M_{\text{H}_2} \cdot W}{t \cdot M_{\text{N}} \cdot Q_m \cdot C_m} \text{ atmos.} \quad (64)$$

Values for: $\alpha_{\text{C}_{10}\text{H}_8}$ can now be calculated and substituted into equation (54).

Values for $D_{\text{H}_2 - \text{C}_{10}\text{H}_8}$ have not been directly determined but have been calculated from considerations of diffusion coefficients of C_{10}H_8 in air, H_2 in air and assuming Graham's law.

$$\text{Since } Sh = \frac{\alpha d}{D_{\text{C}_{10}\text{H}_8 - \text{H}_2}} = A + B (\text{Re})^n (\text{Sc})^{1/3} \quad (65)$$

$$\text{then } \alpha_{\text{C}_{10}\text{H}_8} = \frac{A \cdot D_{\text{C}_{10}\text{H}_8 - \text{H}_2}}{d} + B \cdot \frac{D_{\text{C}_{10}\text{H}_8 - \text{H}_2}}{d} (\text{Re})^n (\text{Sc})^{1/3} \quad (66)$$

A graphical plot of $\alpha_{\text{C}_{10}\text{H}_8}$ versus Re (Figures 24, 25) will therefore, give an intercept value of $D_{\text{C}_{10}\text{H}_8 - \text{H}_2} \cdot A/d$ from which

A is determined.

Similarly values of B and n can be determined from the intercept and slope respectively of a plot of $\log_{10} \frac{Sh - A}{\text{Sc}^{1/3}}$ versus $\log_{10} \text{Re}$. (Figure 26, 27).

From these constants the value of the mass transfer coefficient of hydrogen across a water vapour/ H_2 boundary layer to an oxide sphere can be determined for each reduction unit.

3.1.2. Diffusion Coefficient $D_{\text{H}_2 - \text{H}_2\text{O}}$

$D_{\text{H}_2 - \text{H}_2\text{O}}$, which is used to determine $\alpha_{\text{H}_2\text{O} - \text{H}_2}$, has not been determined experimentally at the reaction temperature used in the present work. It may, however, be calculated using various empirical equations.

$$D_{1,2} = 0.0043 \left[\frac{1}{M_{H_2}} + \frac{1}{M_{H_2O}} \right]^{\frac{1}{2}} \cdot T^{1.5} \text{ after Guilliland (144, 145)} \quad (67)$$

$$P \left[(V_1)^{1/3} + (V_2)^{1/3} \right]^2$$

$$D_{1,2} = 0.00100 \left[\frac{1}{M_{H_2}} + \frac{1}{M_{H_2O}} \right]^{\frac{1}{2}} \cdot T^{1.75} \text{ after Fuller (146, 147)} \quad (68)$$

$$P \left[(\sum V_1)^{1/3} + (\sum V_2)^{1/3} \right]^2$$

The values obtained from equations (67, 68) were compared with two values obtained from the equation:

$$D_{1,2} = \frac{3}{16} \left\{ \left[2 \cdot k \cdot T \cdot \frac{(M_{H_2} + M_{H_2O})}{M_{H_2} \cdot M_{H_2O}} \right]^{\frac{1}{2}} \cdot f_D / n \pi \sigma_{1,2}^2 \Omega_D \right\} \quad (69)$$

Equations (67), (68) are simple equations based on the assumption that the gas molecules are rigid spheres. Equation (69) is based on a rigorous kinetic theory involving the potential energy of interaction between molecules. The force of interaction is the change in potential energy with respect to the distance between the molecules. How the forces between molecules vary as a function of the distance between them is not known exactly. However, a fairly good empirical potential energy function is the Lennard-Jones potential Ω_D is a dimensionless function of the temperature and the intermolecular potential field for one molecule of H_2 and one of H_2O . This potential field is approximated by the Lennard-Jones function. Equation (69) can be simplified to:

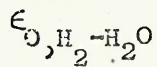
$$D_{1,2} = 0.001858 T^{3/2} \left[\frac{(M_{H_2} + M_{H_2O})}{M_{H_2} M_{H_2O}} \right]^{\frac{1}{2}} / P \cdot \sigma_{H_2-H_2O}^2 \Omega_D \quad (70)$$

Where the Lennard-Jones parameters are:

$$\sigma_{H_2-H_2O} = \frac{1}{2} (\sigma_{H_2} + \sigma_{H_2O}) \quad (71)$$

$$\text{and } \frac{E_{H_2-H_2O}}{k} = \left[\frac{(e_{O, H_2})}{k} \cdot \frac{(e_{O, H_2O})}{k} \right]^{\frac{1}{2}} \quad (72)$$

From k and reading from tables $(147) \int_D$ can be found.



In this way it is possible to predict values of $D_{1,2}$ to within 6% (151) . The parameter \int_D is a measure of the deviation from rigid sphere behaviour.

Values for $D_{1,2}$ were calculated for the temperature range used in this work from equations (67), (68). The values were compared with two values calculated from equation (70). It can be seen from Figure 26 that Fuller's equation (68) corresponds closely to the two values from (70). Consequently, $D_{1,2}$ values calculated from Fuller's equation were used in the mass transfer calculations.

3.2. Discussion of Mass Transfer Results

3.2.1. Determination of A

Despite the extreme care employed in preparation (cast at $80^\circ C \pm 0.5$) and handling of the naphthalene spheres. Figures 24, 25 exhibit a large scatter of data for the naphthalene sublimation work. This may have been caused by loss of material due to friability or to variation in grain structure.

In spite of the scatter of data results reflecting the differences between the two balances used in this work, were obtained.

From the statistical 'best line' plots (Figures 26, 27) the intercepts on the y axis were determined for $Re = 0$.

$$\alpha_{C_{10}H_8} \text{ at } Re = 0 = \frac{D_{H_2}}{d} - C_{10}H_8^A \quad (73)$$

3.2.2. Diffusion Coefficient $D_{H_2 - C_{10}H_8}$

This was determined from the value of the diffusion coefficient for air in $C_{10}H_8$ ($D_o = .0513 \text{ cm}^2 \text{ sec}^{-1}$) (148) and the mean ratio of the diffusion coefficients of hydrogen - organic compounds to

air-organic compounds (148) (mean $\frac{D_{O,H_2-x}}{D_{O,air-x}} = 3.92$)

Thus $D_{H_2-C_{10}H_8} = 0.0513 \times 3.92 = 0.201 \text{ cm}^2 \text{ sec}^{-1}$ at 0°C .

By substituting this value into equation (73) the values of A were found to be:

$A \simeq 1.0$ for the Stanton Balance.

and $A \simeq 4.0$ for the Spring Balance.

3.2.3. Determination of B and n

From equation (66) it can be seen that a plot of $\log_{10} \frac{Sh - A}{Sc^{1/3}}$

versus $\log_{10} Re$ would yield a value of $\log_{10} \frac{Sh - A}{Sc^{1/3}} = \log_{10} B$ at

$\log_{10} Re = 0$

Thus B can be calculated and n is the slope of the line.

From the graphs (Figures 26, 27) the values were found to be:

$B = 0.1454; n = 0.1656$ for the Stanton Balance.

$B = 0.2148; n = 0.4091$ for the spring Balance.

Thus the equation describing the physical characteristics of the two balance systems are

$Sh = 1.0 + 0.14 (Re)^{0.17} (Sc)^{0.33}$ Stanton Balance (74)

and $Sh = 4.0 + 0.21 (Re)^{0.41} (Sc)^{0.33}$ spring Balance (75)

From the values of the constant A in equations (70), (71) it can be seen that the mass transfer coefficient of the spring Balance will be of the order of four times that of the Stanton balance for the same gas flow input. This is associated mainly with the smaller diameter of the spring balance system which results in a higher Reynolds number. The simpler gas flow configuration of the spring balance will also tend to increase the mass transfer coefficient. This difference is clearly exhibited in Figures 29, 30.

3.2.4. Determination of Mass Transfer Coefficients

By evaluating the terms in equations (74), (75), the Sherwood number and hence the mass transfer coefficient may be determined.

The values of $D_{H_2-H_2O}$ (calculated from equation (68) and γ_{H_2} the kinematic viscosity (from tables (152)) are substituted into equations (56), (58), to determine Re and Sc. It should be noted that both γ_{H_2} and $D_{H_2-H_2O}$ vary with temperature. (Figures 23, 28.

The values for Re, Sc and $D_{H_2-H_2O}$ are substituted into the equations below. (Equations (74), (75) rearranged).

$$\alpha_{H_2-H_2O} = \frac{D_{H_2-H_2O}}{d} \left(1.0 + 0.1454 (Re)^{0.1656} (Sc)^{0.33} \right) \text{ Stanton} \tag{76}$$

Balance

$$\alpha_{H_2-H_2O} = \frac{D_{H_2-H_2O}}{d} \left(4.0 + 0.2148 (Re)^{0.4091} (Sc)^{0.33} \right) \text{ spring}$$

Balance

The values for $\alpha_{H_2-H_2O}$ were calculated for each reaction temperature as shown in Table 2. The change in $\alpha_{H_2-H_2O}$ with temperature is shown in Figure 31. It will be noticed that $\alpha_{H_2-H_2O}$ is much less temperature sensitive in the Stanton Balance than in the spring balance. It will also be seen that at all temperatures the mass transfer coefficient for the spring balance is significantly higher than for the Stanton Balance, even though the gas flows used in the reduction tests in both balances considerable exceeded the so called critical gas flow rate as determined previously in this work, (Section 2.4.)

3.2.5. Effect of Mass Transfer Coefficient on Reaction Rate

The rate of a reaction controlled by mass transport through a boundary layer is given by:

$$\dot{n} = \frac{4 \pi r^2}{RT} \alpha_{H_2-H_2O} \left\{ \left[P_{H_2} \right]_b - \left[P_{H_2} \right]_s \right\} \tag{78}$$

On rearranging:

$$\left(\left[P_{H_2} \right]_b - \left[P_{H_2} \right]_s \right) = \frac{\dot{n} \cdot R \cdot T}{4\pi r^2} \alpha_{H_2-H_2O} \quad (79)$$

The expression on the left hand side of equation (79) is the driving force for the reduction reaction and equals the difference between the partial pressure of H₂ in the bulk gas stream ($\left[P_{H_2} \right]_b = 1.0$ at) and the partial pressure of H₂ at the sample surface $\left[P_{H_2} \right]_s$.

The values of $\left[P_{H_2} \right]_s$ have been calculated from equation (79) and are given, for different reducing conditions in Tables 3-6. In these calculations \dot{n} was used relative to a five minute period between the third and eighth minute after the commencement of gas flow rather than from $t = 0$ to allow for possible variations in gas composition during the period immediately following the introduction of H₂.

A plot of partial pressure of hydrogen at the sample surface ($\left[P_{H_2} \right]_s$) against the specific reaction rate ($\dot{n} \times 10^4$) shows that as the reaction rate increases, so the value of $\left[P_{H_2} \right]_s$ decreases. (Figure 32).

It is particularly noticeable that the value of $\left[P_{H_2} \right]_s$ for magnetite pieces reduced in the spring balance is much higher than that for magnetite pieces reduced in the Stanton Balance for the same specific reaction rate. Clearly, this is because the higher value for the mass transfer coefficient in the spring balance is resulting in a reduced resistance to mass transport across the gas film boundary layer around the sample. This means that a lower apparent driving force for reaction is required in the spring balance than in the Stanton balance for the same specific reaction rate.

From examination of a plot of the hydrogen partial pressure at the sample surface versus temperature (Figure 33) it is apparent that the faster reacting magnetite pieces have a value of $[P_{H_2}]_s$ much closer to equilibrium than the untreated sinter pellets. This is in spite of the large difference in mass transfer coefficients which would tend to reverse this effect.

Where the sinter pellets were thermally treated or oxidised their specific reaction rates increased sufficiently for the value of the surface partial pressure of hydrogen to fall below the value required for the sample to reduce to Fe initially. This effect is shown in Figure 34. However, as the reaction rate slows down as reduction proceeds then $[P_{H_2}]_s$ increases to a value above the equilibrium value and reduction from Fe_3O_4 through FeO to Fe can proceed.

This same effect will occur with small magnetite pieces reduced in the Stanton balance (Table 3).

3.3. CONCLUSIONS

Although, in both the Stanton balance and the spring balance, the so called 'critical gas flow rate' was exceeded at all times there is still a large difference in the mass transport behaviour in the gas phase between the two balance systems.

Clearly it can be seen from Figure 34 that where the specific reaction rate (initial) of differently treated sinter pellets was substantially increased when reduced isothermally at $800^{\circ}C$ then the rate at which the reductant gas was consumed became greater than the rate at which it could be supplied to the sample surface. This caused the value of $[P_{H_2}]_s$ at the surface to approach the value, required by the equilibrium, for complete reduction to iron. Thus reduction to FeO only could occur, until the resistance of the FeO

product layer to gaseous diffusion increased, such that, the specific reaction rate decreased and the value of $[P_{H_2}]_s$ was allowed to reach the value required for reduction through iron.

It can be concluded that, where the specific reaction rate increases, the driving force for the reduction reaction in the Stanton balance is decreased. The driving force may, in fact, decrease such that the equilibrium conditions for reduction to iron are not achieved until the reaction rate slows due to product layer resistance.

Where slowly reducing materials are used in the Stanton balance then the value of $[P_{H_2}]_s$ maintains an approximately constant distance from equilibrium over the range of temperatures considered.

For more easily reduced materials, such as the magnetite, the value of $[P_{H_2}]_s$ will always approach the equilibrium, if reduced in the Stanton balance.

When these materials are reduced in the spring balance then $[P_{H_2}]_s$ is always above the equilibrium value. Although the distance from equilibrium is not so great as for the sinter pellets reduced in the Stanton balance.

It is apparent from the above discussion, that comparison between results on the different balances must take into account differences in mass transfer characteristics shown to occur above.

In addition, very fast reducing materials will, on the Stanton balance, be affected by the gaseous mass transport through the boundary layer.

The above effects are a direct result of the four-fold difference in the mass transfer coefficients of the respective balances. This is in turn due to basic design differences between the balances. From Figures 29 and 30 it can be seen that the

simpler design of the spring balance allows the gas to flow smoothly around the sample. The narrow tube diameter, compared with that of the Stanton balance increases the Reynold's number and hence the mass transfer coefficient. This effectively reduces the resistance to mass transfer across the boundary layer. For the same gas flow rate the wider tube diameter of the Stanton balance causes the Reynolds number to fall. Hence the mass transfer coefficient is reduced and the resistance to mass transport across the boundary layer increases. The flow rate cannot be substantially increased since the reaction tube is forced clear of its sealing ring when greater than a slight positive pressure is applied. In addition the gas inlet tube is sited, such that the reducing gas has first to rise and fill up the reaction tube from the top, gradually forcing out the purge gas.

There is no restriction of gas access to the pellet within the crucible. This is apparent on metallographic examination of the reduced samples which shows that the reduced layer evenly penetrates the sample.

For the same gas flow rates the diameter of the Stanton balance reaction tube would have to be reduced in order to achieve the same mass transfer coefficient values as the spring balance.

CHAPTER 4

MATHEMATICAL TREATMENT

4.1. Individual Laws

Some of the reaction rate laws which may be applicable to various stages of gaseous reduction of iron oxides were summarised by Smith. (106)

(i) Exponential Law

$$\frac{(O/Fe)_t}{(O/Fe)_i} = e^{-k_1 t} \quad (80)$$

(ii) Phase Boundary Law

$$1 - \frac{(O/Fe)_t}{(O/Fe)_i} = (k_2 t)^3 \quad (81)$$

(iii) Parabolic Diffusion Law

$$1 - \frac{(O/Fe)_t}{(O/Fe)_i} = k_3 \sqrt{t} \quad (82)$$

(iv) Linear Law

$$\frac{(O/Fe)_t}{(O/Fe)_i} = -k_4 t \quad (83)$$

These laws simplify to $O_t/O_i = e^{-k_1 t}$; $O_t/O_i = (1 - k_2 t)^3$; $O_t/O_i = (1 - k_3 \sqrt{t})$ and $O_t/O_i = -k_4 t$ respectively. (Equation 84 - 87).

The time and weight loss data from the reduction experiments was fitted to each individual law in turn by the 'least squares' method.

The weight loss data was converted to the oxygen-iron atomic ratio:

Initially

$$\left(\frac{O}{Fe} \right)_i = \frac{O \text{ assoc. with } Fe^{3+} + O \text{ asoc. with } Fe^{2+}}{o/oFe_{tot}} \cdot \frac{\text{at.wt. Fe}}{\text{at.wt. O}} \quad (88)$$

and at time t

$$\left(\frac{O}{Fe} \right)_t = \frac{O \text{ assoc. with } Fe^{3+} + O \text{ assoc. with } Fe^{2+} - \text{wt. loss}}{\% Fe_{tot}} \cdot \frac{\% Fe_{tot} \times \text{initial sample wt.}}{\% Fe_{tot} \times \text{initial sample wt.}} \quad (89)$$

The calculations were carried out on an IBM 1130 computer. The language used was Fortran 4. A full programme listing can be seen in Appendix I.

The results of individual computer runs will be discussed in the appropriate sections.

4.2. Combined Laws

From the data plots against the individual law plots (Figures 118 - 126, 175 - 181) it became obvious that a single individual law cannot fully express the reduction situation.

It was, therefore, decided to produce a general law in order to describe the reduction situation more closely.

The individual laws (equations 84 - 87) given by Smith ⁽¹⁰⁶⁾ were examined and it was concluded that a combination of equations (81), (82) could best describe the reduction curve. The linear law was not considered. In addition the exponential or first order law, is normally considered to apply to homogenous situations where all parts of the reactants are taking part in the reaction at the same time, rather than, as in this instance, a heterogenous situation. (However, it will be seen later that a valid exponential law can apply).

The general law developed initially is shown in equation (90).

$$\frac{O_{1,t}}{O_t} = A (1 - k_2 t)^3 + B (1 - k_3 \sqrt{t}) \quad (90)$$

where A, and B were considered to be 'weighing factors' for the two terms.

A 'least squares fit' of equation (90) to the data generally gave a better fit than any of the individual laws.

The terms in equation (90) were considered more closely. The parabolic law was derived for planar surfaces. In the case of a sphere a sphericity factor should be applied. This, however,

assumes a non-contracting reaction surface. The parabolic law as defined by Smith ⁽¹⁰⁶⁾ would, therefore, only apply in the early stages of reduction where area can be regarded as approximately constant. Many corrections, other than the sphericity factor, have been made to this law.

The parabolic law has been shown ⁽³⁹⁾ to be invalid for spheres. Grinstling and Brounshtein ⁽³⁹⁾ used a modification of Barrer's equation for steady-state heat transfer through a shell. This equation was similar to that reported by Themelis and Gauvin ⁽¹²⁰⁾ where:

$$1 - R_x = \left(\frac{6}{\pi^2} \right) e^{-D \pi^2 \theta / r_o^2} \quad (91)$$

Equation (91) was developed from Fick's laws and is, in fact, an exponential law of the same form as equation (80) stated by Smith ⁽¹⁰⁶⁾.

The invalid parabolic term in the general law was, therefore, replaced by the more general diffusion term derived from Fick's laws using spherical co-ordinates.

for radial diffusion

$$\frac{\partial c}{\partial t} = D \left(\frac{\partial^2 C}{\partial r^2} + \frac{2}{r} \cdot \frac{\partial C}{\partial r} \right) \quad (92)$$

with u as Cr

$$\frac{\partial u}{\partial t} = D \cdot \frac{\partial^2 u}{\partial r^2} \quad (93)$$

this solves to

$$R_x = 1 - \frac{6}{\pi^2} \sum_{n=1}^{\infty} \frac{1}{n^2} e^{-D n^2 \pi^2 \theta / r_o^2} \quad (94)$$

For $\theta = 0$

$$\sum_{n=1}^{\infty} \frac{1}{n^2} \rightarrow \frac{\pi^2}{6} \quad (95)$$

and

$$e^{-k\Theta} \rightarrow 1$$

therefore $R_x = 0$ at $\Theta = 0$

For small times

$$R_x = 1 - e^{-k\Theta} \quad (96)$$

this approximates to

$$R_x = 1 - \frac{4}{5} (e^{-k\Theta} + \frac{1}{4} e^{-4k\Theta}) \quad (97)$$

$$\text{or } R_x = 1 - \frac{36}{49} (e^{-k\Theta} + \frac{1}{4} e^{-4k\Theta} + \frac{1}{9} e^{-9k\Theta}) \quad (98)$$

For large times

$$R_x = 1 - \frac{6}{\pi^2} e^{-k\Theta} \quad (99)$$

The magnitude of the additional terms in equations (97), (98) were evaluated for the time scales used in the present work. Newton's iterative technique was used to solve the expressions;

using equation (97)

and letting $e^{-kt} = x$

$$\text{therefore } R_x = 1 - \frac{4}{5} (x + \frac{1}{4} x^4) \quad (100)$$

and solving the bracket

$$\text{therefore } R_x = 1 - \frac{4}{5} x + \frac{1}{5} x^4 \quad (101)$$

simplifying

$$5R_x = 5 - 4x - x^4 \quad (102)$$

Values for R_x were substituted into (102) and the quartic solved iteratively.

Values for D as calculated from equation (96) were compared with those values from the expansion (97).

The comparisons are shown in detail in Table 7; a summary is shown below.

time (mins)	10	80	180	
$D \times 10^5 \text{ cm. sec}^{-1}$	8.3	0.68	0.23	from equation (96)
" "	7.7	0.60	0.19	" " (97)

Because the parabolic law (equation 82) was now considered to be invalid the parabolic term in the general equation was replaced by the exponential law term:

$$\frac{O_t}{O_i} = A(1 - e^{-k_1 t}) + B(1 - k_2 t)^3 \quad (103)$$

The form of the first term is in fact, the same form as equation (80).

However, when one of two terms in a general equation is an exponential term it becomes difficult to programme. The exponential term was therefore expanded to its series.

$$e^{-k_1 t} = 1 - k_1 t + \frac{k_1^2 t^2}{2!} + \dots \quad (104)$$

The first term of the expansion was taken and the general equation became:

$$\frac{O_t}{O_i} = A(1 - k_1 t) + B(1 - k_2 t)^3 \quad (105)$$

for ease of programming.

In addition to the computer calculation for the "best fits" to the reduction data a manual technique was also used.

The data was plotted against each of the exponential and the surface reaction laws in order to obtain a straight line plot, such that:

$$-\log_e \frac{(O_t)}{(O_i)} = k_1 t \quad (106)$$

and a plot of $\log_e \frac{(O_t)}{(O_i)}$ vs t yields a slope of value k_1 .

Similarly

$$1 - \sqrt[3]{\frac{O_t}{O_i}} = k_2 t \quad (107)$$

A plot of $1 - \sqrt[3]{\frac{O_t}{O_i}}$ versus t yielding a slope of k_2

These curves are shown in figures 119-126, 175-181. It can be seen that in almost all cases the straight line portion is only part of a curve.

This shows that neither of the two laws is controlling exclusively the rate of reduction.

From consideration of equation (103) it can be seen that a zero time the exponential term becomes zero and the cubic term becomes one.

The respective k_1 and k_2 values were, therefore, taken from the initial straight line portion in the case of the chemical law (Figures 119-126, 175-181) and the final straight line portion in the case of the exponential law. (Figures 119-126, 175-181). That the final part of the exponential law plot is in fact a straight line is shown by taking the initial (O/Fe) ratio as being the value at the time the exponential straight line was considered to begin. Equation (106) was then re-calculated on this basis and the graphs for the exponential laws replotted. It can be seen that a series of straight lines result indicating that exponential law (diffusion) control is operating over the time considered. (Figure 127).

The k_1 and k_2 values so obtained were substituted into equation (103) and each term evaluated separately. These terms were summed and the results can be seen in Figures (128, 129, 134, 182-184, 188, 190). It will be noted that the cubic term in equation (103) becomes negative at large times. The summation was not carried out past these times.

CHAPTER 5

REDUCTION OF MAGNETITES

5.1. Introduction

Single pieces of magnetite (with physical characteristics previously discussed in 2.1.1.), have been isothermally reduced over the temperature range 400°C to 1000°C. The samples were heated to the reaction temperature in a stream of pure argon and then reduced in hydrogen maintained at a flow rate of .17 litre/sec for all tests. The samples were then furnace cooled in a stream of argon. These reduction tests were carried out using both the Stanton mass flow thermal balance and the semi-automatic spring balance.

The data from the reduction tests have been examined mathematically and the reduced samples have been examined metallographically.

5.2. Effect of Temperature

Initially, dense, regular (Fig 6) magnetite pieces (series 1) were reduced in the spring balance. The weight loss versus time was recorded for each sample. When the reduction rate became too slow to be measured, or when the reduction was complete, the samples were cooled in the furnace tube in a flow of cold argon.

An initial plot of % reduction versus time

$$\text{where \% reduction} = \frac{\text{Wt. of oxygen removed}}{\text{wt. of oxygen present initially}} \times 100$$

showed that between the temperatures 600°C and 900°C there was not a progressive increase in reduction rate as the isothermal reduction temperature was increased. This is shown in Figure 35. Some variation in rate of reduction at constant temperature of the natural magnetite pieces were experienced but the relationships plotted in Fig. 35 show the mean rate temperature relationships.

Similarly a plot of the atomic ratio $(O/Fe)_t$ against time showed no progressive change in reaction rate as the reduction temperature was increased.

In Series 2, magnetite pieces of the same composition but different microstructure were similarly reduced in the temperature range $550^{\circ}\text{C} - 900^{\circ}\text{C}$. These samples have a 'block-type' structure with cracks occurring along the cleavage planes (Fig. 7). Fig. 36 reveals that the reaction rates again do not increase progressively with reduction temperature, although the rates are generally slower than for the previous series.

A third set of samples of the same structure as the series 2 samples were reduced between 400°C and 800°C using the Stanton mass-flow balance. These samples were of necessity smaller than the samples reduced in the spring balance because of the massflow balance's inability to measure weight losses in excess of 200 mg.

The same effect was apparent (Fig. 37) as in the previous two cases.

In general it can be seen that the reduction rates for the second two series of samples are slower than those for the first series.

5.3. Rate Maxima and Minima

Further graphical plots of time vs temperature were made for different levels of $(O/Fe)_t$. These are shown in Figs. 38-40. It can be seen very clearly from these figures that there are distinct reduction rate maxima and minima occurring at specific temperatures. The results are tabulated overleaf.

Tests	Rate Minimum Temperature	Rate Maximum Temperature	Comments
1. Spring balance Series 1 Magnetite	650°C		prominent after (O/Fe) _t = 0.9
	900°C		prominent after (O/Fe) _t = 0.7
		750°C	
2. Spring balance Series 2 Magnetite	650°C		only prominent after (O/Fe) _t = 0.9
	900°C		some indication
		550°C	
		750°C	
3. Stanton balance Series 2 Magnetite	650°C		prominent after (O/Fe) _t = 0.9
		550°C	

The time taken for each of the (O/Fe)_t ratios to be achieved in the series 2 tests is approximately 4 times that for the series 1 tests. For the series 2 tests the times taken to achieve the same (O/Fe)_t ratio were slightly longer on the spring balance than on the Stanton balance.

The existence of rate minima and maxima can be explained by the structures of the reduced samples.

5.4. Metallography of Reduced Magnetite

This section described the detailed metallographic examination carried out on original and reduced samples, special emphasis being given to the structures obtained at temperatures associated with rate maxima and minima.

5.4.1. Unreduced Magnetite Samples

Two types of magnetite have been reduced. The first (Series 1) is a polycrystalline dense magnetite comprising non-porous and

equiaxed grains (Fig. 6). Thermal treatment in argon to 1000°C and furnace cooling in argon gave no visible change in structure, confirming that any differences in micro-structure between the reduced and original samples are associated with the reduction stage and not the heating and cooling stages of the thermal cycles.

The second type of magnetite (Series 2) was also polycrystalline and dense. However, the individual pieces exhibited heavy cracks along the cleavage planes resulting in a 'block type' cracked sample (Fig. 7.) Notwithstanding this fact series 2 samples reduced on the spring balance at the same temperatures as series 1 samples in general reacted more slowly although the rate minima and maxima temperatures remained the same.

5.4.2. Reduced Magnetite Samples

For ease of description the metallography of the reduced magnetite samples will be treated in three sections:-

- i) equiaxed (series 1) magnetite - spring balance
- ii) block type (series 2) magnetite - spring balance
- iii) block type (series 2) magnetite - Stanton balance

The sections will describe samples reduced isothermally at temperatures between 400°C and 1000°C.

5.4.2.1. Series 1 (spring balance)

Samples were reduced isothermally at temperatures in the range 600°C to 900°C. On examination of Fig. 38 reduction rate minima were seen to occur at 650°C and 900°C with a reduction rate maximum occurring at 700°C - 750°C.

5.4.2.1.1. Reduction Rate Minimum 650°C

Samples reduced at temperatures around this rate minimum were examined metallographically.

Micrographs of samples reduced at 600°C, 650°C, and 700°C can be seen in Figs. 41 - 54. It can clearly be seen that there is a definite change in the physical structure of the reduced samples as the isothermal reduction temperatures progress through the rate minimum temperature of 650°C.

Magnetite samples reduced at 600°C form a heavily cracked product containing fine pores (Fig. 41). This is shown more clearly in Fig. 42.

Considerable differences between the structures of the samples reduced at 600°C and at the rate minimum temperature became apparent on metallographic examination. Distinct reduction bands were visible in the latter samples to the naked eye and Fig. 43 shows a low power micrograph of this effect. The outer reduced layer (Fig. 43(a)) was seen to be reduced iron with occasional grains of retained 'wustite' (Fig. 44). The pore size can be seen to be much coarser at the sample edge than in the magnetite reduced at 600°C. The pore size becoming smaller in areas away from the sample edge (Fig. 45), and retained wustite was still evident.

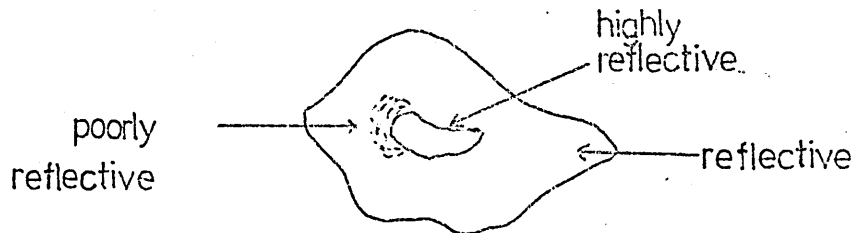
The less reflective area (Fig. 43(b)) consisted of a partly reduced product with extensive coarse porosity and occasional finely porous fully reduced grains (Fig. 46).

A comparable micrograph of the more reflective central zone (Fig. 43c) shows much less coarse porosity in the partly reduced product and extremely finely porous, fully reduced iron grains (Fig. 47).

The existence of fully reduced iron grains in the sample centre showed that some gas access had taken place. However, the low porosity partly reduced product would slow down gas access to the centre such

that a reduction rate minimum could occur.

The variation in microstructure with sample reflectivity for samples reduced at 650°C is shown in Figs. 48-54. Visually the sample considered has a noticeable variation in reflectivity.



The reflecting outer portion of the sample is shown to be porous reduced iron (Fig. 48). The non-reflecting area can be seen to be partly reduced (Figs. 49-51). Partly and fully reduced grains are visible with large pores situated at the grain boundaries (Fig. 49). The large areas of reduced material are porous product iron (Figs. 50, 51). The partly reduced areas have grain boundaries and pores bounded by product iron (Fig. 52). The central reflective area contains less porous iron and a smaller degree of general porosity (Fig. 53). The less porous nature of the reduced product is confirmed by comparison between Figs. 48, 51 and 54.

Reduction of magnetite samples at 700°C gave structures which combined the features of those samples reduced at 650°C and 750°C (Figs. 55-57).

A porous, macro-cracked fully reduced product can be seen at the sample edge (Fig. 55). However a highly reflective central portion of very soft reduced iron can be seen (Fig. 56). The sharply defined porous - non-porous boundary can clearly be seen (Fig. 57).

5.2.2.1.2. Reduction Rate Maximum 750°C

The physical structure of magnetite samples reduced at 750°C is markedly different from those reduced at the rate minima temperatures

as can be seen from the series of micrographs (Figs. 58-61). A reduced area at the sample centre can be seen in Fig. 58. Occasional unreduced grains can be seen surrounded by a layer of reduced iron. The iron product is very porous (Figs. 59, 60) with the more finely porous areas associated with grain boundaries and cracks. Samples which have been nominally 100% reduced show occasional partly reduced grains. This can be seen in Fig. 61. The partly reduced grain is surrounded by an envelope of non-porous product iron. The non-porous product is effectively preventing access of hydrogen to the grain thus preventing gaseous reduction taking place.

Magnetite samples which had been partly reduced at 750°C were also prepared. The topochemical nature of such samples can be seen (Figs. 62-68).

A sample which had been reduced 56% is shown in Fig. 62. The reduced layer at the sample edge can clearly be seen. A partly reduced area in the reduced layer is shown in Fig. 63. The porous nature of the reduced grains can be seen as well as the commencement of reduction of the unreduced grains as shown by the white or lighter coloured grain edges. The non-porous nature of the original grains contrasts markedly with the porous nature of the reduced product (Fig. 63). Coalescence and contouring of pores in the reduced layer are shown in Fig. 64, in which occasional partly reduced areas can also be seen. The formation of pore 'fronts' is also seen in Fig. 65. At the reduced layer - unreduced centre interface partly reduced grains predominate as shown in Fig. 66 in which the early stages of reduction around grain boundaries and internal pores are clearly visible.

A more heavily reduced sample (75% reduction) is shown in Figs. 67, 68. Again the 'whorl' formation of pores in the reduced

outer layer can be seen (Fig. 67). The unreduced grains in the centre are shown (Fig. 68). A distinctive feature is the reduced 'tongue' of iron which follows a single macro-crack into the centre of the sample.

5.4.2.1.3. Reduction Rate Minimum 900°C

A further distinctive change in the structures of reduced magnetite occurs as the isothermal reduction temperature increases from the rate maximum temperature at 750°C, through the temperatures 800°C and 850°C to the rate minimum temperature of 900°C. Micrographs of reduced samples are shown (Figs. 69-77). Samples reduced at 800°C show a variety of structures varying from porous iron product with contoured pores to non-porous reduced iron lining partly reduced grains. Partly reduced areas can exhibit evidence of slight reduction at both grain boundaries and around pores (Fig. 69). The fully reduced grains comprise porous iron. The partly reduced grains show non-porous iron lining the pores (Fig. 70) and fully reduced porous iron structures existing at the sample edges (Fig. 71). A partly reduced grain enveloped by non-porous iron can exist in an almost fully reduced area (Fig. 72), whilst Fig. 73 shows the coalescence and contouring of pores occurring at the sample edges. The non-porous iron layer fully envelops magnetite grains within the sample preventing further reduction from taking place (Fig. 74).

Samples reduced at 850°C exhibit to a lesser degree the characteristics evident in samples reduced at 900°C. (Fig. 75).

At the rate minimum temperature of 900°C reduced samples exhibit to a large extent envelopes of impermeable iron around partly reduced grains. Partly and fully reduced grains are shown in Fig. 76, the fully reduced grains consisting of porous iron product, partly reduced grains being surrounded by a dense iron shell. The compact nature of the product iron envelope is shown in Fig. 77.

As the isothermal reduction temperatures are increased above the rate minimum temperature of 900°C once again extensive areas of porous iron product are evident, contouring of pore fronts also occurs at sample edges. These phenomena are displayed in Figs 78-80.

5.4.2.2. Series 2 (spring balance)

Magnetite samples of a different initial structure (Fig. 7) were reduced isothermally in the spring balance at temperatures between 500°C and 900°C. Reduction rate minima and maxima again resulted as shown in Figure 40. The metallography of the reduced samples is shown in Figs 81-92.

5.4.2.2.1. Reduction Rate Maximum 550°C

Isothermal reduction over the narrow temperature range 500°C to 600°C shows a rate maximum to occur at 550°C.

At 500°C the iron product appears dense at low magnifications (Fig. 81). The 'block-type' nature of the series 2 samples can clearly be seen. Reduction can be seen to have taken place along grain boundaries within the unreduced area (Fig. 82). The finely porous nature of the reduced product can only be seen at high magnifications (Fig. 83).

Fig. 84 shows retention of the initial 'block-type' structure in the sample partly reduced at 550°C. The product iron appears dense at low magnification but the finely porous nature can be seen at a higher magnification (Fig. 85). The pores are larger than in samples reduced at 500°C (Fig. 83). Restricted reduction has again occurred in areas containing gangue (Fig. 86) compared with non-gangue area (Fig. 85). Reduction in advance of the reaction interface can occur (Fig. 87). This effect being usually associated with cracks.

5.4.2.2.2. Reduction Rate Minimum 900°C

The 'block-type' structure series 2 samples reduced on the spring balance exhibit a reduction rate minimum at 900°C in a similar way to series 1 samples. The characteristic non-porous iron shell can be seen.

The macro-porous nature of the reduced product is shown in Fig. 88. At the edge of the sample occasional unreduced grains surrounded by a product iron layer can be seen. Co-existing non-porous unreduced magnetite and porous iron product can be seen (Fig. 89).

Pores within grains and grain boundaries are iron-lined (Fig. 90, 91). The non-porous nature of the reduced iron product is seen in Fig. 92, the progression of reduction from each end of a grain boundary crack being clearly shown.

5.4.2.3. Series 2 (Stanton Balance)

Series 2 'block type' magnetite samples were reduced isothermally between the temperatures 400°C and 800°C on the Stanton balance.

The rate maximum at 550°C and the rate minimum at 650°C are shown on the time vs temperature plots (Fig. 39).

At 400°C the reduced structure is shown in Fig. 93. The topochemical nature of the reduction process at this temperature is shown in Fig. 94. The iron product is seen to be finely porous (Fig. 95).

Samples reduced at the rate maximum temperature 560°C are shown in the micrographs Fig. 96-98. The 'block-type' nature of series 2 samples is clearly seen (Figs. 96, 97). The reduction is of a topochemical nature with product phase nucleating at cracks (Figs. 96, 97). The porous nature of the product is shown in Fig. 98. The pore size is finer than that of samples reduced at 400°C .

5.4.2.3.1. Reduction Rate Minimum 650°C

The rate minimum at 650°C is again characterised by a unique microstructure. Notwithstanding the block-type nature of the unreduced structure. At the sample edge individual grains are completely reduced internally and less fully at the boundary (Fig. 99). The iron product appears to be porous. This is more clearly shown in Figs. 100, 101.

At the grain peripheries the unreduced areas are characterised by the non-porous iron lining the pores, (Fig. 102). A curious feature is the marked variation in degree of reduction on either side of a common crack (Fig. 103, 104) due possibly to the grains on either side of the crack having different orientations.

The variation of porosity within samples reduced at 650°C is shown in Figs. 105-107. A partly reduced sample is shown in Fig. 105. The central area of the sample which is more reflective to the naked eye is also shown (Fig. 106). The iron product is more dense than that in the less reflective area at the sample edge (Fig. 107).

5.5. Porosities

Samples of the equiaxed magnetite as used in series 1 above were reduced to different degrees by hydrogen in a reaction chamber exhibiting the same tube/particle geometry as the spring balance. (16, 138) The isothermal reaction temperatures covered both the upper and the lower reduction rate minima temperatures.

The porosities of the cooled, reduced samples were measured by means of the mercury balance described in Chapter 2 (Fig. 22).

The change in porosity with degree of reduction at 850°C was shown to increase almost linearly up to 55% reduction then exhibit a small plateau until 70% reduction when a linear increase in porosity was continued (Fig. 108). At 900°C the porosity plateau commenced earlier at 50% reduction and was more pronounced (Fig. 108). This porosity plateau is consistent with the occurrence of non-porous product iron which is a feature of the reduced structure at this temperature. The commencement of the plateau almost coincides with the $(O/Fe)_t$ ratio at which the rate minimum becomes prominent (Section 5.3, Fig. 38). As the reaction temperature is increased the plateau disappears (Fig. 109) and the product of reduction becomes porous.

The lower rate minimum temperatures could not be pin-pointed between 650°C and 750°C due to the large reaction temperature intervals selected. However, plots of change in porosity with degree of reduction again showed a porosity plateau. This occurred between 35% and 75% reduction (Fig. 110). Again the commencement of the plateau virtually coincides with the $(O/Fe)_t$ ratio at which the rate minimum becomes prominent (Fig. 39) and the plateau is

is consistent with the existence of a non-porous reaction product. An increase in the reaction temperature shows that the porosity plateau quickly disappears as the temperature leaves the rate minimum value.

5.6. Apparent Activation Energies

The effect of temperature on the rate of simple reactions can be represented accurately by Eyring's Absolute Reaction Rate theory:-

$$k_r = \left(\frac{k_b T}{h} \right) e^{\Delta S^\ddagger/R} \cdot e^{-\Delta H^\ddagger/RT}$$

or more simply by the Arrhenius equation:

$$k_r = A e^{-E/RT}$$

The values of the apparent activation energy can give some guide as to the possible rate controlling steps or to critical temperatures at which such steps may change.

However the predicted linear plot of $\log k_r$ against $\frac{1}{T}$ cannot be achieved for reactions where local rate maxima or minima occur within the temperature range being considered. Since the reduction reactions is a complex chemical and physical process the activation energy more appropriately, should be termed the temperature coefficient or, in order to identify its source, the 'apparent' activation energy as used in this thesis.

The Arrhenius plots for the hydrogen-reduced Kiruna magnetites are shown in (Figs. 112-117).

The series 1 plots (Figs. 112-115) show abrupt changes in slope for all stages of reduction. The middle linear portion of the plot gives a value for the apparent activation energy of 6.3 kJ/mol. for the reduction stage $(O/Fe)_t = 1.3$ to $(O/Fe)_t = 0.9$ (Fig. 113). This value is of the order required for gaseous

diffusion control over the range of temperature and degree of reduction considered. The very definite breaks in linearity occur at the same temperatures at which the rate minima occur.

As the degree of reduction increases so the deviations from the linear portion become more marked (Fig. 113). The values of the slopes over the central portion of the plot increase slightly to 15.5 kJ/mol as the degree of reduction increases.

In the high temperature portions of the plots i.e. 900°C the values of the apparent activation energy increase to 113 kJ/mol. This value approaches that of the energy required for solid state diffusion.

The abruptly changing Arrhenius plot is repeated for the series 2 samples reduced in both the Stanton and the spring balances (Figs. 116, 117), the changes in slope being due to changes in effective surface area and resistance to mass transport through impermeable iron layers.

5.7. Mathematical Treatment

The possible reaction rate laws applicable to the hydrogen reduction of magnetites have been discussed in Chapter 4.

The exponential law and the phase boundary law were considered separately.

In order to determine whether either of these laws were rate controlling the results were expressed graphically.

Typical plots of $1 - \sqrt[3]{\frac{O_t}{O_i}}$ vs time (phase boundary law) and of $\ln \frac{(O_t)}{(O_i)}$ vs time (exponential law) are shown in Figs. 118-121.

The plots shown are for series 1 samples reduced in the spring balance at the rate minima temperature 650°C and 900°C, and the rate maximum temperature 750°C. In no instance does either law hold true for the whole of the reduction time. In every case the

the phase boundary law holds for the first part of the reaction and the exponential law for the last part of the reactions although each law can be said to follow a straight line plot over the same time interval, e.g. 0-20 mins, Fig. 118.

The change in control from one law to another does not occur at a specific $(O/Fe)_t$ ratio. A considerable interim period can elapse between the end of predominantly phase boundary reaction control and the beginning of predominantly exponential diffusion control.

The same effect was clearly apparent for the series 2 samples reduced in the spring balance, (Figs. 122-124) and in the Stanton balance (Figs. 125, 126).

In order to confirm the predominantly exponential law control during the latter stages of reduction the exponential law was plotted for the time periods over which the general exponential plots had given a straight line. A selection of such plots are shown in Figs. 127(a) - 127(d). It is clear that a good straight line relationship applies over the time intervals considered.

Because of the overwhelming evidence for mixed control reduction kinetics a combined reduction rate law was used to describe the reaction.

A manual fit to a mixed control law was attempted. This combined the exponential diffusion law and the phase boundary reaction law. The changeover time between predominant control by phase boundary reaction and by exponential diffusion was taken as t_c .

Thus,

$$\text{up to } t_c \quad \frac{(O)}{(Fe)}_t = \frac{(O)}{(Fe)}_i \cdot (1 - k_2 t)^3$$

$$\text{and beyond } t_c \quad \frac{(O)}{(Fe)}_t = \frac{(O)}{(Fe)}_i \cdot (1 - k_2 t_c)^3 + 1 - e^{-k_1 (t - t_c)}$$

Where the change over time t_c marked an actual change over in control at that time a fairly good agreement between predicted and actual $(O/Fe)_t$ levels could be achieved (Fig. 128(c)). Where the finish of phase boundary reaction control and the start of exponential control were separated by a large time interval a good agreement between actual and predicted values could not be achieved (Fig. 129a, b, c).

This is a result of the continuously changing values of the constants k_1 and k_2 (Fig. 130). Manual general law fits become very difficult at this stage. Computer techniques were employed in order to obtain a general law which would fit the data. The development of the general law is discussed in Chapter 4.

The general law equation:

$$\frac{(O/Fe)_t}{(O/Fe)_i} = A (1 - k_1 t) + B (1 - k_2 t)^3$$

contained weighting factors A and B for the individual terms describing the exponential diffusion and the phase boundary reaction contributions respectively. Additionally, the computer calculated 'best fit' lines for each of four possible controlling laws. The rate constants calculated from the 'best line' fits for the exponential and phase boundary laws were used in the general law equation.

A data plotter was used to plot the curves for each individual law and for the general law versus the data.

Graphs of plots of data abstracted from reduction tests at the rate maxima and minima points for series 1 magnetites (reduced in the spring balance) are shown in Figs. 131-134.

At the rate minimum temperature 650°C the phase boundary law gives good agreement up to 50 minutes and the exponential law good agreement from 50 minutes (Fig. 131a). The computed general law follows exactly the measured values throughout reduction (Fig. 131b). The computed law gives a slightly better fit than the manual fit shown previously (Fig. 128c).

For the second rate minimum temperature at 900°C the agreement between the calculated and the actual degree of reduction for the individual laws is poor (Fig. 133a). The manual fit is also poor (Fig. 134c). A better agreement is obtained from the computed general law (Fig. 133b).

At the rate maximum temperature (750°C) the individual laws do not fit the measured values (Fig. 132a) a better fit is again obtained from a combined general law (Fig. 132b).

The general law weighting factors A and B vary with temperature (Fig. 135b). At the rate minimum temperature 900°C there is a marked change in the values of A and B in opposite directions. At 650°C a slight change in A is apparent. At 750°C a more marked change in B occurs.

The data plots for series 2 (spring) magnetites are displayed in Figs. 136-138. Again it is clear that the use of weighting factors A and B sufficiently corrects the values of the individual items such that a reasonably good fit to the data can be obtained. Additionally the change in values of the weighting factors with temperature pinpoint the rate maximum position at 750°C (Fig. 139b).

The data plots for series 2 (Stanton) magnetites are shown in Figs. 140, 141. The weighting factors again correct a general law curve to the values measured experimentally.

It is manifest from the above observations that no individual law can fully describe the reduction process. Nor, indeed, can it be assumed that the phase boundary reaction controls the reduction kinetics initially followed by a change over to exponential diffusion control at a particular $(O/Fe)_t$ ratio. As previously discussed (Chapter 4) the parabolic diffusion and the linear laws do not apply. In fact the contribution of the individual terms in the general equation varies throughout reduction. The weighting factors A, B are factors which vary throughout the reduction period in order to accommodate variations in physical parameters during reduction. The general law developed can thus empirically define the reduction process.

In order to dynamically describe the reduction, process, mathematical techniques beyond the scope of this thesis are required.

5.8. Discussion

5.8.1. Introduction

It is proposed to discuss the results obtained during the current work at the end of each chapter. The discussion will be limited to the consideration of actual results obtained by the author. A more general discussion will be given in Chapter 7 where consideration will be given to opinions, theories and results postulated in the other published work.

5.8.2. Discussion

Distinct reduction rate maxima and minima have been shown to occur during the hydrogen reduction of naturally occurring magnetites. The existence of such maxima and minima is independent of the unreduced structure of the magnetite. This is shown by the existence of concurrent maxima and minima between series 1 and 2 magnetites.

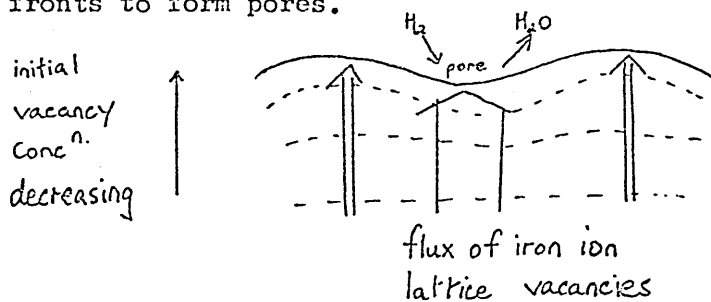
In this thesis the relationship between the reduced structure of magnetites and the rate maxima and minima has been studied in detail.

Rate minima have been shown to occur at the temperatures 650°C and 900°C for both equiaxed (series 1) and 'block type' (series 2) magnetite pieces. The rate minima have occurred at the same temperatures for each material whether reduced in the spring or the Stanton balance. The series 1 samples reduced on the spring balance have reacted faster than the series 2 samples. The series 2 samples reduced on the spring balance reduced slightly faster than on the Stanton balance. This is notwithstanding the smaller sample size used of necessity on the Stanton balance. The reaction rate difference is due to the difference in the mass transfer characteristics discussed previously (Chapter 3) the mass transfer coefficient from the sample to the bulk gas phase being approximately four times greater for the spring balance than for the Stanton balance. Thus the reaction rate for samples reduced in the Stanton balance will have a greater boundary layer resistance to the diffusion of reactant and product gases.

The rate minimum temperature at 650°C is characterised by three distinct macro-bands which can be seen in the reduced sample. The macro-bands result from porosity variations across the sample. The outer band comprises porous spongy iron, the pore size being larger than in those samples reduced at lower temperatures. The reduced grains in the inner band were more finely porous but had coarse porosity at the grain boundaries. The central zone had a much less porous iron product and a much lower degree of coarse porosity. The finely porous inner band and the almost non-porous

product in the core appears to have resulted from the formation of a stable, dense intermediate product phase of wustite. The dense wustite would tend to form dense product iron and hence gas diffusion would be inhibited and the reduction rate would slow down giving rise to the rate minimum. The variation in porosity across the sample may be due to local temperature differences as a result of the endothermic reduction reaction. Above 570°C the intermediate oxide phase, wustite, becomes stable. At the isothermal reduction temperatures 650°C , 700°C the dense wustite formed within the sample is at a temperature less than the bulk gas temperature. This lower temperature causes lower diffusion coefficients, thus resulting in a slower rate of reaction with less diffusion and a less porous product. At temperatures greater than 700°C , the local temperature is sufficiently high to allow increased diffusion coefficients and a high reaction rate with more rapid diffusion resulting in a porous product, thus the reaction progresses unimpeded causing the rate maximum which occurs at 750°C .

The reduction rate maximum at 750°C is characterised by the topochemical nature of the reaction front. This is displayed in samples which are intentionally only partly reduced. The iron is porous and the variation in product porosity is not encountered. However, the non-porous nature of the unreduced core contrasts markedly with the porous nature of the iron. Where cracks allow gas access then reduction in advance of the interface can occur. The formation of pore fronts occurs at and around this temperature. The diagram below shows how vacancies are left behind the reaction fronts to form pores.



As the front progresses then pores are left behind such that their configuration is relict of the original reaction interface. It is noticeable that reduction takes place in advance of the general 'front' where cracks normal to the front allow gases to penetrate.

As the isothermal reduction temperature increases from 750°C the reaction rate decreases until a second rate minimum occurs at 900°C. The metallographic structure of the reduced samples is completely different from those reduced at the 650°C minimum. As the individual grains are reduced the product layer formed is non-porous. Thus each grain becomes enveloped by a non-porous iron layer. Gas access is restricted and reduction stops. Sintering of the product iron probably occurs at this temperature preventing the formation of pores.

As the reduction temperature is increased beyond 900°C the reaction rate increases very rapidly. The product iron being once again porous. This is due to the reaction rate or rate of advance of the reaction front being faster than the rate at which sintering can occur.

Determination of porosity changes with degree of reduction, show definite porosity change plateau at the rate minimum temperature. (15, 138).

The low temperature rate minimum plateau occurs between 35% and 75% reductions. The start of the plateau coinciding with the $(O/Fe)_t$ ratio at which the rate minimum becomes prominent. The plateau is also consistent with the existence of a non-porous reaction product. The same phenomenon is evident at the rate minimum temperature of 900°C.

A study of the metallography of the reduced samples can give, to some extent, the mechanism by which the reaction occurs.

Series 1 and 2 magnetite can be approximated to dense oxide spheres for mathematical purposes. For a chemical controlled reaction the shrinking core would retain the same geometry as the original sample. For transport control the geometric shape would become smoothed out or rounded since diffusion occurs more rapidly at corners.

As the temperature increases transport control would reduce on a macro-scale but may still be detected on a micro-scale in the same manner.

At reduction temperatures below the 650°C rate minimum the reduction can be seen to be topochemical but not geometric (series 2) indicating predominantly mass transport control. The finely porous nature of the product indicating that mass transport within the pores as well as boundary layer mass transport is likely to be rate controlling. As the reduction temperature increases the pore size increases and the resistance to mass transport within the pores and across the boundary layer is reduced and the reaction rate increases. Further support for mass transport control is given by the very good agreement between the exponential diffusion law plot at 550°C and the actual data.

At the low temperature rate minimum series 1 samples have been shown to exhibit topochemical reduction indicating again the possibility of mass transport control. In the case of series 1 samples reduced at 650°C the change in metallographic structure across the sample suggests that both mass transport and solid state diffusion can play a part in the reaction. Manual plots of the reaction rate laws indicate the possibility of initial chemical

reaction control followed by mass transport control as the dense wustite phase is formed. When the time interval between interface and transport control is small it became possible to manually fit a two-stage reaction control model to adequately predict the reaction rate. However, where the time interval is large this is not possible and computer 'best fit' techniques are necessary using empirical constants in order to fit the data. This was carried out by the use of 'weighting factors'.

The rate controlling process at the 650°C minimum is considered to be predominantly interface reaction in the early stages through a mixed control stage to a predominantly mass transport control in the latter stages of reduction.

As the reduction temperature is increased to 750°C the metallurgy of the reduced series 1 samples displays a wholly topochemical but not geometric reduction. This indicates overall mass transport control. Support is given to this by the exponential law plot which holds for a large part of the reduction time. However, interfacial reaction control is shown to be possible in the early stages of reduction.

Apparent activation energy calculations yield a value of 6.4 kJ/mol which is of the same order of energy required for gaseous diffusion.

It is probable that the predominant controlling mechanism is gaseous diffusion within the pores which becomes more difficult as diffusion paths increase in length and tortuosity thus slowing down reduction in the later stages.

As the reduction temperature increases from 750°C the reaction rate slows until a rate minimum is caused at 900°C. The metallography shows that macro-topochemical reduction is now replaced

by micro-topochemical reduction. This indicates that initially the interfacial reaction is controlling to be superseded by iron ion diffusion control through the sintered iron shell. This theory is supported by the individual law plots showing predominantly interface reaction control in the early stages followed by mixed control followed by predominantly mass transport control.

It can safely be concluded that magnetite reduction by hydrogen is not a simple reaction involving one rate controlling step. It has been established beyond doubt that chemical reaction, and mass transfer play a part to varying degrees not only at different isothermal reduction temperatures but also within the reduction path at the same temperature. The only satisfactory way to describe reduction is by a mixed control mathematical model adequately supported by metallography.

The existence of two rate minima is displayed without question, the cause of the rate minima being explained satisfactorily by variations in metallographic structure.

CHAPTER 6

REDUCTION OF A.F. SINTER PELLETS

6.1. Introduction

A batch of lean sinter produced from a home ore mix was crushed, reconstituted into pellets and the pellets re-sintered to a constant porosity. The pellets were heated to the reaction temperature in a pure argon stream and then reduced in a stream of hydrogen maintained at a flow rate of .17 litres/sec for all tests. The samples were then furnace cooled in a stream of argon.

Reduction tests were carried out using the Stanton Massflow thermal balance.

Additionally pellets were preheated thermally in both oxidising and inert atmospheres before reduction. The data from the reduction tests were examined mathematically and the reduced samples examined metallographically.

6.2. Effect of Reduction Temperature and Thermal and Oxidation Treatments, on Reaction Rates.

6.2.1. Effect of temperature

Sintered pellets were reconstituted from crushed sinter, and reduced isothermally by hydrogen at temperatures in the range 700°C - 1100°C . The weight loss versus time was automatically recorded by the Stanton balance. When the reaction rate became too slow to be measured, or after 180 mins, the samples were cooled in the reaction chamber in a flow of cold argon.

A plot of $(\text{O/Fe})_t$ versus time shows that reaction rates increased with increase in temperature (Fig. 142). It is clear that the increase in reaction rate is very large between 800°C and 900°C compared with any other 100°C interval. This effect indicates a change in the controlling step between 800°C and 900°C .

6.2.2. Effect of Oxidation

In order to determine the effect of oxidation on reduction rates, Sinter pellets were fully oxidised to an O/Fe ratio of >1.5 at 500°C , 750°C and 1000°C and reduced at the slow reaction rate temperature 800°C . A plot of $(\text{O/Fe})_t$ vs time shows conclusively that oxidation of sinters enhances reaction rates for low reduction temperatures to a marked degree. (Fig. 143)

6.2.3. Effect of Thermal Treatment

The oxidation cycle is accompanied by thermal treatment. To separate the thermal effect from the chemical effect, sinter pellets were heated to various temperatures in argon, soaked at temperature for 1 hour and allowed to cool. The samples were then reduced at 800°C . A plot of $(\text{O/Fe})_t$ vs time (Fig. 144) for samples heated and cooled at the same rate shows that as the thermal treatment temperature increases so the reaction rate increases. Particularly noticeable is the reaction rate maximum which occurs for a heat treatment temperature of 750°C . This effect was reproduced on several occasions.

Further investigations of the effect of heating and cooling rates (Fig. 145) showed that this effect was only apparent for the combination of slow heating and slow cooling.

It can be seen that raising the reaction temperature from 800°C to 900°C , full oxidation, or thermal treatment at 750°C can markedly increase reduction rates.

It is noticeable that the pronounced rate minima established for magnetite reduction are not present. This may be a function of the matrix surrounding the magnetite grains.

For example mass transfer through the matrix may be the predominant rate controlling step. Such a mechanism would tend to

give increasing reaction rates with increasing temperature.

Mechanisms operating within the ferruginous grain which cause the existence of rate minima in relatively pure magnetites may not have such a strong influence where a matrix is present.

The increase in reaction rate as a result of thermal treatment at 750°C may also be caused by a physical change in the matrix.

6.3. Metallography of Reduced Sinters

The physical structure of the sinter pellet before and after reduction and after pre-treatment has been extensively studied.

6.3.1. Unreduced Sinter Pellets

On microscopic examination the sinter pellet before re-sintering was seen to consist of cuboid magnetite grains surrounded by a matrix. The matrix contained wustite denrites, ferrite laths, some hematite and occasional grains of free iron (Fig. 8, 9).

On sintering the matrix homogenised, the hematite, wustite and ferrites were absorbed and the general porosity decreased. (Fig. 10, 12, 146) The matrix apparently became two phase (Fig. 147). Some bridging of the magnetite cuboids (Fig. 146) and some evidence of compositional variation within the cuboids was apparent (Fig. 11).

6.3.2. Reduced Sinter Pellets

For ease of description the metallography of the reduced pellets will be dealt with in three sections. i) Untreated Sinter Pellets ii) Oxidised Sinter Pellets iii) Thermally Treated Sinter Pellets.

6.3.2.1. Untreated Sinter Pellets

Samples reduced at 700°C display topochemical reduction (Fig. 148). No reaction could be seen to have occurred in advance of the interface. At a higher magnification using oil immersion techniques the reduced grains can be seen to be porous and relict of the original magnetite cuboids (Fig. 149). Examination of grains

at the interface shows partly reduced grains. Some grains have reduced from the edge (Fig. 150) and some from within the grain (Fig. 151) along specific planes.

The topochemical nature of reduction is continued at 800°C (Fig. 152). The reduced grains can be seen to be more finely porous than those at 700°C and again relict of the original cuboids. (Fig. 153) In general the grains were reduced from the edge adjacent to the sample surface (Fig. 154). An anomalous situation occurred on one sample where reduction of grains in the centre of the sample occurred (Fig. 156).

As the reaction temperature increased to 840°C reduction occurs in advance of the main interface (Figs. 157, 158, 159). This effect is enhanced as the temperature increases to 870°C (Fig. 160, 161). Samples reduced at 900°C, 1000°C and 1100°C were found to be reduced throughout. The grains were porous but the porosity appeared fine as the temperature increased (Fig. 162, 163, 164). The change in reduction from topochemical to general suggests a change in the rate controlling step from mass transfer within the matrix to chemical reaction control.

6.3.2.2. Oxidised Sinter Pellets

Pellets oxidised at 750°C and 1000°C exhibited typical hematite laths occupying the original cuboid structure (Fig. 165a). From the colour of the matrix it could be seen that some matrix oxidation had also occurred. The samples on reduction showed porous iron grains throughout (Fig. 165b).

Those pellets oxidised at 500°C did not display any hematite laths (Fig. 166) the samples had, however, increased in weight to a fully oxidised condition. It is considered that maghemite was formed which is metallographically indistinguishable from magnetite.

The reduced iron product was seen to be porous (Fig. 167).

6.3.2.3. Thermally Treated Sinter Pellets

Although many of these samples in the unreduced state were examined, no observable differences were noted between them and the original sintered untreated pellet. No change in porosity had occurred and no cracks or fissures had developed in the matrix. The samples were to all intents and purposes unaffected by the treatment. There was also no detectable difference between the sample thermally treated by slow heating and slow cooling at 750°C and any other thermally treated sample.

6.4. Porosities

Porosity determinations were carried out on all pellets before and after treatment and reduction (Fig. 168).

Where untreated pellets were reduced the increase in porosity was found to be almost directly proportional to the degree of reduction. In no case was there any measurable change in the sample dimensions. Thus the porosity was a direct result of the reduction reaction removing ions as gas, thus causing residual vacancies which coalesced to form pores within the ferruginous grain.

The dependence of porosity change on degree of reduction persisted for oxidised and thermally treated samples.

Little or no changes in porosity were found after thermal treatment and only small changes resulted from oxidation treatment.

6.5. Apparent Activation Energies

In order to determine the values of the apparent activation energies the logarithmic rates were plotted against the reciprocal of the isothermal reaction temperatures. (Figs. 169-174)

The energy values are given below.

Reduction interval (O/Fe) _{at.}	Temperature range °C (approx)	Apparent Activation Energy KJ/mol	Suggested Mechanism
1.34 - 1.10	800 - 900 >900	250 13	diffusion of ferric ions in magnetite
1.10 - 0.80	800 - 900 >900	260 100	diffusion of ferric ions in magnetite diffusion of ferric ions in wustite
0.80 - 0.25	800 - 900 >900	280 66	diffusion of ferric ions in magnetite Chemical reaction.
20 mins	< 800 800 - 900 >900	43 220 53	gaseous diffusion diffusion of ferric ions in magnetite Chemical reaction
40 mins	< 800 800 - 900 >900	43 220 28	gaseous diffusion diffusion of ferric ions in magnetite gaseous diffusion
100 mins	< 800 800 - 900 >900	50 190 8	gaseous diffusion diffusion of ferric ions in magnetite gaseous diffusion

For the intermediate temperature range 800 - 900°C for both constant reduction and time intervals the value of the apparent activation energy is consistent with the value of energy required for the diffusion of ferric ions in magnetite. (220-280 kJ/mol)

For the low temperature range <800°C the constant time calculations give energy values commensurate with the energy levels required for gaseous diffusion (40-50 kJ/mol).

For the high temperature range >900°C the value varies and it is difficult to assign consistently a possible reaction mechanism.

Positively the points at which the apparent activation energy plots change slope coincide with the temperatures at which probable changes in reaction mechanism occur.

6.6. Mathematical Treatment

The possible reaction rate laws applicable to the hydrogen reduction reaction have been discussed in Chapter 4.

The exponential law and the phase boundary law were considered separately. In order to determine whether either of these laws were rate controlling the data were plotted against each of them.

The untreated sinters were considered first. The oxidised and thermally treated sinters were considered separately and the results compared with the untreated samples reduced at 800°C.

6.6.1. Untreated Sinter Pellets

Typical plots of $1 - \sqrt[3]{\frac{(O/Fe)_t}{(O/Fe)_i}}$ vs. time and of $\ln \frac{(O/Fe)_t}{(O/Fe)_i}$

vs time i.e. the phase boundary reaction and the exponential diffusion laws respectively are shown in Figs. 175-181. The results are summarised in the table overleaf.

For reduction at 700°C a straight line relationship applies for the phase boundary law up to 7½ mins. which corresponds to an (O/Fe)_t ratio of 1.3. After this point the exponential law plot gives a straight line.

As the isothermal reaction temperature is increased to 800°C the phase boundary law is controlling for up to 10 minutes ((O/Fe)_t = 1.28). The exponential law takes over after 30 minutes. ((O/Fe)_t = 1.24).

On further increasing the temperature to 840°C the phase boundary reaction law again applies up to 10 mins. ((O/Fe)_t = 1.25). The exponential law appears to have two straight line regions from 10 mins. to 90 mins. ((O/Fe)_t = 1.25 to 1.02) and from 90 mins to 180 mins. ((O/Fe)_t = 1.02 to 0.75).

On further increasing the temperature to 870°C the phase boundary control now persists for 90 mins ((O/Fe)_t = 0.54) the exponential

law taking over at 140 mins. ($(O/Fe)_t = 0.19$).

At 900°C it becomes difficult to draw valid straight lines through the plots.

For 1000°C the phase boundary law controlled for 60 mins. ($(O/Fe)_t = 0.11$) and the exponential law plot was assumed to control throughout.

At 1100°C the phase boundary law controlled almost throughout.

Examination of the individual law plots showed that for the slow reaction rates predominantly chemical reaction control extended for only a very small change in O/Fe ratios, and was quickly overtaken by predominantly mass transport control. For the fast reaction rates (1000°C, 1100°C) the chemical control extended much further with mass transport control becoming predominant in the final stages. For the intermediate temperature ranges several changes in slope occurred and mixed control predominated.

°C	(O/Fe) range for predominantly chemical reaction	(O/Fe) range for predominantly mass transfer control
700	1.34-1.31	1.30-1.27
800	1.34-1.28	1.22-1.10
840	1.34-1.28	1.25-1.02, 1.02-0.75
870	1.34-0.61	1.34-0.61, 0.46-0.19, 0.19-0.10
900	1.34-1.16	0.08-0.07
1000	1.34-0.28	0.07-0
1100	1.34-0.11	0.55-0

It is apparent that as the reaction temperature increases so the balance between chemical reaction control and diffusion control also changes. The possible rate controlling factors at low temperature may initially be chemical reaction at the surface of the

pellet followed by mass transport control due to resistance to gas diffusion through the matrix. As the reaction temperature increases so the diffusion through the matrix becomes easier and the rate of reaction at the phase boundary becomes controlling. As the degree of reduction increases so the diffusion path within the ferruginous grain also increases and resistance to mass transfer becomes once more rate controlling for the final stages of reduction.

Thus, both chemical reaction and mass transport processes will be controlling to a greater or lesser degree during the isothermal reduction of lean magnetite sinters.

If the individual laws are applied over the reduction intervals indicated by the individual law plots then a composite calculated curve very close to the actual data can be derived. (Fig. 182, 183).

An extension of this technique to the fitting of a manual general law is difficult (Fig. 184) especially where there is a large time interval between almost exclusively phase boundary reaction control and almost exclusively mass transfer control.

A more satisfactory method can be carried out by computer techniques where weighting factors are applied to the individual terms. In this case the calculated line is very close to the actual data. (Figs. 185, 186)

6.6.2. Oxidised sinter Pellets

Typical sinter pellets oxidised fully at 750°C were taken. The predominantly chemical reaction control extended from $(O/Fe)_i = 1.55$ to $(O/Fe)_t = 0.31$ and the exponential law predominating in the later stages from $(O/Fe)_t = 0.12$ to $(O/Fe)_t = 0.11$ (Fig. 187). Thus the resistance of the matrix to diffusion in oxidised materials must be much less than otherwise. This may be due to changes in the crystalline nature of the matrix. Final mass transfer control will be as a result of diffusion paths becoming comparatively long.

The removal of transport control is even more marked when the known increased reaction rates as a result of oxidation are taken into account.

The change in reaction control as a result of oxidation will have caused the very marked increase in reduction rates between samples oxidised and then reduced at 800°C and samples untreated and reduced at 800°C.

It is noticeable that phase boundary reaction control persists until $(O/Fe)_t = 0.31$ for oxidised samples compared with $(O/Fe)_t = 1.28$ for non-oxidised samples.

Computerised individual law plots (Fig. 189) for oxidised sinters did not give good agreement with the data compared with the non-oxidised sinters reduced at 800°C. The general law plot gave better agreement (Fig. 190) but became unstable after 80 mins. due to the long linear portion from 80 mins to 180 mins.

The dramatic increase in reaction rates as a result of oxidation treatment is due to a change in reaction control from mass transport resistance to chemical reaction resistance except in the latter stages of reduction.

6.6.3. Thermally treated sinter pellets

Sinter pellets were thermally treated in an inert atmosphere. The isothermal treatment temperatures were 500°C, 650°C, 750°C, 850°C and 1000°C. The treated samples were reduced by hydrogen at 800°C.

The optimum treatment temperature was found to be 750°C. At this temperature the rate of reduction was at a maximum (Fig. 144).

Variations in heating and cooling rates at this temperature showed that this improvement in reaction rates over untreated pellets only occurred at slow heating and cooling rates.

Individual law plots showed that for slow heating and cooling

at 750°C the chemical reaction law controlled from $(O/Fe)_i = 1.35$ to $(O/Fe)_t = 1.2$ compared with 1.35 to 1.28 for untreated sinters. The chemical reaction rate constant increased almost three-fold and the exponential rate constant ten fold (Fig. 191).

The very large increase in the exponential law constant indicates an improvement in diffusion rates as a result of the thermal treatment.

A general law plot as calculated by the computer was found to give a good fit to the data indicating the necessity of mixed control reaction laws to describe the course of reduction (Fig. 193).

The restriction of the improvement in reaction rates to slow heating and slow cooling regimes indicates that some physical change is occurring within the matrix. X-ray diffraction studies indicate that this is not due to stress relieving effects which would in any case tend to reduce reaction rates. It is possible that sub-microscopic cracks are forming during the heating and cooling cycle which are undetectable by normal metallographic techniques.

6.7.

Discussion

Isothermal reduction of untreated, reconstituted sinter pellets indicated a progressive increase in reaction rate with increase in temperature. Slow reaction rates were experienced at 700°C and 800°C and fast reaction rates at 1000°C and 1100°C. For the intermediate temperatures intermediate reaction rates were found. The change in rate of reaction over a particular temperature range 300°C - 900°C indicated a change in reaction control mechanism. Examination of the reduced structures, the apparent activation energy plots and the individual reaction rate laws supported the existence of a change in reduction mode as the isothermal reaction temperature was increased.

For the low reaction temperatures 700°C, 800°C wholly topochemical reduction occurred. Partly reduced ferruginous grains could be seen at the interface and some reduction had occurred within the grains along specific planes. The grains had reduced from the edge nearest to the sample surface. The iron product was finely porous and relict of the original emboids. Although topochemical reduction is consistent with both chemical and mass transport control examination of partly reduced grains lead to the conclusion that mass transport was the controlling mechanism. The activation energy values also supported this belief.

Examination of the individual reaction rate laws showed that, for the low temperatures, chemical reaction control was limited to the very early stages of reduction ($O/Fe = 1.34 - 1.28$). It is probable therefore that initially the rate is controlled by chemical reaction at the sample surface. Once the surface layer has reacted then mass transport control becomes predominant. From the values of apparent activation energies this may possibly be gaseous diffusion. Examination of the microstructures indicate that gaseous diffusion through the matrix is controlling.

Therefore it can be concluded that for the low temperature reduction of lean magnetite sinter pellets the rate of reduction is initially controlled by the rate of reaction at the sample surface. Once the surface has reacted then mass transport through the matrix becomes rate controlling.

As the temperature increases through the intermediate range 840°C, 870°C reduction was seen to occur in advance of the main interface. This effect was more pronounced at 870°C thus indicating an increase in the rate of mass transport and the growing influence of the chemical reaction rate.

Apparent activation energy calculations give values of the order required for the diffusion of ferric ions in magnetite.

Examination of the individual reaction rate laws showed that chemical reaction rate control predominated over the range $(O/Fe)_t = 1.34 - 1.28$ and $1.34 - 0.61$ respectively. Changes in the slope of the exponential law straight lines indicated the possibility of changing diffusion modes controlling the transport mechanism.

Clearly as the reduction temperature increases diffusion through the matrix will increase and the rate of chemical reaction will become more significant in the early stages. In the later stages ferric ion diffusion may become controlling.

For the high reaction temperatures 900°C , 1000°C , 1100°C topochemical reduction disappears. This indicates that mass transport is no longer the controlling mechanism.

For the temperature range $900^{\circ}\text{C} - 1100^{\circ}\text{C}$ the values of the apparent activation energies vary and it becomes difficult to use such values to determine the possible controlling mechanism.

Analysis of the individual rate laws show that the influence of chemical control extends from $(O/Fe) = 1.34 - 1.16$ at 900°C , $1.34 - 0.28$ at 1000°C and $1.34 - 0.11$ at 1100°C with mass transport predominating only in the final stages. The probability is that at higher reaction temperatures matrix diffusion rates increase and the chemical reaction becomes rate controlling. Except in the final stages where diffusion paths are long and mass transport control predominates.

Clearly the reduction of sinter pellets even in the present idealised conditions is characterised by complex reduction mechanisms. Chemical reaction and mass transfer both play a part to a greater or lesser degree.

Because of the low reaction at 800°C it was considered that oxidation of sinter pellets prior to reduction may enhance the reaction rate. Oxidation at varying temperatures gave typically higher oxide structures except at 500°C when maghemite (γ -Fe₂O₃) was formed.

Metallographically the reduced microstructures changed from the topochemical reaction of the untreated pellets to general reduction in the oxidised pellets, indicating a change in the reduction mechanism from predominantly mass transport to predominantly chemical control.

Study of the reaction rate laws showed that the extent of chemical control was, typically, from $(O/Fe)_t = 1.55 - 0.31$ with diffusion control becoming predominant in the final stages. The improvement in diffusion is doubtless due to the change in structure of the ferruginous grains and the change in structure of the matrix. Matrix oxidation has clearly occurred since the gain in weight on oxidation is greater than the stoichiometric weight gain of $Fe_3O_4 \rightarrow Fe_2O_3$, possibly by oxidation of $MnO \rightarrow Mn_2O_3$.

The change from diffusion to chemical control is even more marked when the known increased reaction rates as a result of oxidation are taken into account.

It was considered that thermal treatment of sinters may have an effect separately from that encountered on oxidation. It has been shown that isothermal heat treatment in an inert atmosphere can result in increases in reaction rates. The optimum treatment temperature was found to be 750°C. A study of various heating and cooling rates for this temperature revealed that only slow heating and cooling cycles could successfully induce the required increase in reaction rate. The necessary combination of slow heating and slow heating and slow cooling may mean that time above a critical temperature

is important. Such a critical temperature may be the 'triple point' where $4\text{FeO} \rightleftharpoons \text{Fe}_3\text{O}_4 + \text{Fe}$.

Metallographic examination of the reduced samples showed some reduction in advance of the interface indicating an increase in the extent of chemical control.

This was borne out by a study of the reaction rates laws the chemical control extending from $(\text{O}/\text{Fe})_t = 1.35-1.28$ to $(\text{O}/\text{Fe})_t = 1.35-1.20$. The chemical reaction rate constant was found to have increased threefold and the diffusion rate constant tenfold.

No metallographic, crystallographic or chemical change could be detected in the thermally treated samples. There was undoubtedly an increase in reaction rates. The restriction to the slow heating and cooling cycles indicating the probability that some physical change had taken place.

In addition to the improvement of reaction rates of untreated sinters as the reaction temperature increases there was found to be a critical temperature range $800^\circ\text{C} - 900^\circ\text{C}$ above which the rate increased markedly.

Further the low temperature oxidation of sinters to either maghemite or hematite can greatly enhance reaction rates.

Significantly the low temperature (i.e. < devitrification temperature) thermal treatment of sinters can be used to enhance reaction rates provided the correct heat treatment of sinters can be used to enhance reaction rates provided the correct heat treatment cycle can be selected.

CHAPTER 7

General Discussion

In this thesis the hydrogen reduction of naturally occurring magnetite and lean magnetite sinters has been studied closely.

The progress of reduction of single pieces of magnetite and of single sinter pellets with time has been monitored by automatic and semi-automatic measurement of weight loss.

The effect of isothermal reduction temperature on reaction rates has been closely studied. Exhaustive metallographic studies have been supported by mathematical techniques in order to deduce the controlling mechanisms. An empirical general law using computer techniques and combining chemical and diffusion terms has been developed. The effect of thermal and oxidation treatment of sinter and their effect on reaction rates have been studied.

Additionally a study of the mass transfer characteristics of the thermogravimetric balances has been made using ambient modelling techniques. This last item is adequately discussed in Chapter 4.

Previously there has been considerable doubt as to the rate controlling mechanism of magnetite reduction and the reasons for the occurrence of rate minima.

In this thesis two distinct rate minima have been displayed at 650°C and 900°C when magnetite is reduced isothermally by hydrogen within the temperature range $400^{\circ}\text{C} - 1000^{\circ}\text{C}$. The minima occurred at the same temperatures not withstanding the difference in physical structures between the series 1 and 2 samples and the use of different balances, spring and Stanton, with different mass transfer characteristics.

Generally only one rate minimum is reported and that over a temperature range. Where a second minimum is indicated it is normally as a discontinuity in reaction rate. Such minima have been reported to occur within the temperature range $600^{\circ}\text{C} - 900^{\circ}\text{C}$ (15, 118).

An exhaustive metallographic study of the reduced structures has been carried out.

For the samples reduced at 650°C the rate minimum is shown to be associated with the formation of three distinct macro-bands which result from porosity variations across the sample. The finely porous inner band and the non-porous product in the core is considered to inhibit mass transport and thus slow down reaction rates. The finely porous inner band and non-porous core are thought to result from the formation of a stable, dense intermediate product phase of wustite. The wustite layer itself was not visible due to extended degree of reduction and the moderate cooling rates of the samples. Hydrogen reduction of series 1 magnetites for intermediate degrees of reduction did give evidence of dense wustite formation. (15, 138)

Variation in reaction rate during reduction is considered to be responsible for the porosity variation across the samples. The formation of dense wustite resulting in a dense iron product thus slowing down reaction has been supported previously. (29)

Apparent activation energy plots show definite breaks in the slope which occur at the rate minima temperatures 650°C and 900°C thus indicating a structure sensitive control mechanism.

Further support for mass transport control is given by the topochemical reduction of series 1 samples at the low temperature rate minimum (15). The change in porosity across the samples indicates the possibility of changes in the controlling mechanism.

Accordingly reaction rate laws were plotted against time. This revealed the possibility of initial predominantly chemical reaction control at the surface followed by mass transport control in the later stages with mixed reaction control in the intervening stages. A computed general law using weighting factors gave good agreement with the actual data. Strangway et. al. (118, 119) also postulated a mixed control mechanism. Temperature coefficients of 65 KJ/mol for 10% reduction and 41KJ/mol (139) also indicate interfacial and gaseous diffusion control respectively. The existence of the high temperature rate minimum has been shown by Edstrom (29) this has been confirmed in this work.

The metallography of the samples reduced at 900°C is quite different from those reduced at lower temperatures. Macro-topochemical reduction is replaced by micro-topochemical reduction indicating initial interface reaction control superseded by diffusion control. Dense iron shells are seen to surround the individual grains. It is thought that at this temperature sintering of the iron layer takes place. Analysis of individual rate law plots confirms that chemical reaction control predominates initially followed by a period of mixed control with diffusion control predominating in the final stages.

Apparent activation energy plots show a definite slope change at 900°C. The value of the apparent activation energy above 900°C is 113 KJ/mol which approaches the value required for the diffusion of ferrous ions in wustite.

It is clear that again a mixed control mechanism operates for the reduction rate minimum at 900°C. Initially the rate is controlled by the reaction at the interface. As the reaction product forms it sinters and becomes dense thus preventing gas access to the

oxide. Iron ion diffusion through the product layer then becomes rate controlling.

For the temperatures between the two rate minima a rate maximum occurs at 750°C. Metallographically the reduction is topochemical but not geometric indicating diffusion control and the product is cracked and porous. The apparent activation energy measured over this temperature range was found to be 6 KJ/mol which is of the order required for gaseous diffusion. Analysis of the individual rate laws shows that mass transport control holds for most of the reduction time. However, interface reaction control is shown to be possible in the early stages.

It is evident that controlling mechanism is the diffusion of the binary gas mixture H_2-H_2O within the pores of the product layer. The pores being formed from vacancies left behind as the reaction front advances. The reduction rate slows down in the later stages as the diffusion paths increase in length and tortuosity.

It is noticeable that the porosity increases continually with reduction at 750°C compared with the porosity plateaus which are evident at the low and high temperature rate minima. (15, 133)

Over the temperature ranges considered the overall reaction rate has depended in part on the thermo-gravimetric balance used for the reduction. This is due to the mass transfer coefficient across the boundary layer being four times greater for the spring balance than for the Stanton balance.

Several theories on the mechanism of the hydrogen reduction of magnetite have been postulated and are discussed in Section 1.5.

There is now no doubt from the evidence submitted in this thesis that more than one mechanism controls the rate of reaction for the hydrogen reduction of magnetite. Additionally the precise position-

ing of reaction rate minima has been carried out.

In general the hydrogen reduction of magnetites is controlled initially by chemical reaction and then predominantly by mass transport as reduction proceeds. The nature of mass transport varies depending on the developing reduced structure of the samples.

At 650°C the mass transport control is probably a combination of gaseous and ionic diffusion. At 750°C the control becomes wholly gaseous diffusion within the product pores. At 900°C the control again becomes subject to ionic diffusion control.

Previously many workers have suggested that a single rate controlling mechanism is probable. Gaseous⁽¹¹²⁾ and ionic diffusion⁽²⁷⁾ controls have separately been postulated. A linearly contracting interface has been widely considered to support the probability of rate control at the iron-iron oxide interface,^(79, 80) further support being given to this theory by temperature coefficient considerations which can be clouded by changes in physical parameters. It has been pointed out in this thesis and elsewhere^(43, 129) that linearly contracting interfaces are not exclusive to interface reaction control and are possible for mass transport controlled reactions.

Support for mixed control mechanisms has been reported. There is some evidence that low temperature diffusion control may be superseded by high temperature chemical reaction control above 900°C for magnetite reduction.^(15, 83) Also variation of control mechanism with degree of reduction has been postulated.⁽¹³⁸⁾

It is evident that for very fast reduction rates on a commercial basis that diffusion resistance must be minimised. Hydrogen reduction

of magnetites should not take place where rate minima are likely to occur. Also porous oxide must be used in order to promote ease of gas access.

All commercial iron bearing materials consist of ferruginous grains surrounded by a matrix. The amount and composition of the matrix has a significant effect on reducibility.

Matrices comprise, in, general, crystalline silicates, silicate glasses containing iron oxides and calcium ferrites together with other minor constituents. The amounts of each phase vary with the basicity of the matrix.

The primary constituents of a commercially available lean magnetite sinter as used in this work consist of hematite, magnetite, wustite, calcium ferrites, lime, mellilite, di-calcium silicate, glass and olivines. The magnetite being formed by recrystallisation as euhedral crystals. The wustite occurring as fernleaf dendrites. Hematite was formed by oxidation of the magnetite along the octahedral planes.

The sinter used in this work contained all the above constituents. On crushing, pelletising and resintering the minor constituents were absorbed leaving a sinter pellet comprising magnetite cuboids in a silicate matrix.

The pellets were then reduced isothermally over the range 700°C to 1100°C . Reconstituted sinter pellets were used in order to remove variabilities inherent in commercial sinter pieces and to ensure a constant porosity.

An increase in reaction rate over the range 700°C - 1100°C , was found to occur. Between 800°C and 900°C . Careful metallographic examination was carried out on the reduced samples.

At the low reaction temperatures 700°C, 800°C the reduction was wholly topochemical. Ferruginous grains at the reduced-unreduced interface were partly reacted from the edge of the grain nearest to the sample surface. The metallographic evidence is consistent with matrix diffusion control. However a study of the apparent activation energy plots showed that the energy values for $E=42-50\text{KJ/mol}$ which are on the border for the energies required for gaseous diffusion control and for chemical reaction control.

Examination of the individual reaction laws shows that in the very early stages of reduction that the reaction at the sample surface is controlling. As reduction proceeds then diffusion control predominates. The approximate value of the bulk volume diffusion coefficient was found to lie between $1.2-1.7 \text{ cm}\cdot\text{sec}^{-1} \times 10^{-5}$ which is of the order of hydrogen diffusion in silicates.

It is evident that the rate controlling mechanism in the 700°C - 800°C range is the diffusion of $\text{H}_2\text{-H}_2\text{O}$ in the silicate matrix. Interface reaction control operates until the pellet surface is reduced.

As the reaction rate increased through the critical temperature range 800°C - 900°C reduction was found to take place in advance of the interface. The interface becomes diffuse and a change to overall chemical reaction control was indicated. This effect was more pronounced at 870°C than at 840°C indicating an increase in diffusion rate with the increase in temperature.

Chemical reaction control predominates for almost 50% of reduction at 870°C. The diffusion law plot indicated changes of slope suggesting the possibility of different diffusion modes contributing to the diffusion control mechanism in the later stages.

Calculation of the apparent activation energies for both constant time and constant reduction gave values between 190-220KJ/mol and 250-280KJ/mol respectively which is consistent with the energy required for the diffusion of ferric ions in magnetite.

Clearly as the reduction temperature increases, so the rate of diffusion increases and the interfacial reaction becomes more significant. In the later stages of reduction iron-ion diffusion within the ferruginous grains may become controlling.

Further increase in reduction temperature to 900°C leads to much increased reaction rate compared with 800°C and reduction is no longer topochemical. This indicates predominantly chemical reaction control.

Apparent activation energy calculations show a gradually reducing value of E from 53KJ/mol through 28KJ/mol to 8KJ/mol as the constant time increases. This indicates a change from chemical reaction control in the early stages of reduction through to gaseous diffusion control in the later stages. The constant reduction plots indicate that gaseous diffusion controls in the early stages followed by iron-ion diffusion control to interface reaction control in the final stages.

Analysis of the individual rate laws show that chemical reaction control increases in extent as the reaction temperature is increased.

It is evident therefore that chemical reaction control becomes predominant as temperatures are increased. Diffusion control operates in the final stages of reduction.

In all cases the mixed-control mechanism gave better agreement with the data than either of the individual laws.

Previously (57, 106) it has been supposed that chemical reaction at the interface solely controls reaction rates. Some support for

the possibility of mixed reaction control was given. (106) From the current work there is no doubt that both chemical and diffusion control play their part during reduction. Gaseous diffusion controls predominantly at 700°C, 800°C and chemical reaction control predominantly at 900°C, 1000°C 1100°C. Between 800°C and 900°C both chemical and diffusion controls play significant roles.

Edstrom pointed out the superior reducibility of hematite compared with magnetite and showed that a small degree of oxidation can significantly affect the rate of reduction. Heat treatment of sinters in oxidising atmospheres between 900°C and 1100°C has been shown to improve sinter properties (98) by oxidising the magnetite to hematite and by devitrification. Improvement as a result of devitrification has been pointed out by other workers (98, 128). In general the treatment temperatures have varied between 900°C and 1250°C thus allowing devitrification to take place.

Smith (106, 107) confirmed that more highly oxidised lean magnetite sinters were more reducible but considered that low temperature treatments were ineffective.

In the present work lean magnetite sinter pellets were fully oxidised isothermally at 500°C, 750°C and 1000°C. In all cases significant improvements in reaction rates at 800°C were obtained compared with the slow reduction of the untreated pellets at that temperature.

Metallographically the sinter pellets oxidised at 750°C and 1000°C showed that the structure had fully oxidised confirming the weight gain in oxidation. Hematite laths had formed in the magnetite cuboids. Further oxidation within the matrix had also occurred thus improving matrix permeability. (98, 106, 107).

At 500°C the pellets were found to increase in weight to that

required for full oxidation. However the samples remained magnetic. Metallographic examination revealed no optical difference between the magnetite cuboids after treatment compared with before. It was concluded that maghemite the magnetic form of hematite, had been formed. There is substantial evidence for its low temperature formation from magnetite (11, 21, 127). Its formation in sinter (27) has been confirmed in this work. Maghemite is stable in impure magnetites between 300°C and 800°C. However, hematite has been shown to form on oxidation.

The reduced microstructures indicated general reduction behaviour contrasting markedly with the topochemical behaviour of untreated pellets reduced at 800°C. This indicated a change in the controlling mechanism from predominantly gaseous diffusion control to predominantly interface reaction control.

A study of the reaction rate laws showed that chemical control extended typically to 80% of reduction. Diffusion control becomes significant in the final stages. The improvement in diffusion rates is undoubtedly due to the oxidation of the matrix and the oxidation of the ferruginous grains.

The change from diffusion to chemical control is even more pronounced when the known increased reaction rates as a result of oxidation are considered.

It has previously been considered that thermal treatment of sinters in oxidising atmospheres improves reducibility as a result of devitrification, (69, 87, 98, 128). In this thesis it has been considered that part of the improvement in reducibility as a result of oxidation may have been the thermal cycle notwithstanding the fact that it is below devitrification temperatures.

Consequently it has been shown that isothermal heat treatment in an inert atmosphere over the temperature range 500°C to 1000°C can improve the reaction rate. The optimum improvement on the reducibility 800°C reaction was found to occur at the treatment temperature 750°C.

A study of various combinations of heating and cooling rates for this temperature revealed that only slow heating and slow cooling cycles could successfully induce the required increase in reaction rate.

Metallographic examination of the reduced samples showed some reduction in advance of the interface indicating an increase in the extent of chemical control compared with untreated samples reduced at 800°C.

This was supported by a study of the reaction rate laws which indicated that chemical control extended for a greater proportion of the reduction. The chemical reaction control rate constant was found to have increased threefold and the diffusion rate constant by tenfold.

No metallographic, crystallographic or chemical change could be detected in the thermally treated samples. There was, however, a significant increase in reaction rates after heat treatment. The restriction in improvement to the slow heating and cooling cycles, indicates the probability that some annealing effect had occurred. It has previously been pointed out ⁽⁴⁸⁾ that annealing of oxides enhances reduction rates due to equilibration of surface defects, by reducing positive hole concentration and increasing vacant cation sites thus enhancing reduction. Some similar effect may have occurred in the matrix in the current case.

CONCLUSIONS

The conclusions are given in the order they are presented in the thesis.

1. The mass transfer characteristics of the two balances used in the work have been determined. The mass transfer coefficient for the tube-particle geometry of the spring balance was found to be four times that for the Stanton balance.

Comparisons between reaction rates determined by the two balances must take the above differences into account.

Mass transfer control becomes important particularly where easily reducible materials were reacted in the Stanton balance.

2. An empirical general reaction two term equation rate combining an exponential diffusion term and a chemical reaction term has been developed. Using weighting factors to the individual terms the equation can adequately describe the reduction reaction.

3. Isothermal reduction of naturally occurring magnetite between 400°C - $1,000^{\circ}\text{C}$ revealed the existence of two rate maxima at 550°C and 750°C and two rate minima at 650°C and 900°C .

Metallographic studies gave evidence that the rate minima were the result of the formation of dense, impervious macro and micro product phases respectively. The rate maxima were found to be the result of the formation of porous, cracked product phase.

4. A study of the individual reaction rate laws applied to magnetite reduction displayed conclusively that neither the exponential diffusion law nor the interface reaction law apply exclusively over a range of temperatures or within reduction at a single temperature.

In general the phase boundary law was shown to hold for the initial stages of the reaction and the exponential law for the final stages of reaction. The change in control was shown not to occur at a specific degree of reduction and considerable time lapses could be seen to occur between the end of predominantly phase boundary reaction control and predominantly exponential diffusion control.

5. A manual mixed control law was found to give good agreement where the time lapse between the first and final stages was small. Where this time lapse was large a computerised mixed control law using empirical weighting factors was found to give reasonable agreement.
6. Isothermal reduction of lean magnetite sinters between 700°C - 1,100°C did not reveal the existence of any rate minima. However, there was a large increase in reaction rate between 800°C and 900°C.
7. Metallographic examination of the reduced sinters showed a change from topochemical reduction at the low temperatures to general reduction at high temperatures. This indicates a change in control from mass transport to chemical diffusion.. Support for the low temperature mass transport control by the apparent activation energy values. Examination of the individual reaction rate laws showed that chemical reaction control was limited to the initial reduction of the sample surface. The evidence suggests that probably gaseous diffusion through the matrix predominates.

As the temperature increased the increase in extent of chemical reaction control was supported by examination of the individual reaction laws. At the higher temperatures exponential diffusion was found to predominate only in the final stages.

8. Oxidation of sinter pellets prior to reduction at 800°C gave greatly enhanced reaction rates. The oxidation temperature ranged from 500°C - 1,000°C with γ -Fe₂O₃ being formed at 500°C. In all cases considerable increases in reaction rates could be seen.

A study of the metallography and of the reaction rate laws indicated a change from mass transport to chemical reaction control.

9. Thermal treatment of sinter pellets between 500°C - 1,000°C also gave increased reaction rates at 800°C. The optimum treatment temperature was found to be 750°C. A study of various heating and cooling rates revealed that only slow heating and cooling cycles could successfully induce the increased reaction rates.

No change in metallographic or crystallographic structure could be detected. It is thought that some undetected physical change must have occurred perhaps associated with the triple point $4\text{FeO} \rightleftharpoons \text{Fe}_3\text{O}_4 + \text{Fe}$.

on figures re the same

Suggestions for Future Work

1. Magnetites should be reduced using carbon monoxide, mixtures of carbon monoxide and hydrogen, simulated blast furnace gas and hydrocarbons in order to determine whether there is any variation in the occurrence of rate maxima and minima.
2. The effect of matrix on the existence of such minima should be studied by a gradual increase in the amount of matrix from zero to the amount involved in sinters.
3. Further investigations are needed specifically at the rate minima temperatures particularly by reducing samples to varying degrees and their subsequent examination. Such studies could further examine the reasons for the minima and suggest means by which they may be avoided.
4. Low temperature thermal treatment of sinters, (i.e. sub de-vitrification temperature) will be fruitful in order to determine how maximum reducibility may be achieved.

In particular exhaustive physical examination could reveal the reason for the enhancement in reaction rates described in this thesis.
5. The reduction of enriched sinters would be of considerable benefit particularly with the increasing world wide useage of high foreign ore sinter burdens.
6. A mathematically designed universal, mixed control law with well defined terms should be developed in order to determine the contribution to the reaction of the various mechanisms.

7. Fundamental pure crystal reduction should also be fruitful in that variables introduced by uncontrolled factors would be removed, e.g. naturally occurring gangue, physical structure variation, dissolved cations.

8. Electron microscope studies of reduced samples may also be useful in determining modes of reduction within crystals.

REFERENCES

1. ANDERSON J.S., ROBERTS L.E.J., Reviews of Pure and Applied Chemistry 1972.
2. ANDRUSSOW L., Z. Electrochemie, 54 1950, 567
3. BARRER R.M. Phil. Mag. 35, (12), 1944, 802.
4. BOGBANDY L., JANKE W., Z Electrochemie 61, 1957, 1146
5. BICKNESE E., CLARK R., Trans. Met. Soc. AIME 236, 1966, 2
6. BEETON T.B., J.I.S.I. Nov. 1953
7. BARNER N.E., MANNING F.S., PHILBROOK W.O., Trans. Met. Soc. AIME, 227, Aug. 1963, 897
8. BRILL-EDWARDS H., SAMUEL R.L., J.I.S.I. Apr. 1965, 361
9. BRILL-EDWARDS H., STONE H. E. N., DANIELL B.L., J.I.S.I. Dec. 1969
10. BARRIE D.J., CARMICHAEL I.F., KINLOCH E.D., J.I.S.I. May 1969
11. BALL D.F., BUTTLER F.G., RATTER H., Iron and Steel, Apr. 1966, 150
12. BYTKIN V.N., et al., Stal in English, July 1965, 509
13. BOJARSKI Z., BARSZEZ E., ZIELINSKII S., J.I.S.I. Aug. 1965, 792
14. BRUNNER M., Jernkont, Ann., 152, 1968
15. BROADBENT P.A., B.Sc. project Sheffield Polytechnic 1969
16. BITSIANES G., JOSEPH T.L., Trans. Met. Soc. AIME May 1955, Journal of Metals
17. CARTER R.E., J. Chem. Phys. 34, 6, 1961, 2010
18. COX J.H., ROSS H.U., Blast Furnace, Coke Ovens, Raw Mat. Proc., AIME, 20, 1961, 266
19. CHUFAROV G.I., AVERBUKH B.D., J. Phys. Chem. (USSR) 5, 1934, 1292
20. CHUFAROV G. I., LEONT'EV L.I., et al Russ. J. of Inorg. Chem. Feb. 1965
21. COLOMBO U. et al La Chimica e L'Industria 46, 1964, 357
22. COHEUR P., J.I.S.I. Oct. 1969, 1291
23. DALLA LANA. I.G., AMUNDSEN N.R., Ind. Eng. Chem. 53, 1961, 22
24. DARKEN L.S., GURRY R.W., J. Am. Chem. Soc. 68, 1946, 798

25. DAVIES M.H., SIMNAD M.T., BIRCHENALL C.E., J.O.M., 3, 1951, 142
26. EDSTROM J.O., Jernkontorets Ann, 141, 1957, 809
27. EDSTROM J.O., J.I.S.I. Nov. 1953
28. EDSTROM J.O., Jernkontorets Ann, 141, 1957, 55
29. EDSTROM J.O., Iron and Steel Dec. 11, 1953, 612
30. EDSTROM J.O., Iron and Steel 1955
31. EDSTROM J.O., BITSIANES G., J.O.M. June 1955, 760
32. FENSHAM P.J., J. Aust. Inst. Metals V.7 No. 2 May 1962
33. FEINMAN J., SMITH N.D., MUSKAT D.A., I and E.C. Process Design and Development v.4 No. 3, 1965, 270
34. FRANK van der MERWE
35. FITTON J.T., GOLDRING D.C., J.I.S.I. May 1966, 452
36. ENGELL H.J., Acta Mét 6, 1958
37. EGGAR K., FEITKNECHT W., Helva.Chim.Acta 45, 1962, 2042
38. EGUBAEV S.Kh., et. al Zh. Prikl, Khimii 39, No. 1 Jan. 1966, 20
39. GINSTLING A.M., BROUNSHTEIN B.I., J. Appl.Chem. USSR 23, 1950, 1327
40. GEISS E.A., J.Amer.Chem. Soc. 46, 8, 1963, 374
41. GELLNER O.H., RICHARDSON F.D., Nature No. 4262 July 1951, 23
42. GRAY N.B., HENDERSON J., Trans Met. Soc. AIME 236, Aug. 1966, 1213
43. HILLS, A.W.D., Proc. Symp. John Percy Research Group Imperial College London, Ecl. Hills (Inst. Min. Met) 1967
44. HANSEN J.P., BITSIANES G., JOSEPH T.L., Blast Furnace, Coke Oven, Raw Mat. Conf. AIME 1960
45. HANSEN J.P., RUSHTON T.N., SCHULTZ C.W., Rep. Invest. No. 6827, 1966 U.S. Bureau of Mines
46. HANSEN J.P., RUSHTON T.N., KHALAFALLA S.E., Rep. Invest. No. 6712 U.S. Bureau of Mines
47. HOCKINGS W.A., Blast Furnace, Coke Oven and Raw Mat. Arc. AIME 1960
48. HAUFFE
49. HIMMEL L., MEHL R.F., BIRCHENALL C.E., Trans AIME, 197, 1953
50. HENDERSON J.B., Physical Chemistry of Process Metallurgy part 2 (Interscience Pub) 1961 New York

51. HOEPMANN K., Z. anorg. Chem. 38, 1925, 715
52. HUEBLER J., Proc. Electrochem Soc. Iron Ore Reduction
Ed. Rogers 1960, 24
53. HAUFPE , RAHMELL , Z. Phys. Chem. 199, 1952, 152
54. HAAS K.P., BITSIANES G., JOSEPH T.L., Blast Furnace,
Coke Oven and Raw Mat. Conf. 1960, 429
55. HARBORD W.H., GOLDRING D.C., J.I.S.I. Apr. 1965, 349
56. HANCART J., LEROY V., BRAGARD A., C.N.R.M. No. 11, June 1967
57. HICKLING D., A.C.T. Project Sheffield College of Technology
1965
58. JANDER W., J. Appl. Chem. 163 (1/2) 1927
59. JOSEPH T.L., Trans AIME 120, 1936, 72
60. JERVIS J., Steel Times, April 1966
61. KOSTELOV O.L, ROSTOVTSSEV S.T., Stal no. 3 1965, 209
62. KROGER C., ZEIGLER G., II Glastechn. Ber. 26, 11, 1953, 346
63. KROGER C., ZEIGLER G., III Glastechn. Ber. 27, 6, 1954, 199
64. KAWASAKI, E., SANSCRAINTE J., WALSH T.J., A.I.Ch. E.J, 8, 1963, 48
65. KNACKE, O., Arch. Eisenhüttenw, vol.30 (1959) p581 - 584
66. KOHL, H.K. MARINECEK B., Arch. Eisenhüttenw, 36, Dec. 1965
67. KHALAFALLA S.E., WESTON P.L. Jnr. Trans AIME, 239, Oct 1967,
1494
68. KHALAFALLA S.E., SCHULTZ C.W., RUSHTON T.N., Rep. Invest.
No. 6832 1966 U.S. Bureau of Mines
69. KISSIN D.A., LITVINOVA T.I., Stal in English, 5, 1960, 318
70. LAIDLER K.J.
71. LEWIS, Trans AIME 1947, 27
72. LEVENSPIEL O., Chemical Reaction Engineering Ch.12
J. Willey and Sons New York 1962
73. LU, Wei-Kao, Trans. Met. Soc. AIME vol. 227 Feb.1963 p203 - 206
74. LEVIN R.L., WAGNER J.B., Jnr., Trans. Met. Soc. AIME
233, Jan. 1965, 159
75. LANDLER P.F.J., KOMAREK K.L., Trans. Met. Soc. AIME
236, Feb. 1966, 138
76. LLOYD W.A., AMUNDSEN N.R., Ind. Eng. Chem. 53, 1961, 19
77. McKEWAN W.M., Trans. Met. Soc. AIME, 212, 1958, 791

78. McKEWAN W.M., Trans.Met. Soc. AIME, 218, 1960, 2
79. McKEWAN W.M., Trans.Met. Soc. AIME, 221, 1961, 140
80. McKEWAN W.M., Trans.Met. Soc. AIME, 224, 1962, 2
81. McKEWAN W.M., Trans.Met. Soc. AIME, 224, 1962, 387
82. MORAN V.J., J.Aust. Inst, Metals, v7, No. 2, May 1962, 100
83. MORAN V.J., Jenkins A.E., J.I.S.I. Sept. 1961, 26
84. MANNING F.S., PHILBROOK W.O., Blast Furnace Theory and Practice v2, Ed. Strassburger, Gordon and Breach 1969, 859
85. MEYER H.N., Mitt, Kaiser-Wilhelm Inst. Eishforsch, Dusseldorf, 10, 1928, 107
86. MOREAU J., BARDOLLE J., BERNARD J., REV. MET. 48, 1951, 486
87. MAZANEK E., JASIENSKA S., J.I.S.I. Jun.1963, 60
88. MAZANEK E., JASIENSKA S., J.I.S.I. Apr. 1964, 319
89. MAZANEK E., JASIENSKA S., J.I.S.I. Apr. 1966
90. MOREAU J., BARDOLLE J., AMUNDSEN N.R., Ind. Eng. Chem. 53, 1961
91. NAKAMURA Y., Jap. Acad. Proc. 40, No. 3 Mar 1964
92. OLSSSEN R.G., McKEWAN W.M., Trans Met. Soc. AIME 236, Nov. 1966
93. OATES W.A., TODD D.D., J. Aust. Inct Metals v7, No. 2 May 1962
94. PHILBROOK W.O. B.F. and Steel Plant 1947, 893
95. PEPPER M.D., DANIELL B.L., J.I.S.I. July 1969
96. PEPPER M.D., DANIELL B.L., J.I.S.I. June 1970
97. POKHVISNEV A.N., et al Stal in English, Feb. 1970
98. POKHVISNEV A.N., VEGMAN E.F., et al Stal No. 3 Mar. 1967
99. QUETS J.M., WADSWORTH M.E., LEWIS J.R., Trans AIME 218, 1960, 545
100. QUETS J.M., WADSWORTH M.E., LEWIS J.R., Trans AIME 221, 1960, 1186
101. ROTH W.L., Acta Cryst., 13, 1960, 140
102. RUECKL R.L., Blast Furnace, Coke Oven and Raw Mat. Conf. 1962
103. RAVIKOVICH I.M., BRATCHIKOV S.G. et al Stal in English no.2 1967
104. RICHARDSON E.C. A.C.T. project Sheffield College of Technology 1965
105. SPITZER R.H., MANNING F.S., PHILBROOK W.O., Trans Met. Soc. AIME 236, 1966, 726

106. SMITH T.J.J., MADDOCKS W.R., NIXON E.W., 9th Commonwealth Mining and Metallurgical Congress, 1969 paper 21
107. SMITH T.J.J., M. Met. thesis. University of Sheffield 1964
108. ST. CLAIR H.W., Rep. Invest. No. 6975 19 U.S. Bureau Mines
109. SETH B.B.L., ROSS H.U., Can. Met. Quart, 2, No. 1, 1963, 15
110. SETH B.B.L., ROSS H.U., Trans. Met. Soc. AIME 1233, 1965, 180
111. SCHURMAN E., BEER H., WILLEMS J., Arch. Eisenhüttenw v31, 1960 ~~7~~ 9
112. SPECHT O.G. Jnr. JAPPEFFE C.A., Trans AIME 167 (1946) 237
113. STALHANE B., MALMBERG T., Jernkontorets Ann., 114, 1930, 609
114. STONE H.E.N., DANIELL B.L., J.I.S.I. Jan 1969 7
115. STONE H.E.N., DANIELL B.L., J.I.S.I. Feb. 1969
116. SCHMIDT E.R., VERMAAS F.H.S., Econ. geol., 40, 1955, 422
117. SMERCEK K., Sb Praci. Vyzkum Ustava ZDHE, 1962, 3, 99
118. STRANGWAY P.K., ROSS H.U., Can. Met. Quart v.4 No. 1 Jan - March 1965
119. STRANGWAY P.K., LIEN H.O., ROSS H.U., Can. Met. Quart v.8 No. 2 ? 235
120. THEMELIS N.J., GAUVIN W.H., Can. Min. Met. Bull. July 1962, 444
121. TAMMAM G., Z. Anorg. Chem., 149, 21, 1925
122. TENENBAUM M, JOSEPH T.L. Trans. AIME v.135 1939 p59 - 72
123. THEMELIS N.J., GAUVIN W.H., Trans AIME 227, 1963, 290
124. STONE H.E.N., DANIELL B.L., J.I.S.I. Apr. 1970
125. UDY M.C., LORIG C.H., Trans AIME, 1943, 154
126. VALENSI G., Congot. Rend. 202 (4), 1936 309
127. VASYUTINSKII N.A., VOLGAI V.F., Z. Prikladnos Khimiii v38 No. 8 Aug. 1965, 1740
128. VEGMAN E.F., Metallurg No. 10 1966
129. WARNER N.A., Aust. Inot. Min and Met. 1963, 31
130. WARNER N.A., Trans Met. Soc. AIME v230, Feb. 1964, 163
131. WILHELEM A.J., ST. PIERRE G.R., Trans AIME 211, 1961, 545
132. WAGNER C., J.O.M. Feb. 1952, 214
133. WIBERG M., Jernkont, Ann. v124, 5 1940 p179 - 213
134. WILD R., J.I.S.I. June 1953

135. YANAGIHARA T., KOBAYASHI T., Nippon Kinsoku Jakkai S.I., 33, 3,
136. ZHURAVLEV, LESOKHIN I.G., TEMPEL'MAN R.G. J. Appl. Chem. USSR. 21,9, 1948, 887, 1969, 314
137. KINGERY W.D., Kinetics of High Temperature Processes
138. GOTH G., A.P. project Sheffield Polytechnic 1970
139. STRANGWAY P.K., ROSS H.U., Trans Met. Soc. AIME, 242, Sept. 1968, 1981
140. WETHERILL W.H., FURNAS C.C., Ind. Eng. Chem. 1934, vol. 26
141. WINDING C.C., CHEYNEY A.J., Ind. Eng. Chem. 1948, 40, p 1087-1093
142. FRANCIS W.E., MOPPETT B.E., READ J.P., I.G.E. Journal May 1967 p 335-352
143. CAMPBELL F.R., Ph.D. Thesis, Imperial College 1971
144. GILLILAND , Ind. Eng. Chem, 26, 681, 1934
145. PERRY J., CHILTON C.H., KIRKPATRICK S.D., Chemical Engineers Handbook, ed. PERRY J.H., 4th edn. p14-21
146. FULLER E.N., SCHEFFLER P.D., GIDDINGS J.C., Ind. Eng. Chem. Fundamentals Nov. 1965
147. REID R.C., SHERWOOD T.K., Properties of Gases and liquids ed. REID R.C., 2nd edn. p531
148. International Critical Tables p62
149. International Critical Tables v.3. p208
150. RANZ W.E., MARSHALL W.R., Jr., Chem. Eng. Prog. 48, 141-146, 173-180 (1952)
151. Transport Phenomena, BIRD R.B., STEWART W.E., LIGHTFOOT E.N., p511 pub. WILEY, 1960
152. Technical Data on Fuel, SPIERS H.M. (1962) p159

NOMENCLATURE

Chapter 1

A	-- area	C _g	-- activity
A ₀	-- Frequency factor	c	-- concentration
C	-- concentration	k	-- constant, specific rate constant
C ₁	-- intergration constant	k ₁	-- chemical rate constant
D	-- diffusion coefficient	k _c	-- mass transfer coefficient
D _{eff}	-- effective diffusion coefficient	r	-- radius
E	-- activation energy	r ₀	-- initial radius
ΔE [‡]	-- activation energy	r _i	-- unreacted radius
G	-- gas	t	-- time
ΔH [‡]	-- enthalpy of activation	x	-- fraction reacted
J	-- flux	Δx	-- diffusion path length
K'	-- specific rate constant	S	-- boundary layer, diffusion path length
K ₀	-- surface factors constant	ρ ₀	-- initial density
N	-- molar reaction rate	μ	-- Frictional coefficient
Nu	-- Nusselt number	ψ	-- labyrinth factor
P	-- total pressure	θ	-- time
Q	-- amt. water vapour produced on total reduction	ω	-- gm moles O ₂ per cm ³ of oxide
Q	-- amt. water vapour produced at time t	ε	-- porosity of unreduced layer
R	-- fraction of oxygen removed	ε _r	-- porosity of reduced layer
R	-- general gas constant	K	-- transmission coefficient
R ₀	-- reaction rate		
Re	-- Reynolds number		
S	-- solid		
Se	-- Schmidt number		
ΔS [‡]	-- entropy of activation		
T	-- absolute temperature		

Superscripts

-- activated complex

Subscripts

- b -- Boltzmanns constant
- e - effective, equilibrium
- g - bulk gas
- s - surface
- r - reaction

Chapter 3

A - constant
A' - cross - sectional area
B - constant
D - diffusion coefficient
M - molecular wt
P - total pressure
Pr - Prandtl number
Q_m - flow rate
R - gas constant
Re - Reynolds number
S - surface area
Sh - Sherwood number
Sc - Schmidt number
V₁ - Atomic volume (H₂)
V₂ - molar volume (H₂O)
V - linear velocity
VP - vapour pressure
W - weight loss

a - cross - sectional area
d - particle diameter
f_D - *second order correction*
k - Boltzmann constant
n - constant
n' - specific reaction rate
p - partial pressure
t - time

Subscript

eff- effective
n' - naphthalene
b - bulk gas
s - surface

α - mass transfer coefficient
γ - kinematic viscosity
E - energy of molecular interaction
σ - inter molecular distance
Ω - Lennard-Jones potential

Chapter 4

A - weighting factor

r - radius

θ - time

B - weighting factor

t - time

D - diffusion coefficient

O - oxygen

Fe - iron

APPENDIX I

PROGRAMME LISTING

* IOCS (Card, 1403 Printer, Plotter, Typewriter)

* List Source Programme

```
Dimension W(100), X(100), Y(100), Z(100, 4), V(100), NTITL (75)
10 DO 12 I = 1, 4
    DO 11 J = 1, 100
        Z(J,I,) = 0.0
11 Continue
12 Continue
    AK = 0.0.
    BK = 0.0
    CK = 0.0
    DK = 0.0
    Read (2, 13) N, NTITL
13 Format (15, 75 A 1)
    IF(N) 130, 130, 14
14 Read (2, 20) A, B, C, NX, NA, NB, NC, ND.
20 Format (3E 10.6, 5 I 5)
    IF (NX * (NX - 101) 30, 130, 130
30 Read (2, 40) (X (I), I = 1, NX)
40 Format (7E10.6)
    Read (2, 40) (W (I), I = 1, NX)
    DO 50 I = 1, NX
        Y (I) = A - B * W (I)/C
50 Continue
    IF (NA) 70, 60, 70
60 CALL FIT 1 (X, Y, Z, A, AK, NX)
70 IF (NB) 90, 80, 90
80 CALL FIT 2 (X, Y, Z, A, BK, NX)
90 IF (NC) 110, 100, 110
100 CALL FIT 3 (X, Y, Z, A, CK, NX)
110 IF (ND) 122, 120, 121 .
120 CALL FIT 4 (X, Y, Z, A, DK, NX)
121 Write (5, 122) N, NTITL
122 Format ('1 Problem No' 15, 10X, 75A1)
    CALL FIT 5 (X, Y, Z, NX, BK, CK, A, AA, BB)
    Write (5, 123) NX, AK, BK, CK, DK, AA, BB
```

```
123 Format ('O Curve fitted to '13' Points'// Time Wt.loss)
      10/Fe) '9X' Law 1 Law 2 Law 3 Law 4 Law 5 '/30X'K =
      2' 5F10.5/75X, F10.5/)
      . Do 125 I = 1, NX
      Wirte (5, 124) X(I), W(I), Y(I), (Z (I,J,), J = 1,4), V(I)
124 Format (3F 10.5, 5X, 5F10.5)
125 Continue
      Call DATSW (1,I)
      IF (I - 1) 127, 126, 127
126 Call GIRAF (X, Y, Z, NX, 4, NTITL)
127 Call DATSW (2, I)
      IF (I - 1) 10, 128, 10
128 Call GIRAF (X, Y, V, NX, 1, NTITL)
      Go to 10
130 Call EXIT
      END
```

```
* LIST SOURCE PROGRAM
Subroutine FIT 1 (X, Y, 2 A, AK, NX)
Dimension X(100), Y(100), Z(100, 4)
SA = 0.0
SB = 0.0
SC = 0.0
DO 10 I = 1, NX
SA = SA + X(I)
SB = SB + X(I) * X(I)
SC = SC + X(I) * Alog (Y(I))
10 Continue
AK = (ALOG (A) * SA - SC)/SB
DO 20 I = 1, NX
z(I, 1) = A/EXP (AK * X(I))
20 Continue
Return
End
```

* LIST SOURCE PROGRAM

```
Subroutine FIT2 (X, Y, Z, A, AK, NX)
Dimension X(100), Y(100), Z(100, 4)
Dimension S(6), T(6), Q(5), R(5), W(5, 100)
DO 20 I = 1, 6
S(I) = 0
T(I) = 0
DO 10 J = 1, NX
AX = X(J) * * I
S(I) = S(I) + AX
T(I) = T(I) + Y(J) * AX
10 Continue
20 Continue
S(1) = A * S(1) - T(1)
S(2) = 2.0 * T(2) = 5.0 * A * S(2)
S(3) = 10.0 * A * S(3) - T(3)
S(4) = -10.0 * A * S(4)
S(5) = 5.0 * A * S(5)
S(6) = -A * S(6)
CALL POLRT (S, T, 5, Q, R, I)
J = 0
DO 50 I = 1, 5
IF (R (I)) 50, 40, 50
40 J = J + 1
Q (J) = Q (I)
50 Continue
IF (J - 5) 70, 70, 60
60 J = 5
70 DO 90 I = 1, J
S(I) = 0.0
DO 80 K = 1, NX
W (IK) = A * (1.0 - X(K) * Q(I) * * 3
S (I) = S (I) + (W (I, K) - Y (K)) * * 2
80 Continue
90 Continue
```

```
NS = 1
AK = Q (1)
IF (J - 1) 130, 130, 100
100 SMIN = S(1)
DO 120 I = 2, J
IF (S (I) - SMIN) 110, 120, 120
110 SMIN = S(I)
NS = I
AK = Q (I)
120 Continue
130 DO 140 K = 1, NX
Z(K, 2) = W (NS, K)
140 Continue
Return
End
```

* LIST SOURCE PROGRAM

```
Subroutine FI T 3 (X, Y, Z, A, AK, NX)
Dimension X(100), Y(100), Z(100, 4)
SA = 0.0
SB = 0.0
SC = 0.0
DO 10 I = 1, NX
XA = SQRT (X (I))
SA = SA + XA
SB = SB + Y (I) * XA
SC = SC + X (I)
10 Continue
AK = (A * SA - SB) / (A * SC)
DO 20 I = 1, NX
Z (I,3) = A * (1.0 - AK * SQRT (X (I)))
20 Continue
Return
End
```

* LIST SOURCE PROGRAM

Subroutine FLT5 (X, Y, XK, NX, BK, CK, A, AA, BB)

Dimension X (100), Y(100), XI(100), XJ(100), XK(100)

S1 = 0.0

S2 = 0.0

S3 = 0.0

S4 = 0.0

S5 = 0.0

DO 10 I = 1, NX

XI (I) = (1.0 - BK * X (I)) * * 3

XJ (I) = (1.0 - CK * SQRT (X (I)))

S1 = S1 + XI(I) * XJ (I)

S2 = S2 + XI (I) * XI (I)

S3 = S3 + XJ (I) * XJ (I)

S4 = S4 + XI (I) * Y (I)

S5 = S5 + XJ (I) * Y (I)

10 Continue

D = A * (S2 * S3 - S1 * S1)

AA = (S4 * S3 - S1 * S5) / D

BB = (S5 * S2 - S1 * S4) / D

DO 20 I = 1, NX

XK (I) = A * (AA * XI (I) + BB * XJ (I))

20 Continue

Return

End

* LIST SOURCE PROGRAM

Subroutine FIT5 (X, Y, XK, NX, K1, K2, A, AA, BB,)

Dimension X (100), Y(100), XK(100)

T 1 = 0.0

T 2 = 0.0

T 3 = 0.0

T 4 = 0.0

T 5 = 0.0

T 6 = 0.0

C**** Evaluate the six co-efficients

DO 10 I = 1, NX

T1 = T2 + Y (I) * (1 - K1 * X (I))

T2 = T2 + (1 - K1 * X (I)) * * 2

T3 = T3 + (1 - K1 * X (I)) * (1 - K2 * X(I)) * * 3

T4 = T4 + Y(I) * (1 - K2 * X(I)) * * 3

T5 = T3

T6 = T6 + (1 - K2 * X(I)) * * 6

10 Continue

C**** Solve for D and E

E = ((T4/T5) - T1/T2)/((T6/T5) - (T3/T2))

D = (T1 - E * T3) / T2

BB = E/A

AA = D/A

DO 20 I = 1, NX

XK(I) = D * (1 - K1 * X(I)) + E * (1 - K2 * X(I)) * * 3

20 Continue

Return

End

* LIST SOURCE PROGRAM

```
Subroutine GIRAF (A, B, C, NO, NP NTITL)
Dimension A(100), B(100), C(100, 4) NTITL (75)
IA = A(1)
IA = (IA)/10) * 10
AI = IA
BI = AI + 10
JA = A(NO)
JA = (JA/10 + 1) * 10
NS = (JA - IA)/10
CALL SCALF (0.2, 4.0, AI, 0.0)
CALL FGRID (1, AI, 0.0, 0.5, 4)
CALL FGRID (0, AI, 0.0, 10.0, NS)
CALL FCHAR (BI, 2.0, 0.15, 0.2, 0.0)
WRITE (7, 2) NTITL
2 Format (75A1)
X = AI - 4.0
Y = 0.0
DO 4I = 1, 5
CALL FCHAR (X, Y, 0.1, 0.1, 0.0)
WRITE (7, 3) Y
3 Format (F 3.1)
Y = Y + 0.5
4. Continue
X = AI 2.0
Y = -.075
DO 6I = 1, NS
CALL FCHAR (X, Y, 0.1, 0.1, 0.0)
IX = X + 2.5
WRITE (7, 5) IX
5. Format (I 3)
X = X + 10
6. Continue
DO 10 I = 1, NO
X = A (I)
Y = B (I)
CALL FPLOT (2, X, Y)
CALL FPLOT (2, X, Y)
CALL POINT (1)
```

```
10  Continue
    DO 30 I = 1, NP
      X = A(1)
      Y = C(1, I)
      CALL FPLOTT (1, X, Y)
      CALL FPLOTT (2, X, Y)
    DO 20 J = 1, NO
      X = A(J)
      Y = C(J, I)
      CALL FPLOTT (0, X, Y)
20  Continue
30  Continue
    X = X + 40.0
    Y = 0.0
    CALL FPLOTT (1, X, Y)
    Return
    End
```

TABLE 2

Temperature °C	Mass Transfer Coefficient $\alpha_{\text{H}_2\text{H}_2\text{O}}$ cm. sec ⁻¹	
	Spring Balance	Standard Balance
400	22.6	6.0
560	28.7	7.7
550	32.1	8.6
600	35.6	9.5
650	39.1	10.4
700	43.0	11.5
750	46.9	12.5
800	50.9	13.6
840	54.1	14.4
850	55.2	14.7
870	56.7	15.2
900	59.6	15.9
950	64.2	17.1
1000	68.7	18.4
1050	73.5	19.6
1100	78.2	20.9

TABLE 3

KIRUNA MAGNETITE

°C	Balance	$(P_{H_2})_b - (P_{H_2})_s$	$(P_{H_2})_s$
400	Stanton	.045	.955
500	Spring	.08	.92
500	Stanton	.39	.61
500	"	.33	.67
550	Spring	.10	.90
560	Stanton	.26	.74
600	Spring	.095	.905
650	Stanton	.17	.83
650	Spring	.09	.91
600	"	.21	.79
650	"	.13	.86
700	"	.23	.77
750	"	.15	.85
750	"	.20	.80
750	"	.19	.81
750	"	.18	.82
800	Stanton	.39	.61
800	Spring	.19	.81
850	"	.17	.83
900	"	.20	.80
950	"	.22	.78
1000	"	.40	.60
750	"	.14	.86
750	"	.11	.89
900	"	.13	.82

TABLE 4

A.F. Sinter Pellets

$^{\circ}\text{C}$	Balance	$(P_{\text{H}_2})_{\text{b}} - (P_{\text{H}_2})_{\text{s}}$	$(P_{\text{H}_2})_{\text{s}}$
700	Stanton	.025	.975
800	"	.05	.95
800	"	.03	.97
800	"	.03	.97
840	"	.04	.96
870	"	.055	.945
870	"	.06	.94
870	"	.055	.945
900	"	.075	.925
1000	"	.14	.86
1100	"	.215	.785

TABLE 5

Thermally Treated

A.F. Sinter Pellets

800	"	.04	.96
"	"	.05	.95
"	"	.10	.90
"	"	.12	.88
"	"	.08	.92
"	"	.05	.95
"	"	.11	.89
"	"	.05	.95
"	"	.05	.95
"	"	.03	.97
"	"	.04	.96
"	"	.04	.96

TABLE 6

Oxidised Sinter Pellets

Reduced 800°C

in
Stanton balance

$(P_{H_2 b}) - (P_{H_2 s})$	$(P_{H_2 s})$	Oxidation Temperature °C
.46	.54	500
.31	.69	750
.21	.79	750
.31	.69	750
.11	.89	1000
.48	.52	1000
.33	.67	1000
.35	.65	1000

TABLE 7

$$R_x = 1 - e^{-kt}$$

$$k = D\pi^2/r_0^2$$

$$\pi^2 = 9.868$$

For $t = 600$ sec $R_t = 1.271$

$$r_0^2 = 0.16 \text{ cm}^2$$

$t = 4,800$ sec $R_t = 1.155$

$t = 10800$ sec $R_t = 1.038$

$$R = \frac{R_t}{R_i}$$

$$R_i = 1.334$$

Table 7 continued on next page.

Table 7 (Continued)

= 600 secs. Rk = 0.954	6 = 4800 secs. Rk = 0.866	6 = 10800 secs. Rk = 0.778
<p>om (25) $0.954 = 1 - e^{-\frac{D \times 600 \times 9.868}{0.16}}$</p> <p>In $0.954 = -D \times 600 \times 9.868 / 0.16$</p> <p>$D = 0.0000832$ cm sec⁻¹</p> <p>om (59) $4.770 = 5 - 4x - x^4$</p> <p>$x^4 + 4x - 0.23 = 0$</p> <p>t $f(x) = x^4 + 4x - 0.23$</p> <p>en $f^1 = 4x^3 + 4$</p> <p>ess $D = 0.0000832$</p> <p>d $x = e^{-kt}$</p> <p>$x = 0.0450$</p> <p>bsituting</p> <p>$f(x) = 0.05$</p> <p>d $f^1(x) = 4.0001375$</p> <p>w $x^1 = x - f(x)/f^1(x)$</p> <p>$x^1 = 0.00575$</p> <p>ing x^1</p> <p>$f(x^1) = + 0.00001093$</p> <p>d $f^1(x^1) = 4.0007607$</p> <p>w $x^1 = x^1 - f(x^1)/f^1(x^1)$</p> <p>$x^1 = 0.0575 - 0.0000027$</p> <p>using x^1 in $x = e^{-kt}$</p> <p>$D = 0.00007714$</p>	<p>$0.866 = 1 - e^{-\frac{D \times 4800 \times 9.868}{0.16}}$</p> <p>$\therefore \ln 0.866 = -D \times 4800 \times 9.868 / 0.16$</p> <p>$\therefore D = 0.00000679$ cm sec⁻¹</p> <p>$4.330 = 5 - 4x - x^4$</p> <p>$\therefore x^4 + 4x - 0.67 = 0$</p> <p>$f(x) = x^4 + 4x - 0.67$</p> <p>$f^1(x) = 4x^3 + 4$</p> <p>$D = 0.00000679$</p> <p>$x = e^{-kt}$</p> <p>$\therefore x = 0.1353$</p> <p>$\therefore f(x) = -0.13$</p> <p>$f^1(x) = 4.000984$</p> <p>$x^1 = 0.1676$</p> <p>$f(x^1) = + 0.0012693$</p> <p>$f^1(x^1) = 4.01884$</p> <p>$x^1 = 0.1676 - 0.0003207$</p> <p>$\therefore D = 0.000006033$</p>	<p>$0.778 = 1 - e^{-\frac{D \times 10800 \times 9.868}{0.16}}$</p> <p>$\therefore \ln 0.778 = -D \times 10800 \times 9.868 / 0.16$</p> <p>$\therefore D = 0.00000226$ cm sec⁻¹</p> <p>$3.890 = 5 - 4x - x^4$</p> <p>$\therefore x^4 + 4x - 1.11 = 0$</p> <p>$f(x) = x^4 + 4x - 1.11$</p> <p>$f^1(x) = 4x^3 + 4$</p> <p>$D = 0.00000226$</p> <p>$x = e^{-kt}$</p> <p>$\therefore x = 0.2231$</p> <p>$\therefore f(x) = 0.21$</p> <p>$f^1(x) = 4.04435$</p> <p>$x^1 = 0.2764$</p> <p>$f(x^1) = 0.000824$</p> <p>$f^1(x^1) = 4.08433$</p> <p>$x^1 = 0.2764 - 0.0002018$</p> <p>$\therefore D = 0.000001931$</p>

FOR THE IRON OXYGEN SYSTEM

AFTER DARKEN AND GURRY⁽²⁴⁾

(DARKEN L.S, GURRY RW, J. Am. Chem. Soc. 68 798 (1946))

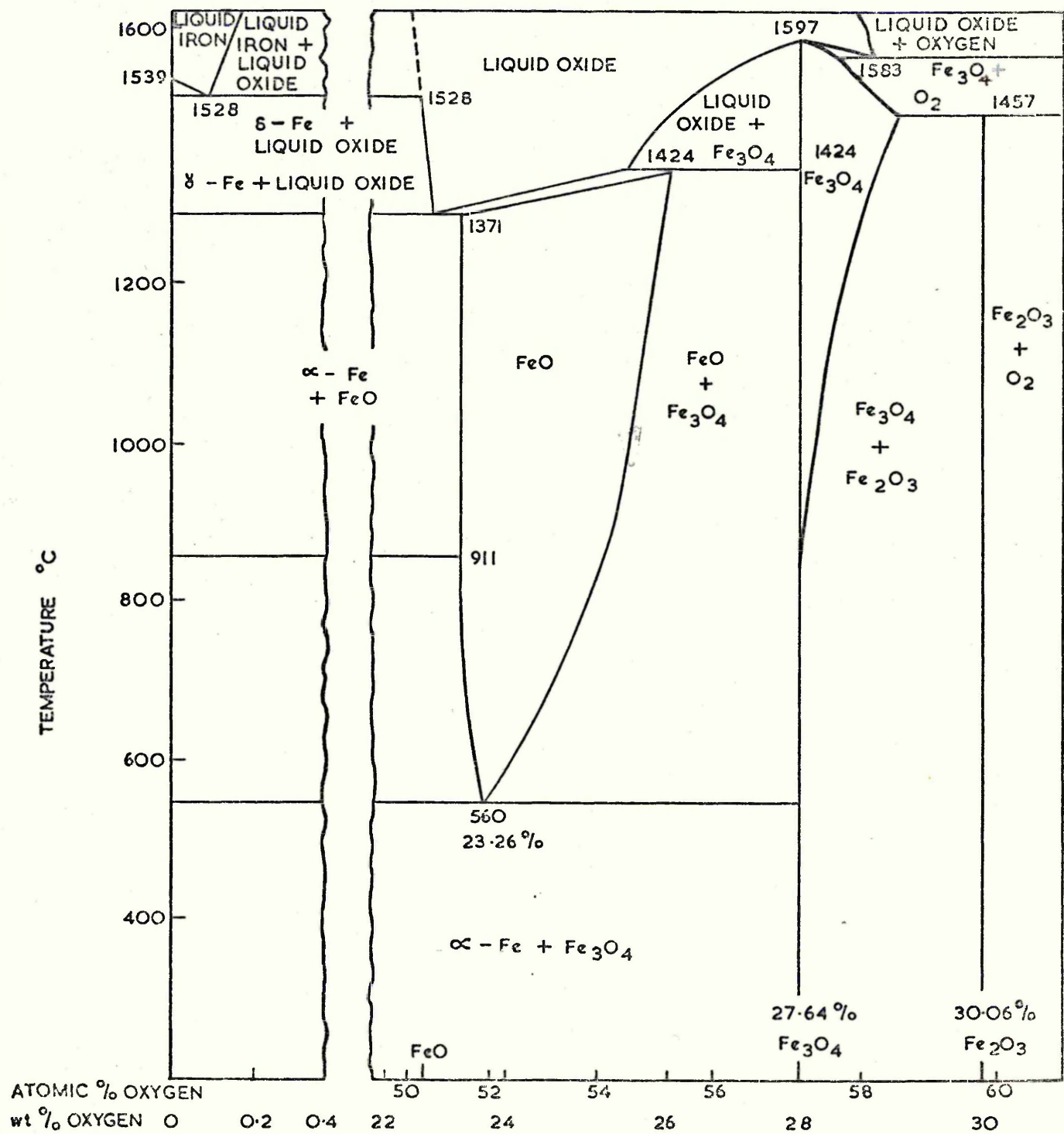


FIG. 1

SCHEMATIC DIAGRAM OF REDUCTION
MODIFIED BY EDSTRÖM FROM HAUFFE.
MODIFIED HERE FOR HYDROGEN REDUCTION.

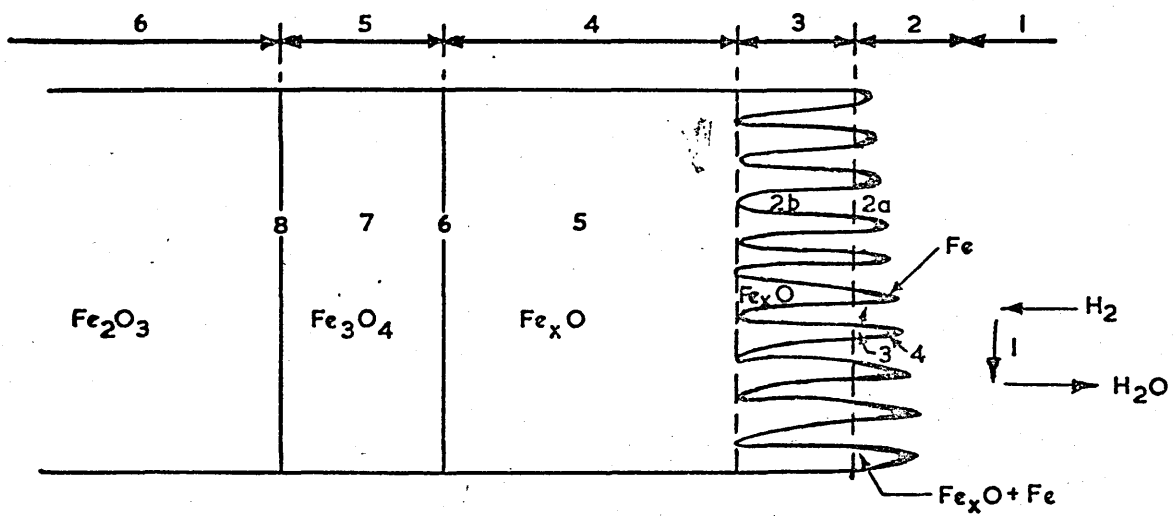


FIG. 2

SCHEMATIC DIAGRAM FOR REDUCTION
BY SMITH AFTER HUEBLER
MODIFIED HERE FOR HYDROGEN REDUCTION

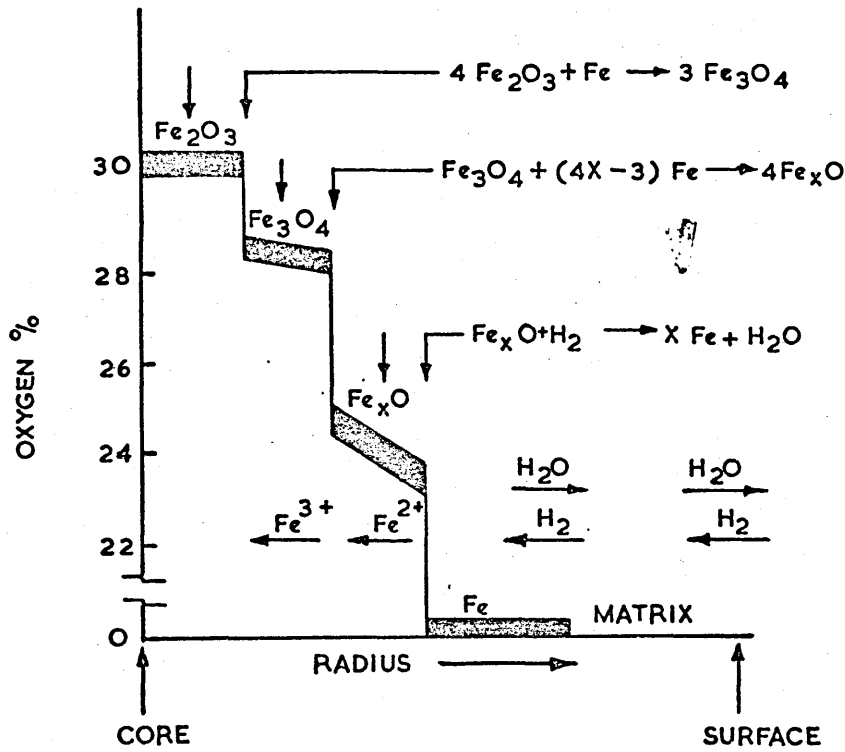


FIG.

GASEOUS REDUCTION OF AN OXIDE SPHERE

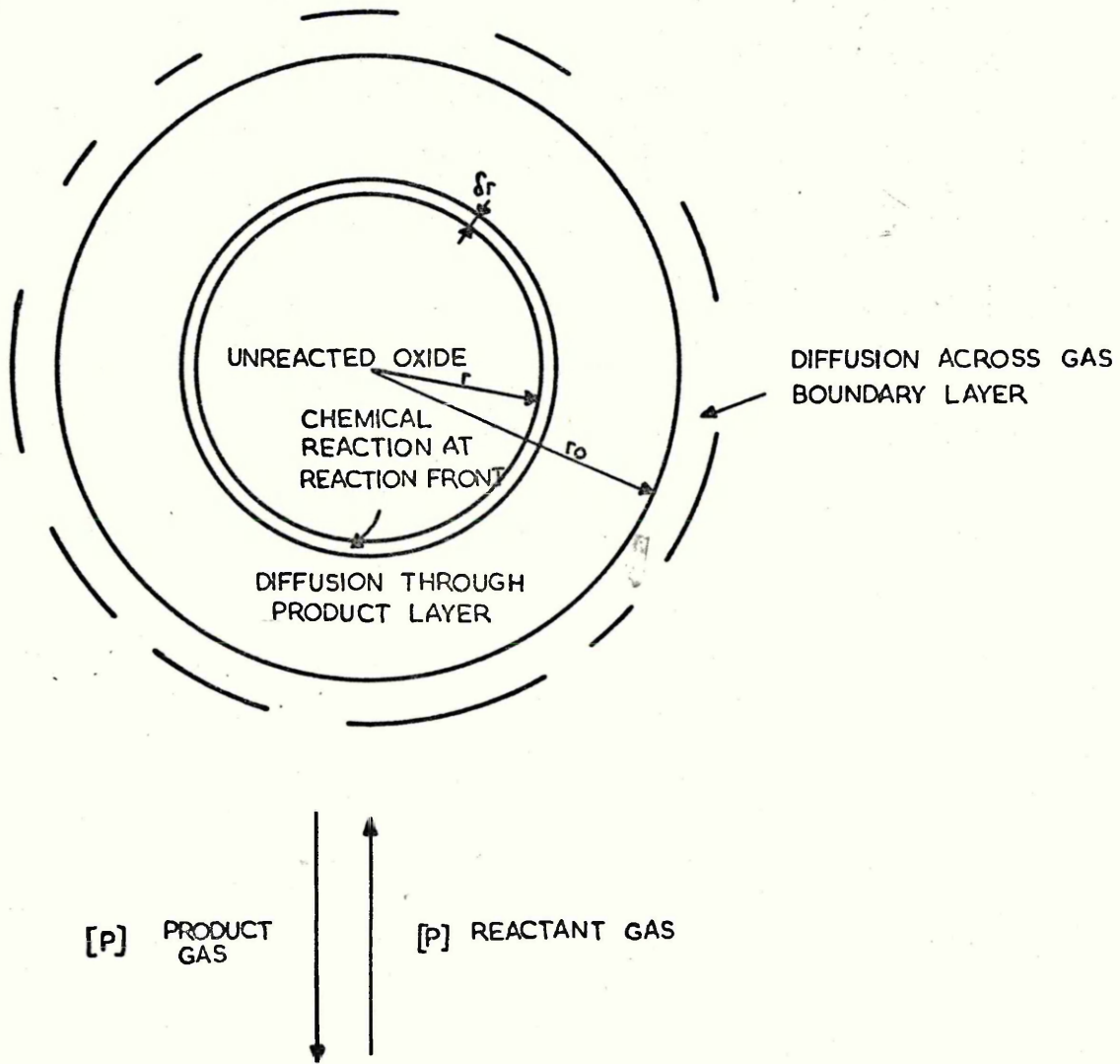


FIG. 4

ACTIVATION ENERGY DIAGRAM

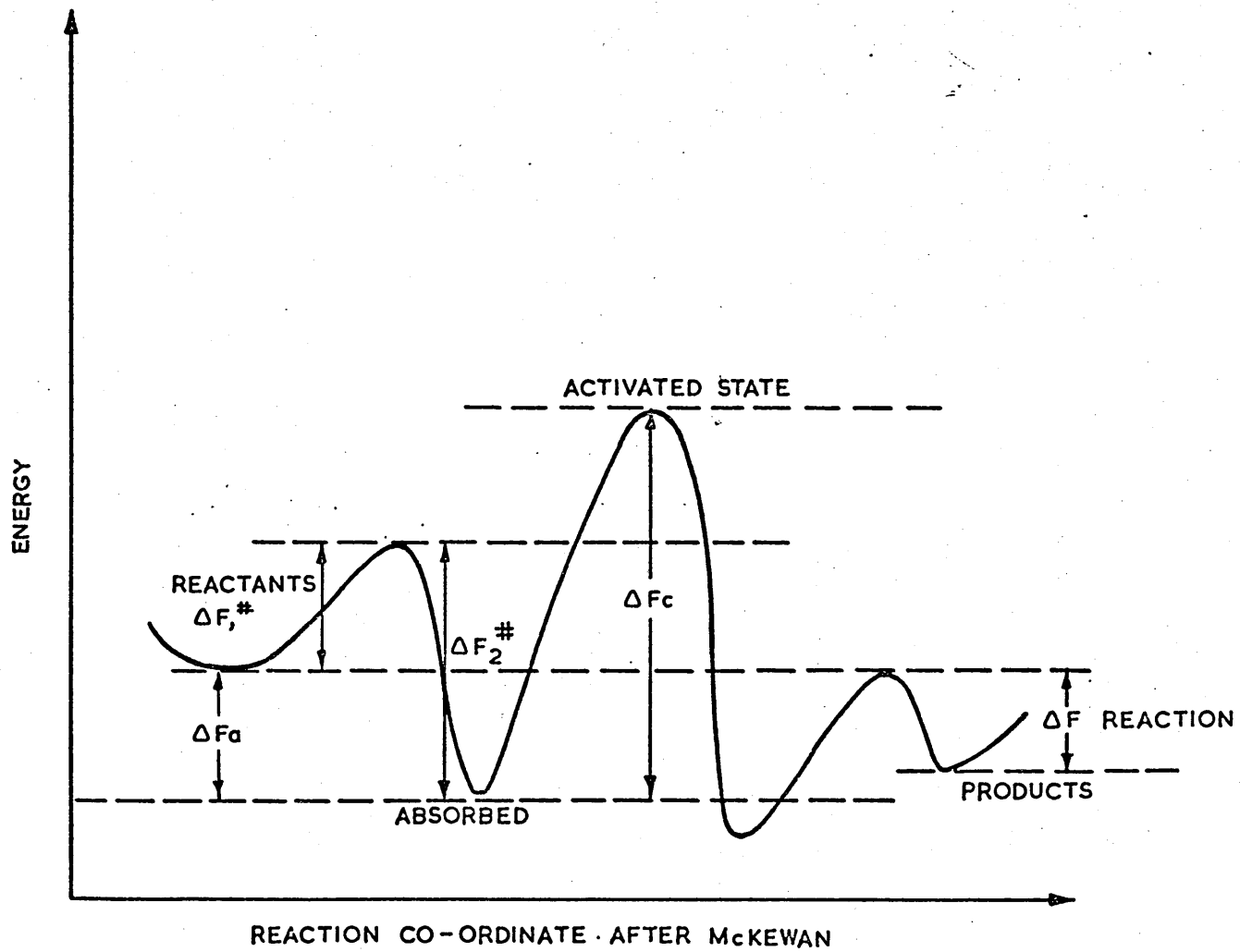


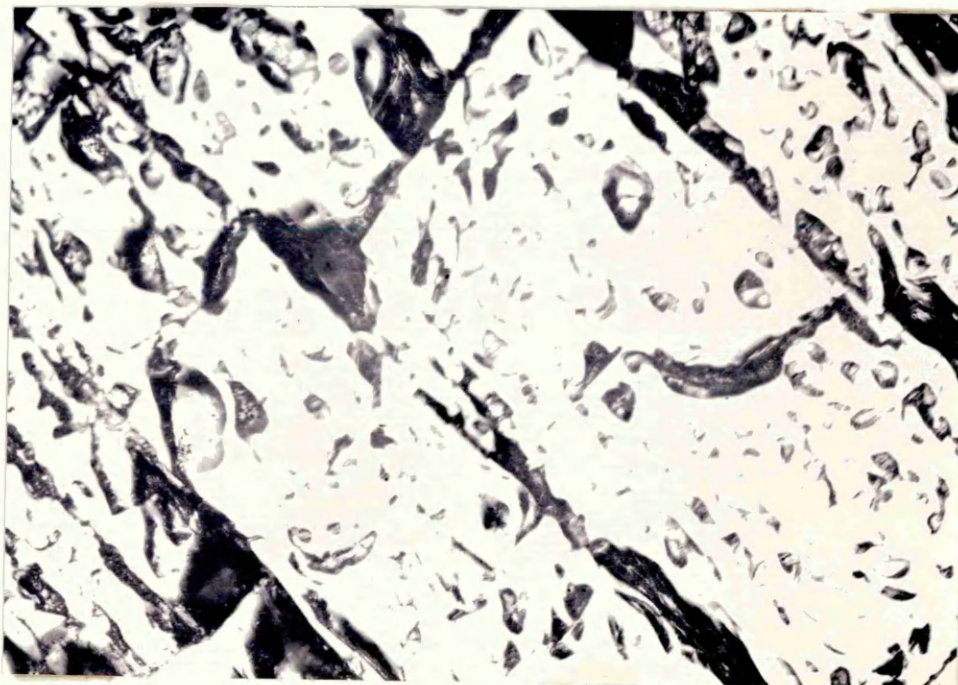
FIG. 5

Fig. 6

Equi-axed Series 1
Kiruna Magnetite
500x

Fig. 7

'Block type' Series 2
Kiruna Magnetite



Faint, illegible text, likely a caption or label for the micrograph above.

Fig. 8

Unsintered, unreduced

A.F. sinter

160x

Fig. 9

Unsintered, unreduced

A.F. sinter

400x

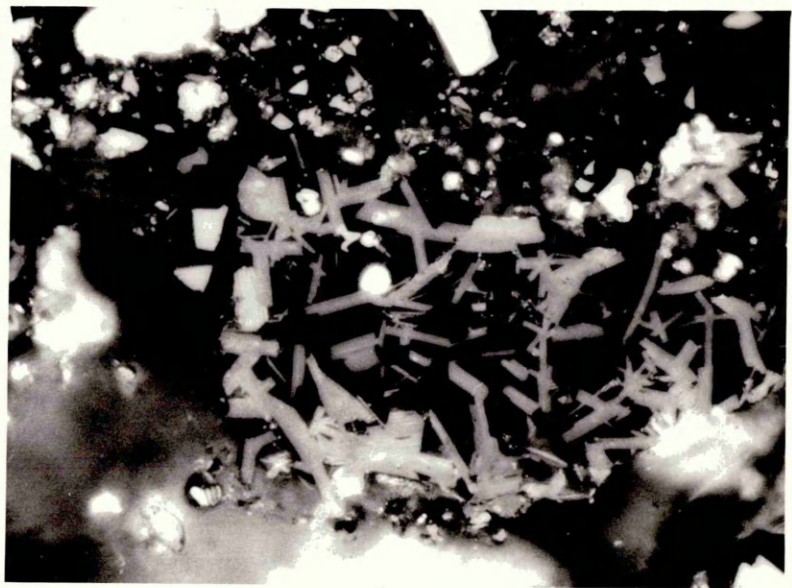


Fig. 10

Sintered, unreduced
A.F. sinter pellet

16x

Fig. 11

Sintered, unreduced
A. F. sinter pellet

400x

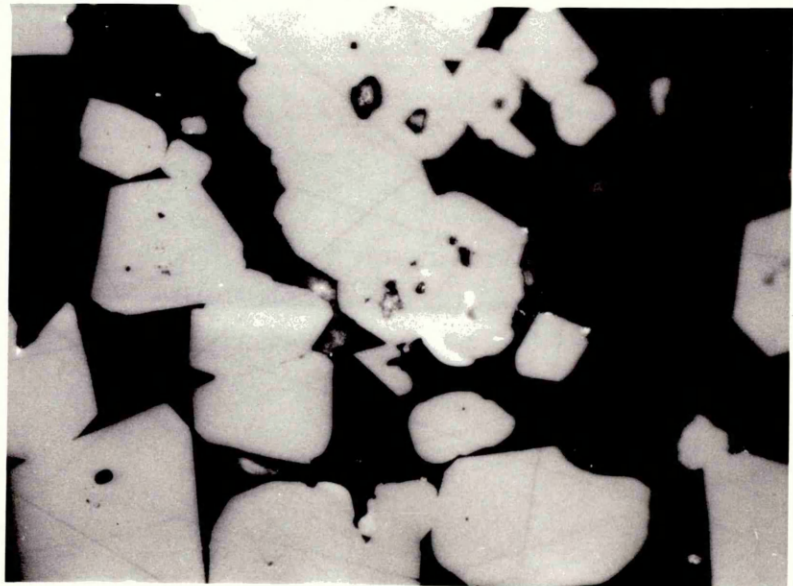
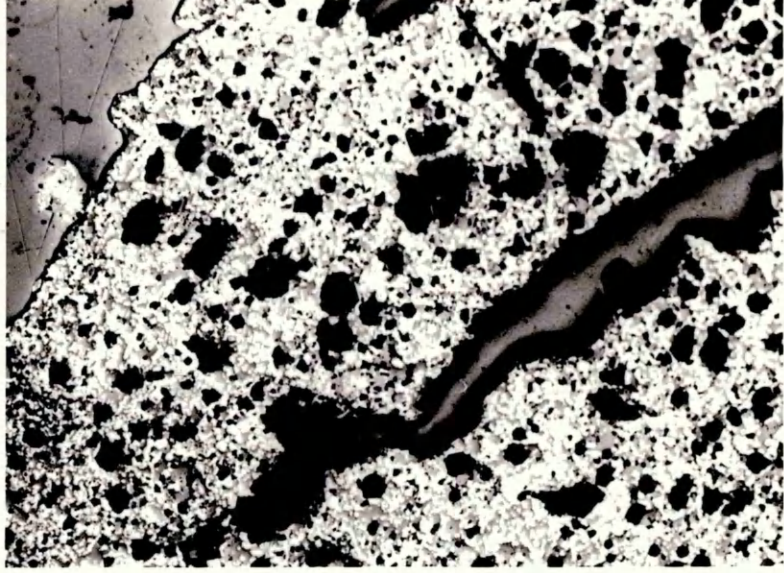


Fig. 12

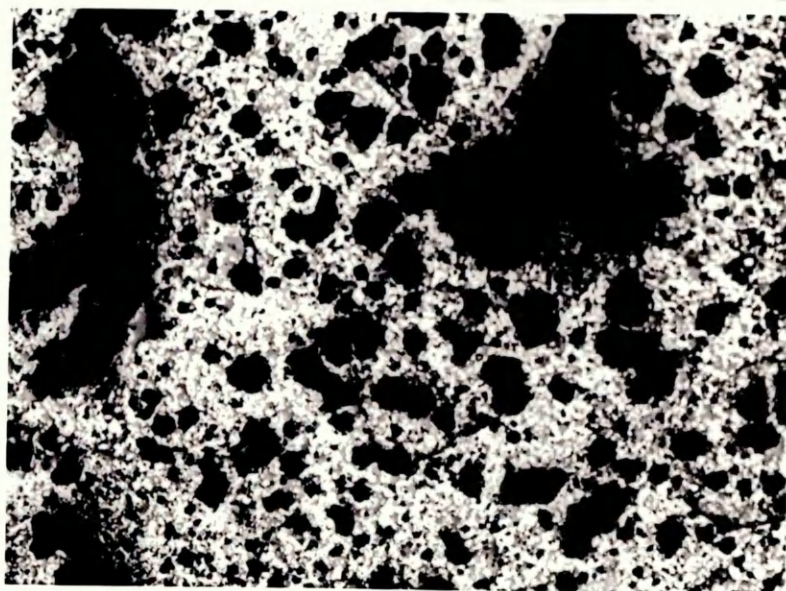
Sintered, unreduced
A.F. Sinter pellet

32 x

Fig. 13

Sintered, unreduced
A.F. sinter pellet

63 x



SPRING BALANCE

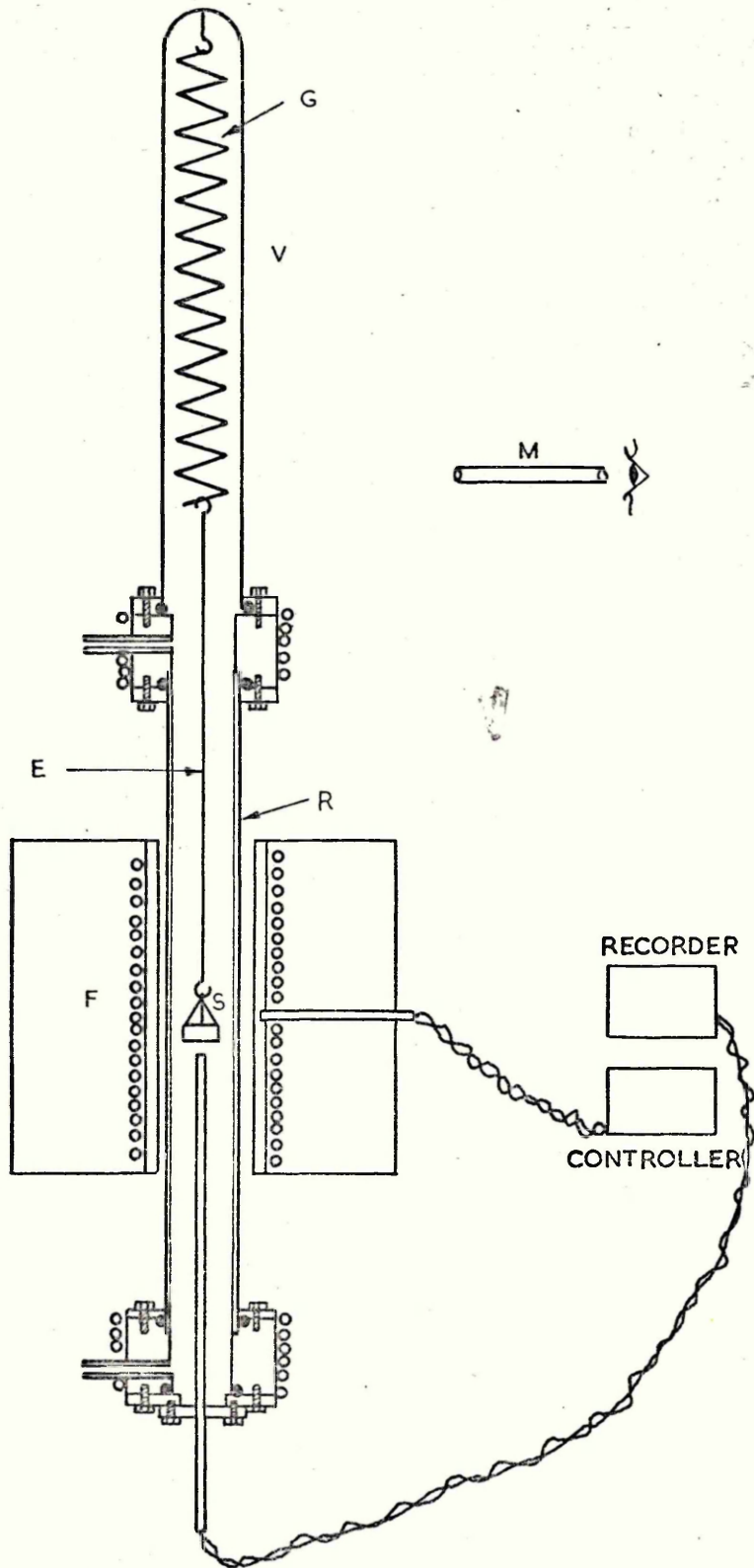
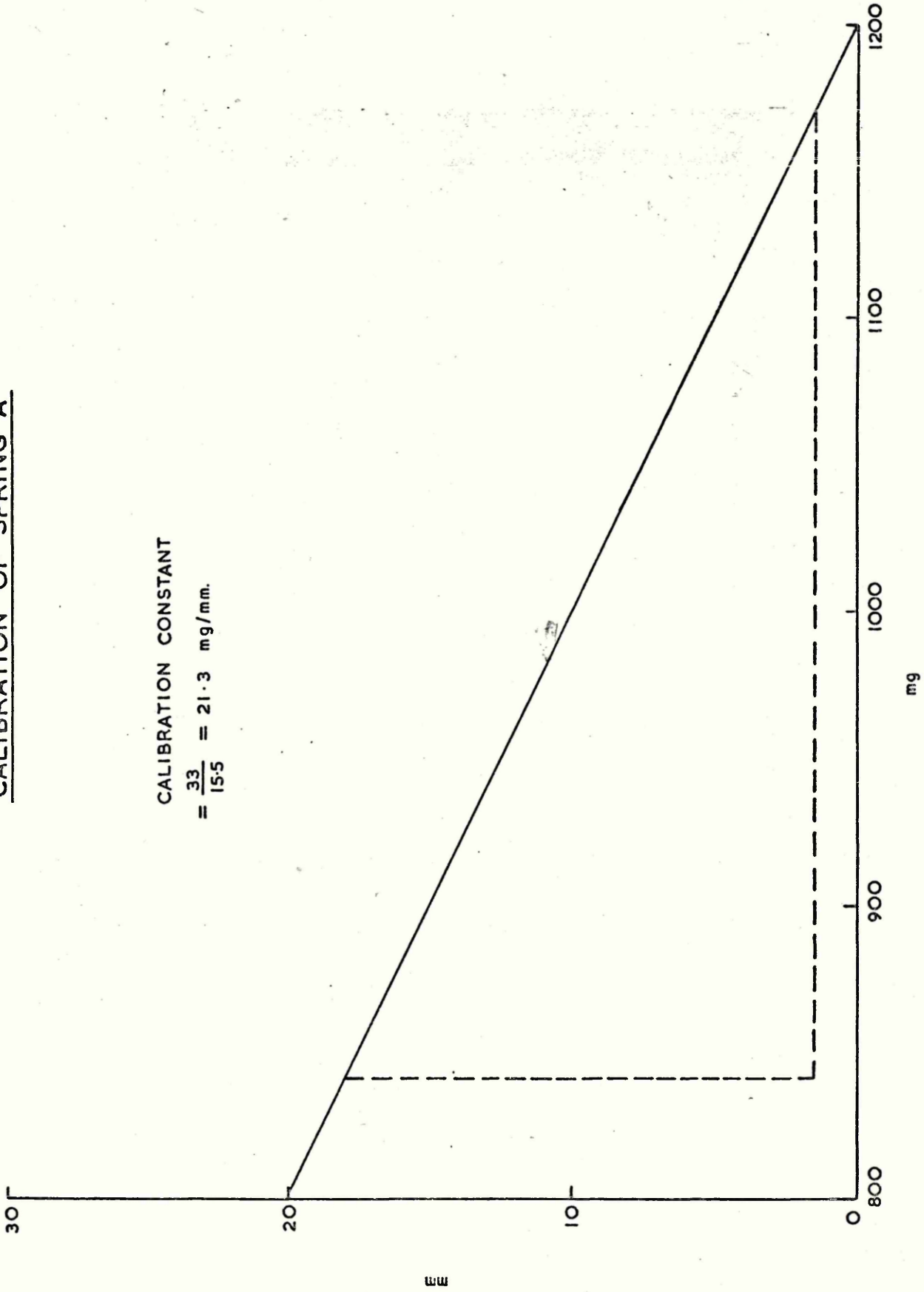


FIG. 14

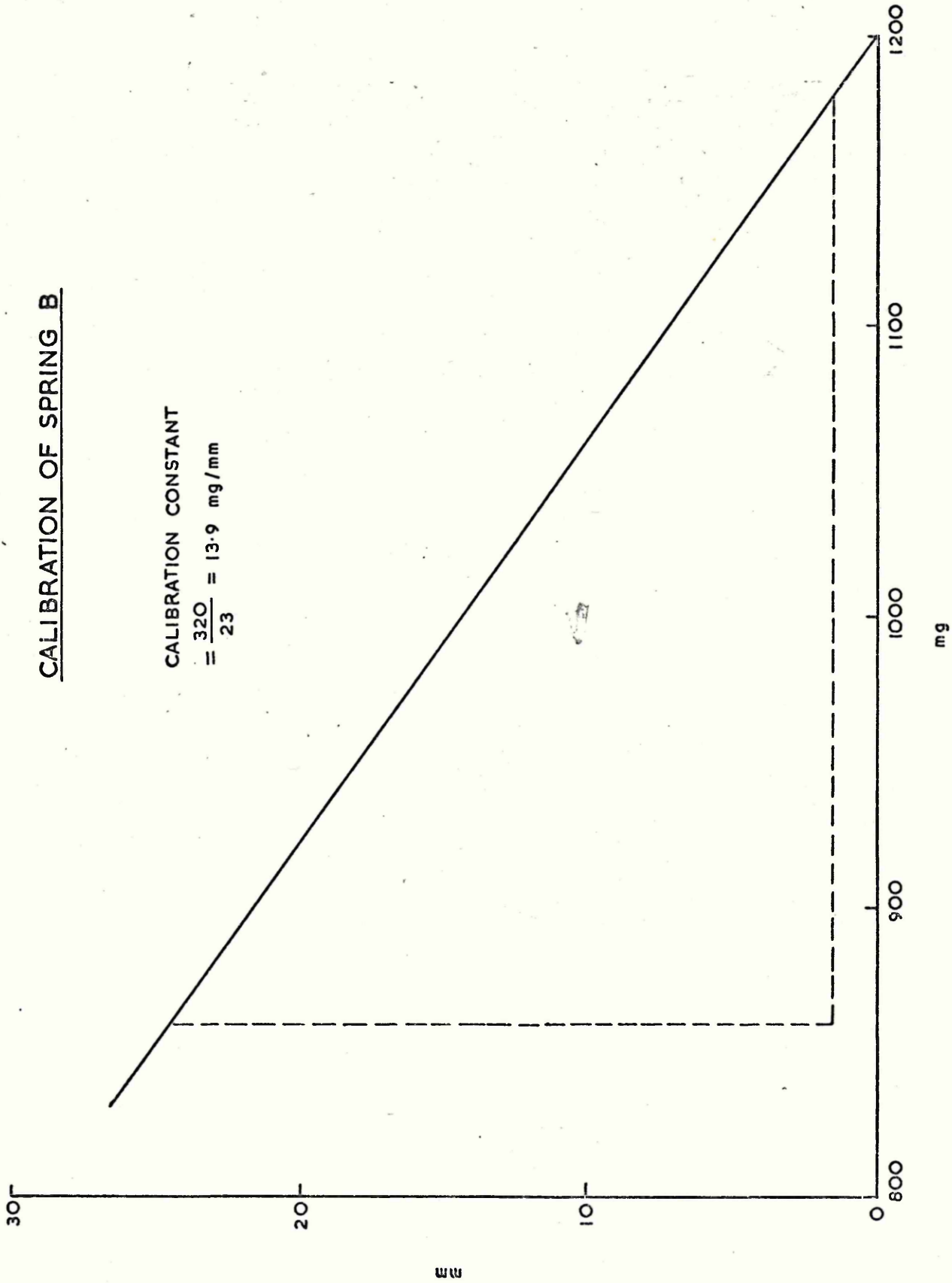
CALIBRATION OF SPRING A

CALIBRATION CONSTANT
 $= \frac{33}{15.5} = 21.3 \text{ mg/mm.}$

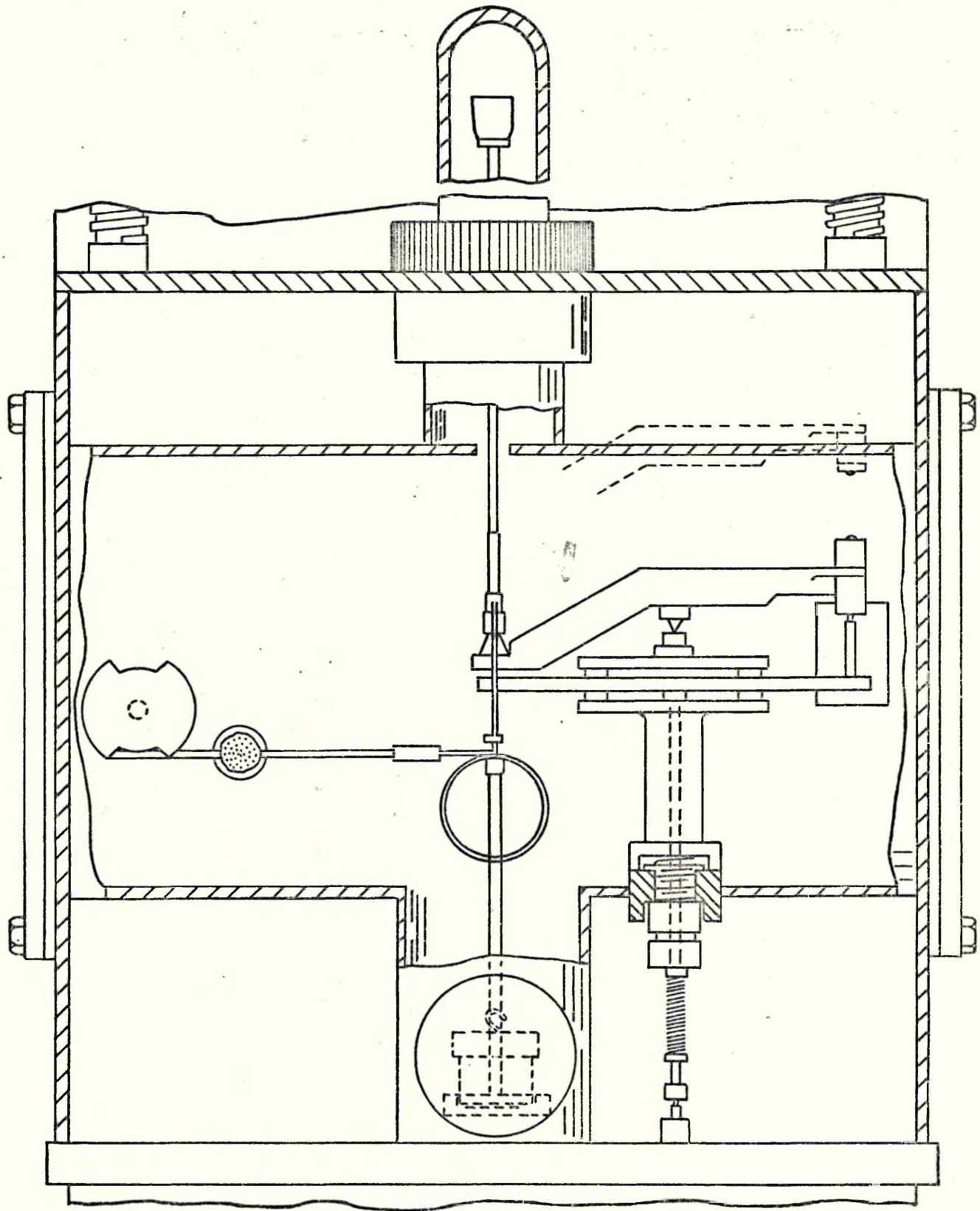


CALIBRATION OF SPRING B

CALIBRATION CONSTANT
 $= \frac{320}{23} = 13.9 \text{ mg/mm}$



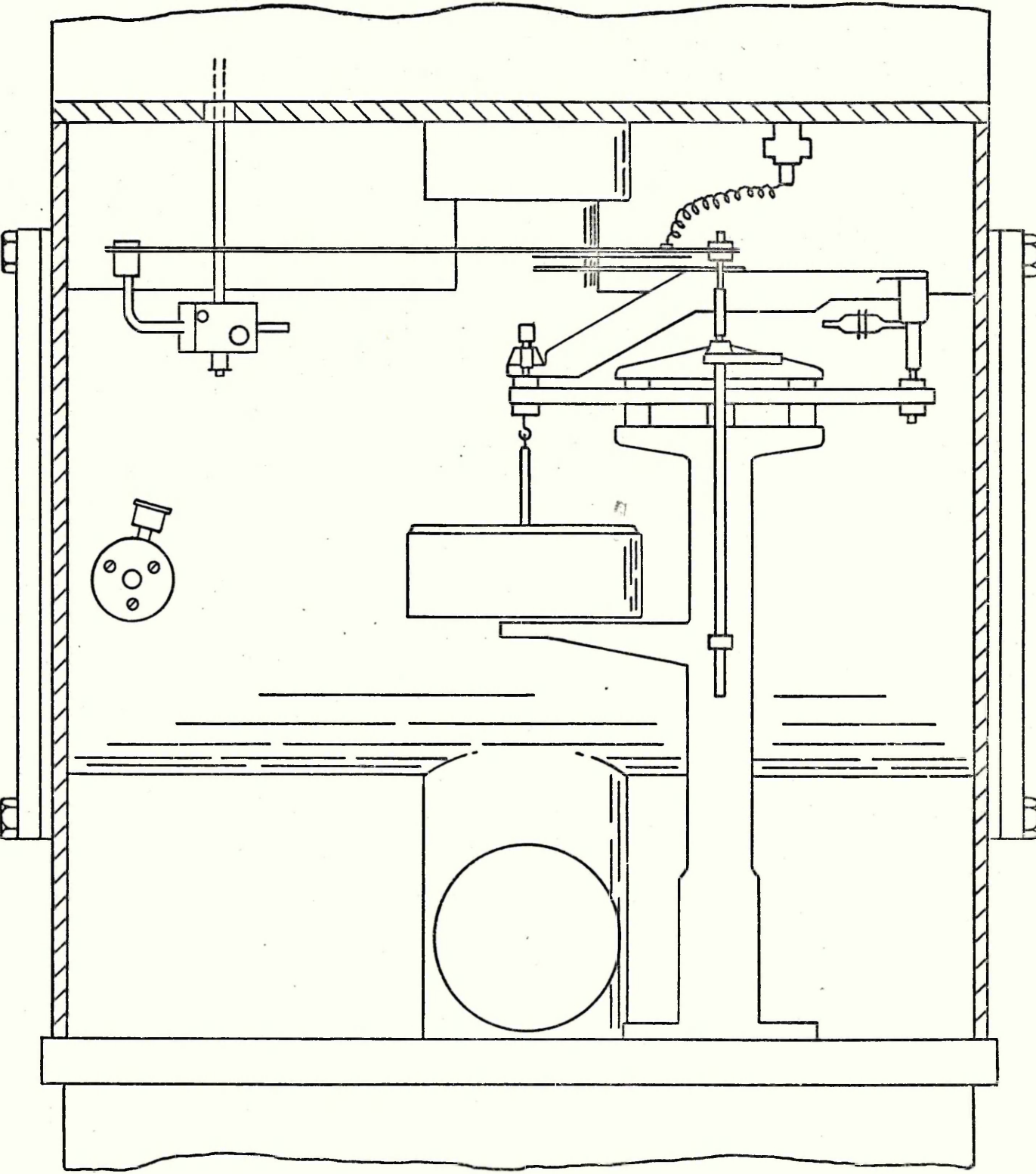
ARRANGEMENT OF INNER BEAM
AND COUNTERPOISE ASSEMBLY IN MAIN CHAMBER
STANTON "MASSFLOW" THERMOBALANCE



SCALE : in. 0 1 2
 cm. 0 1 5

FIG. 17

STANTON "MASSFLOW" THERMOBALANCE



SCALE: in. 0 1 2
 cm. 0 5

FIG. 18

STANTON "MASSFLOW" THERMOBALANCE

Pt: 13% Rh - Pt (0.02" \equiv 0.5 mm dia.)
THERMOCOUPLE

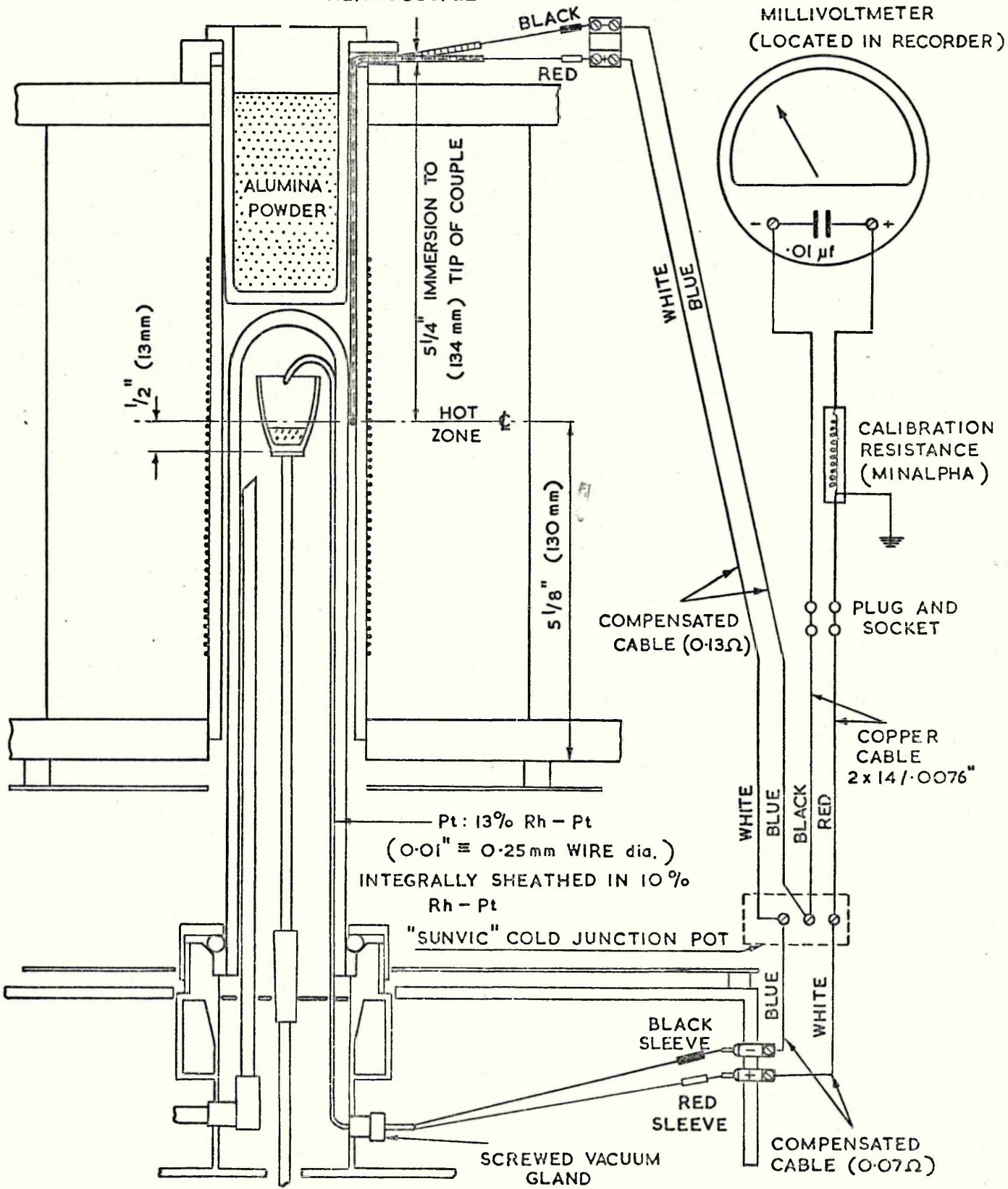


FIG. 19

DRYING TRAIN

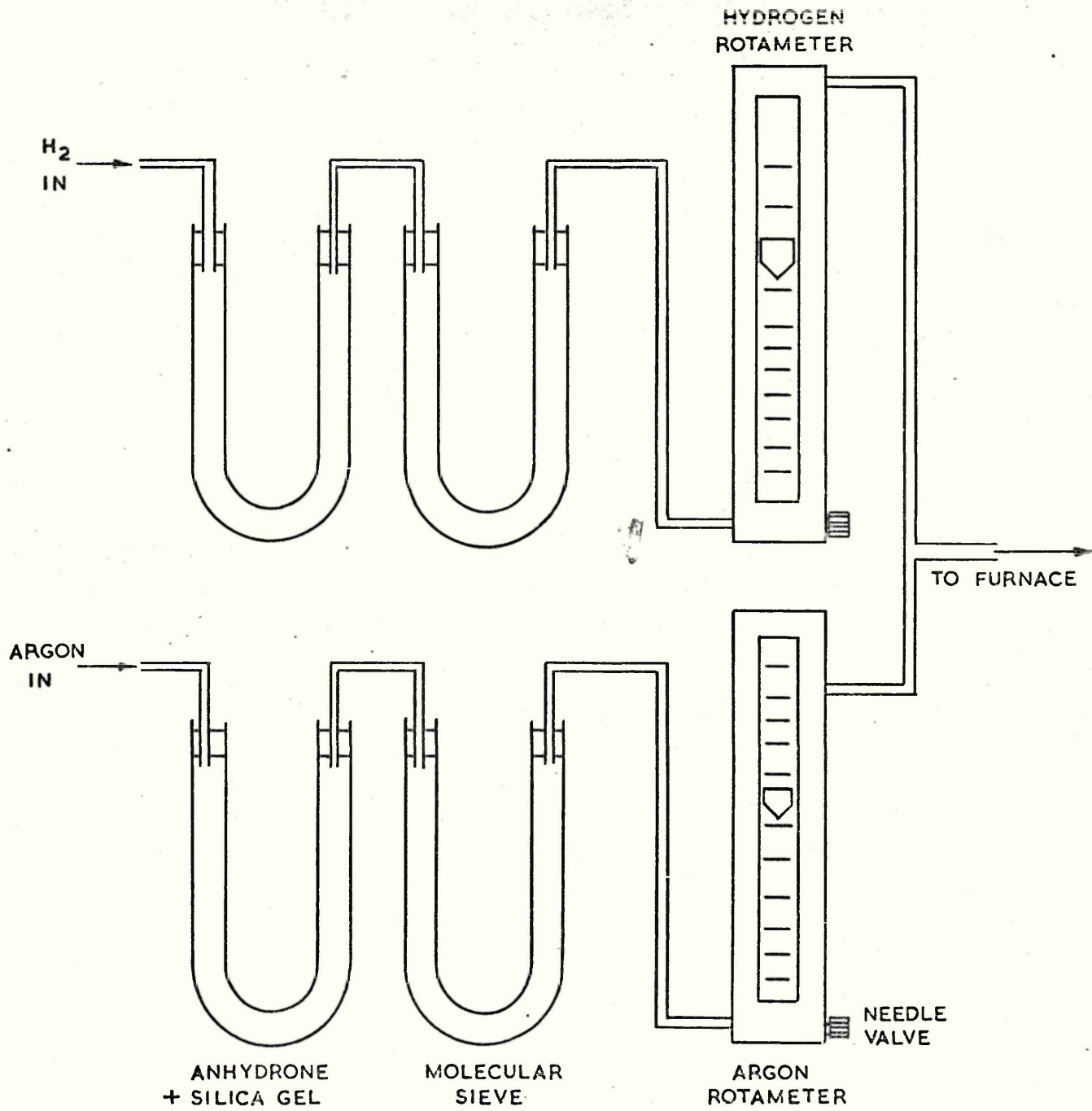
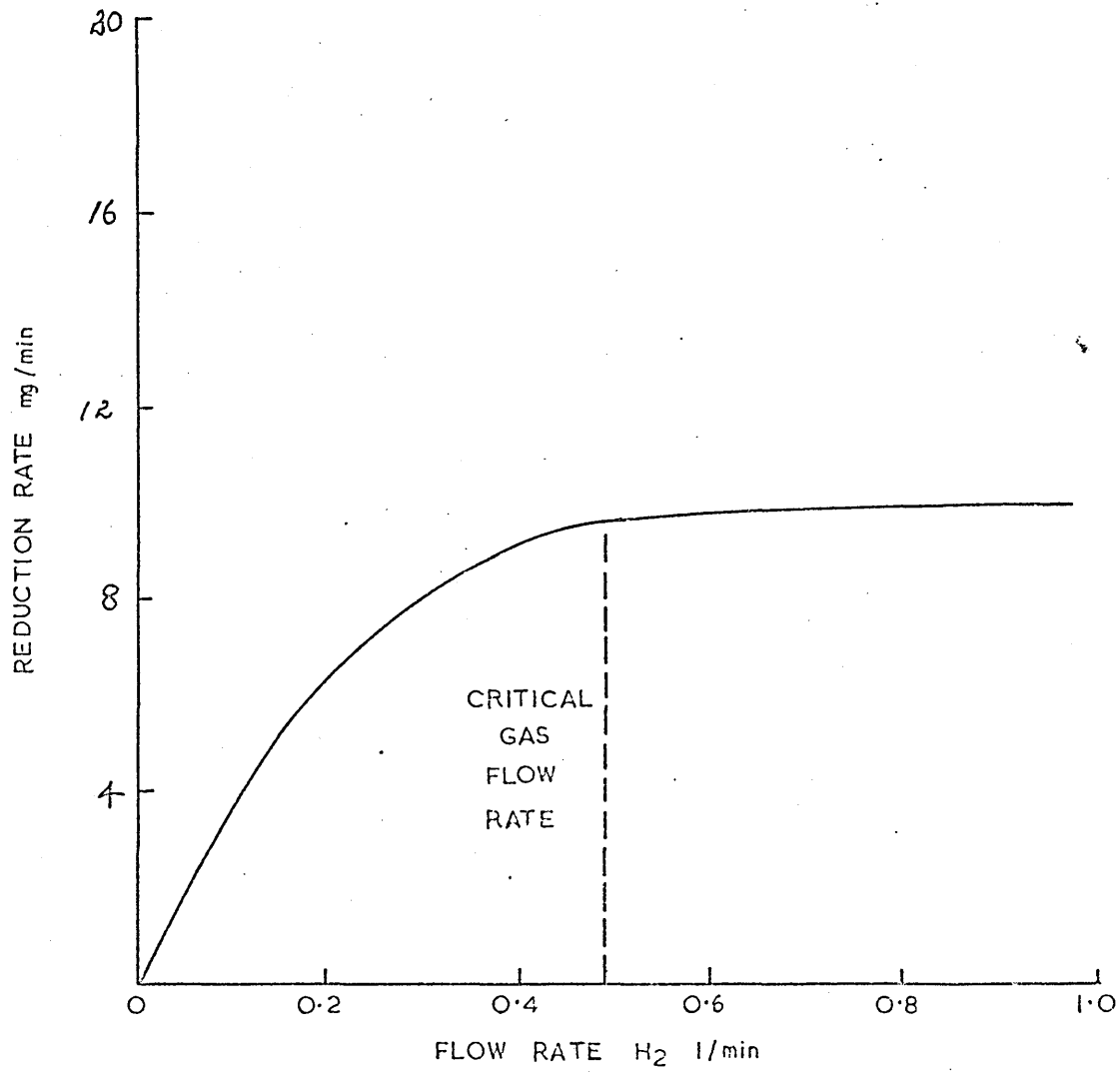


FIG. 20

CRITICAL GAS FLOW RATE



MERCURY BALANCE

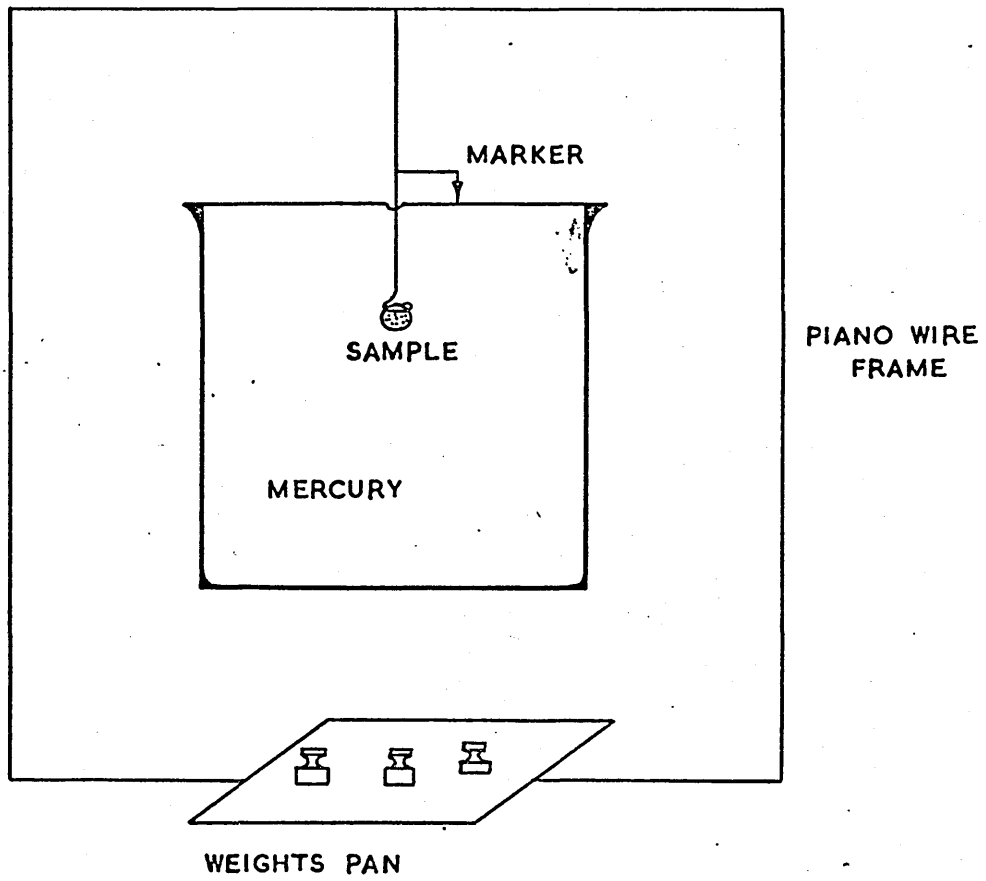


FIG. 22

PLOT OF γ_{H_2} VS. $^{\circ}C$

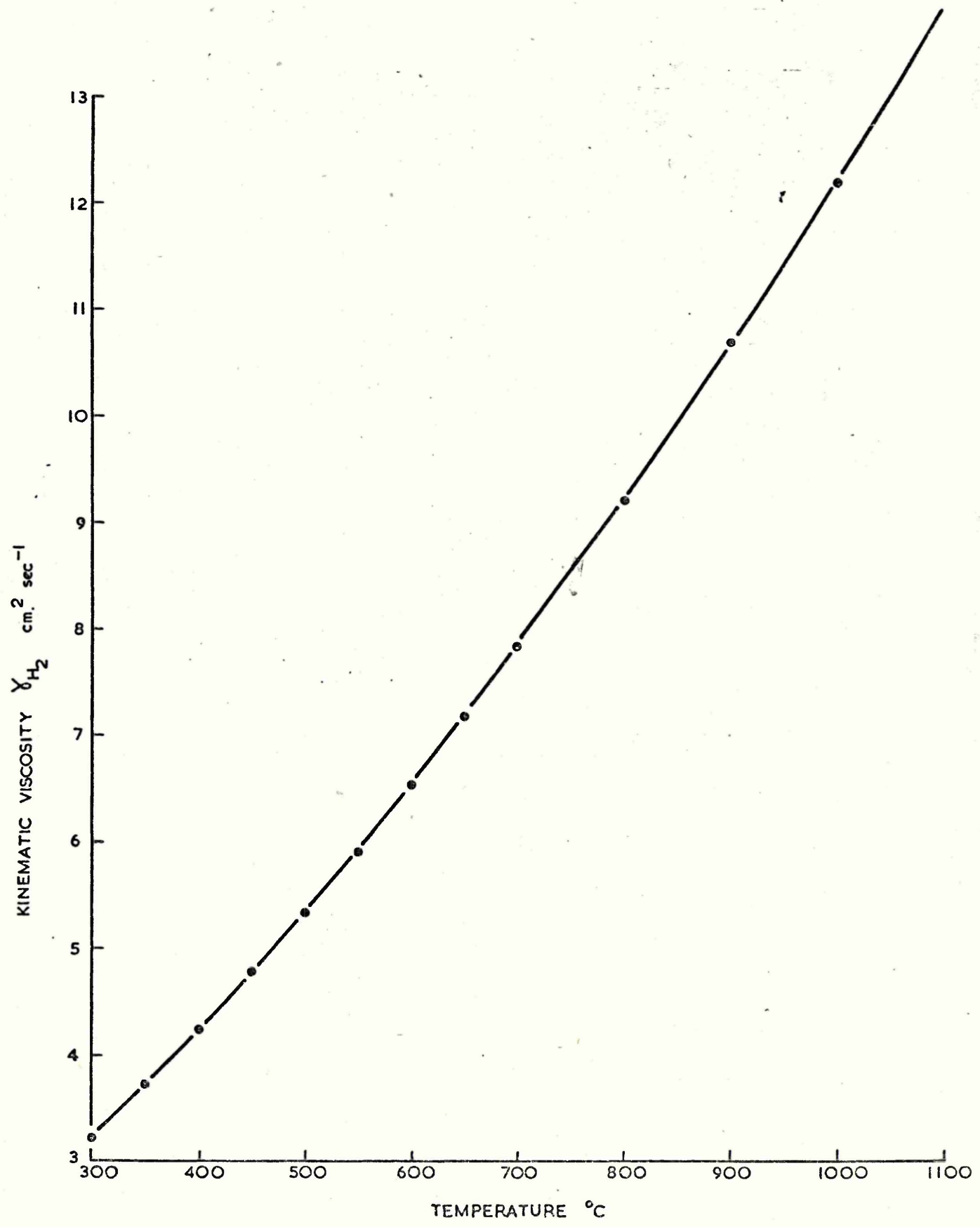
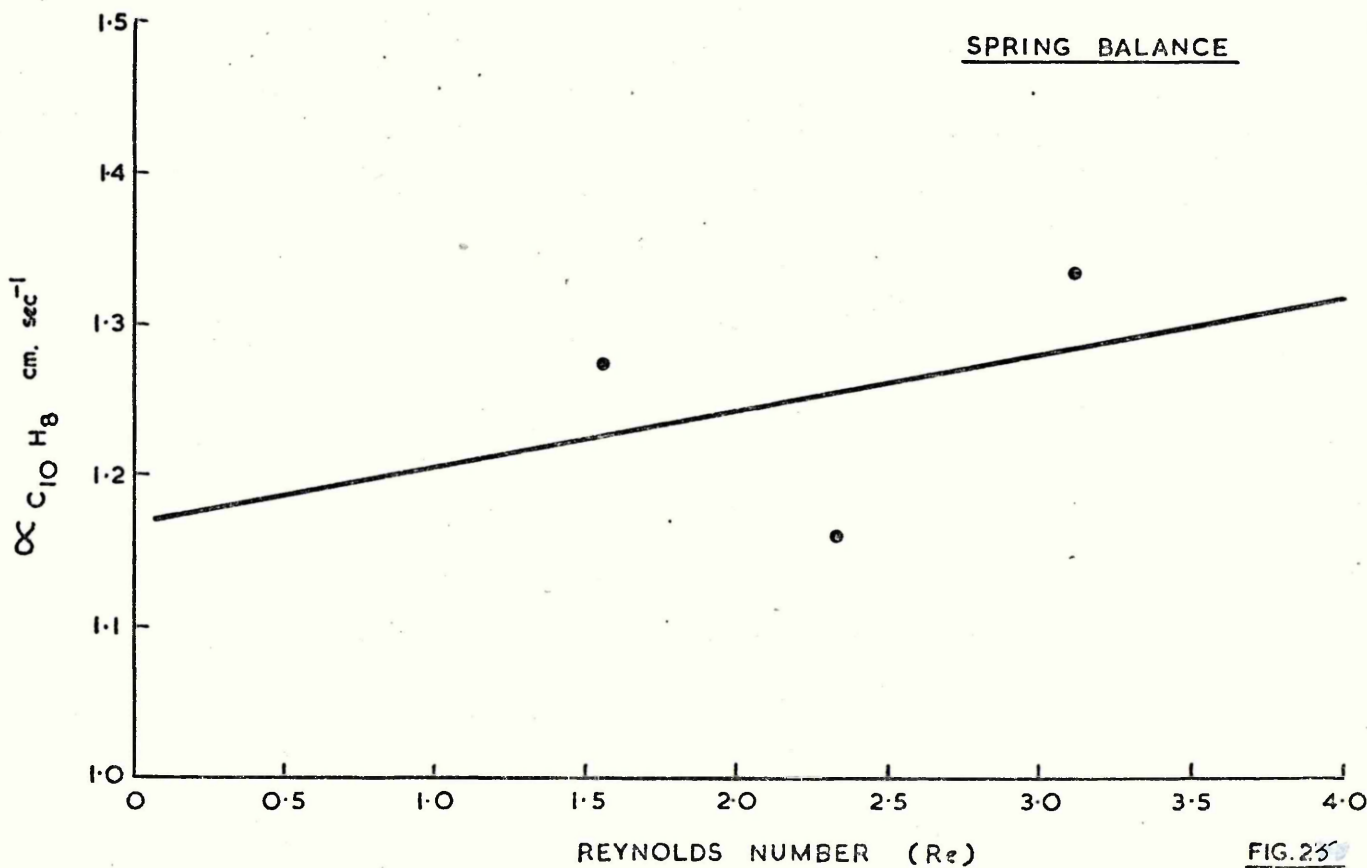
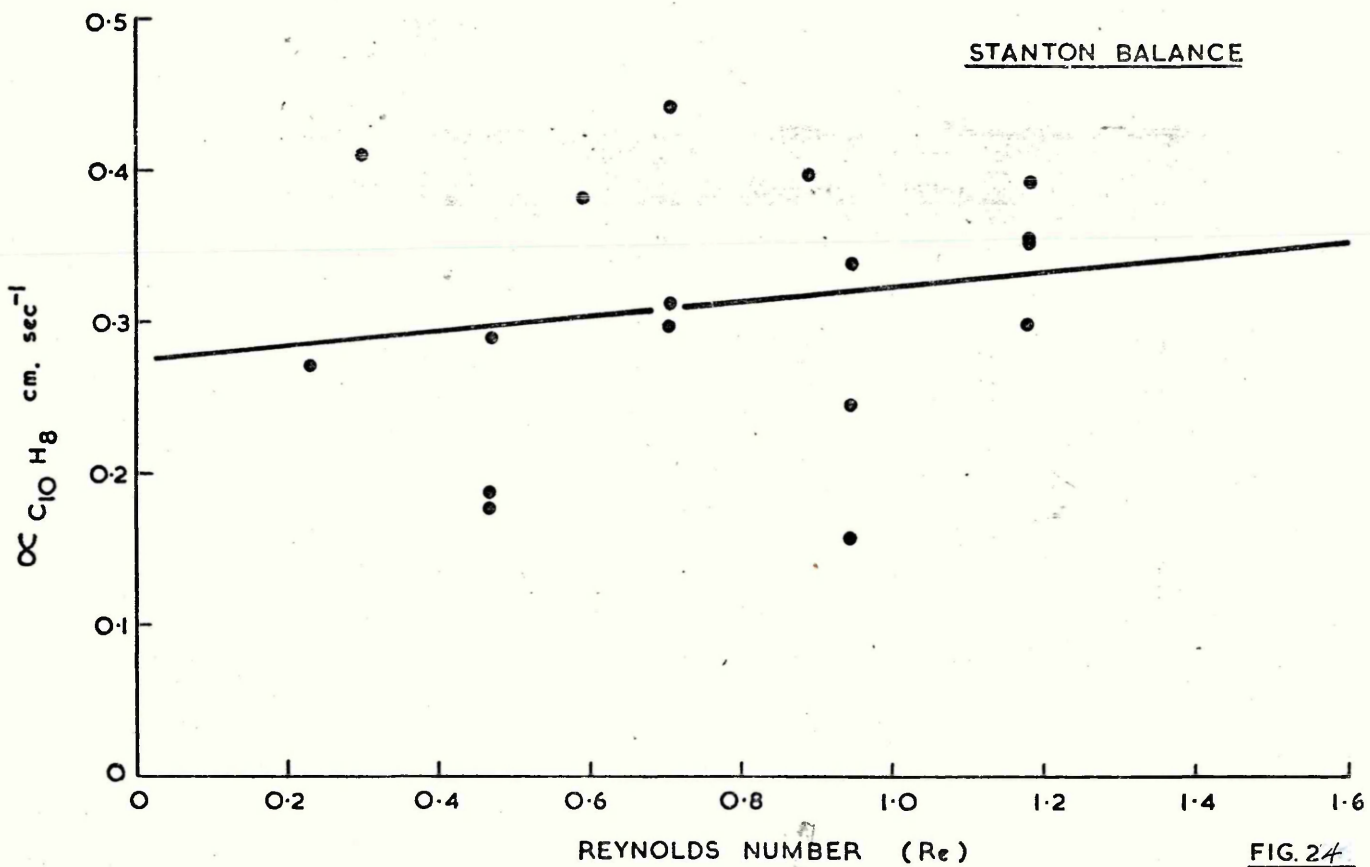
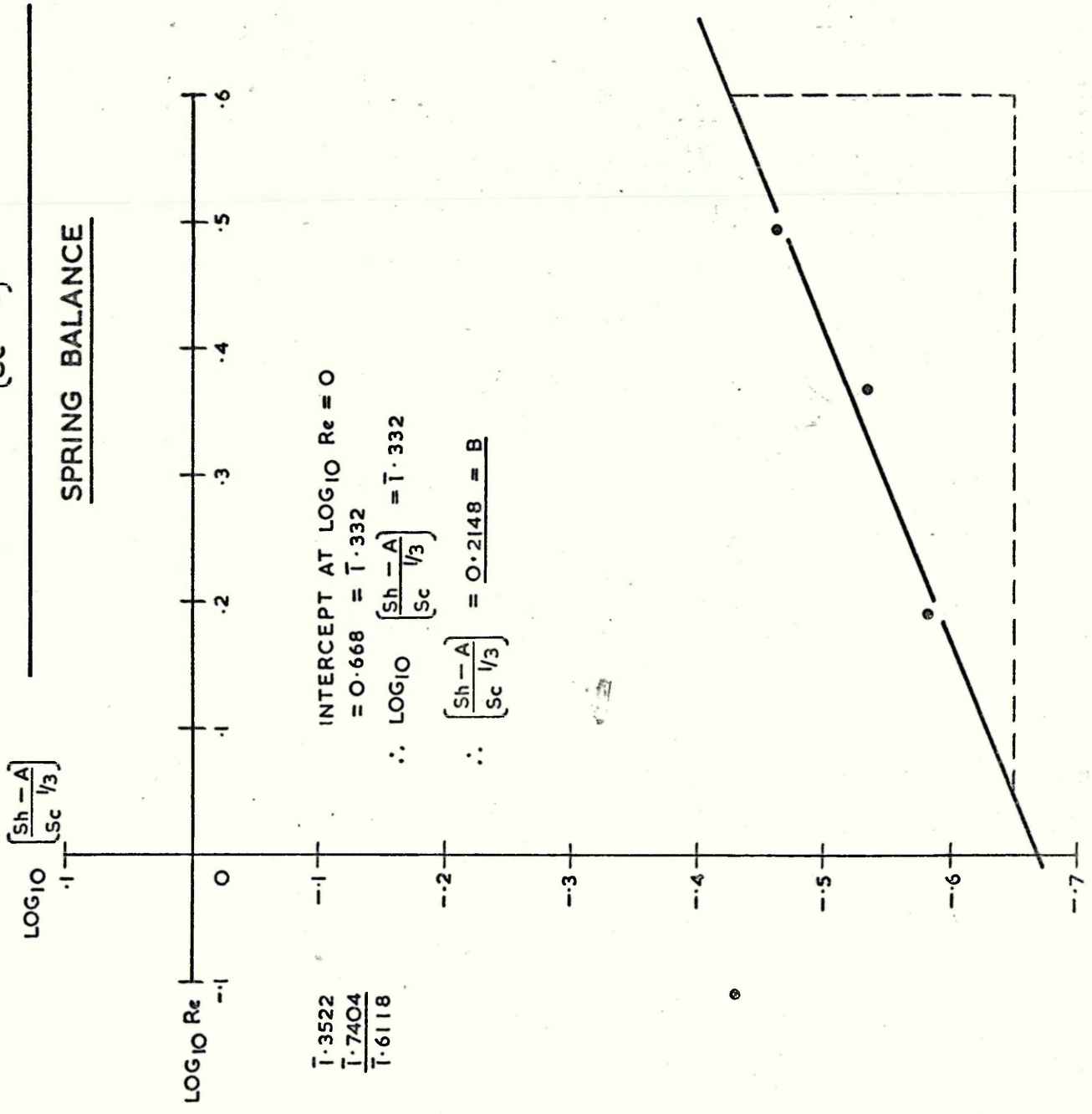


FIG.23

Re VS. $\propto C_{10} H_8$



PLOT OF $\text{LOG}_{10} \left[\frac{Sh-A}{Sc^{1/3}} \right]$ VS. $\text{LOG}_{10} Re$



PLOT $\cdot \text{LOG}_{10} \left[\frac{Sh-A}{Sc-1/3} \right]$ VS. $\text{LOG}_{10} Re$

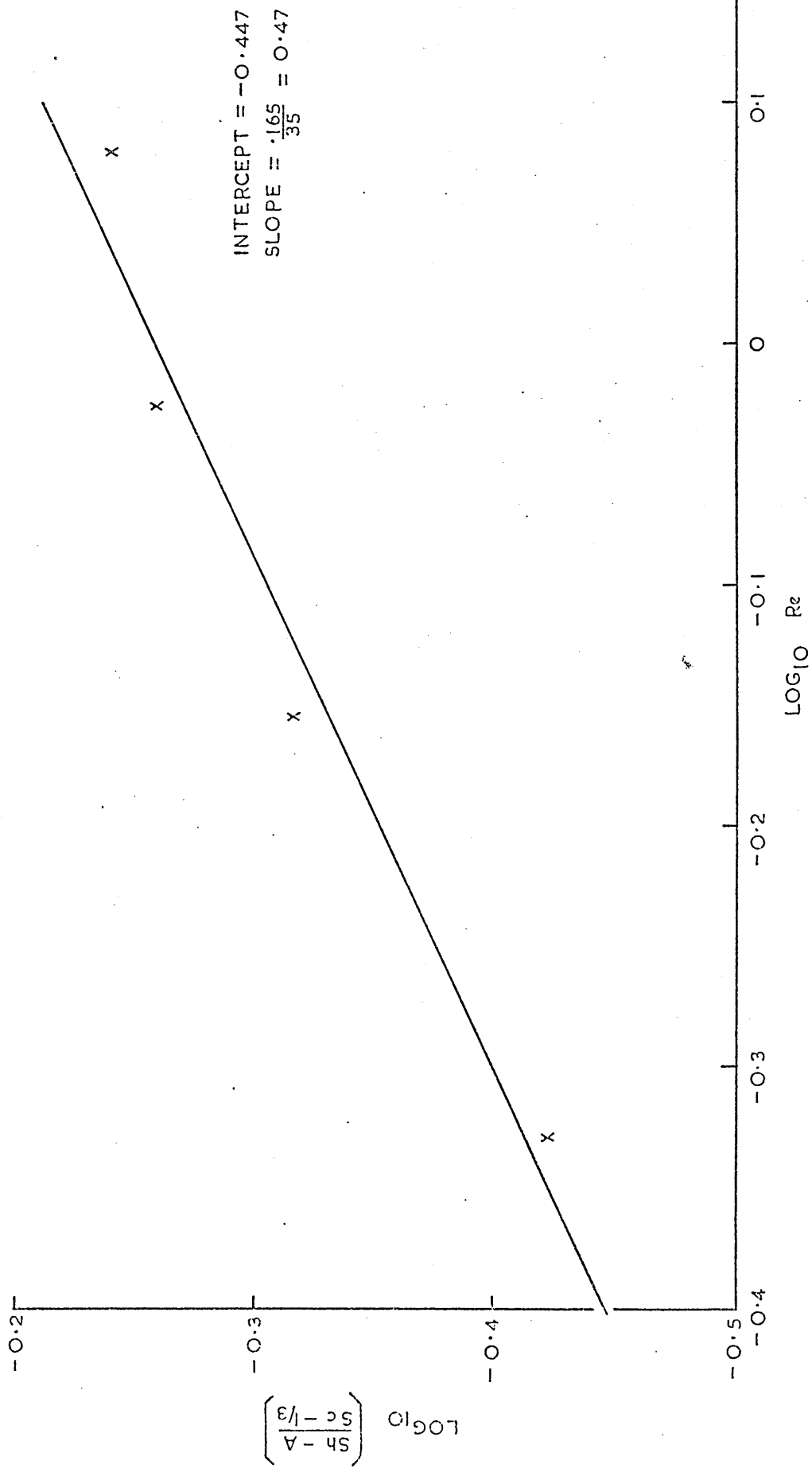


Fig. 2

PLOT OF D VS. °C

- D FROM FULLERS EQUATION (7)
- X—X D FROM GILLILANDS EQUATION (4,5)
- VALUES FOR D WHEN ATTRACTIVE AND REPULSIVE EFFECTS HAVE BEEN ACCOUNTED FOR.

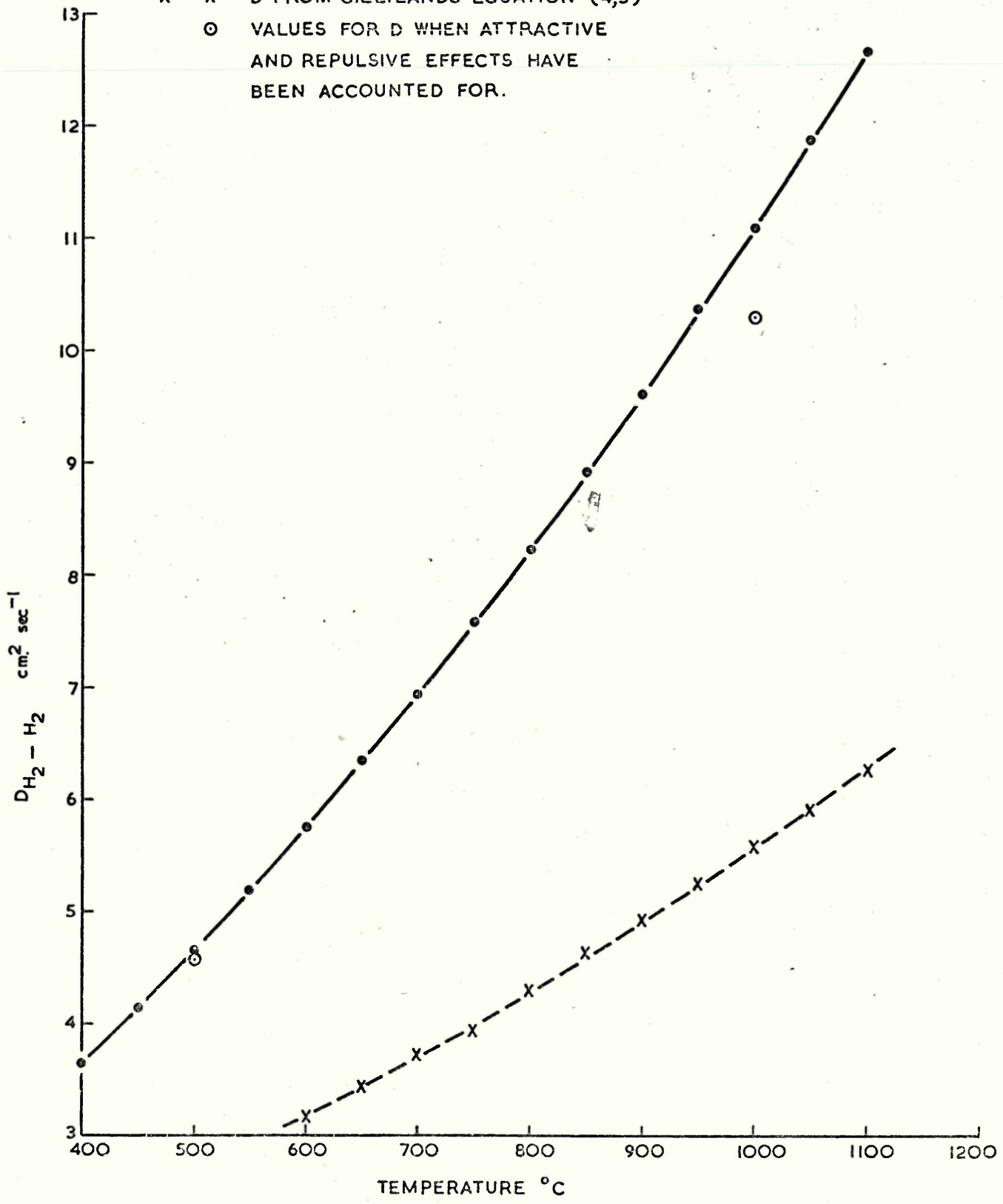


FIG. 28

STANTON BALANCE

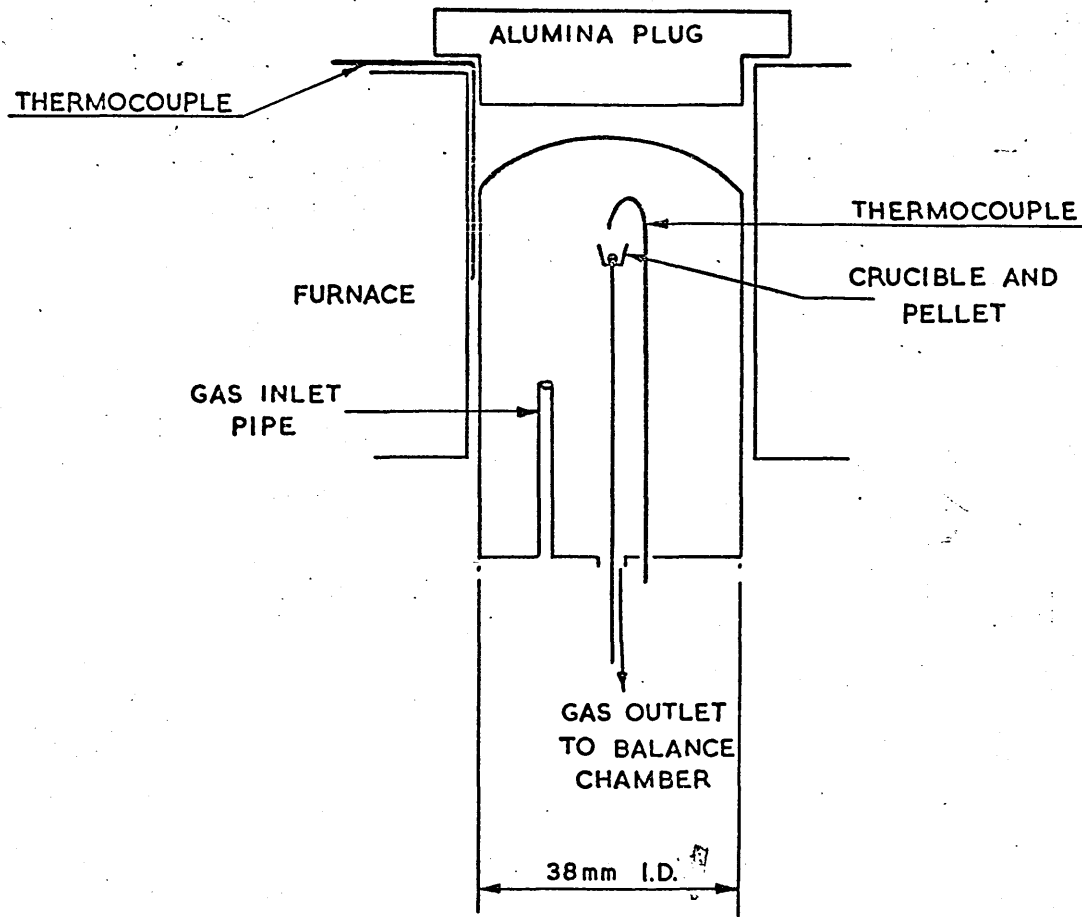


FIG. 29

SPRING BALANCE

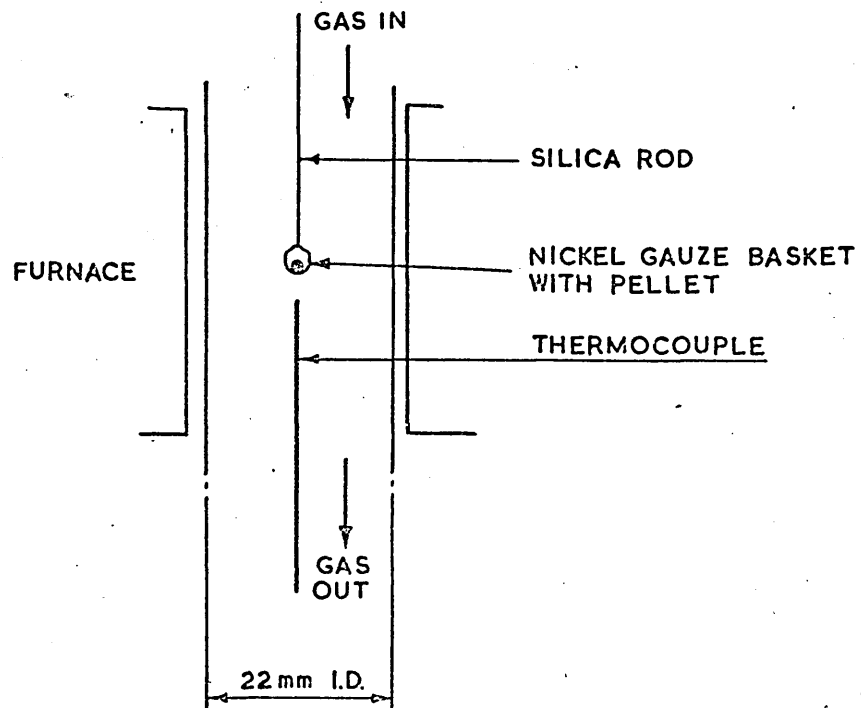


FIG. 30

$\text{OCH}_2 - \text{H}_2\text{O}$ VS. TEMPERATURE $^{\circ}\text{C}$

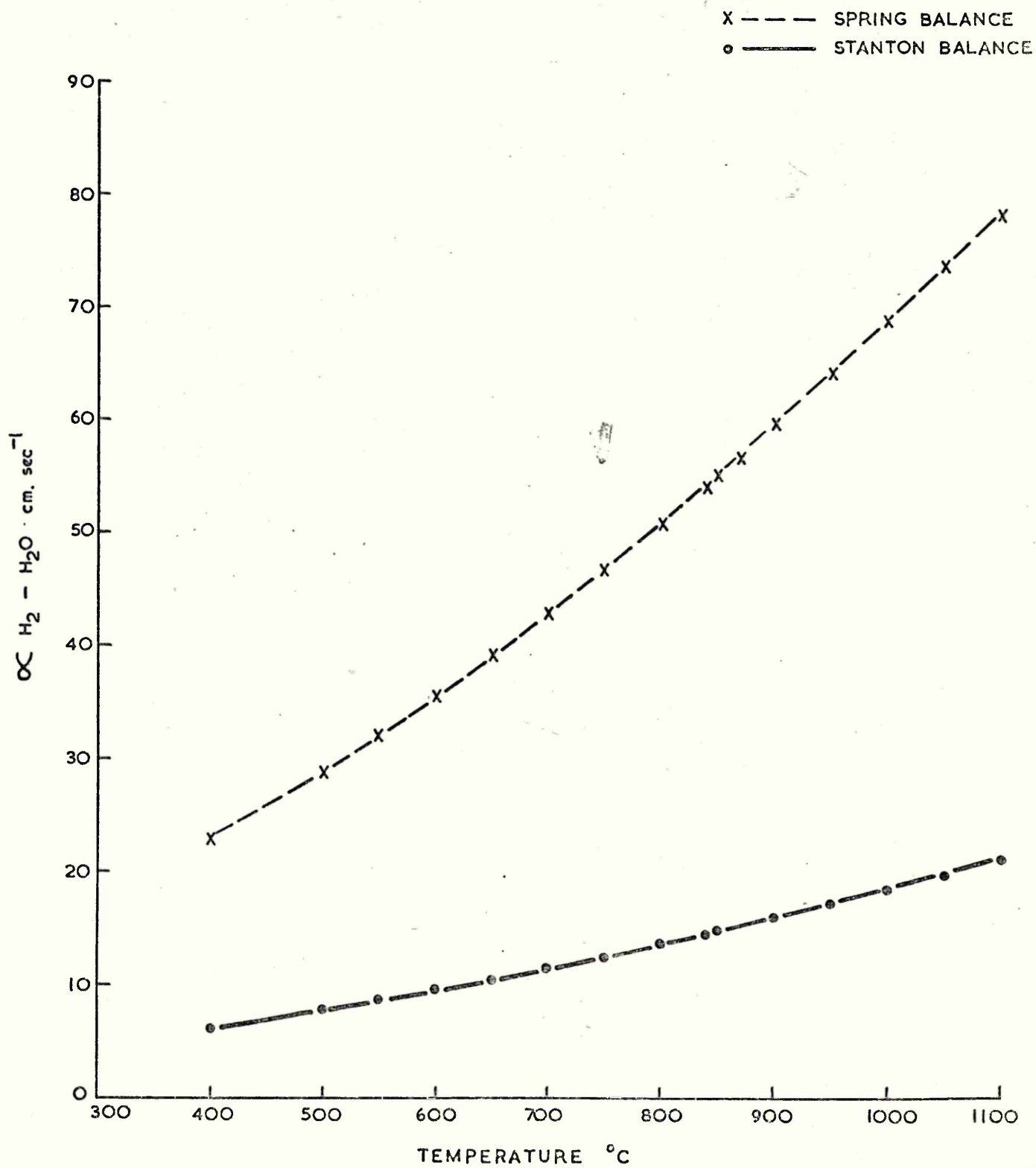
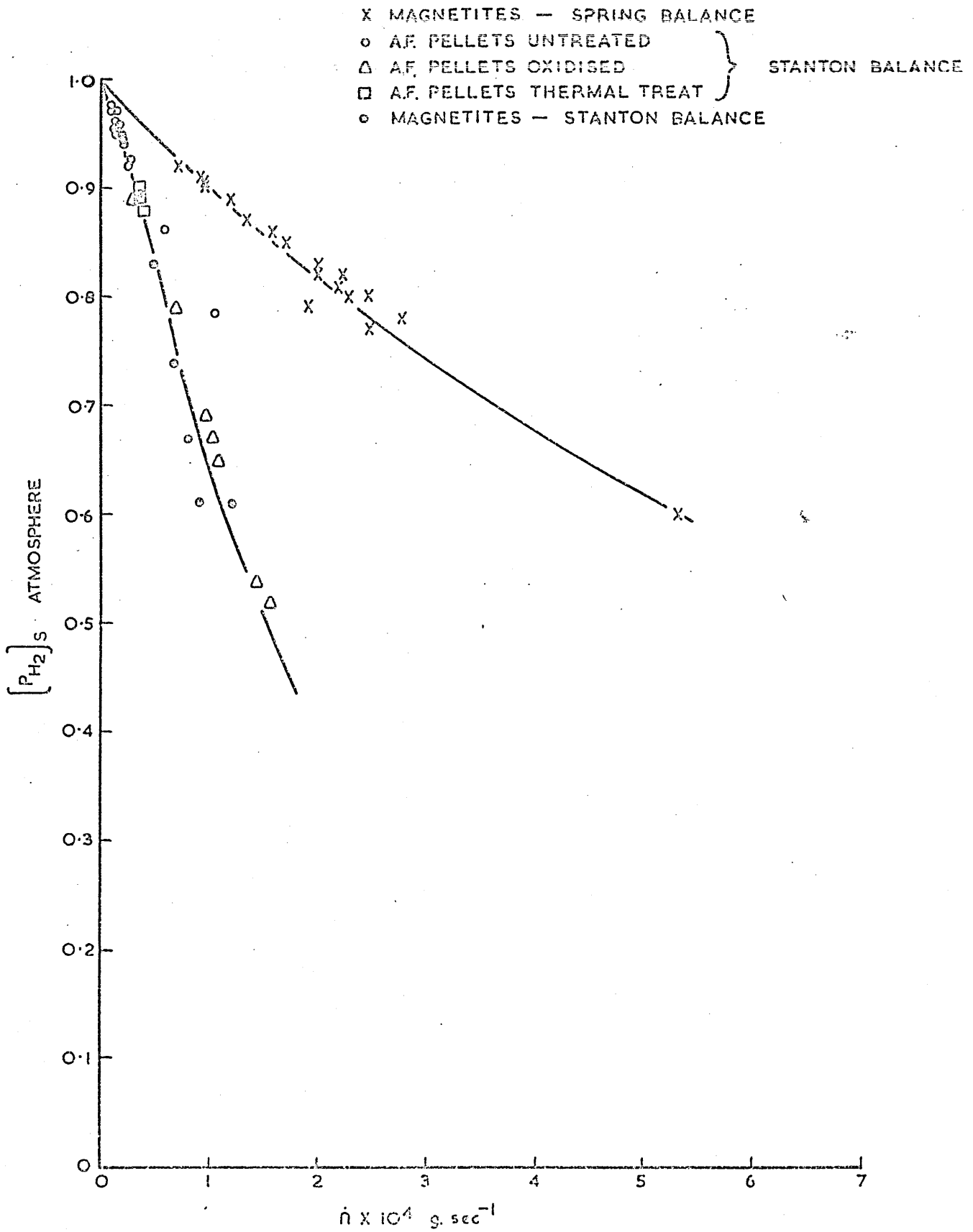
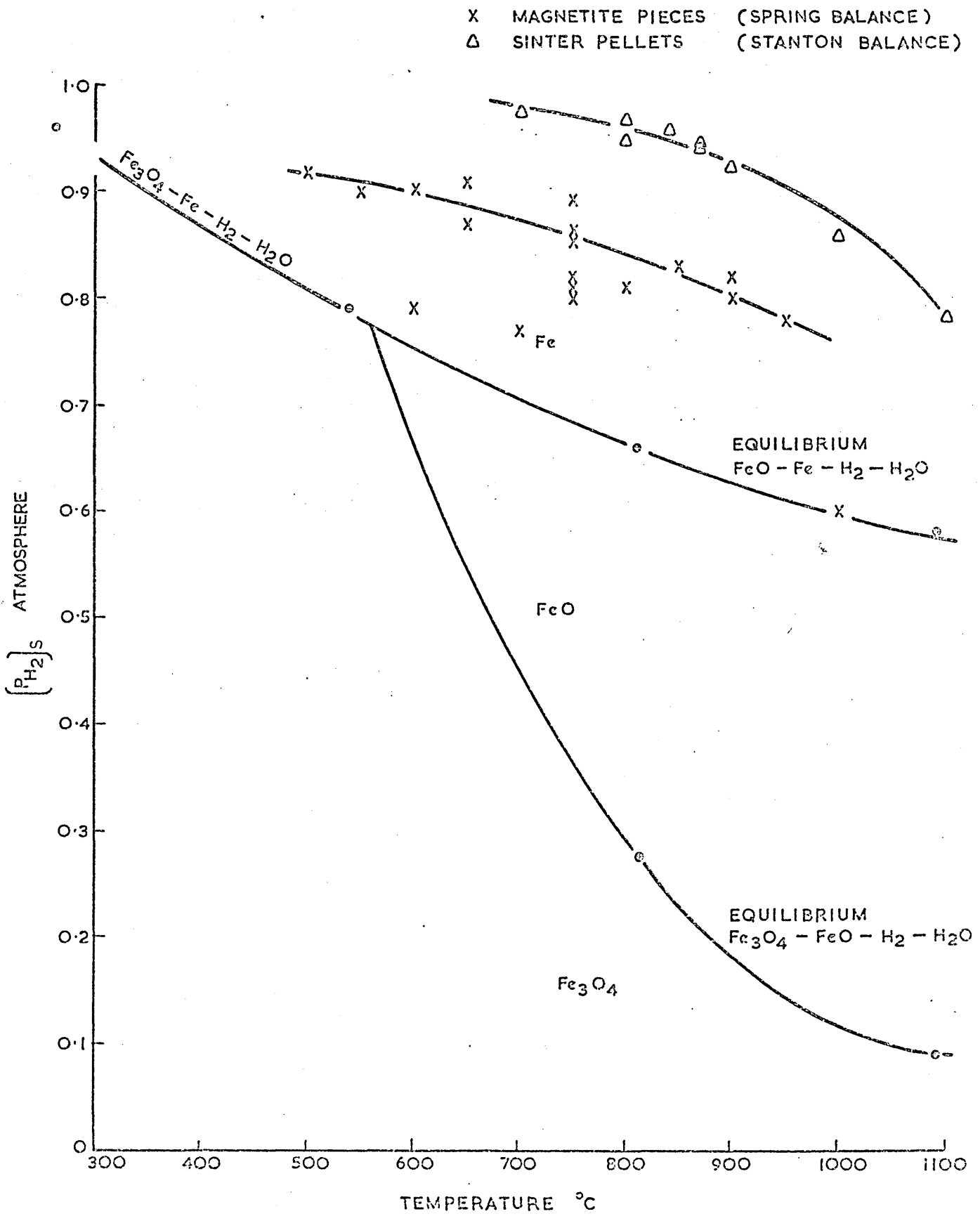


FIG. 31

$[P_{H_2}]_s$ vs. $\dot{n} \times 10^4$

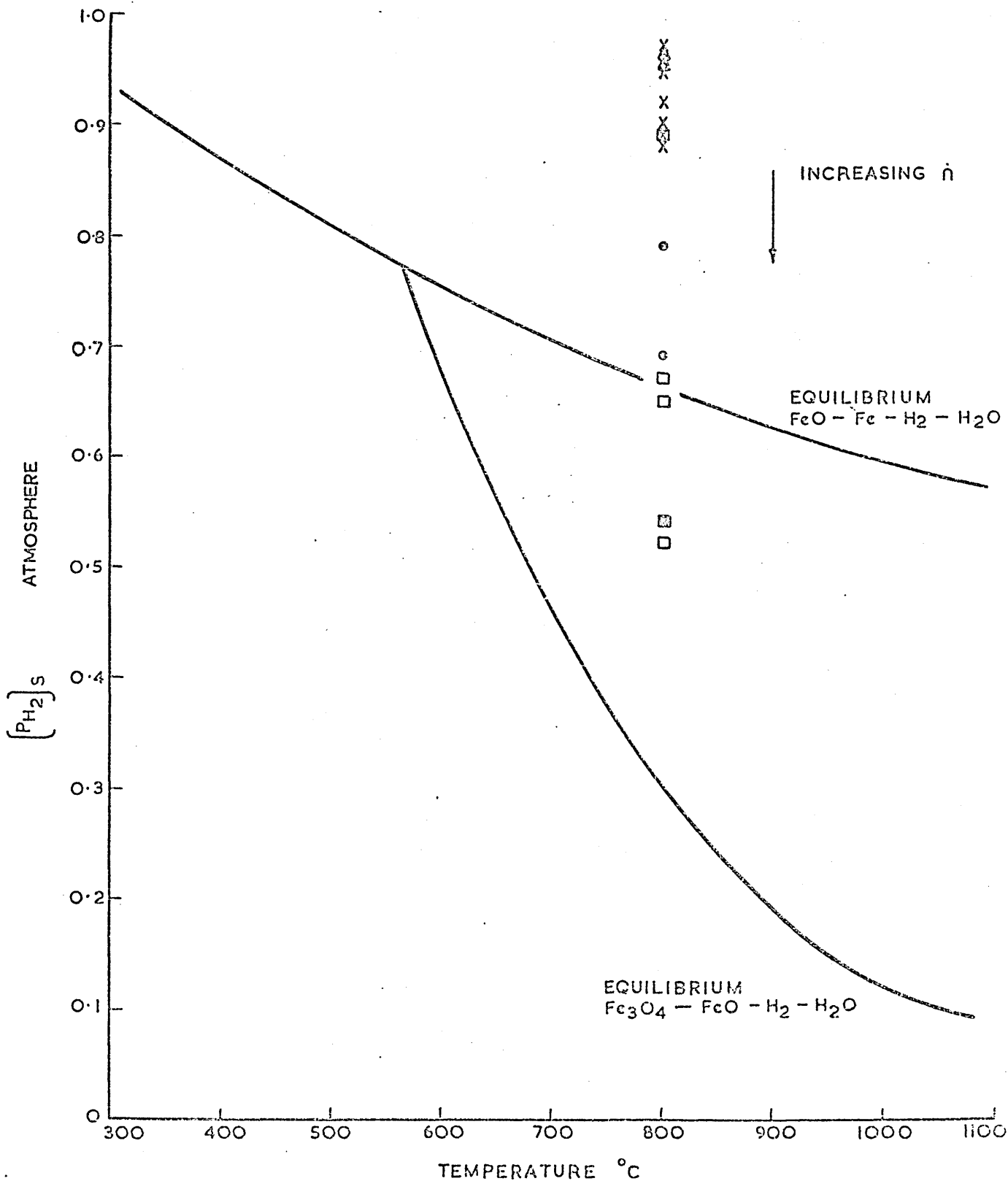


$[P_{H_2}]_S$ VS. REACTION TEMPERATURE °C



$[PH_2]_s$ VS. REACTION TEMPERATURE °C

- | | | | |
|---|--------------|-----------------------|--|
| X | HEAT TREATED | SLOW HEAT - SLOW COOL | } REDUCED
800°C
STANTON
BALANCE |
| Δ | HEAT TREATED | FAST HEAT - FAST COOL | |
| ○ | HEAT TREATED | SLOW HEAT - FAST COOL | |
| ◦ | OXIDISED | 250°C | |
| □ | OXIDISED | 1000°C | |
| ▣ | OXIDISED | 500°C | |



% REDUCTION VS. TIME CURVES

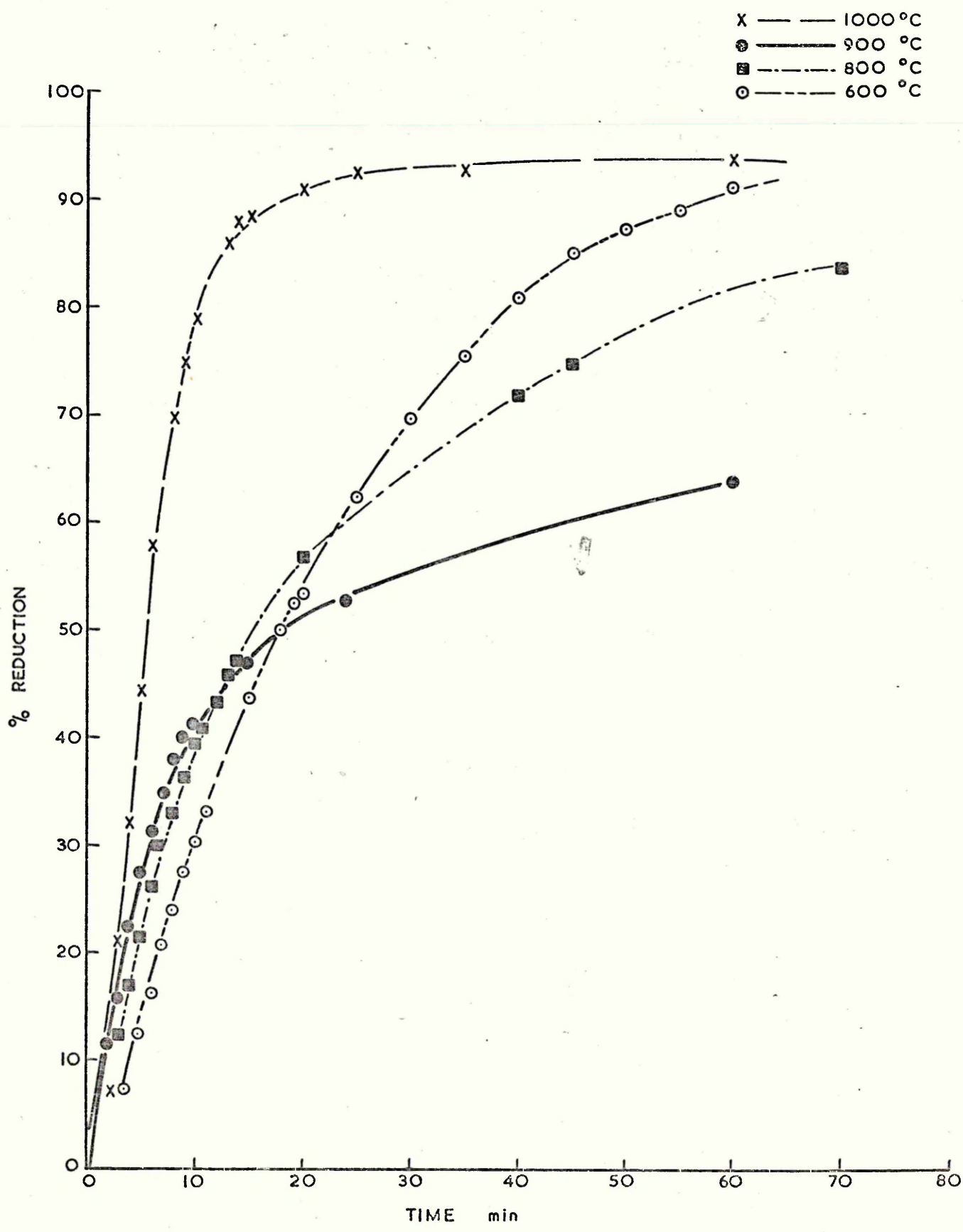
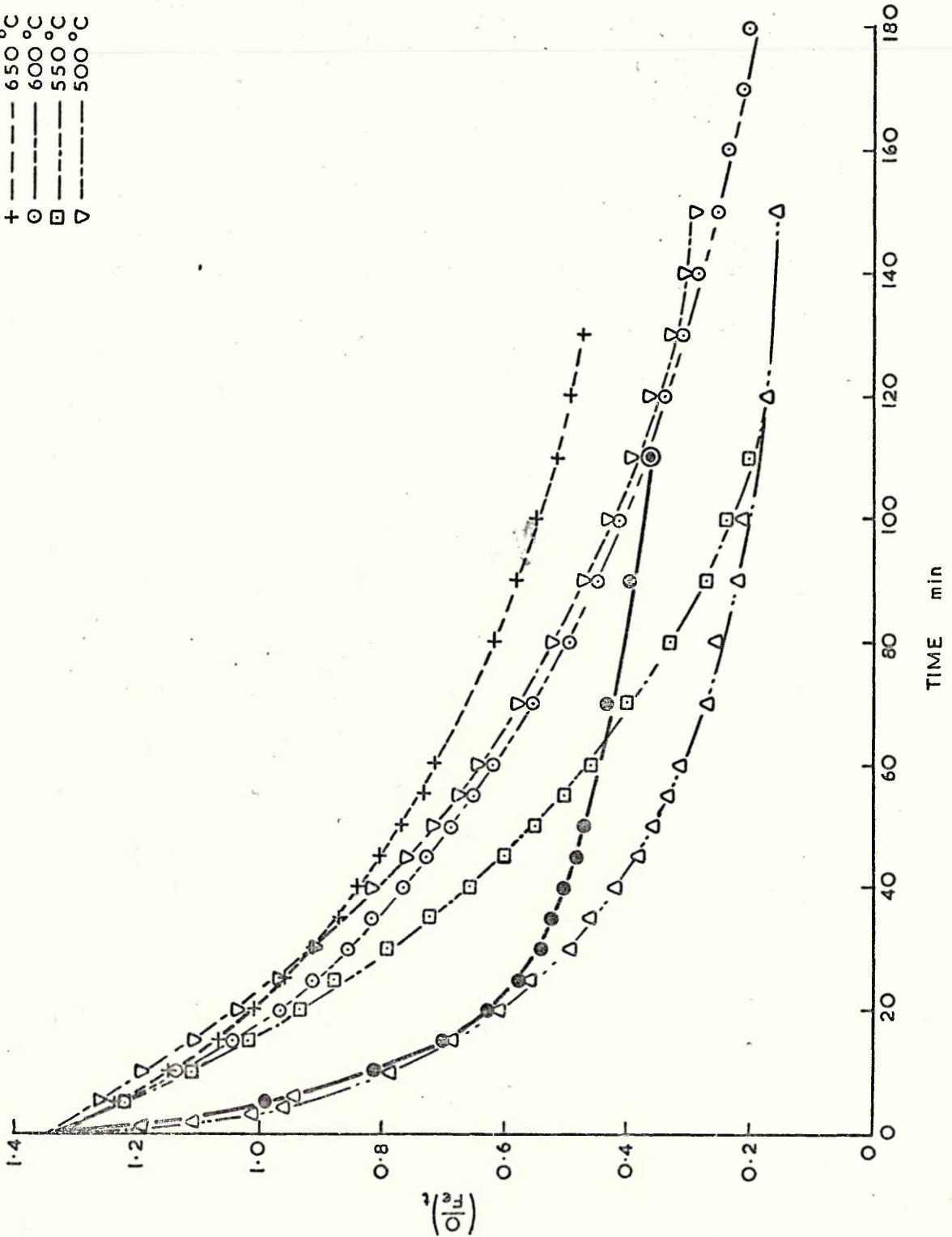
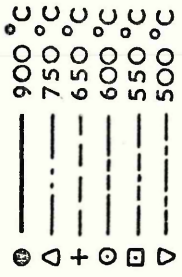
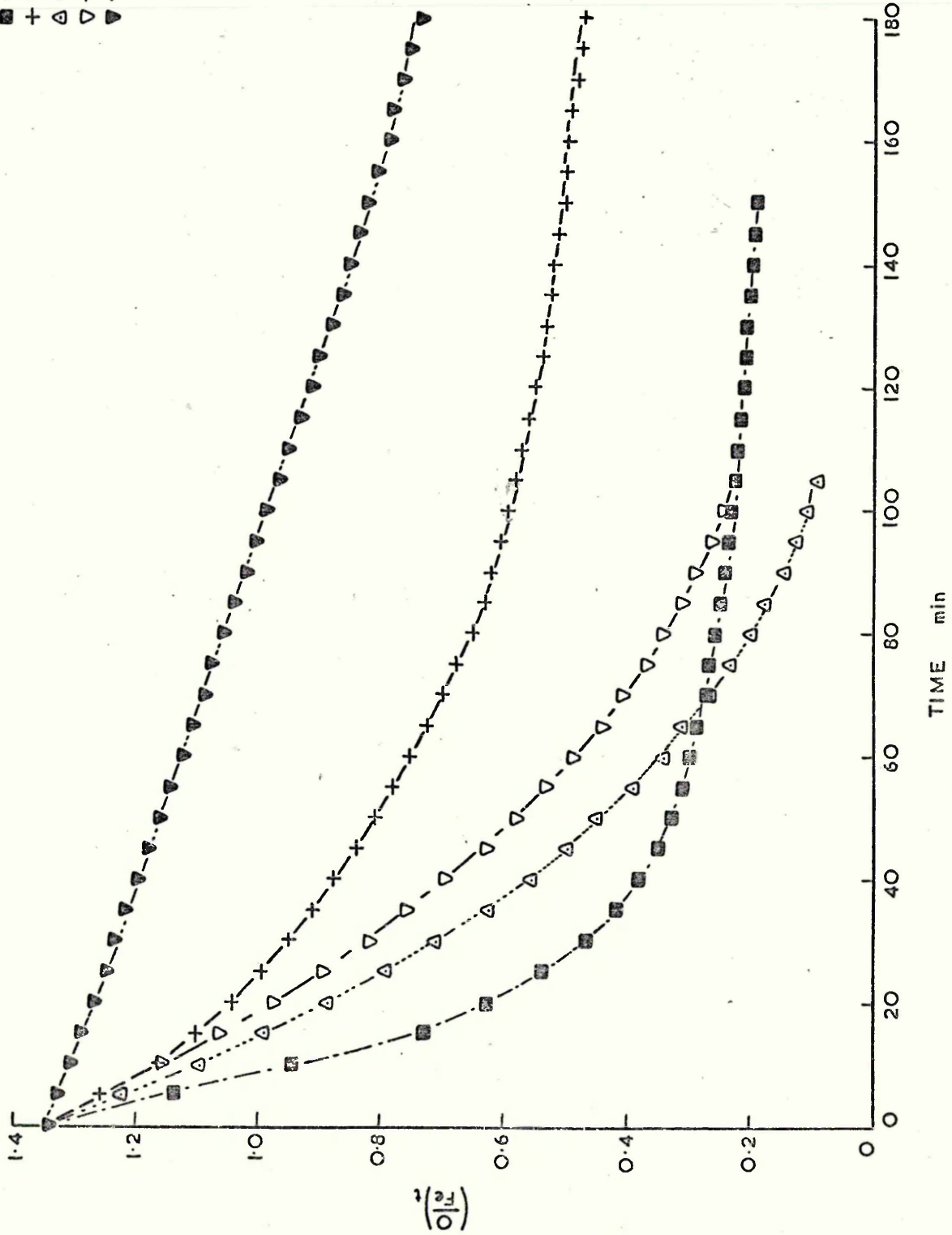
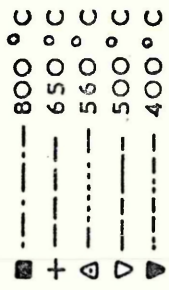


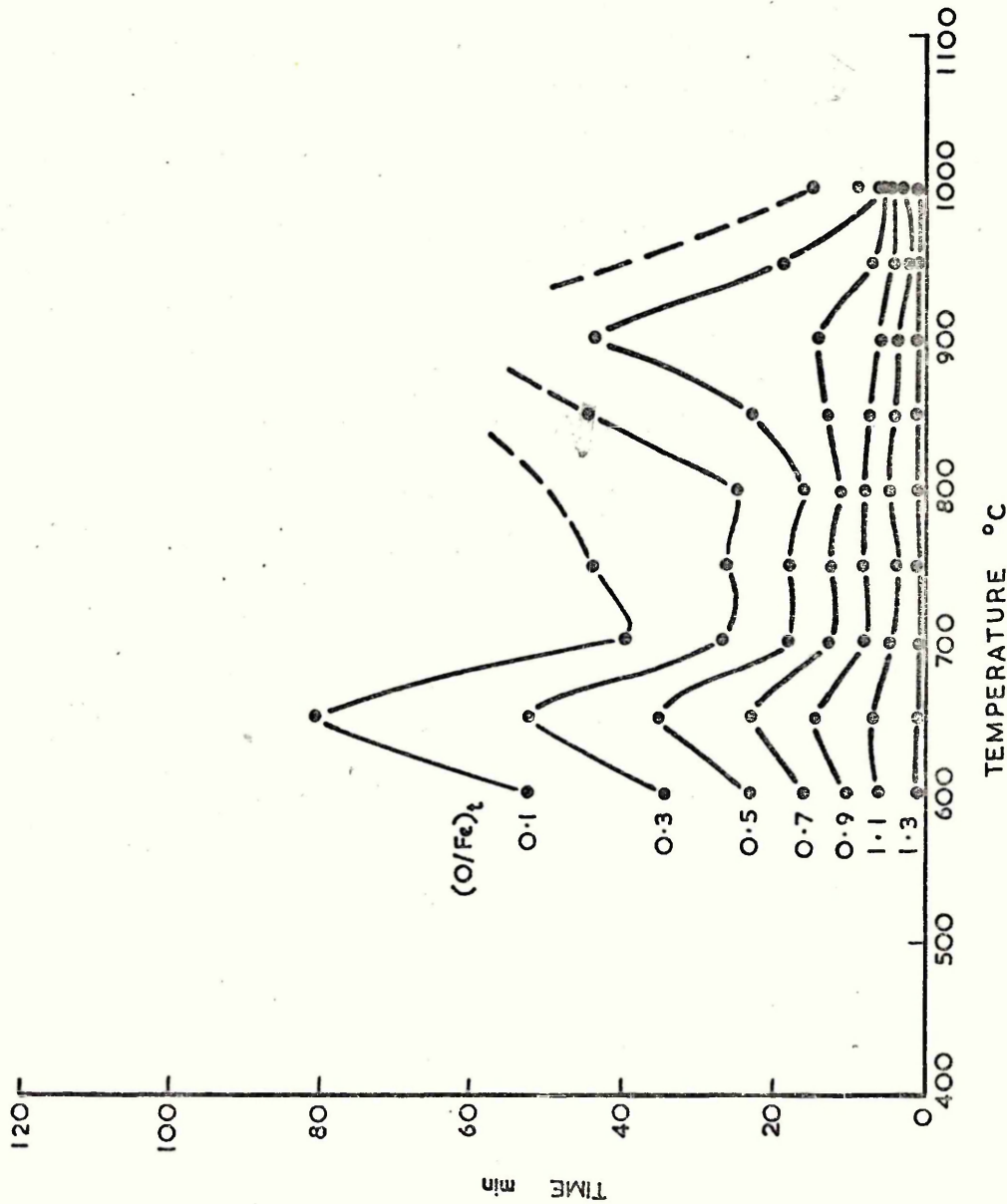
FIG. 35

KIRUNA MAGNETITES SERIES II
REDUCED USING SPRING BALANCE

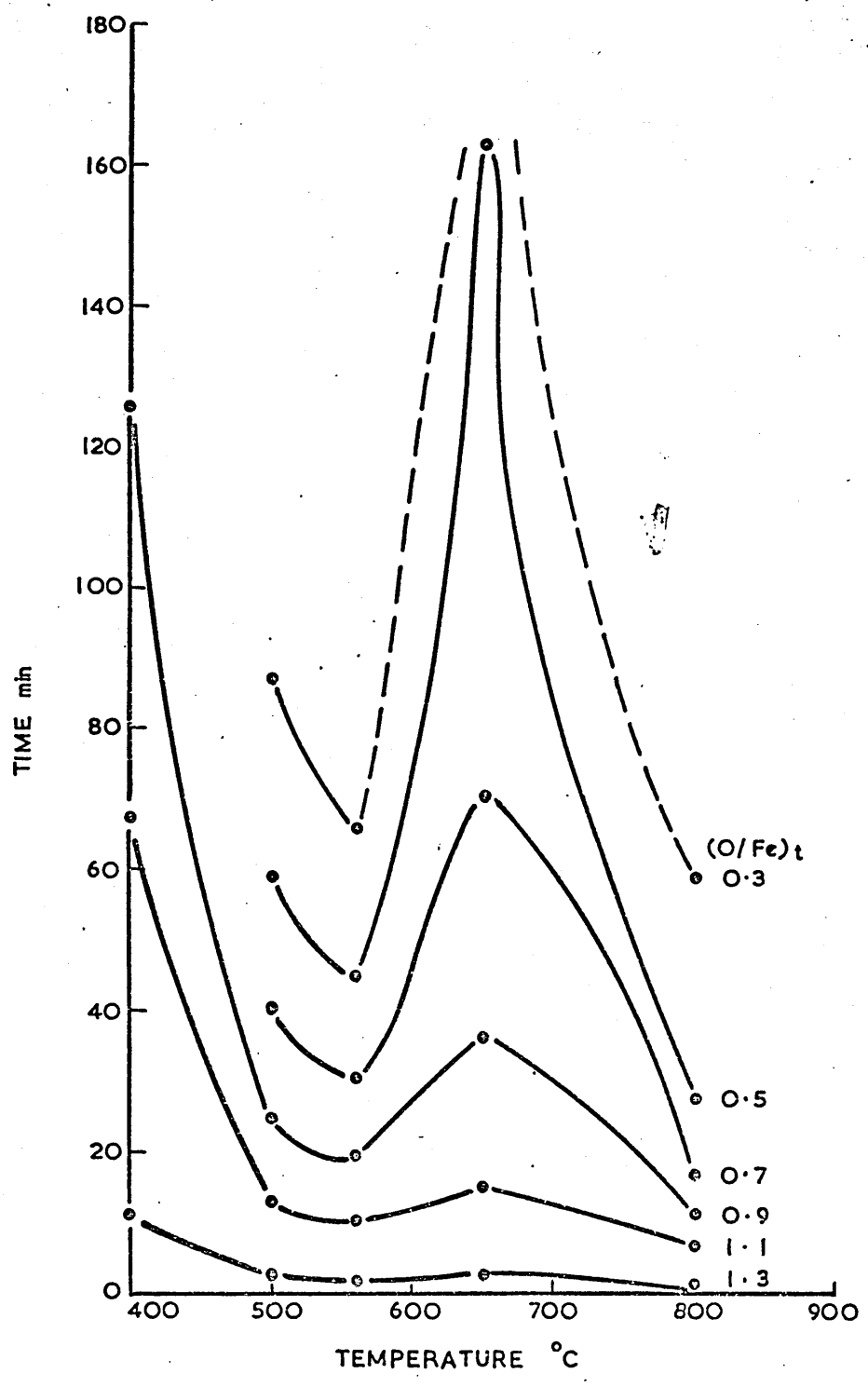


KIRUNA MAGNETITES SERIES II
REDUCED USING STANTON BALANCE





KIRUNA MAGNETITES SERIES II
RATE MINIMA AND MAXIMA
STANTON BALANCE



KIRUNA MAGNETITES SERIES II

RATE MINIMA AND MAXIMA

SPRING BALANCE

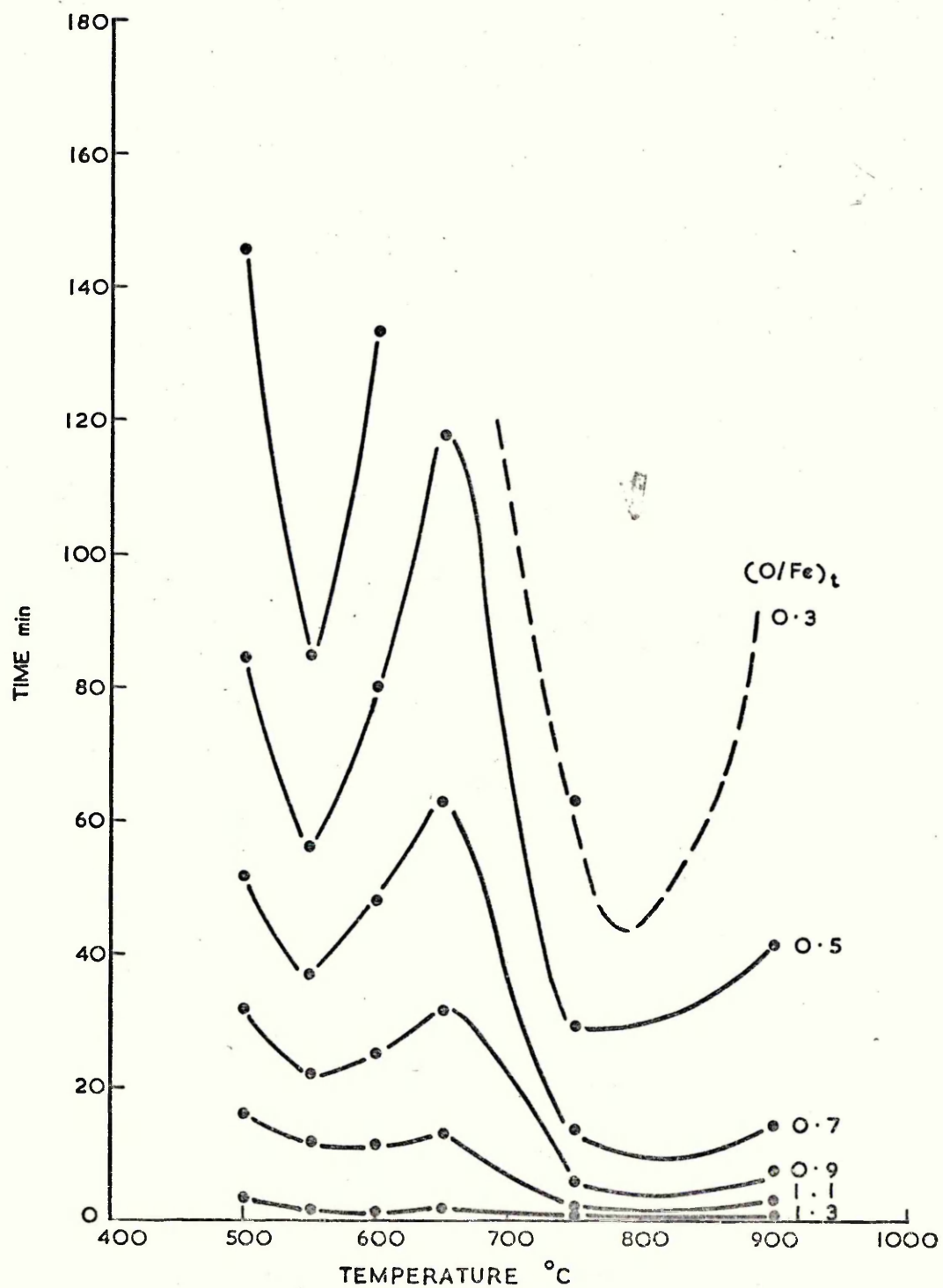


FIG. 40

Fig. 41

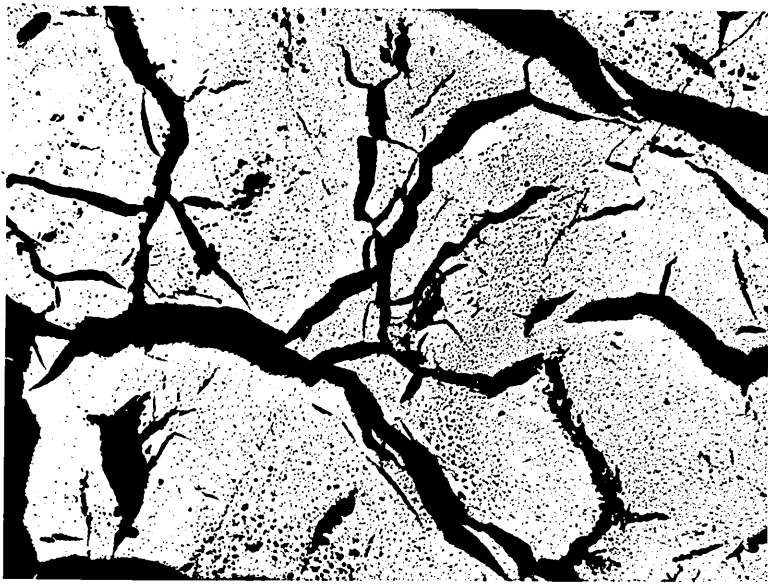
Kiruna Magnetite Reduced H_2 $600^\circ C$
Series 1 (spring balance)

63x

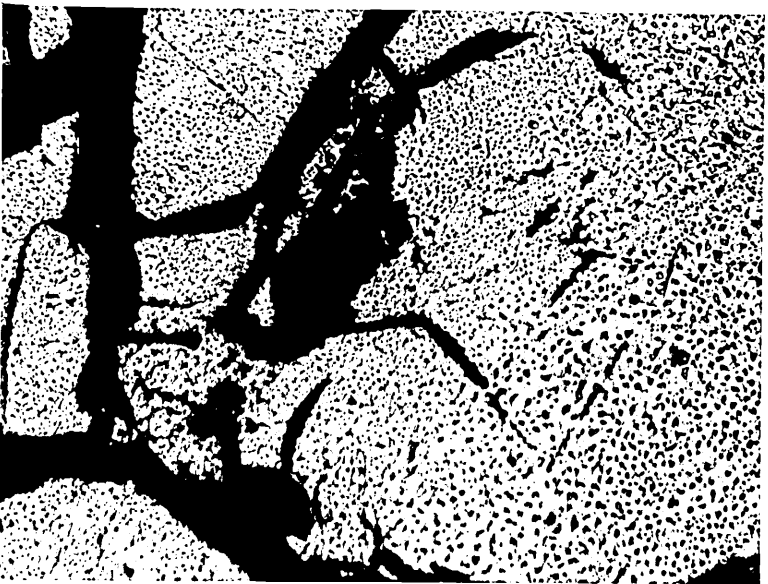
Fig. 42

Kiruna Magnetite Reduced H_2 $600^\circ C$
Series 1 (spring balance)

320x



21



22

Fig. 43

Kiruna Magnetite Reduced H_2 $650^\circ C$

Series 1 (spring balance)

16x

Fig. 44

Kiruna Magnetite Reduced H_2 $650^\circ C$

Series 1 (spring balance)

200x

Fig. 45

Kiruna Magnetite Reduced H_2 $650^\circ C$

Series 1 (spring balance)

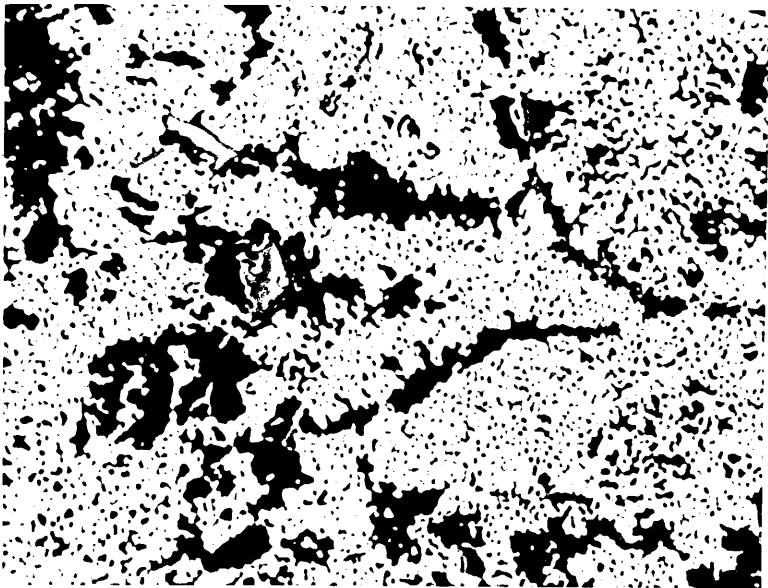
200x



23



24



25

Fig. 46

Kiruna Magnetite Reduced H_2 $650^\circ C$

Series 1 (spring balance)

500x

Fig. 47

Kiruna Magnetite Reduced H_2 $650^\circ C$

Series 1 (spring balance)

500x

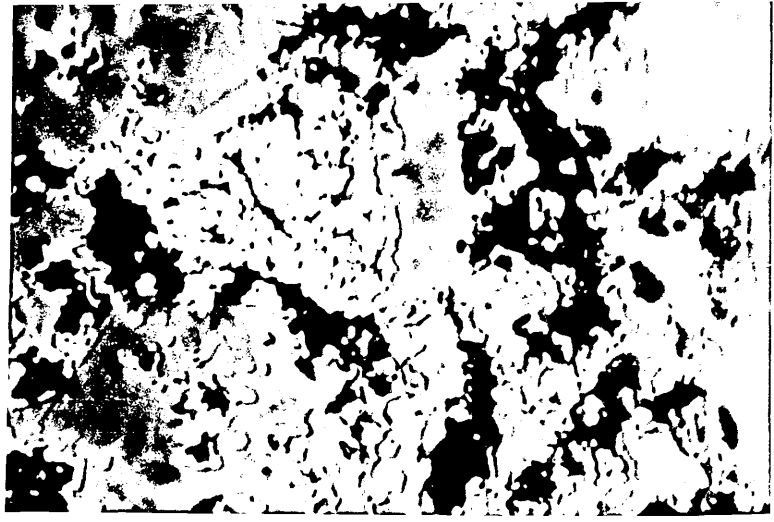
Fig. 48

Kiruna Magnetite Reduced H_2 $650^\circ C$

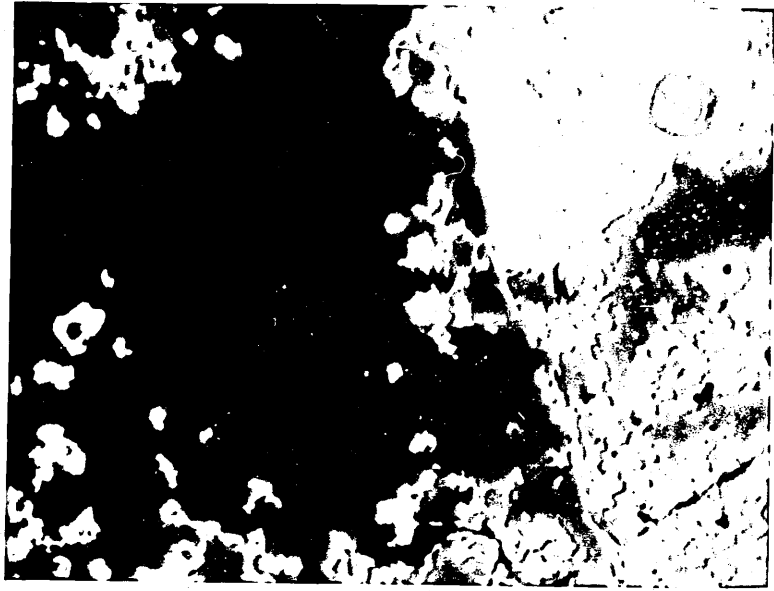
Series 2 (stanton balance)

320x

46



47



48

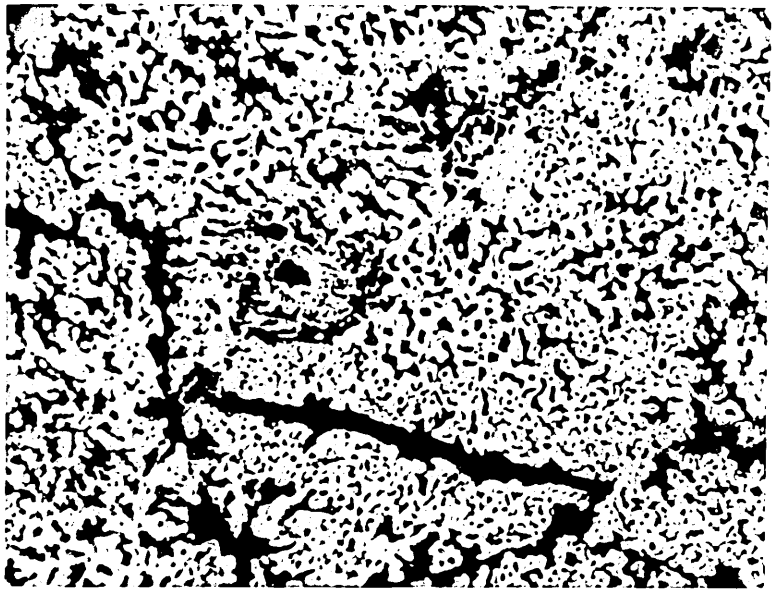


Fig. 49

Kiruna Magnetite Reduced H_2 $650^\circ C$
Series 2 (stanton balance)

63x

Fig. 50

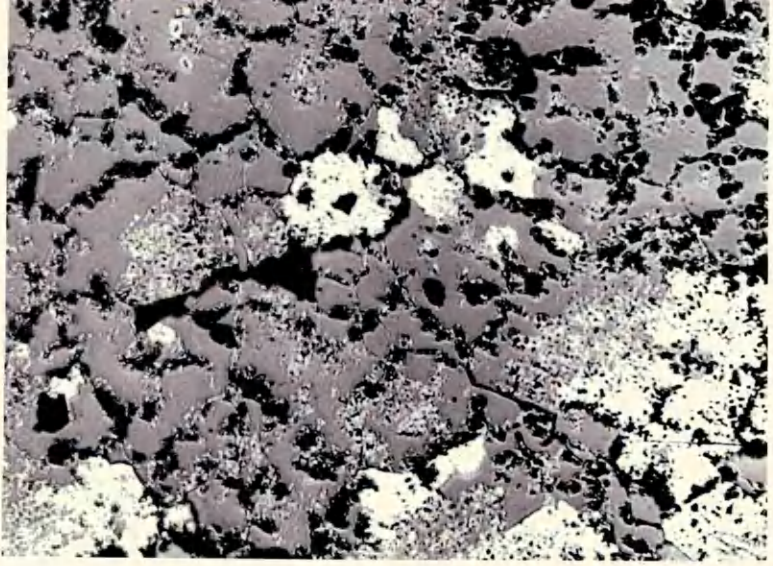
Kiruna Magnetite Reduced H_2 $650^\circ C$
Series 2 (stanton balance)

200x

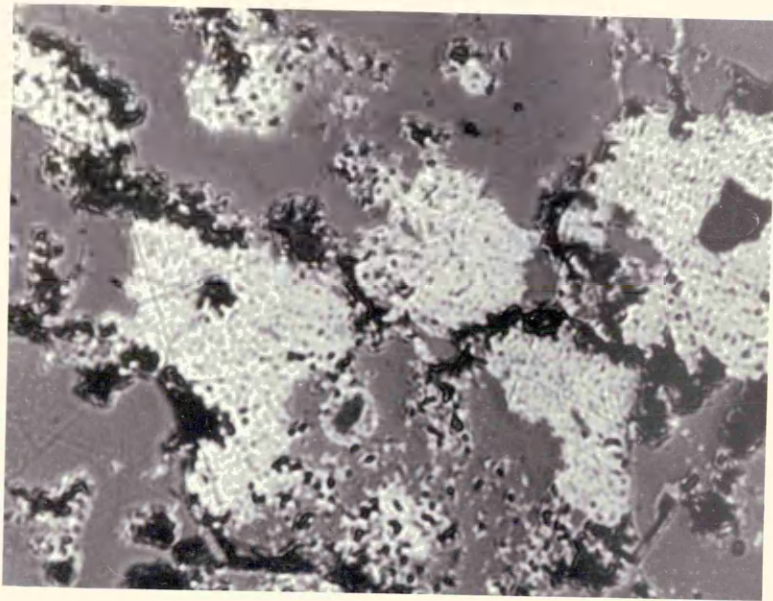
Fig. 51

Kiruna Magnetite Reduced H_2 $650^\circ C$
Series 2 (stanton balance)

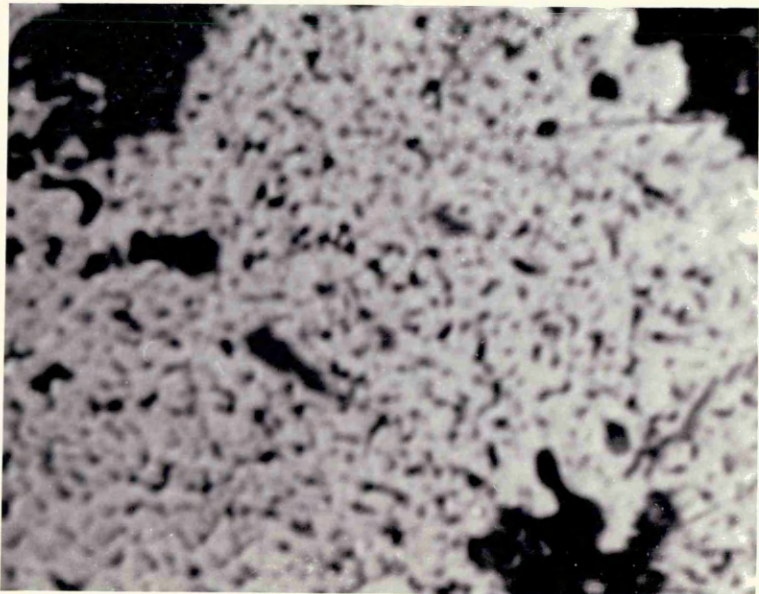
1000x



59



60



57

Handwritten notes or labels, possibly including the number 58, located to the left of the bottom micrograph.

Fig. 52

Kiruna Magnetite Reduced H_2 $650^\circ C$
Series 2 (stanton balance)

1000x

Fig. 53

Kiruna Magnetite Reduced H_2 $650^\circ C$
Series 2 (stanton balance)

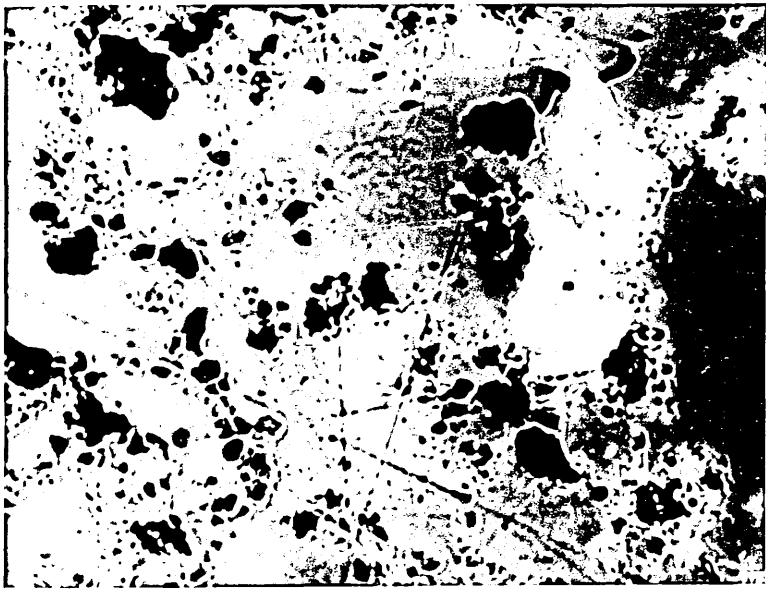
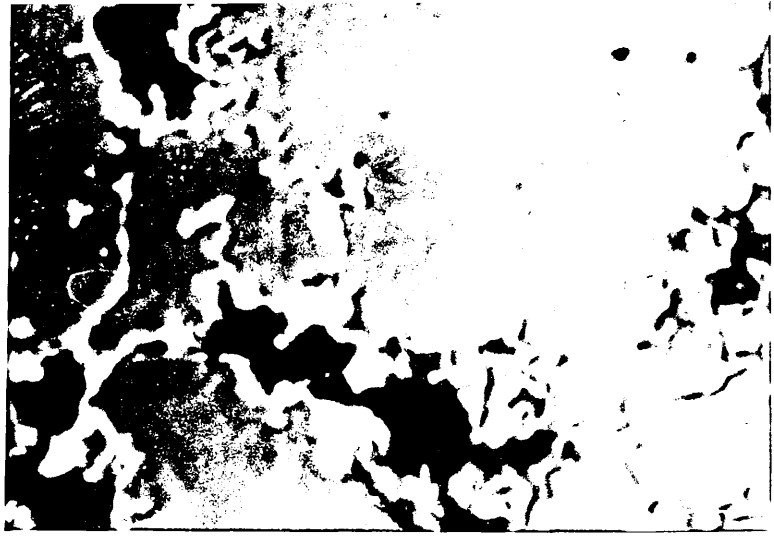
200x

Fig. 54

Kiruna Magnetite Reduced H_2 $650^\circ C$
Series 2 (stanton balance)

1000x

52



53



54

Fig. 55

Kiruna Magnetite Reduced H_2 $700^\circ C$
Series 1 (spring balance)

100x

Fig. 56

Kiruna Magnetite Reduced H_2 $700^\circ C$
Series 1 (spring balance)

100x

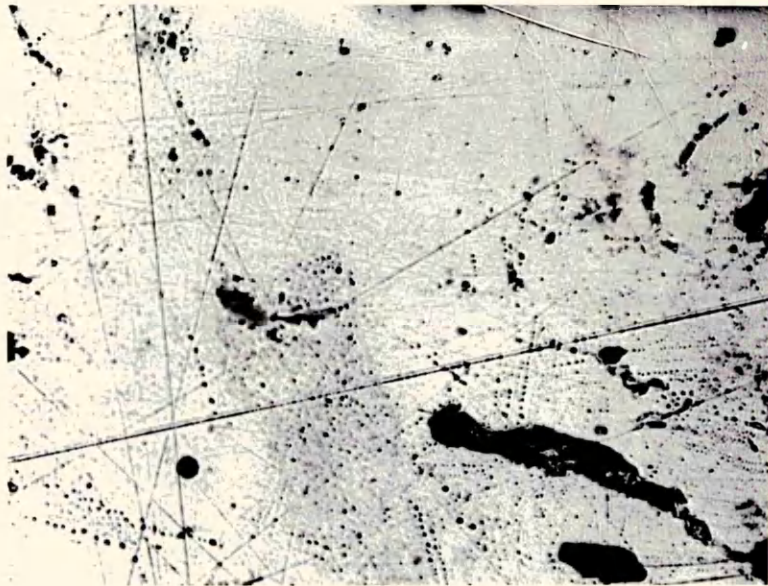
Fig. 57

Kiruna Magnetite Reduced H_2 $700^\circ C$
Series 1 (spring balance)

512x



55



56



57

Fig. 58

Kiruna Magnetite Reduced H_2 $750^\circ C$

Series 1 (spring balance)

63x

Fig. 59

Kiruna Magnetite
Reduced H_2 $750^\circ C$

Series 1
(spring balance)

125x

Fig. 60

Kiruna Magnetite Reduced H_2 $750^\circ C$

Series 1 (spring balance)

250x

Fig. 61

Kiruna Magnetite
Reduced H_2 $750^\circ C$

Series 1
(spring balance)

630x



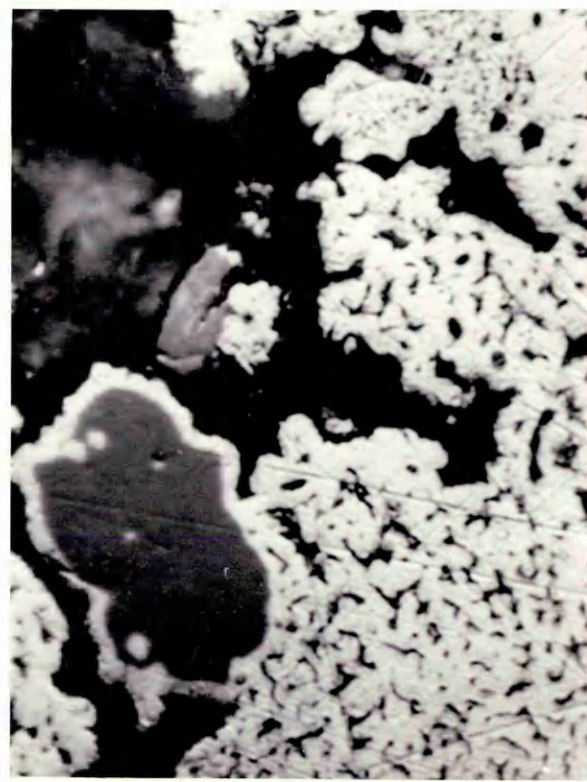
58



59



60



61

62

Fig. 62

Kiruna Magnetite Reduced H_2 750°C

Series 1 (spring balance)

16x

Fig. 63

Kiruna Magnetite
Reduced H_2 750°C

Series 1
(spring balance)

125x

Fig. 64

Kiruna Magnetite Reduced H_2 750°C

Series 1 (spring balance)

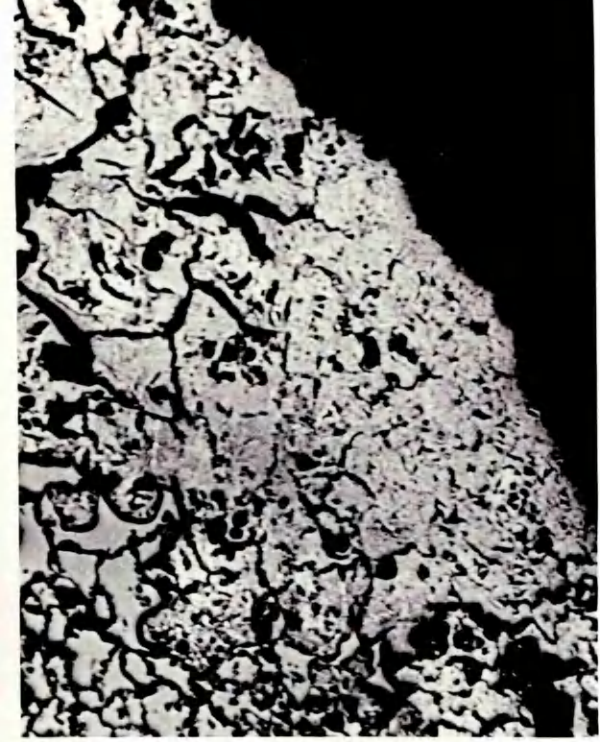
125x

Fig. 65

Kiruna Magnetite
Reduced H_2 750°C

Series 1
(spring balance)

500x



62



63

64



65

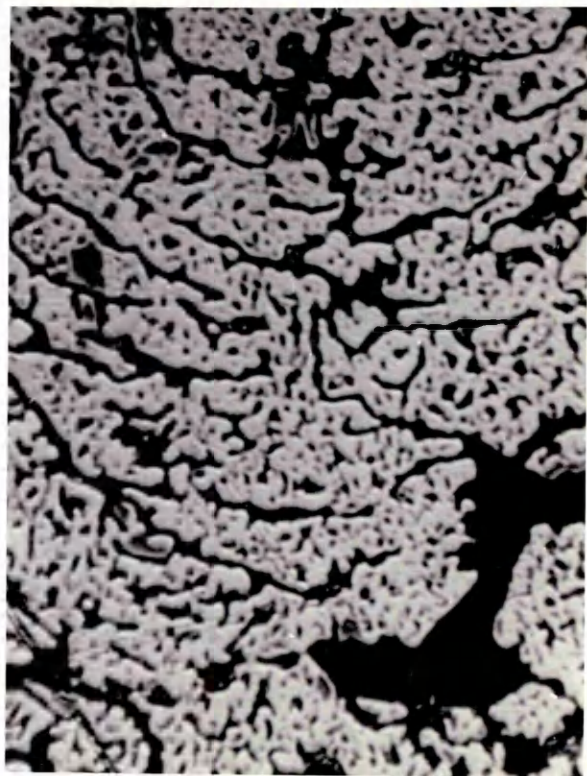


Fig. 66

Kiruna Magnetite Reduced H_2 750°C

Series 1 (spring balance)

500x

Fig. 67

Kiruna Magnetite Reduced H_2 750°C

Series 1 (spring balance)

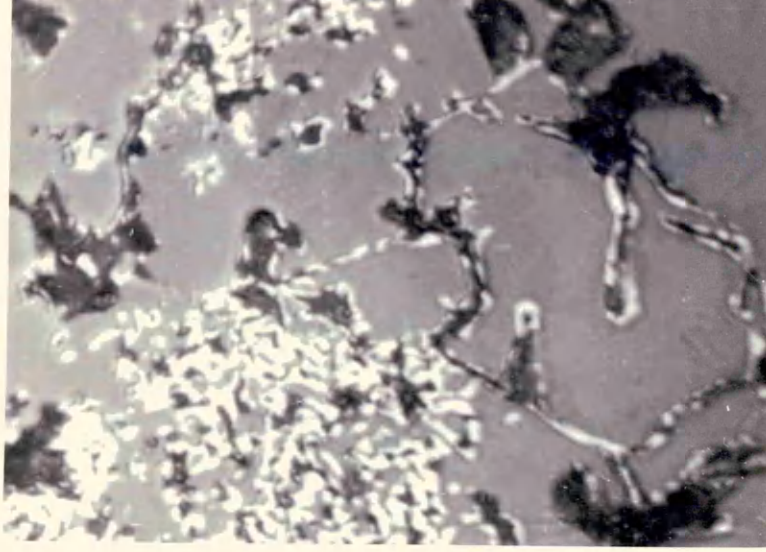
16x

Fig. 68

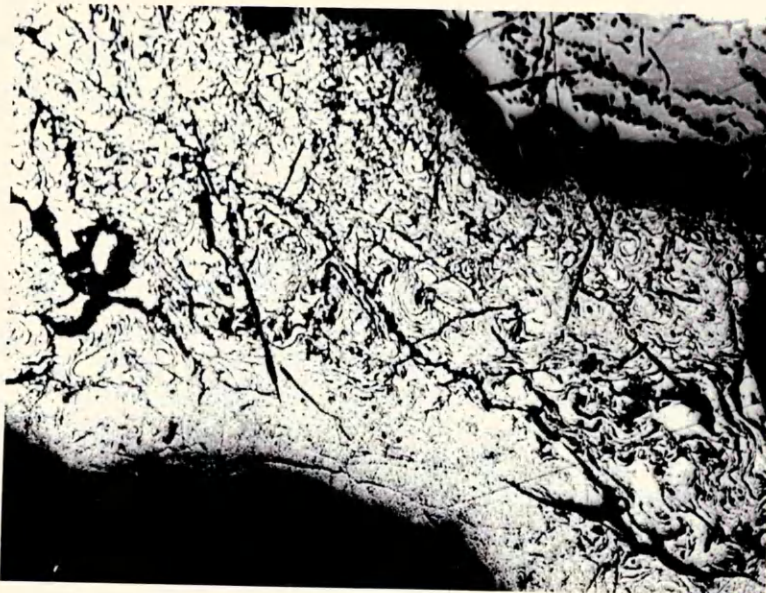
Kiruna Magnetite Reduced H_2 750°C

Series 1 (spring balance)

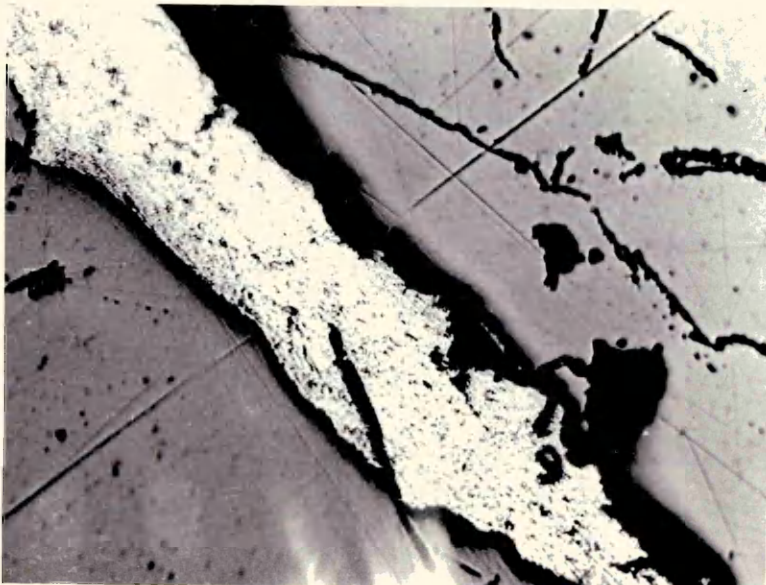
100x



66



67



68

Fig. 69

Kiruna Magnetite Reduced H_2 $800^\circ C$
Series 1 (spring balance)

63x

Fig. 70

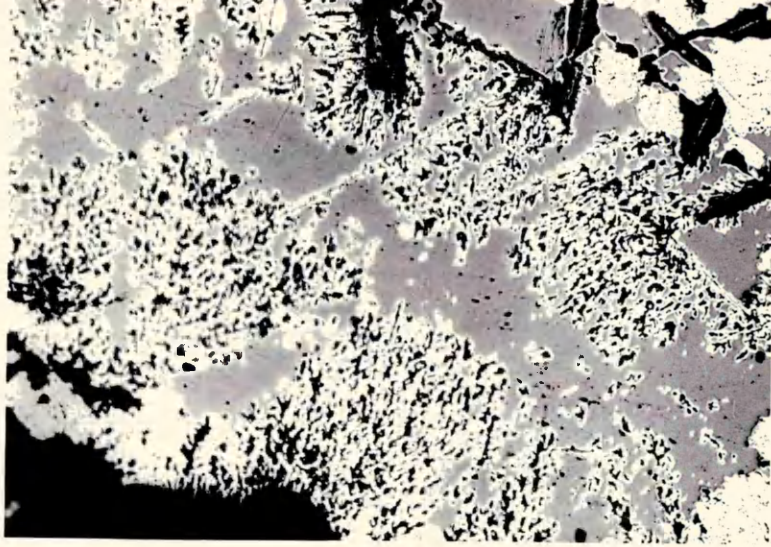
Kiruna Magnetite Reduced H_2 $800^\circ C$
Series 1 (spring balance)

512x

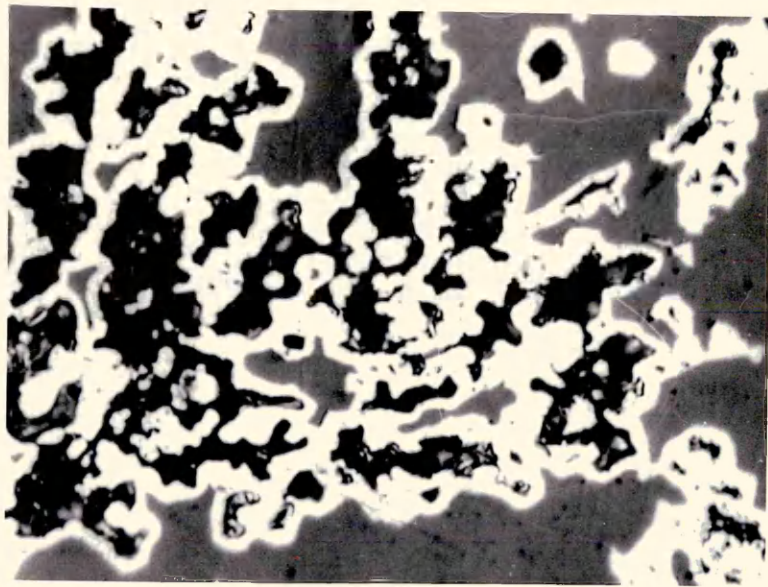
Fig. 71

Kiruna Magnetite Reduced H_2 $800^\circ C$
Series 1 (spring balance)

160x



69



70



71

Fig. 72

Kiruna Magnetite Reduced H_2 $800^\circ C$

Series 1 (spring balance)

160x

Fig. 73

Kiruna Magnetite
Reduced H_2 $800^\circ C$

Series 1
(spring balance)

63x

Fig. 74

Kiruna Magnetite Reduced H_2 $800^\circ C$

Series 1 (spring balance)

160x

Fig. 75

Kiruna Magnetite
Reduced H_2 $800^\circ C$

Series 1
(spring balance)

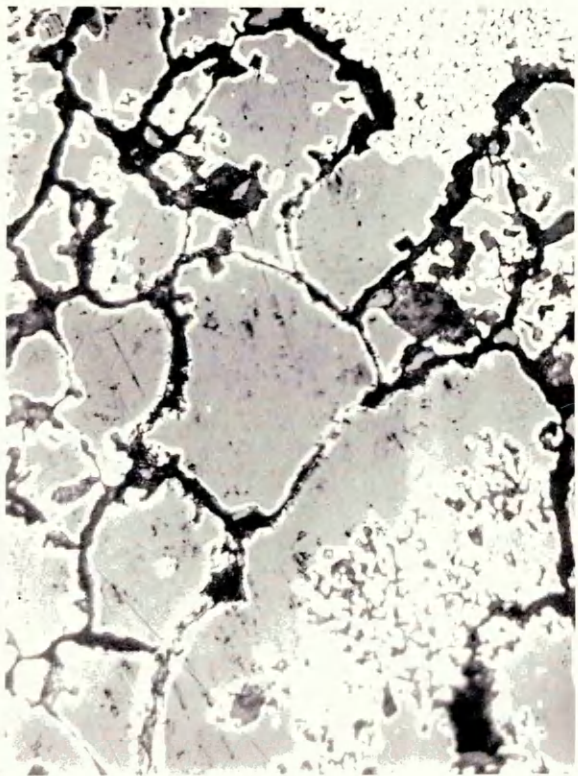
63x



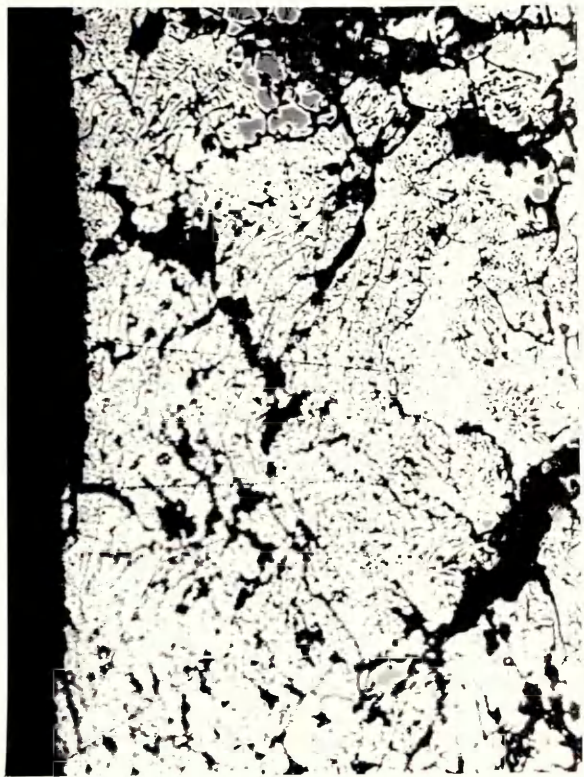
72



73



74



75

Fig. 76

Kiruna Magnetite Reduced H_2 $900^\circ C$

Series 1 (spring balance)

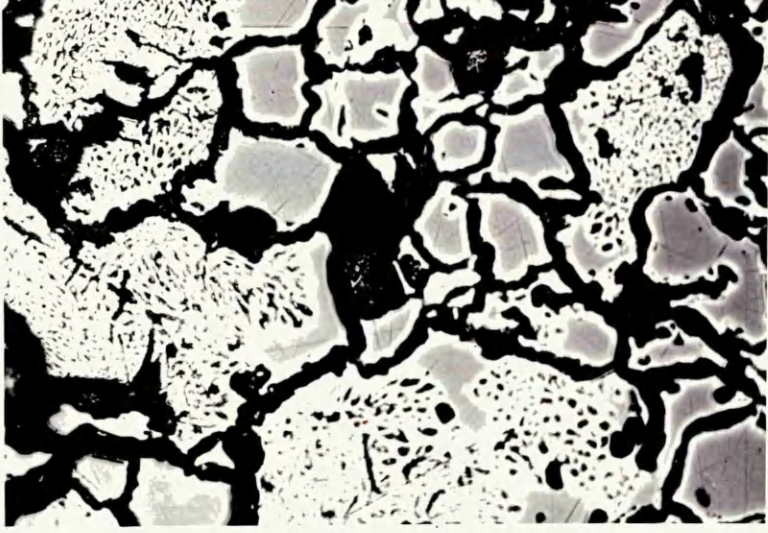
63x

Fig. 77

Kiruna Magnetite Reduced H_2 $900^\circ C$

Series 1 (spring balance)

250x



76

77

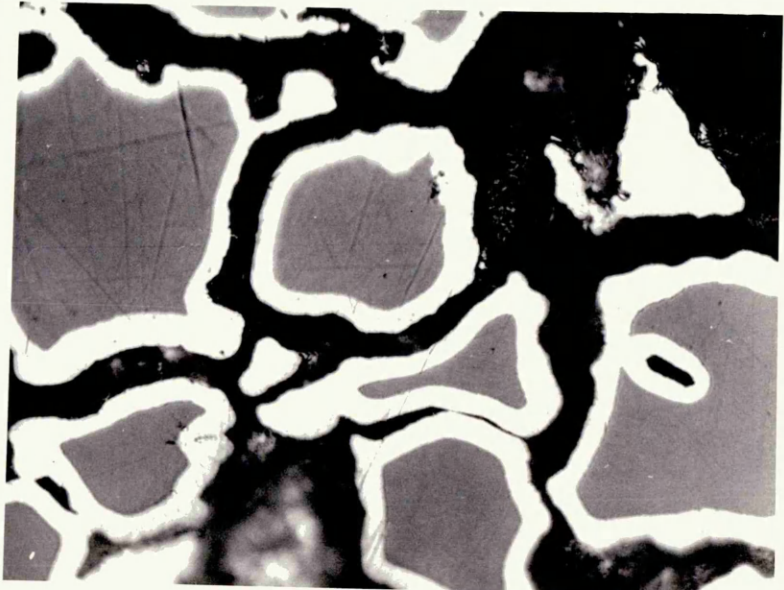


Fig. 78

Kiruna Magnetite Reduced H_2 $1000^\circ C$

Series 1 (spring balance)

16x

Fig. 79

Kiruna Magnetite Reduced H_2 $1000^\circ C$

Series 1 (spring balance)

63x

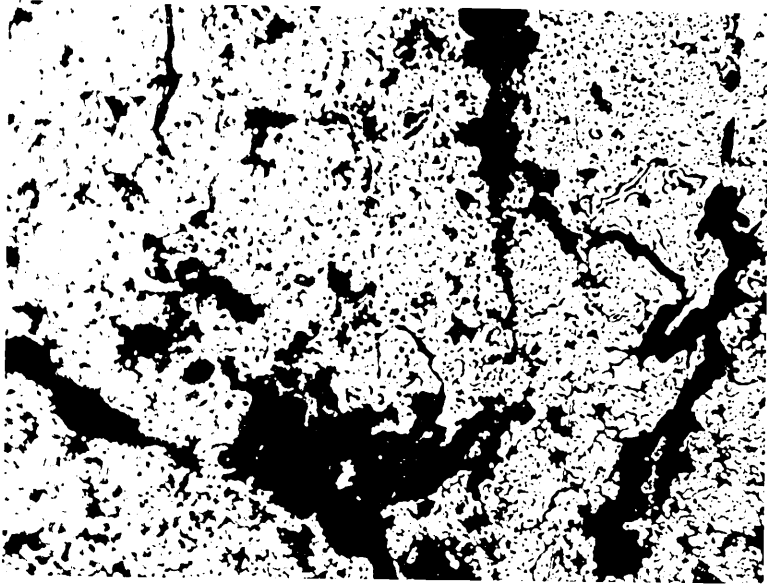
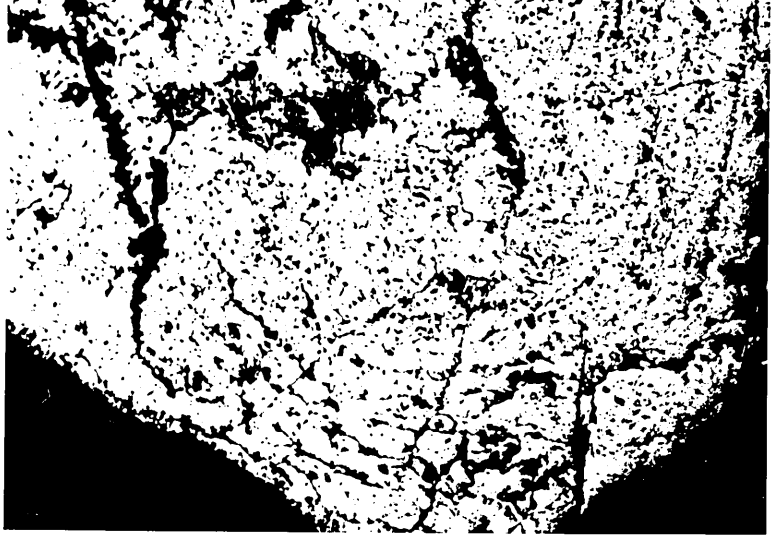
Fig. 80

Kiruna Magnetite Reduced H_2 $1000^\circ C$

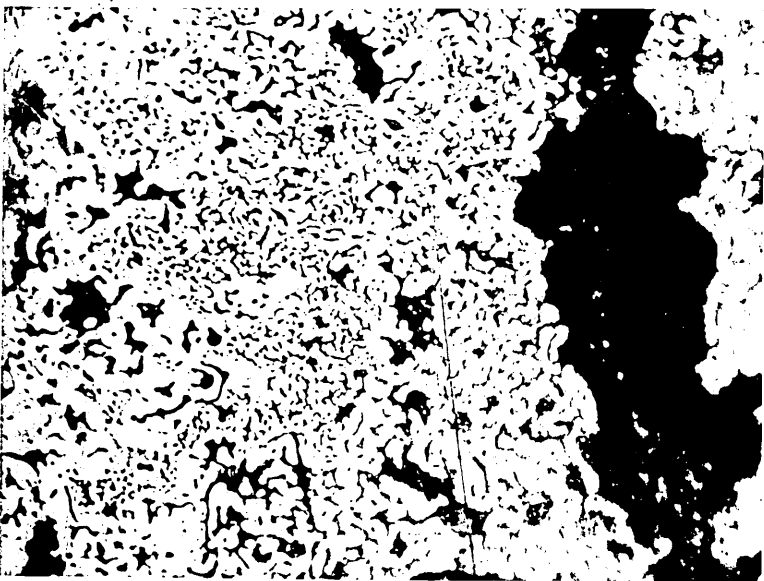
Series 1 (spring balance)

63x

78



79



80

Fig. 81

Kiruna Magnetite Reduced H_2 $500^\circ C$

Series 2 (spring balance)

16x

Fig. 82

Kiruna Magnetite Reduced H_2 $500^\circ C$

Series 2 (spring balance)

63x

Fig. 83

Kiruna Magnetite Reduced H_2 $500^\circ C$

Series 2 (spring balance)

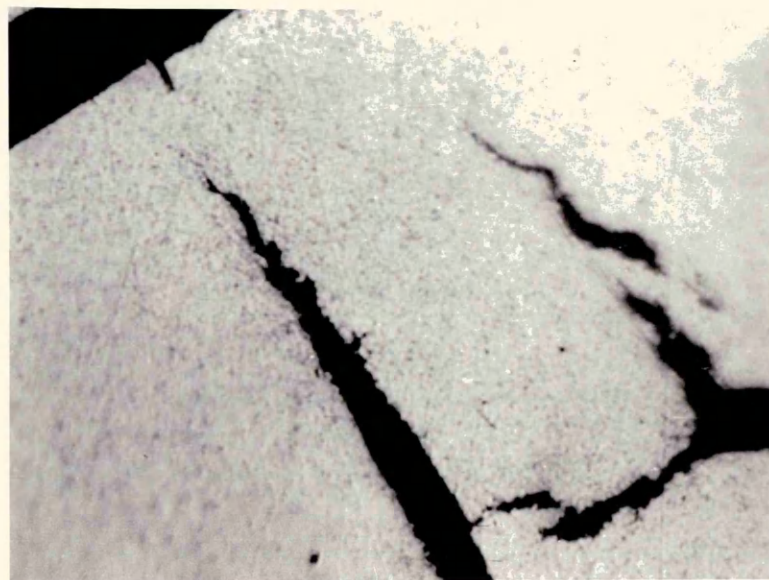
512x



81



82



83

Fig. 84

Kiruna Magnetite Reduced H_2 $550^{\circ}C$

Series 2 (spring balance)

63x

Fig. 85

Kiruna Magnetite
Reduced H_2 $550^{\circ}C$

Series 2
(spring balance)

320x

Fig. 86

Kiruna Magnetite Reduced H_2 $550^{\circ}C$

Series 2 (spring balance)

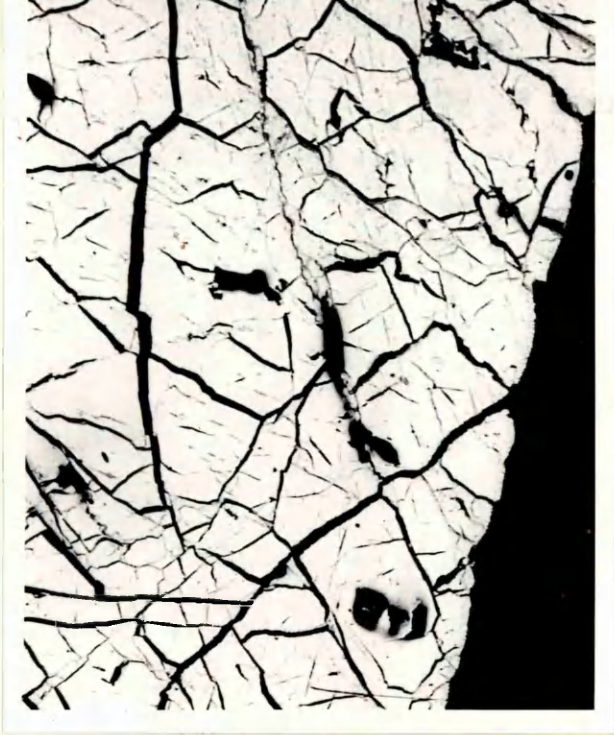
32x

Fig. 87

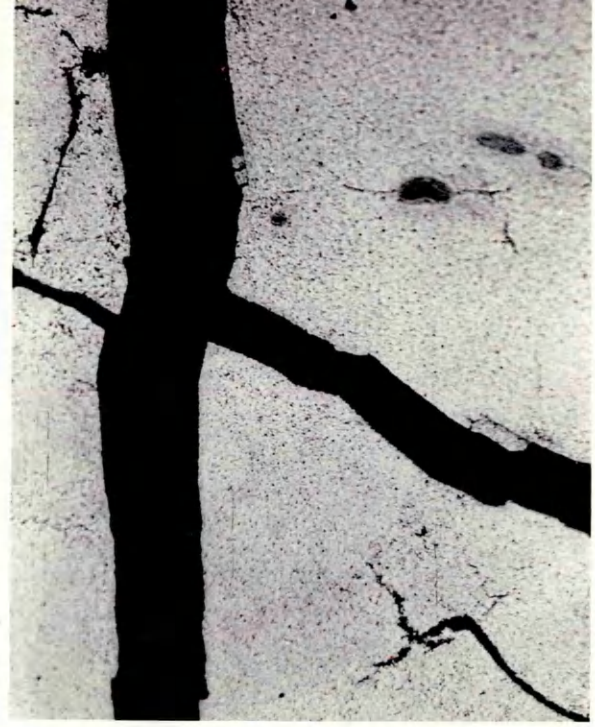
Kiruna Magnetite
Reduced H_2 $550^{\circ}C$

Series 2
(spring balance)

160x



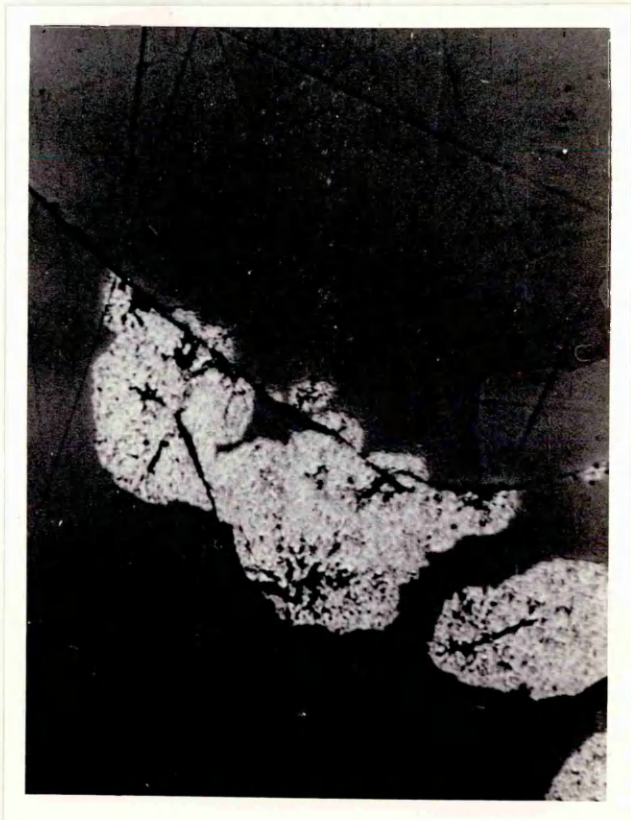
84



85



86



87

Fig. 88

Kiruna Magnetite Reduced H_2 $900^\circ C$

16x

Fig. 89

Kiruna Magnetite Reduced H_2 $900^\circ C$

32x

Fig. 90

Kiruna Magnetite Reduced H_2 $900^\circ C$

100x

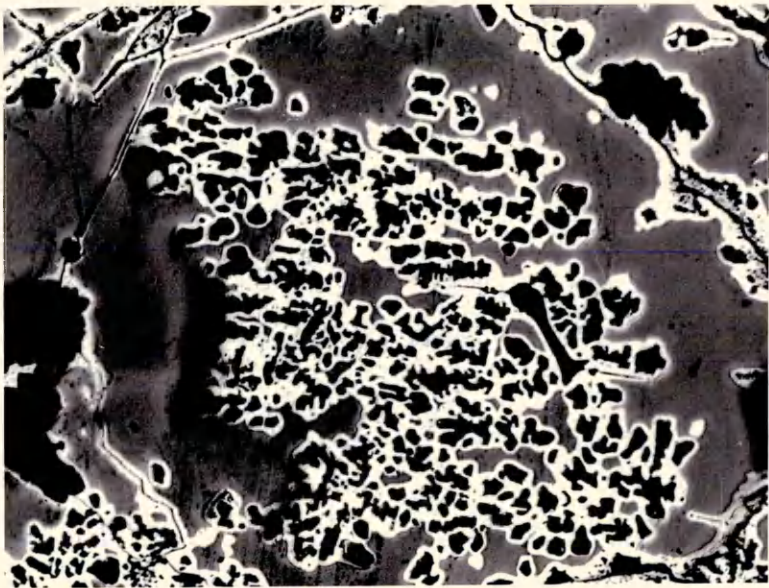
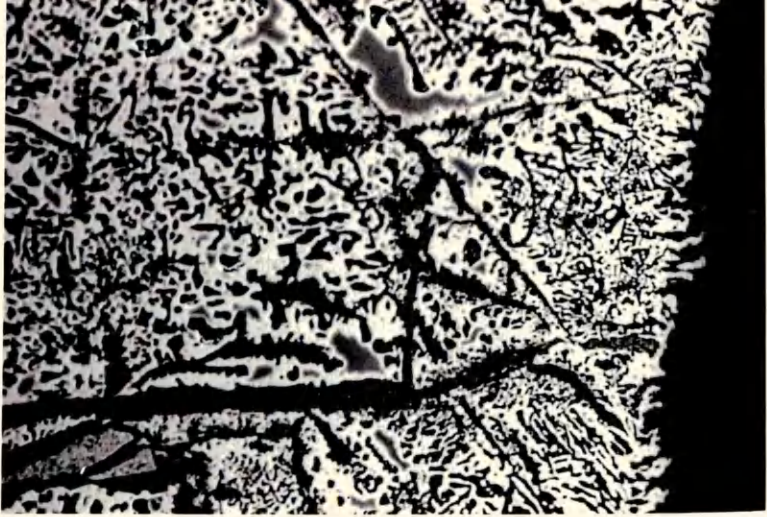


Fig. 91

Kiruna Magnetite Reduced H_2 $900^\circ C$

Series 2 (spring balance)

100x

Fig. 92

Kiruna Magnetite Reduced H_2 $900^\circ C$

Series 2 (spring balance)

250x



91



92

Fig. 93

Kiruna Magnetite Reduced H_2 $400^\circ C$
Series 2 (stanton balance)

32x

Fig. 94

Kiruna Magnetite Reduced H_2 $400^\circ C$
Series 2 (stanton balance)

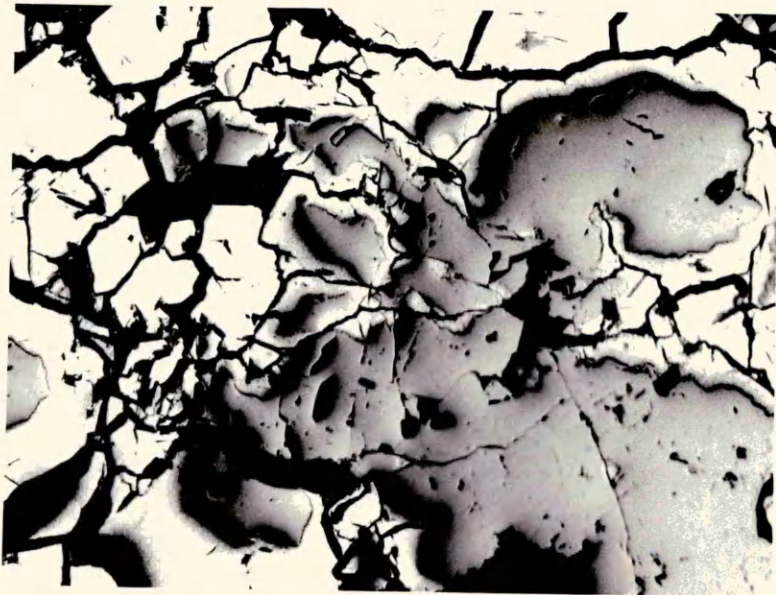
32x

Fig. 95

Kiruna Magnetite Reduced H_2 $400^\circ C$
Series 2 (stanton balance)

160x

93



94



95

Fig. 96

Kiruna Magnetite Reduced H_2 $560^\circ C$
Series 2 (stanton balance)

16x

Fig. 97

Kiruna Magnetite Reduced H_2 $560^\circ C$
Series 2 (stanton balance)

63x

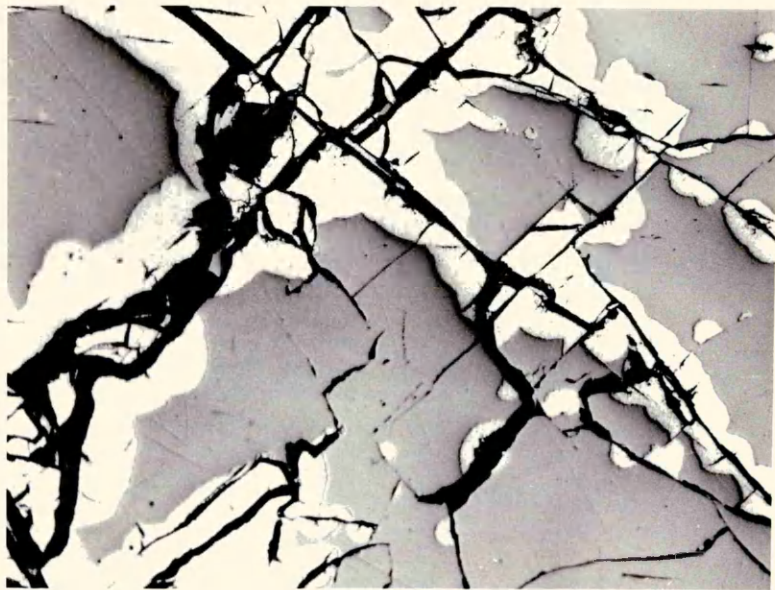
Fig. 98

Kiruna Magnetite Reduced H_2 $560^\circ C$
Series 2 (stanton balance)

320x



96



97



98

Fig. 99

Kiruna Magnetite Reduced H_2 $650^\circ C$
Series 2 (stanton balance)

16x

Fig. 100

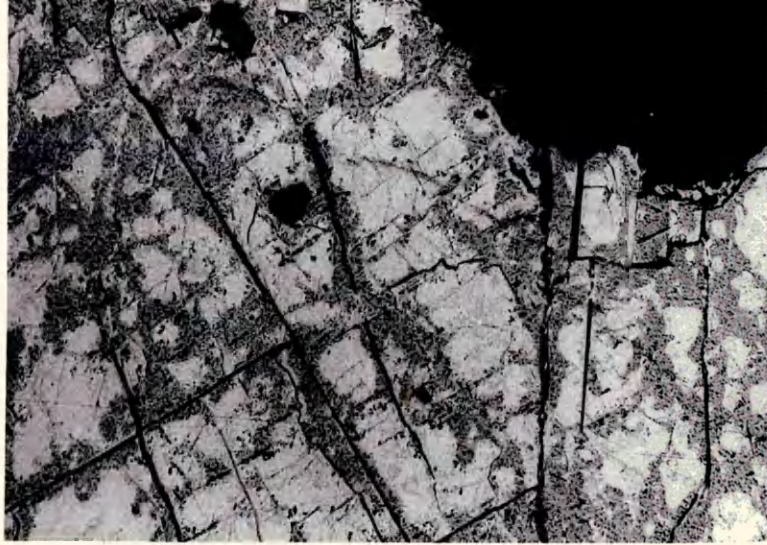
Kiruna Magnetite Reduced H_2 $650^\circ C$
Series 2 (stanton balance)

160x

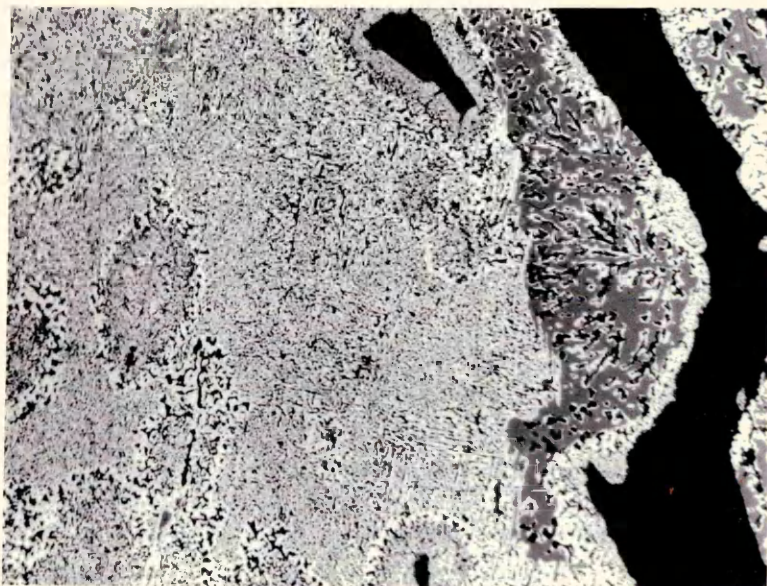
Fig. 101

Kiruna Magnetite Reduced H_2 $650^\circ C$
Series 2 (stanton balance)

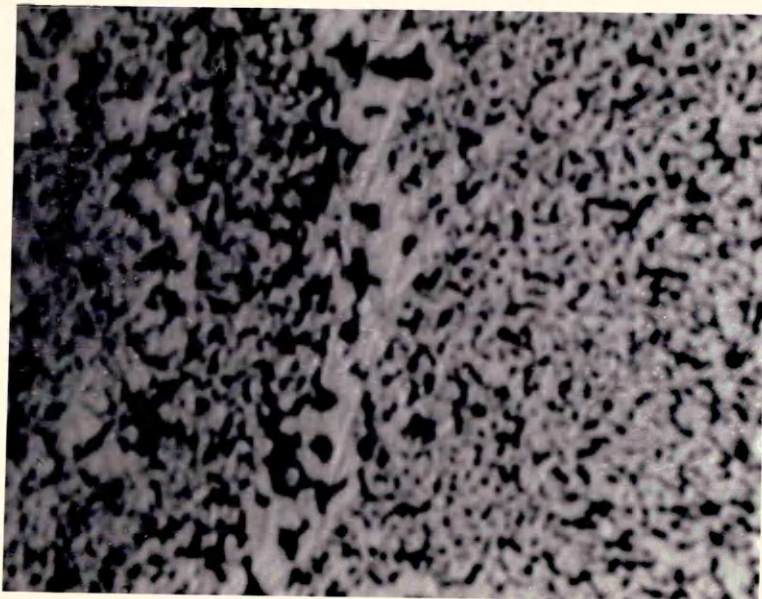
1000x



99



100



101

Fig. 102

Kiruna Magnetite Reduced H_2 $650^{\circ}C$
Series 2 (stanton balance)

1000x

Fig. 103

Kiruna Magnetite Reduced H_2 $650^{\circ}C$
Series 2 (stanton balance)

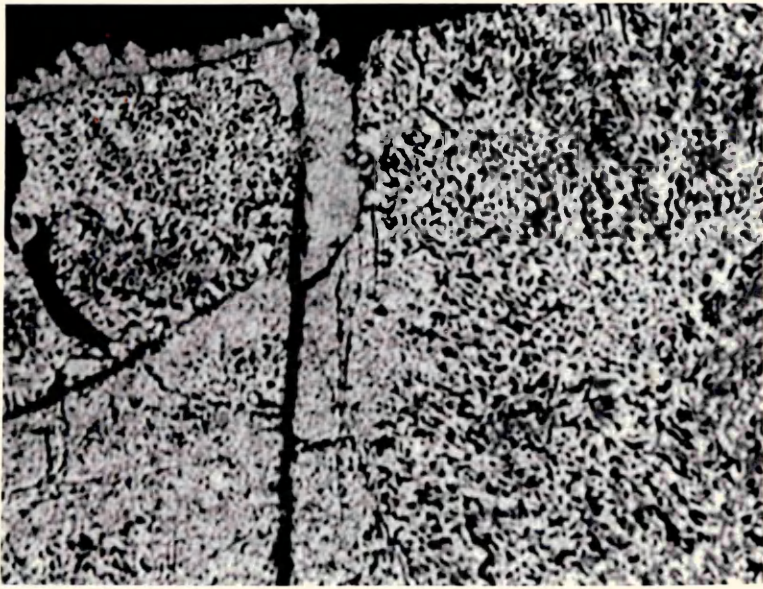
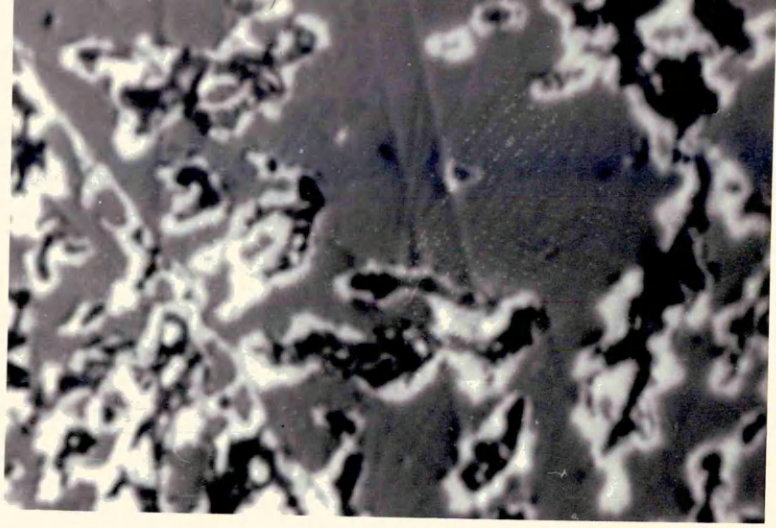
200x

Fig. 104

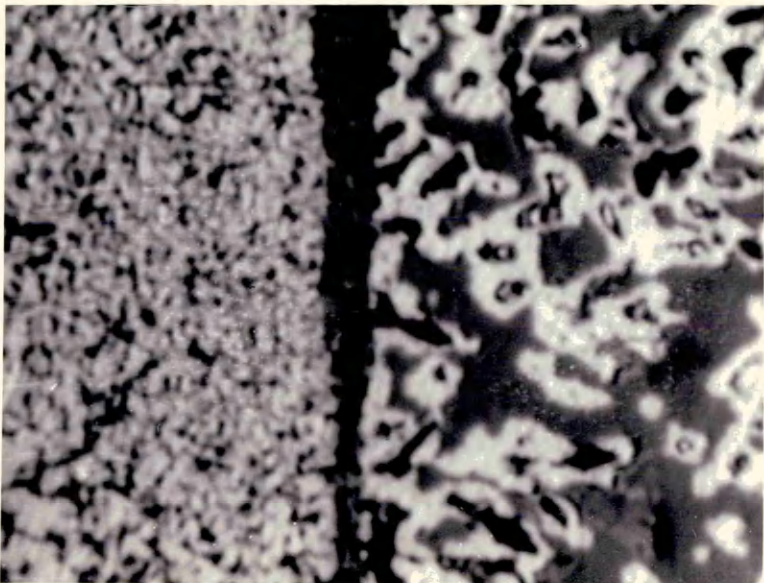
Kiruna Magnetite Reduced H_2 $650^{\circ}C$
Series 2 (stanton balance)

1000x

102



103



104

Fig. 105

Kiruna Magnetite Reduced H_2 $650^\circ C$

Series 2 (stanton balance)

16x

Fig. 106

Kiruna Magnetite Reduced H_2 $650^\circ C$

Series 2 (stanton balance)

320x

Fig. 107

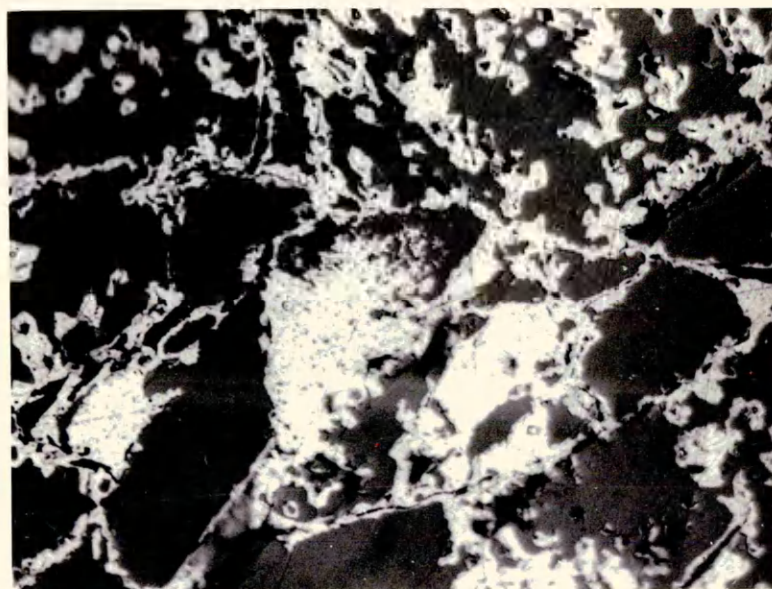
Kiruna Magnetite Reduced H_2 $650^\circ C$

Series 2 (stanton balance)

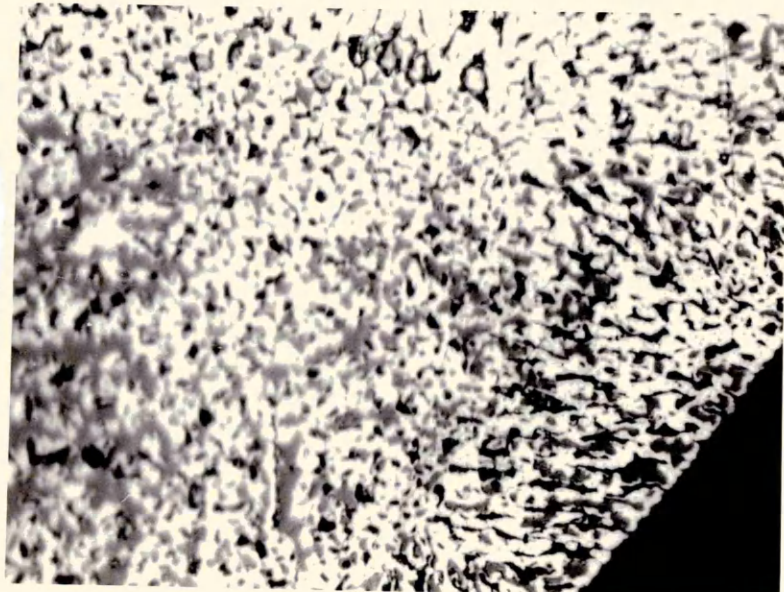
320x



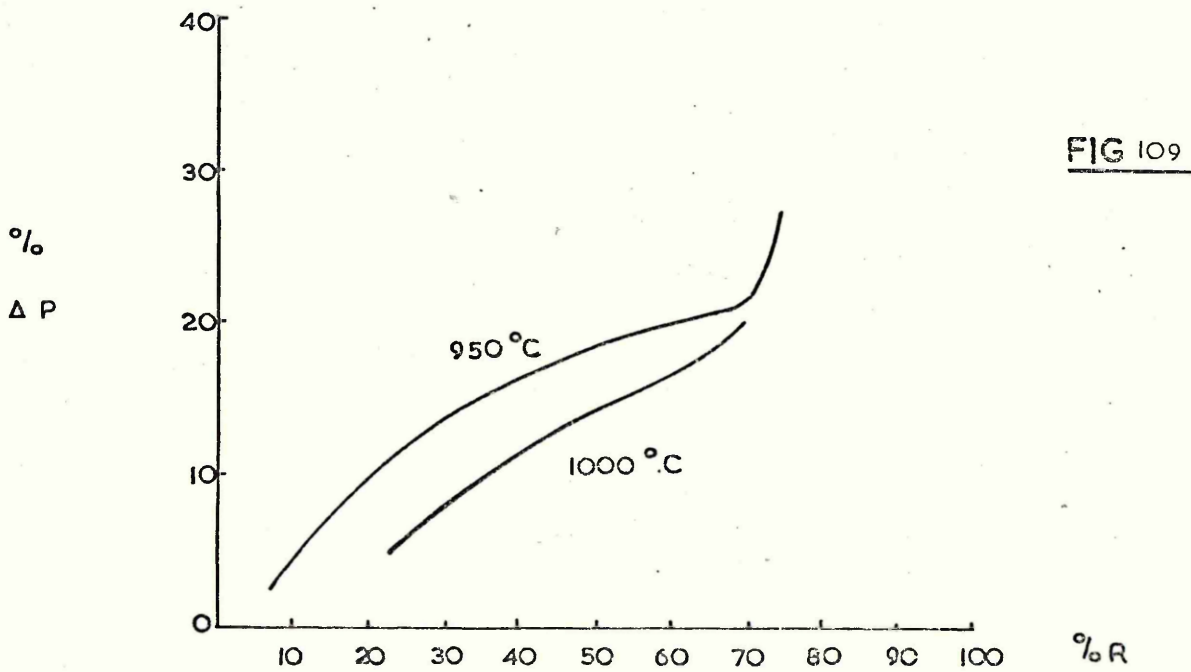
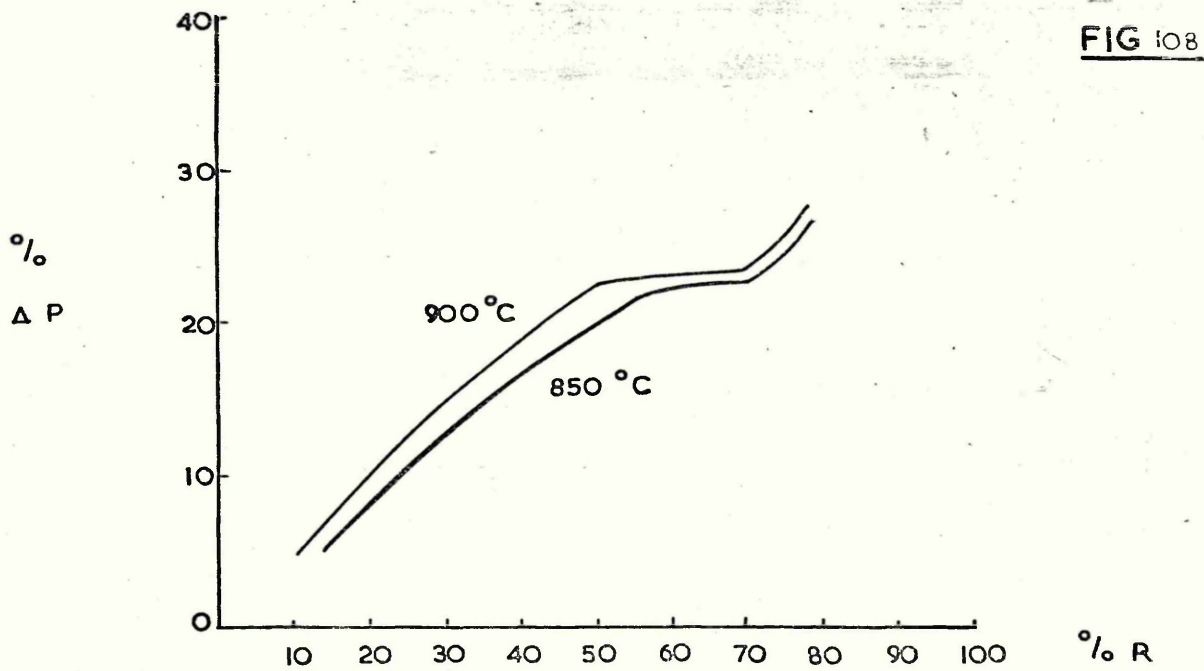
105



106



107



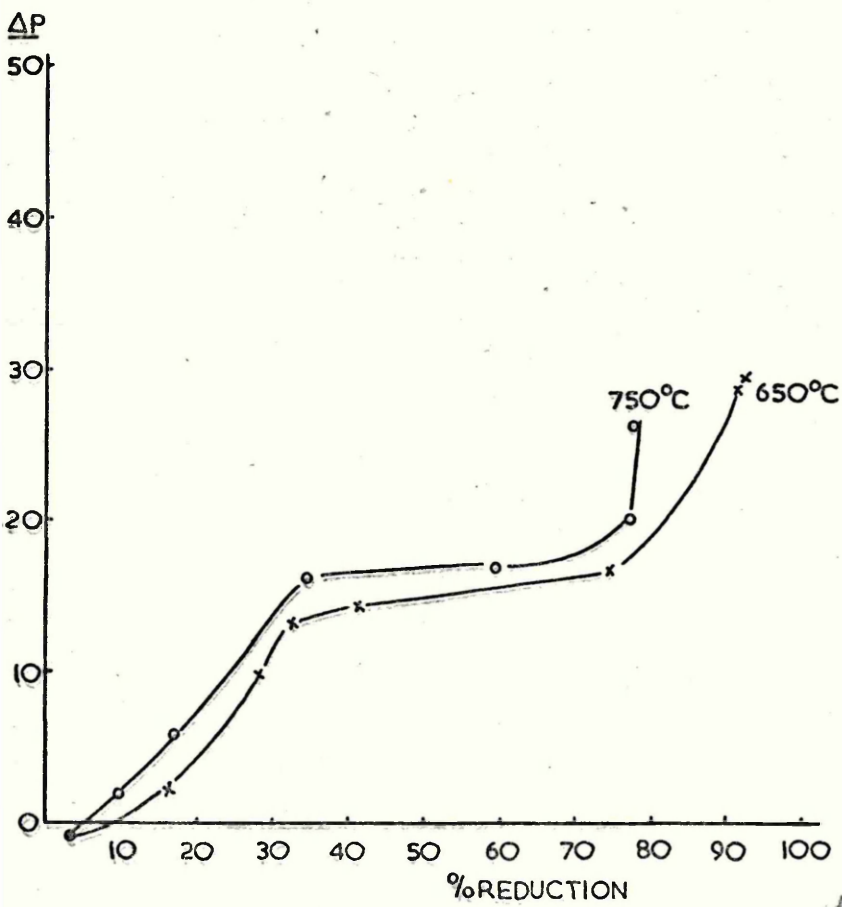


FIG. 110

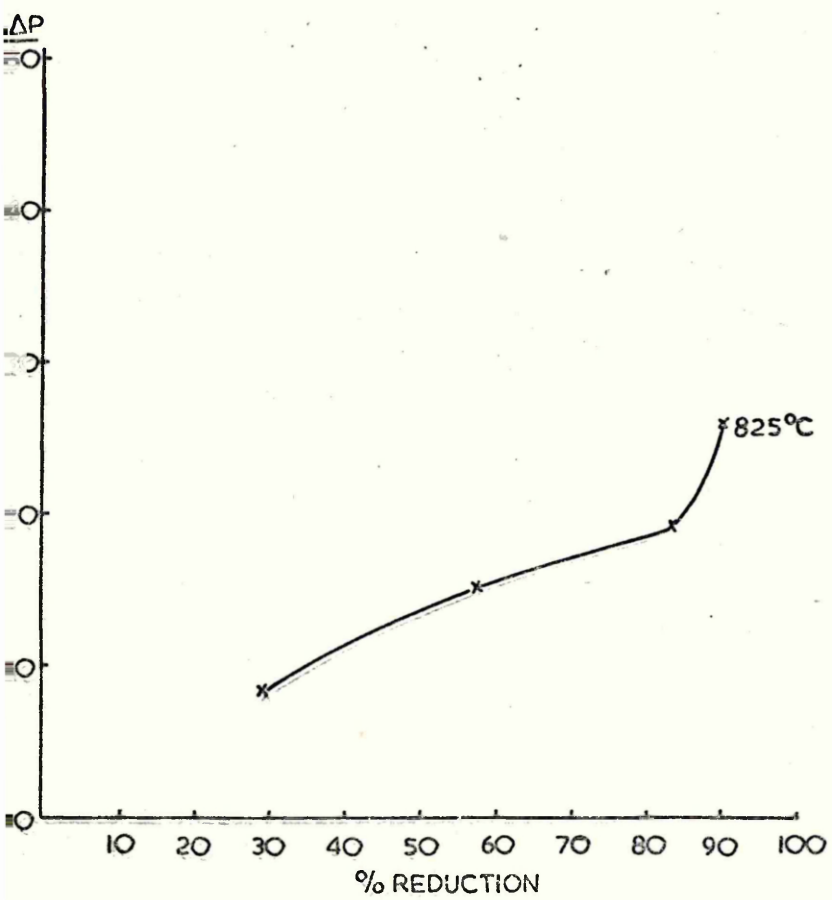
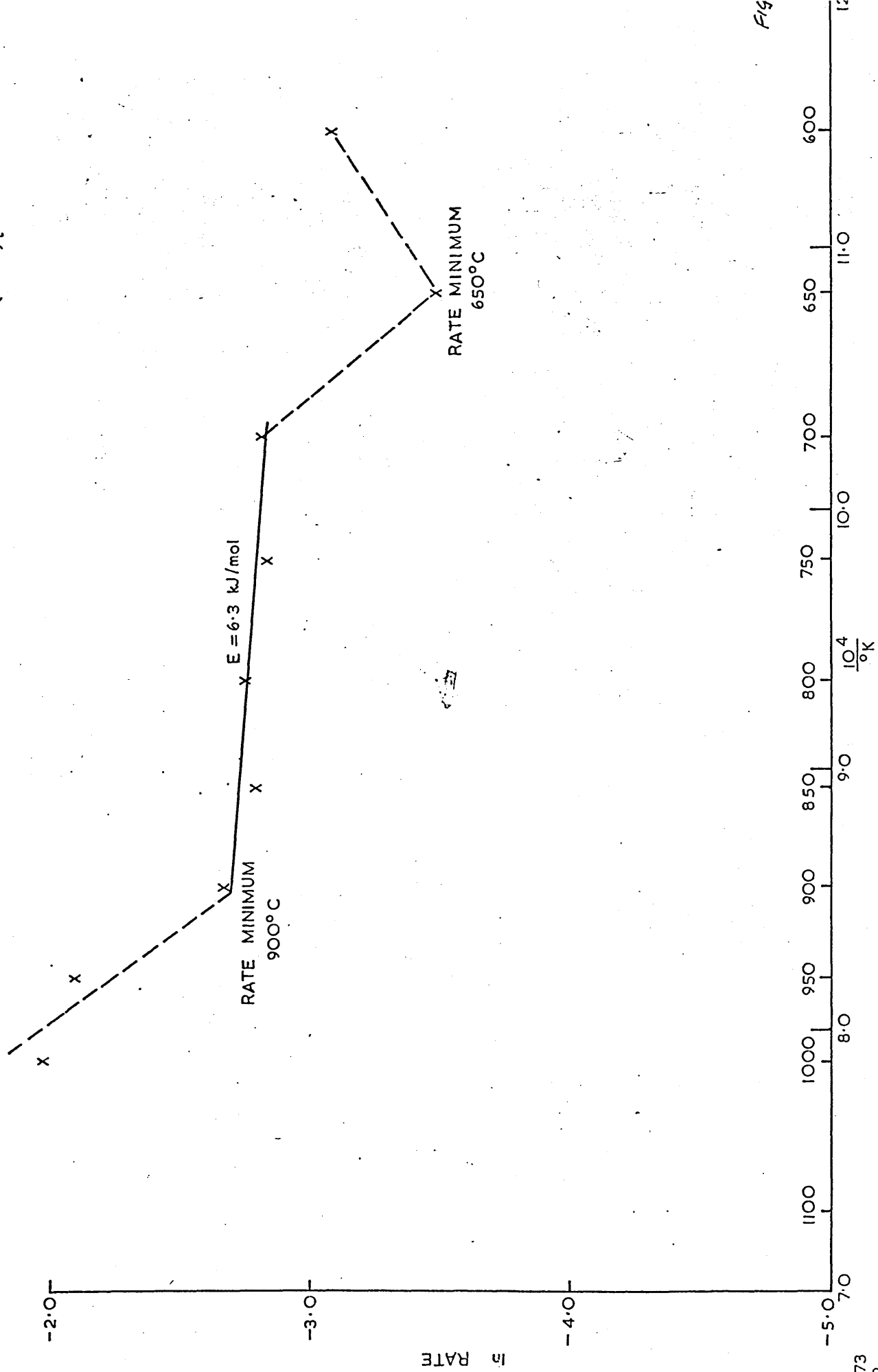


FIG. 111

SERIES I

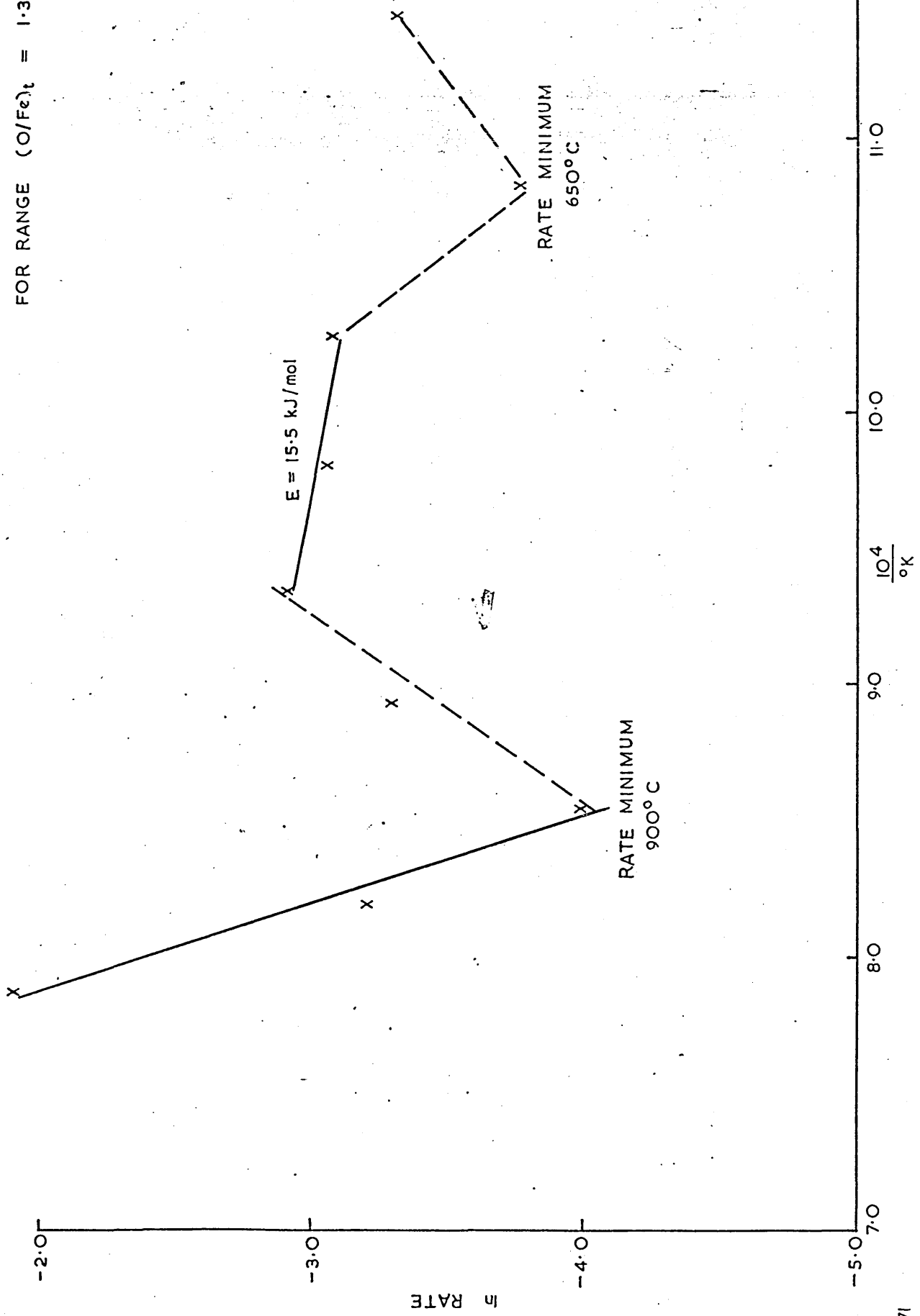
FOR RANGE $(O/Fe)_t = 1.3 - 0.9$



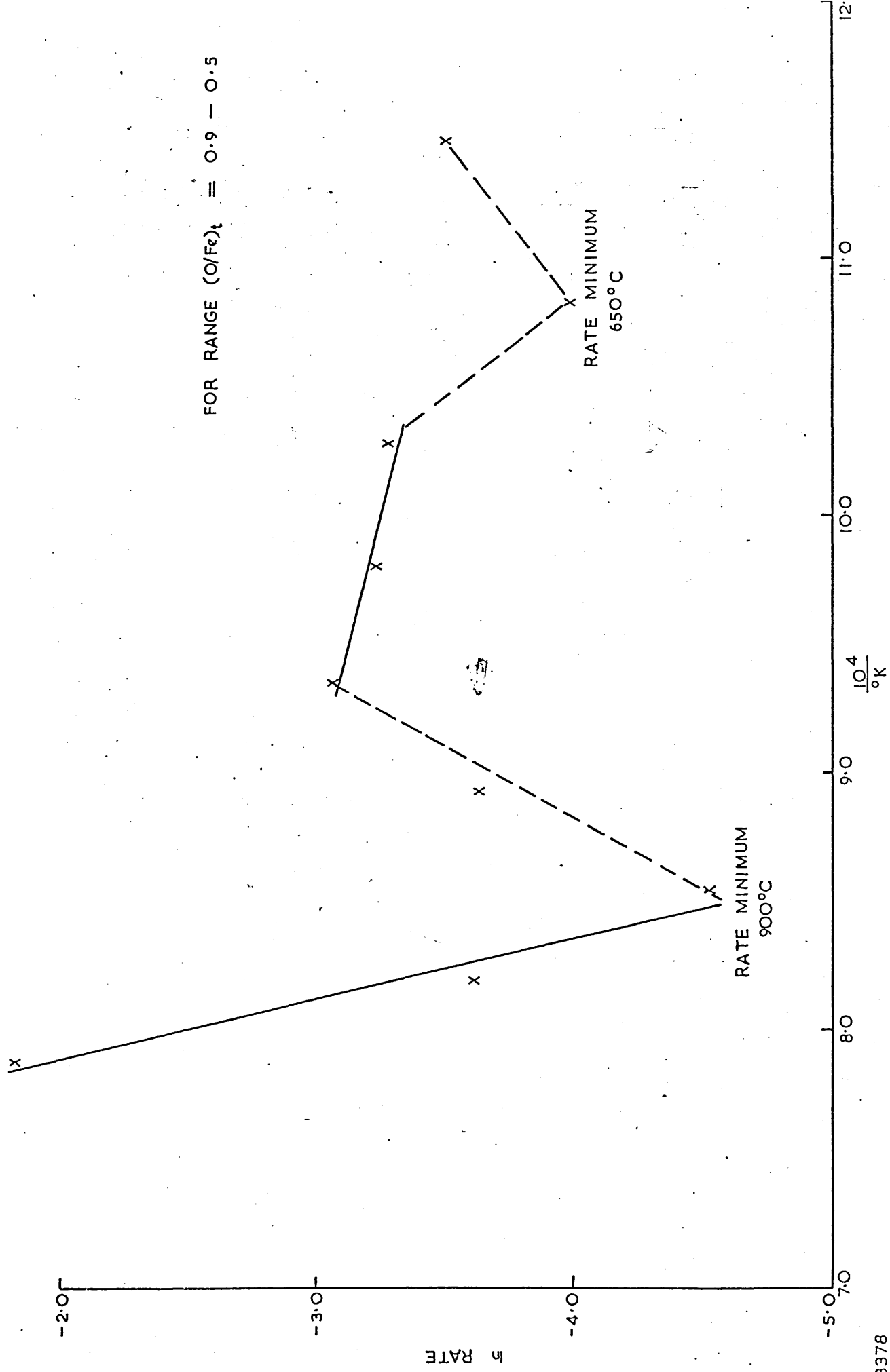
Fig

SERIES I

FOR RANGE (O/Fe)_t = 1.3 — 0.5

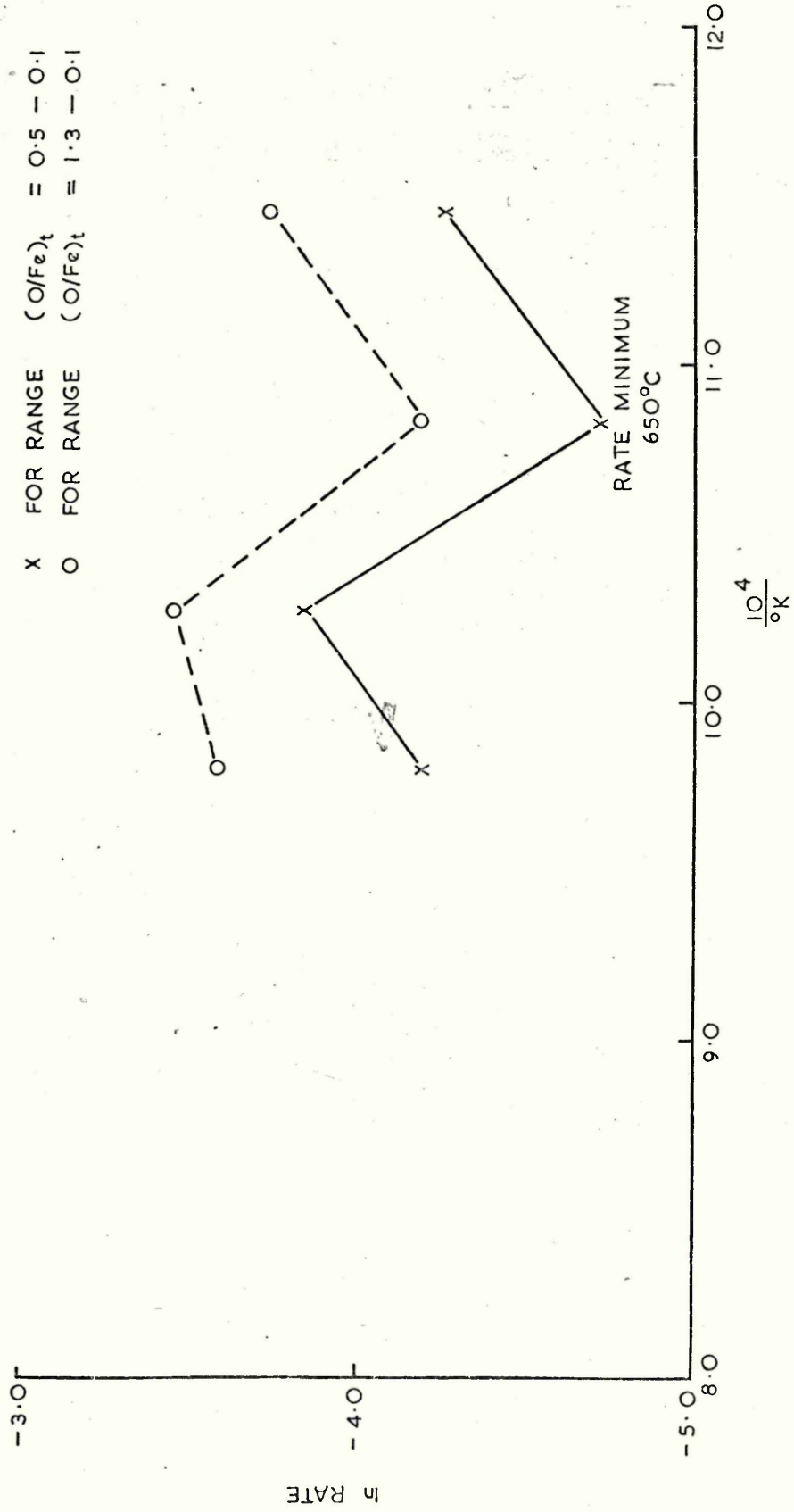


FOR RANGE (O/Fe)_t = 0.9 - 0.5

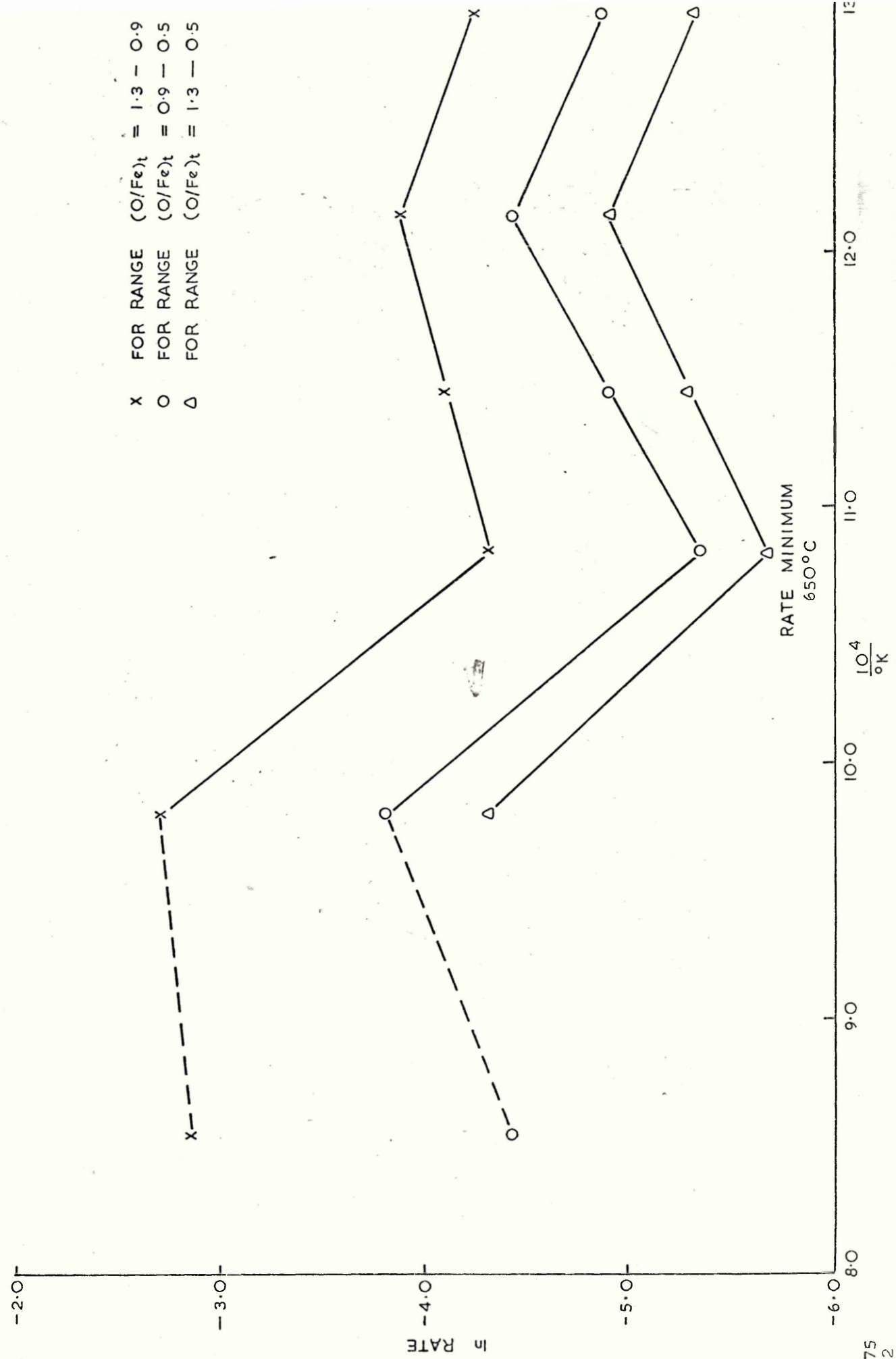


SERIES I

X FOR RANGE (O/Fe)_t = 0.5 - 0.1
 O FOR RANGE (O/Fe)_t = 1.3 - 0.1



SERIES 2 (SPRING)



SERIES 2 (STANTON)

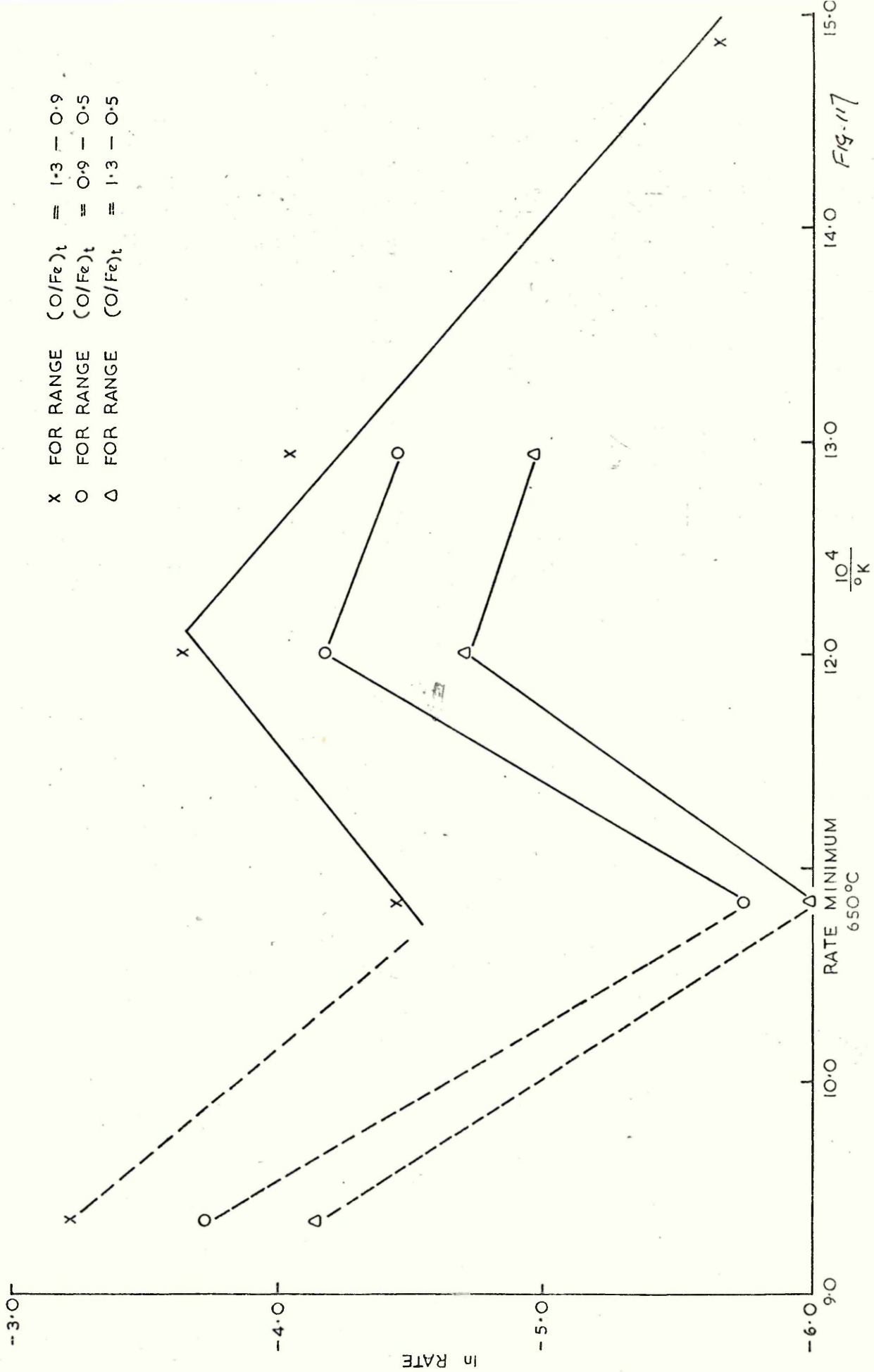


Fig. 117

SERIES I (SPRING)

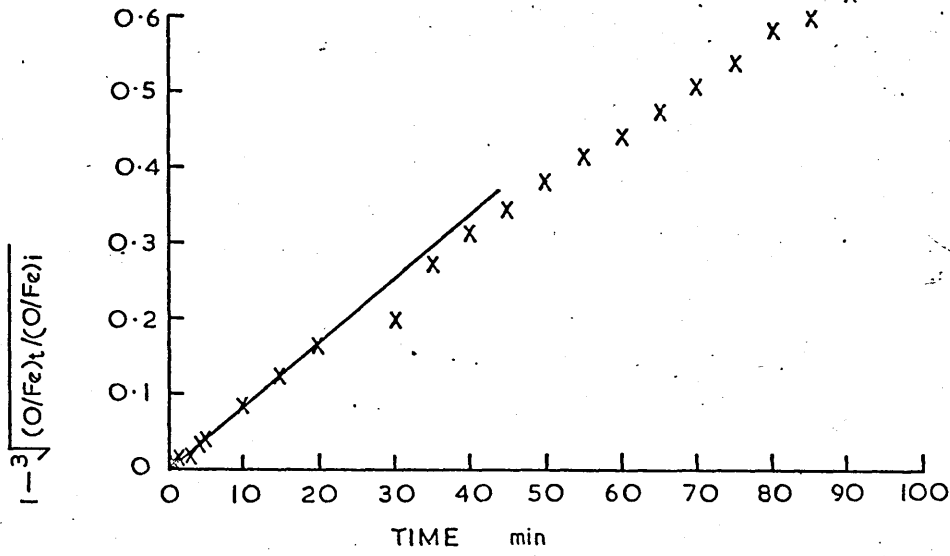


FIG. 118

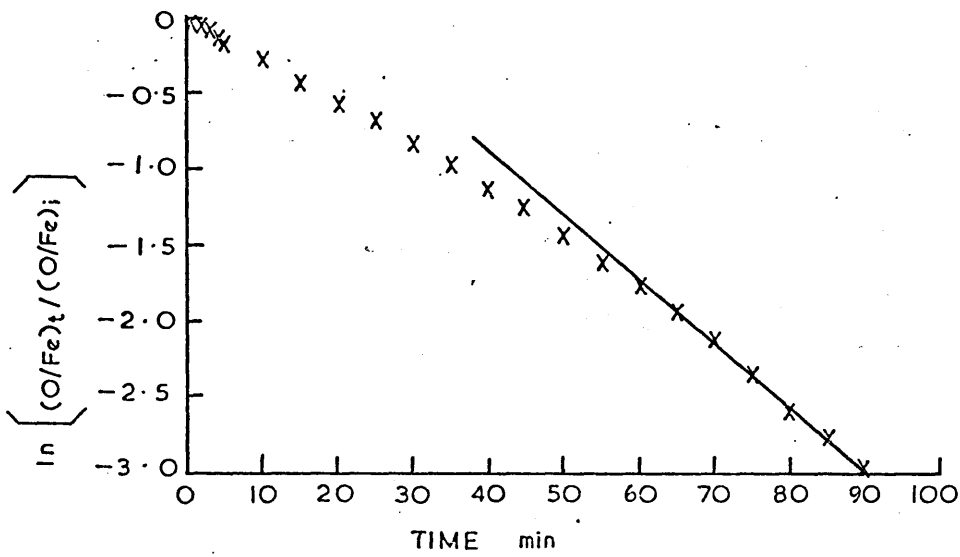


FIG. 119

SERIES I (SPRING)

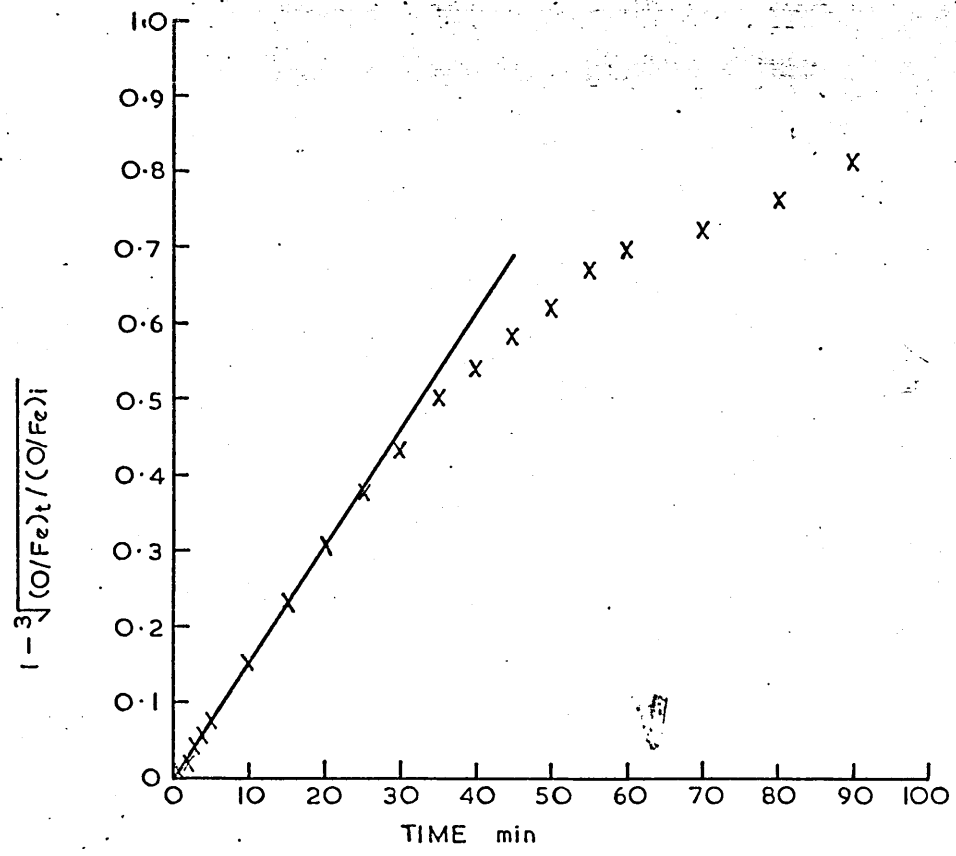


FIG. 120a

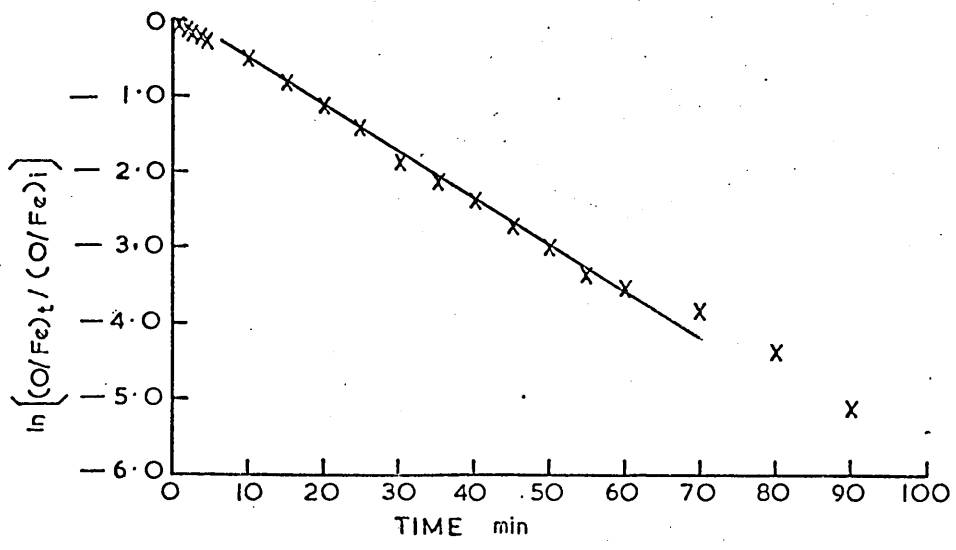


FIG. 120b

SERIES I (SPRING)

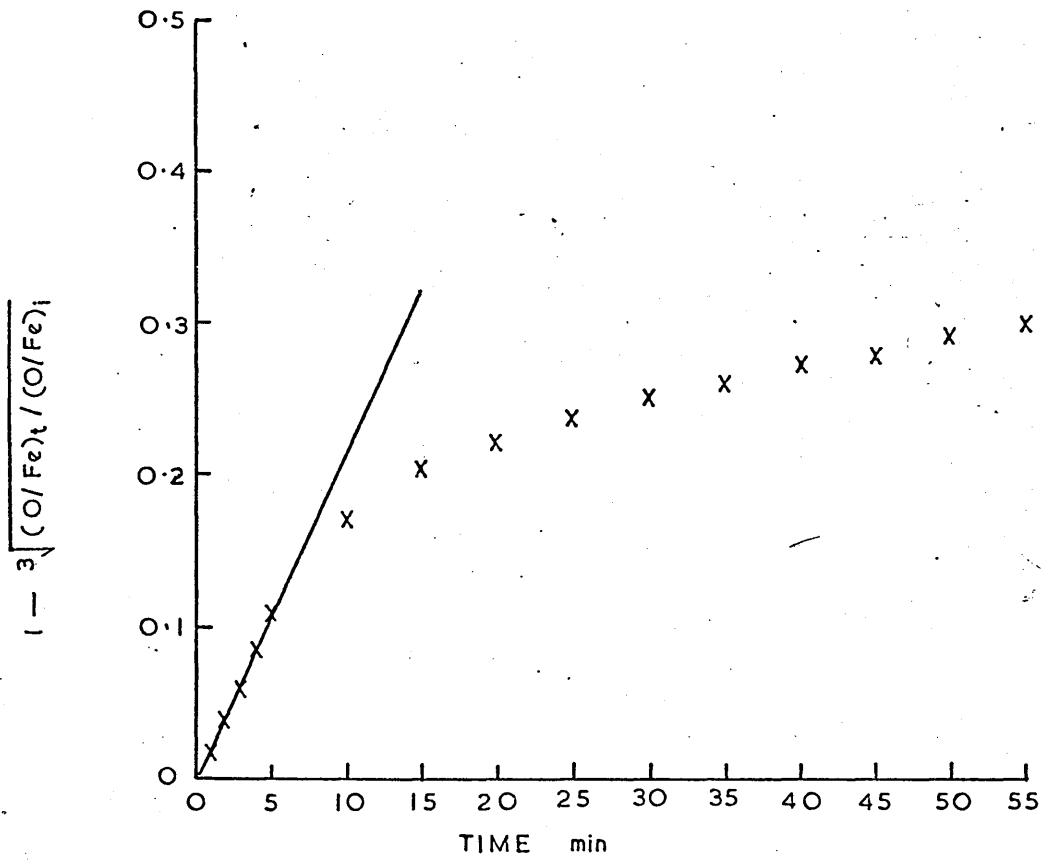


FIG. 121 a

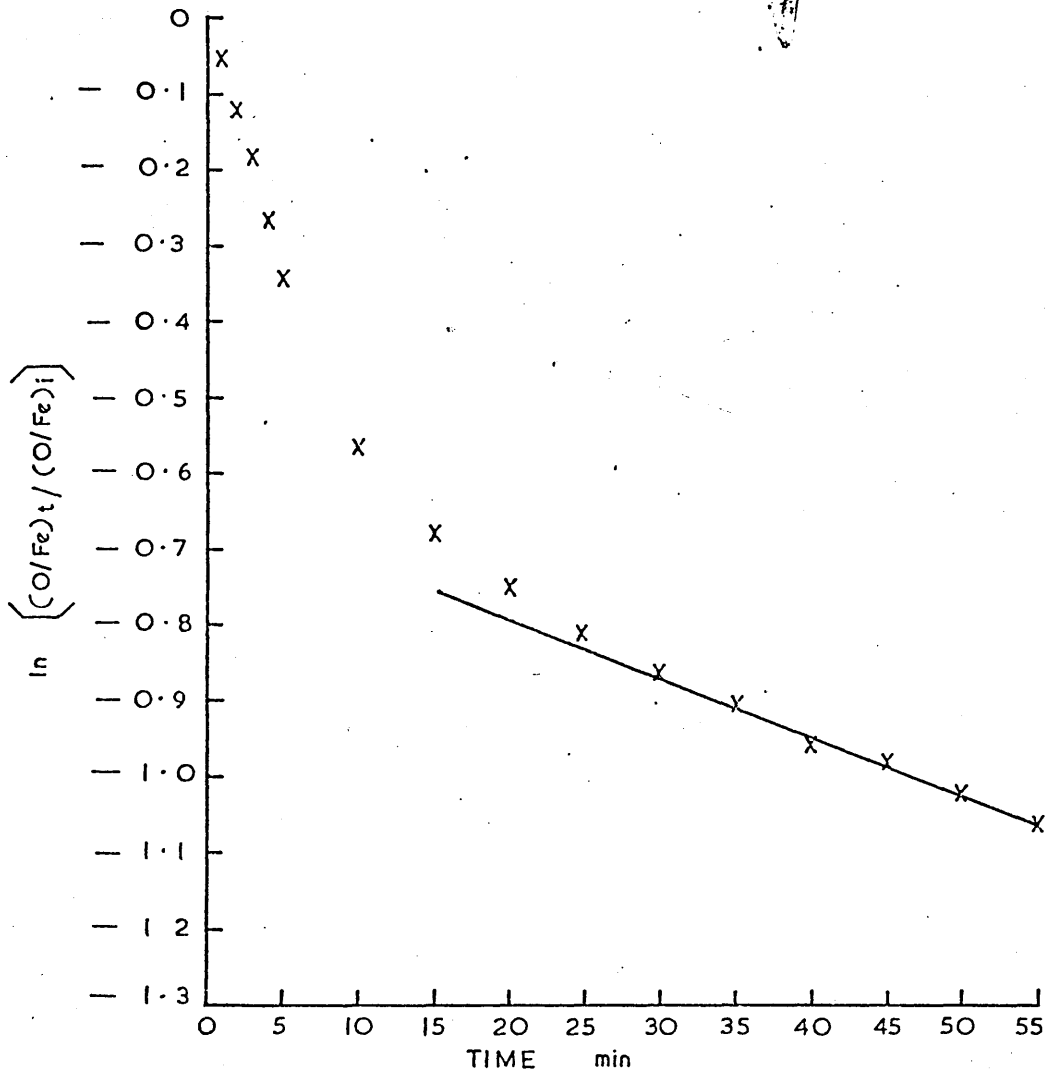


FIG. 121 b

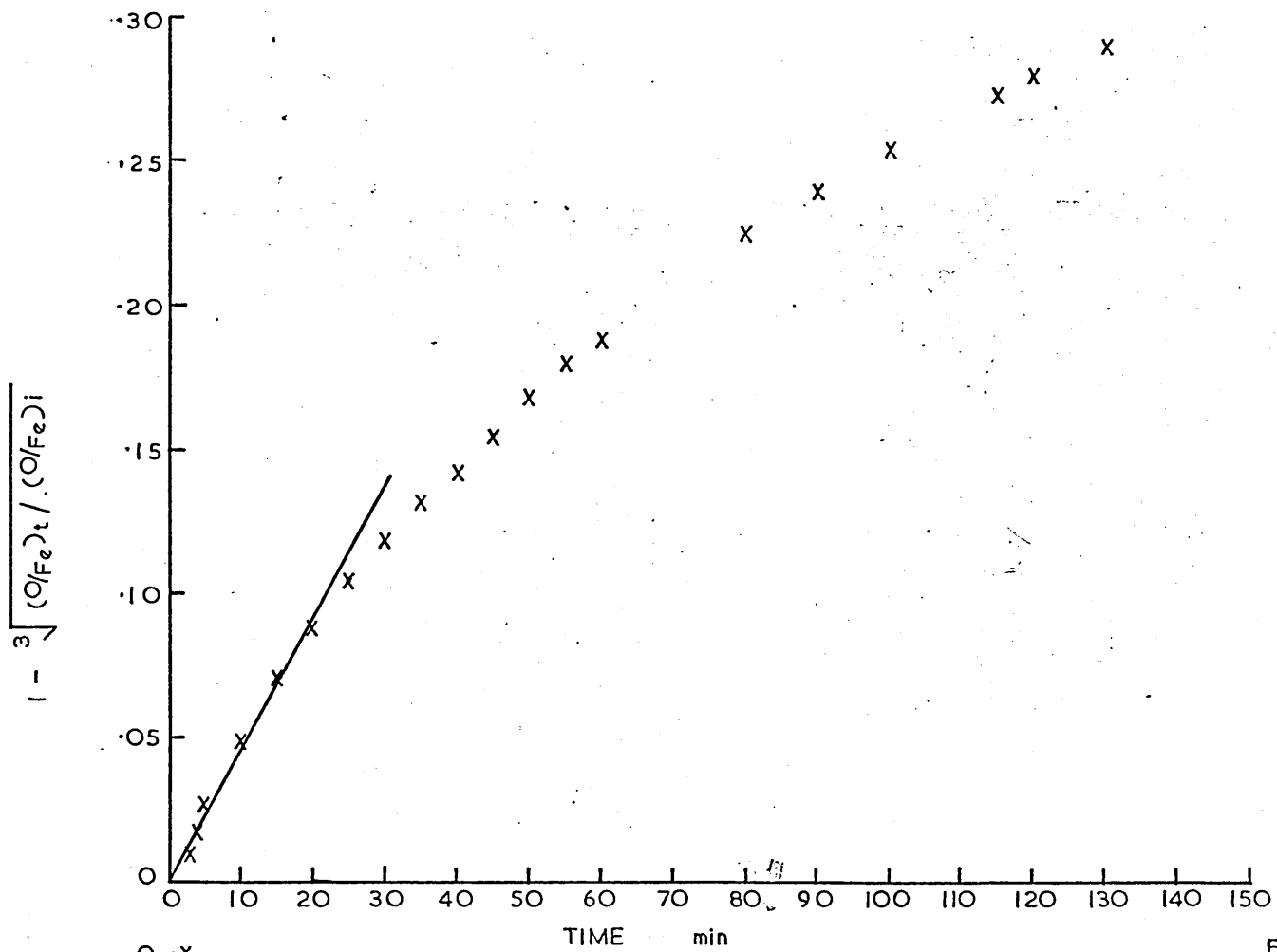


FIG. 122a

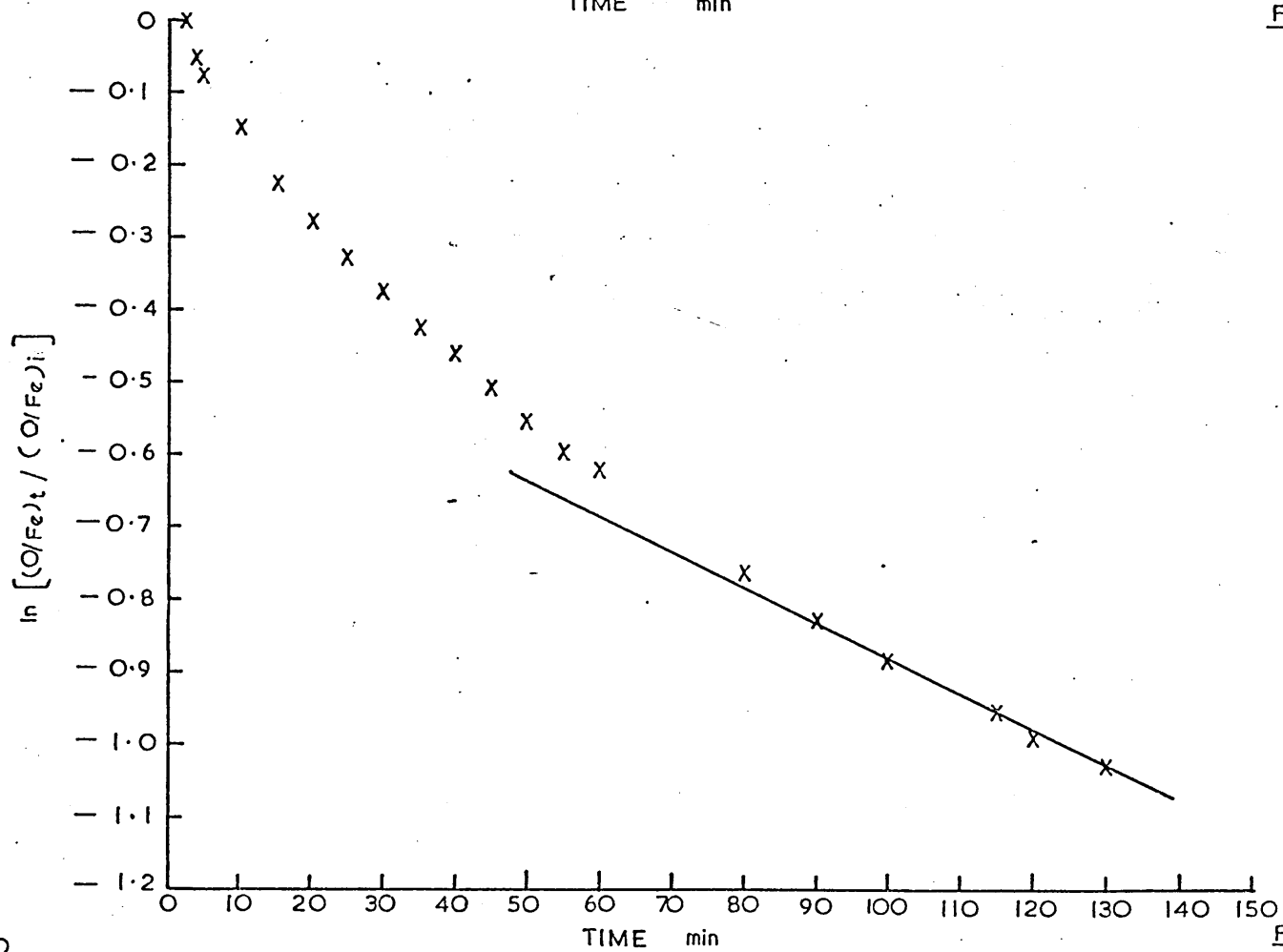


FIG. 122b

FIG. 122a & 122b

SERIES 2 (SPRING)

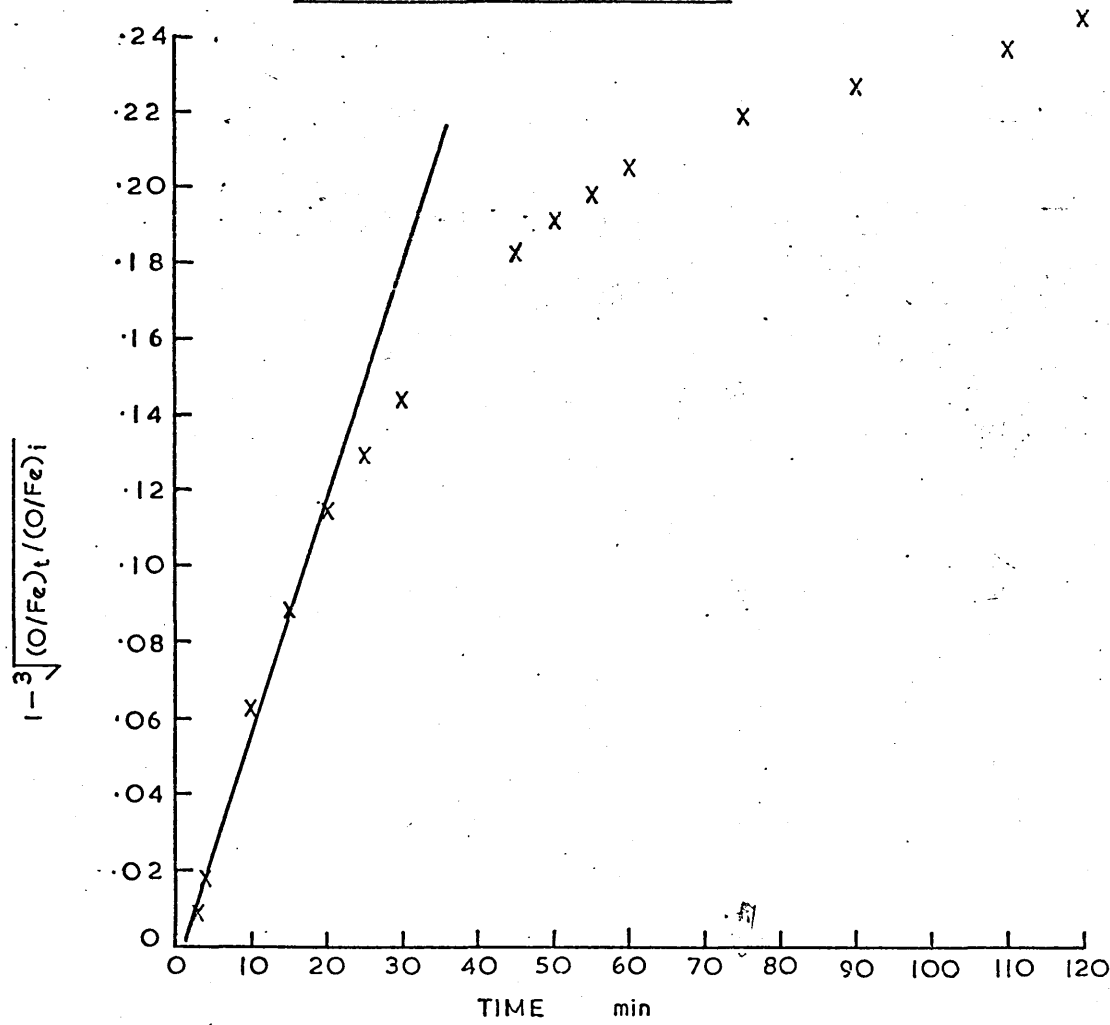


FIG. 123a

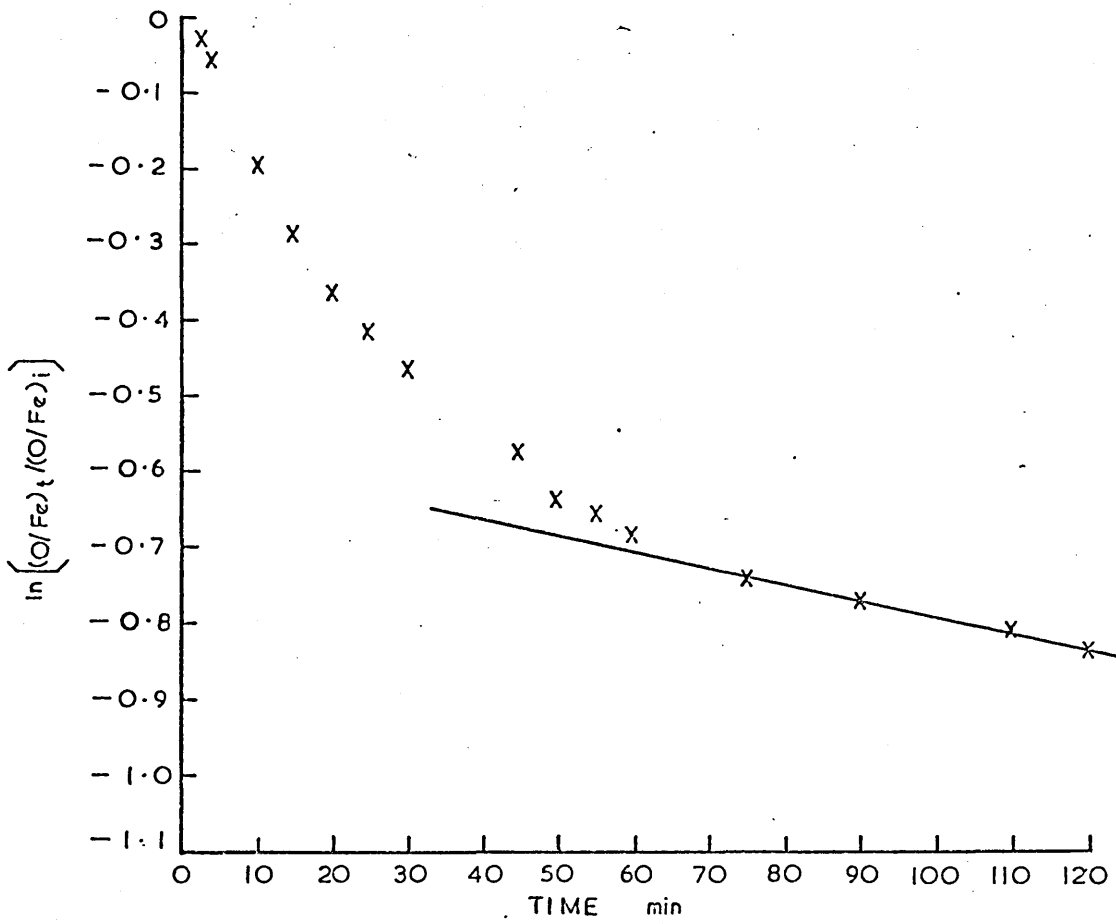


FIG. 123 b

FIG. 123a & 123b

SERIES 2 (SPRING)

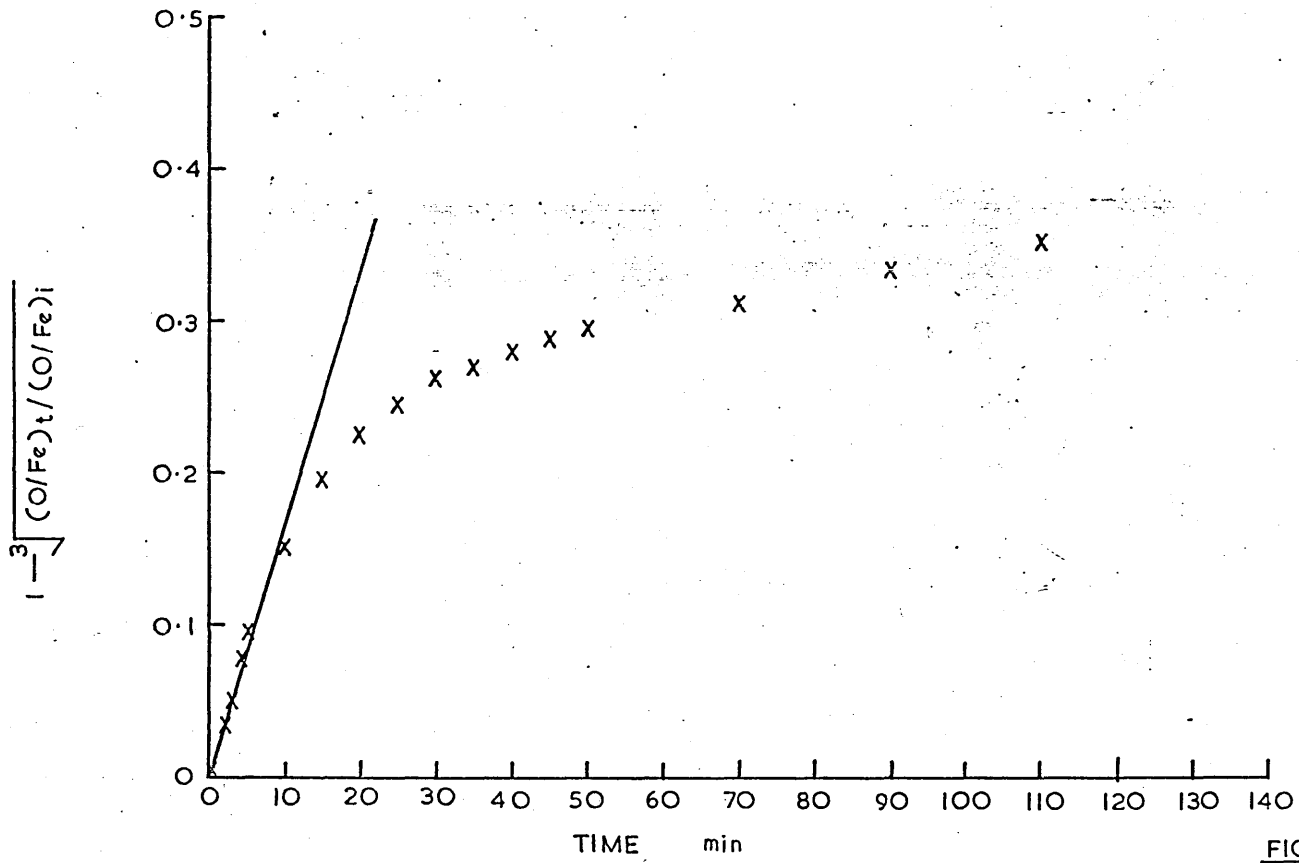


FIG. 124 a

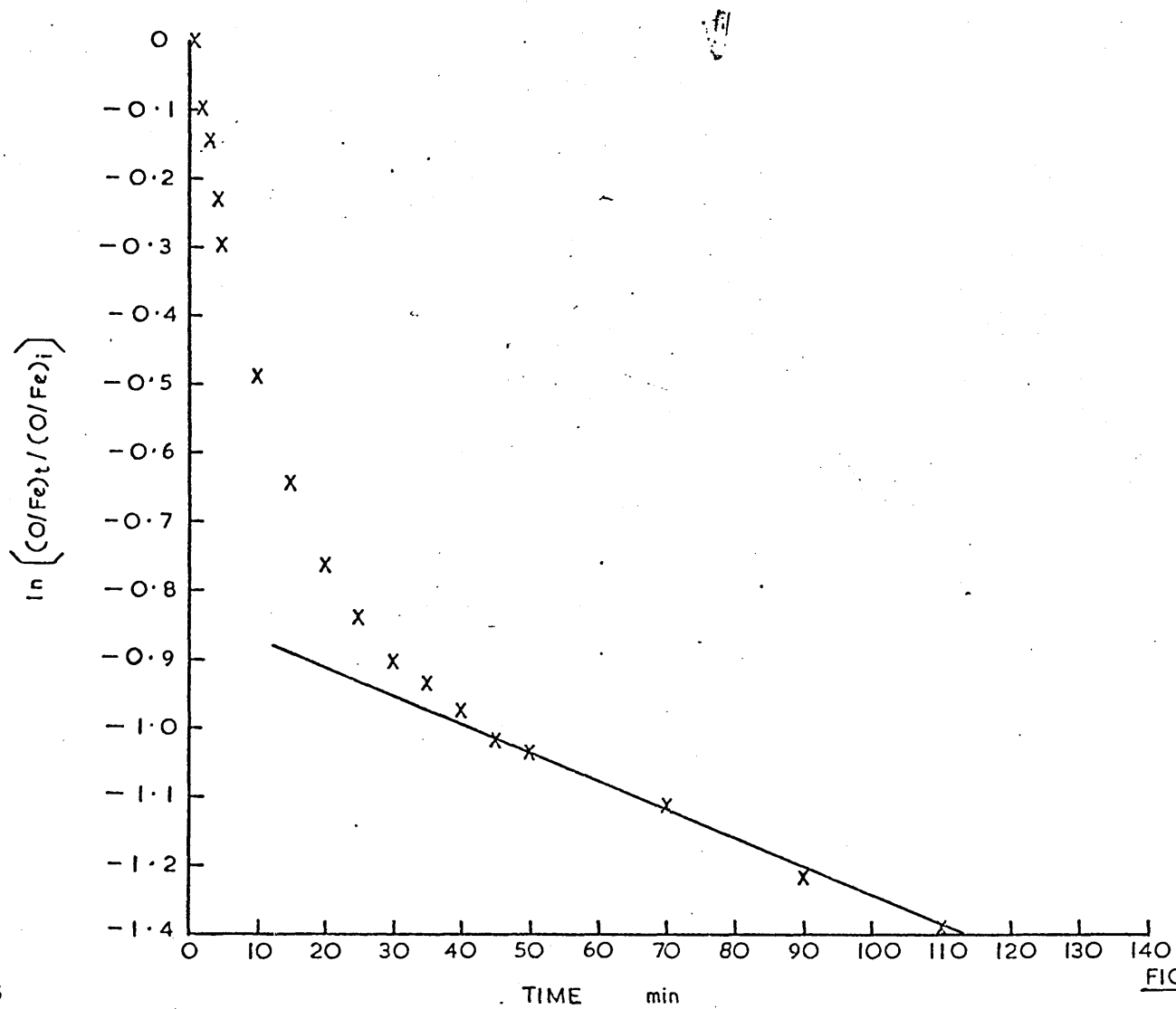


FIG. 124 b

FIG. 124 a & 124 b

SERIES 2 (STANTON)

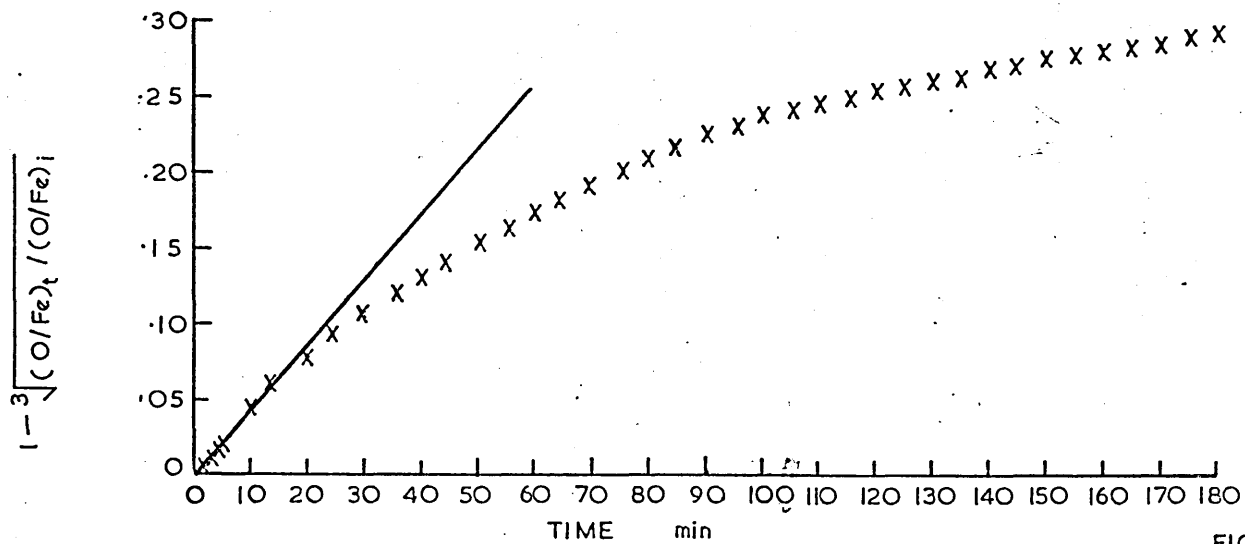


FIG. 125a

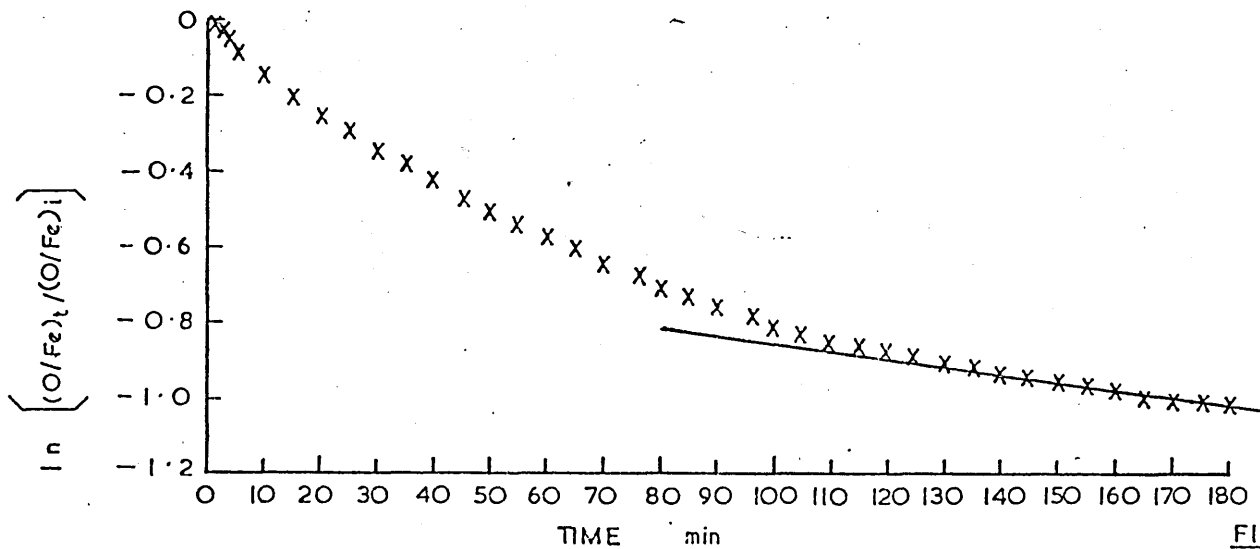


FIG. 125b

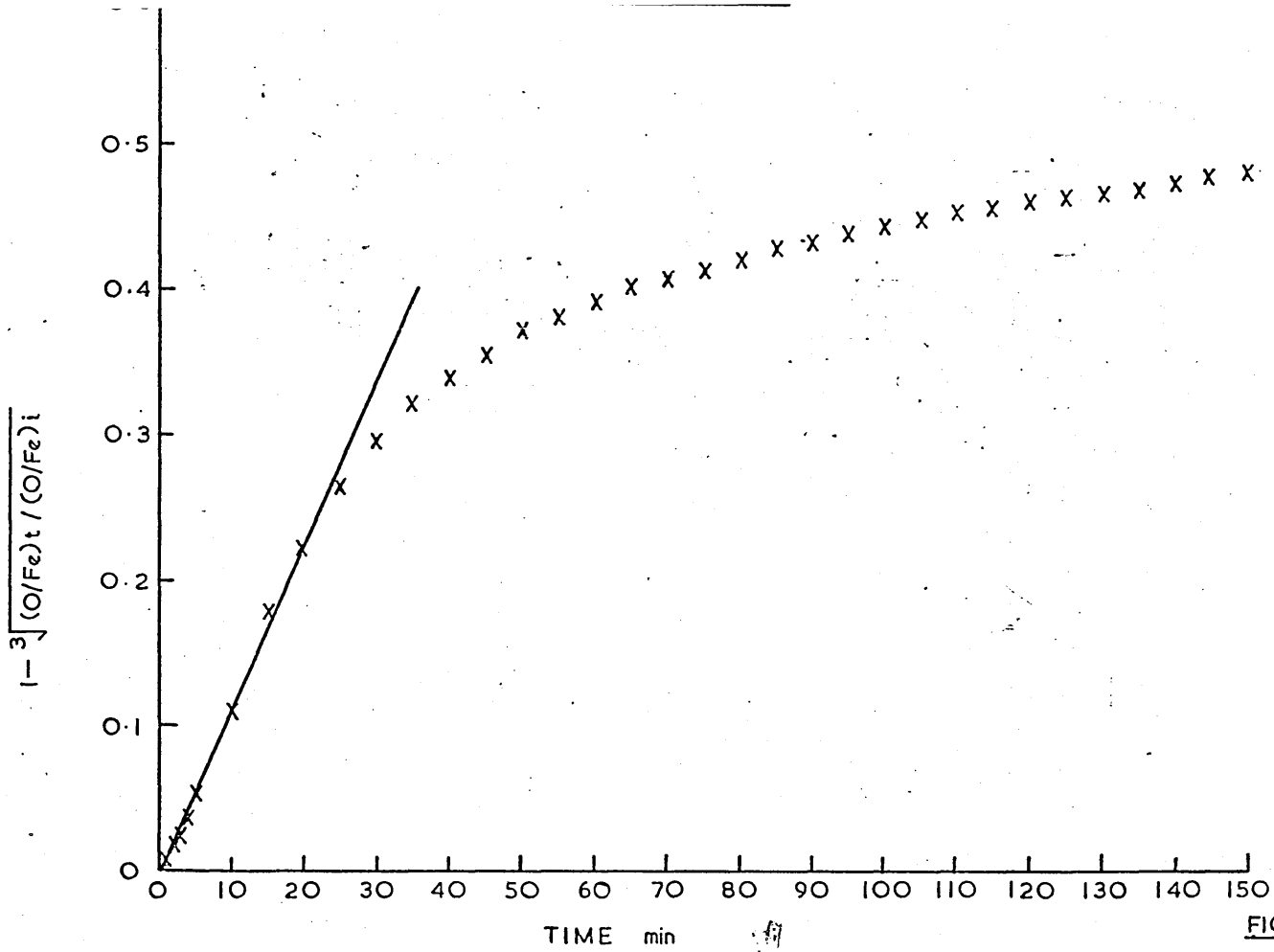


FIG. 126a

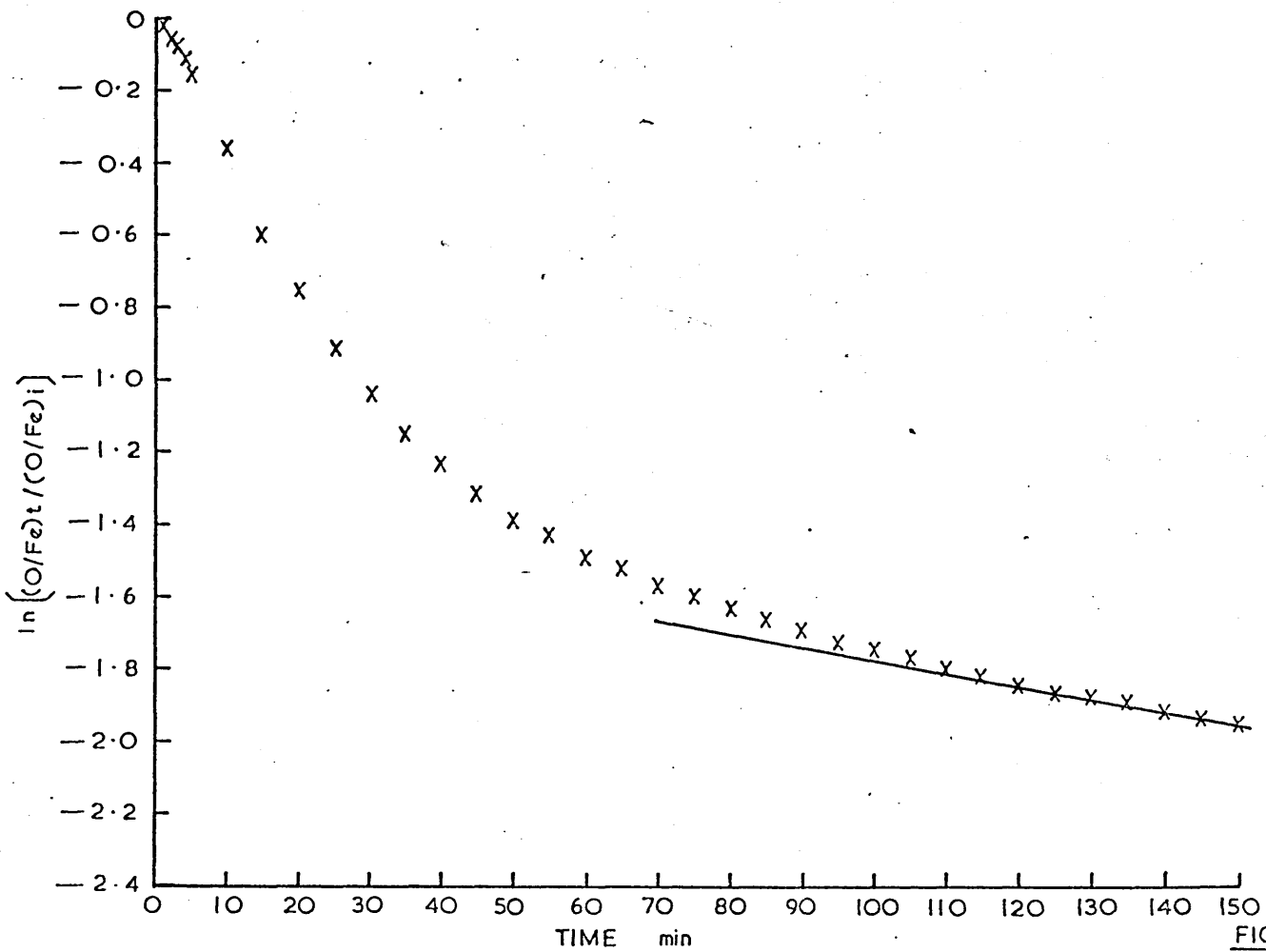


FIG. 126b

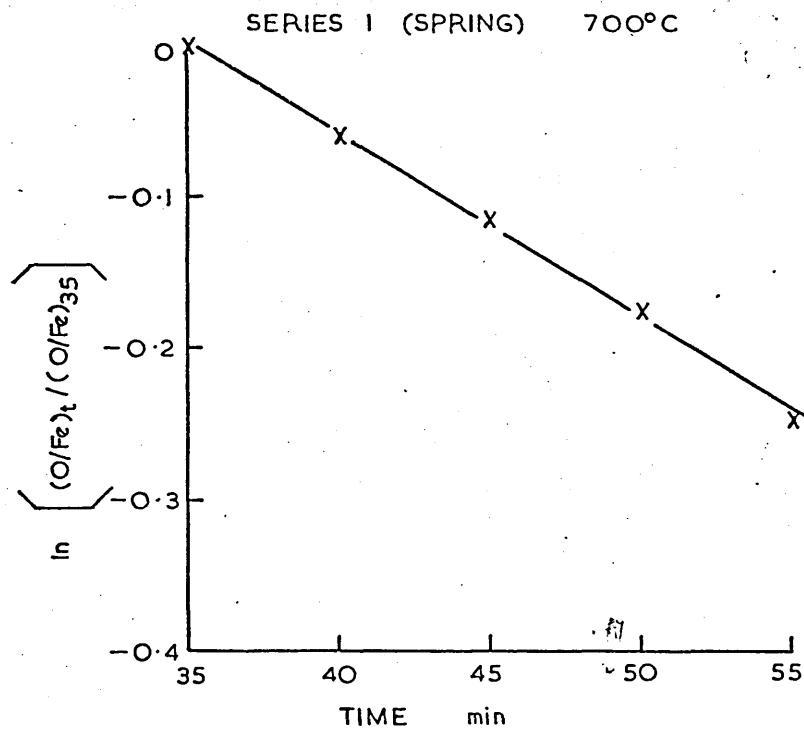


FIG. 127a

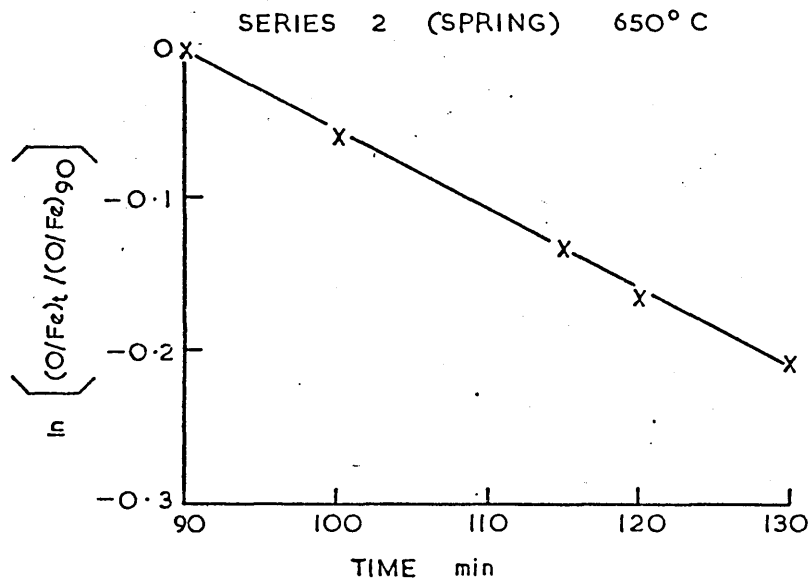


FIG. 127 b

SERIES 1 AND 2 EXPONENTIAL LAW PLOTS

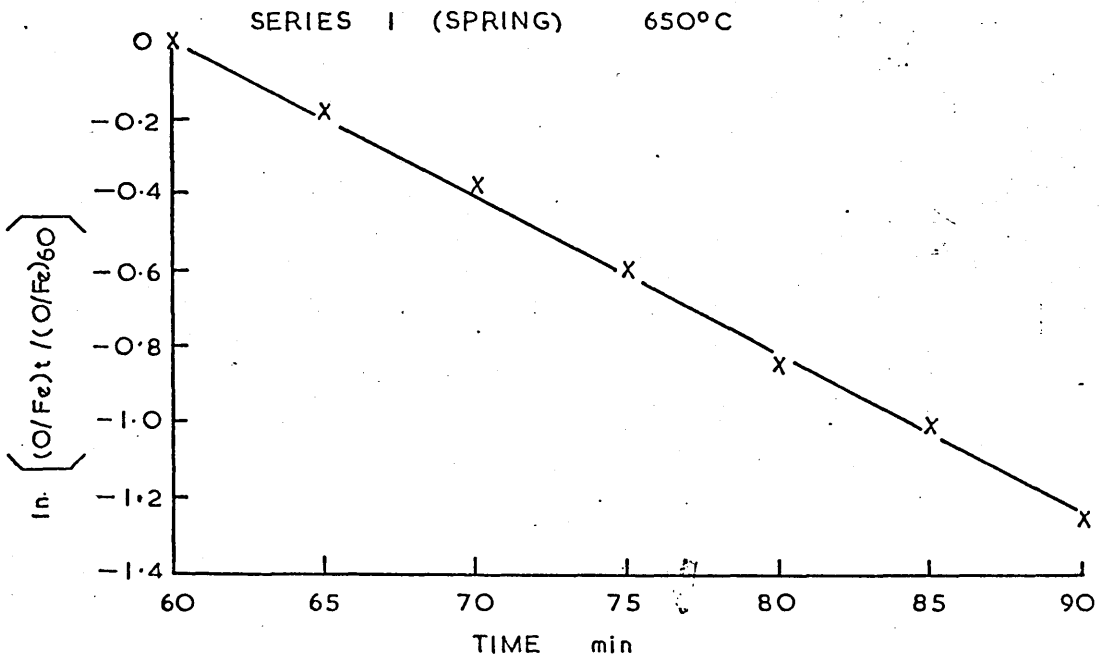


FIG. 127c

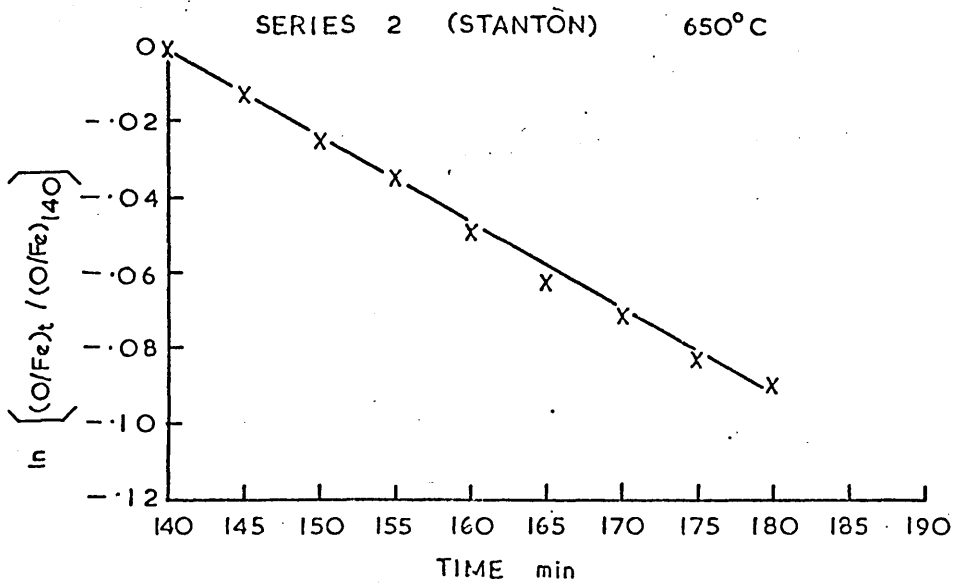


FIG. 127d

SERIES I (SPRING) PHASE BOUNDARY AND
EXPONENTIAL LAW PLOTS

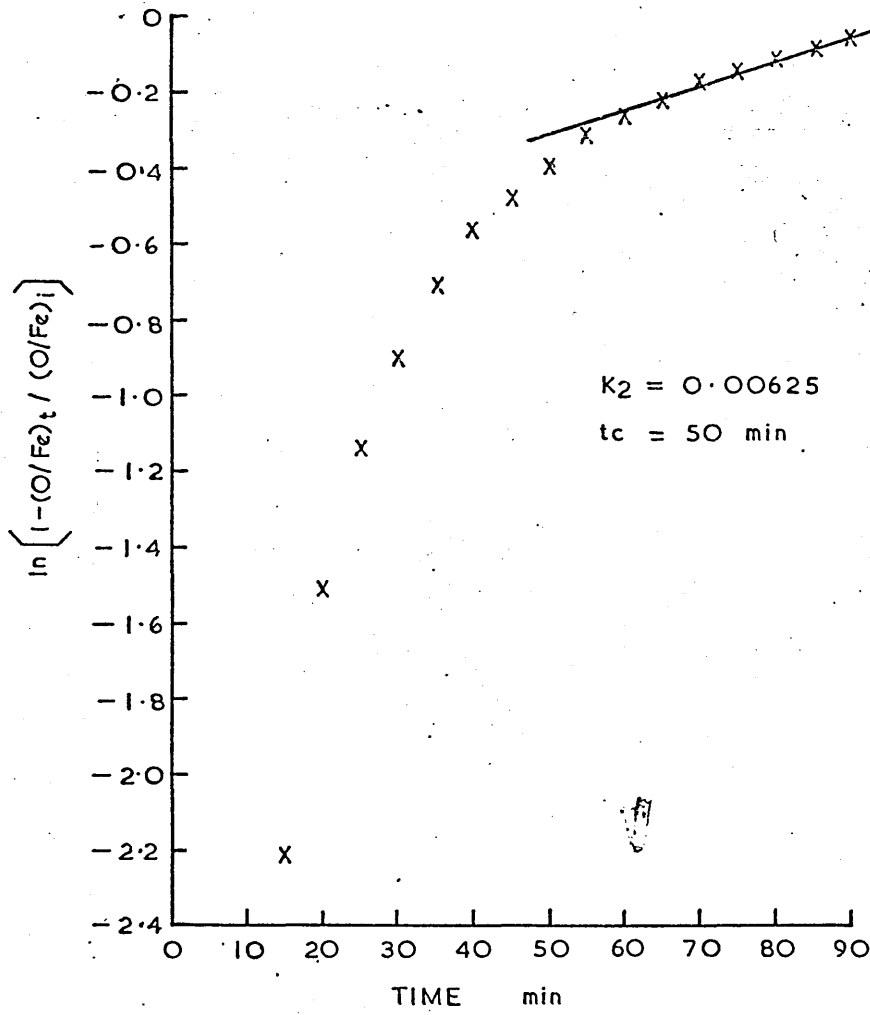


FIG. 128a

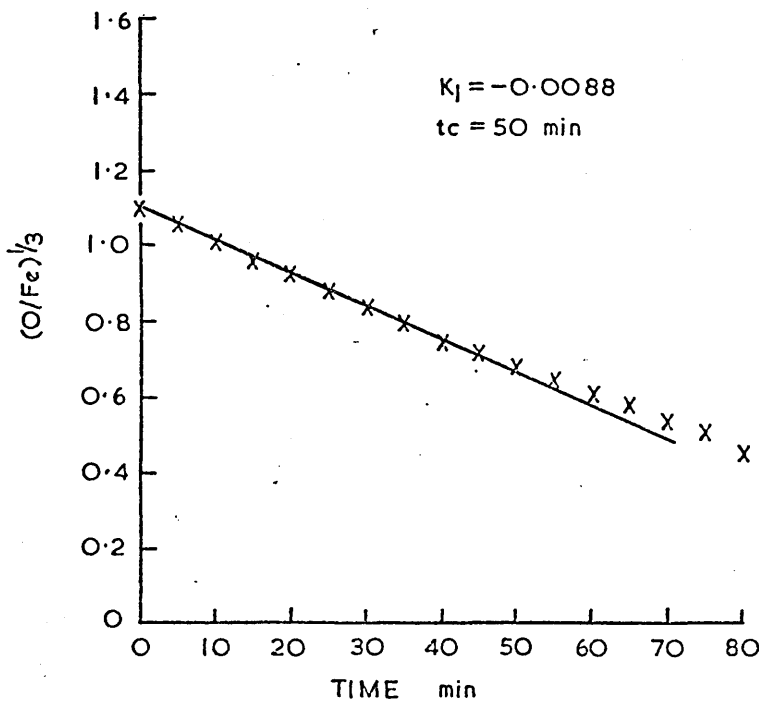


FIG. 128b

KIRUNA MAGNETITE REDUCED H₂ 650°C
SERIES I (SPRING) PHASE BOUNDARY AND
EXPONENTIAL LAW PLOTS

— CALCULATED $(O/Fe)_t = (1 - K_1 t_c)^3 + (1 - e^{-K_2(t-t_c)})$
X MEASURED $(O/Fe)_t$

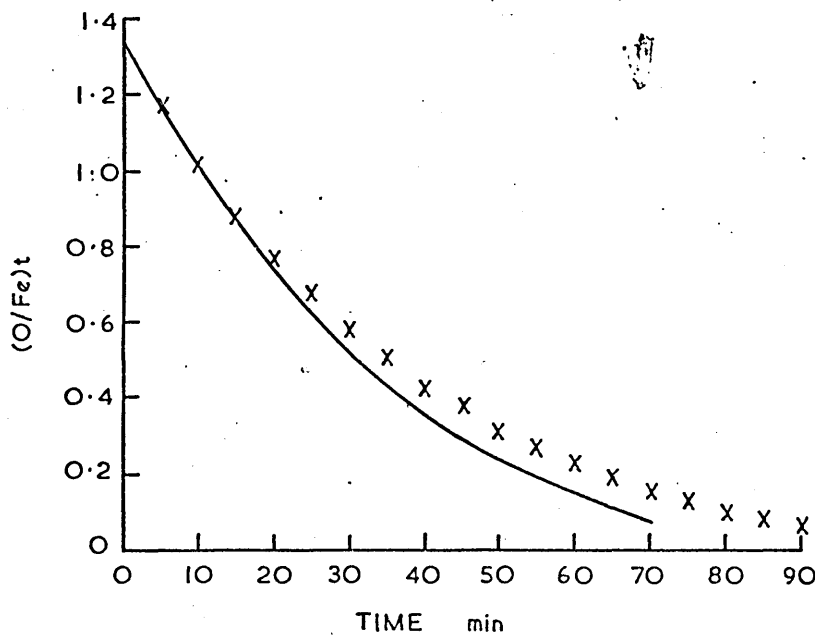


FIG. 128c

EXPONENTIAL LAW PLOTS

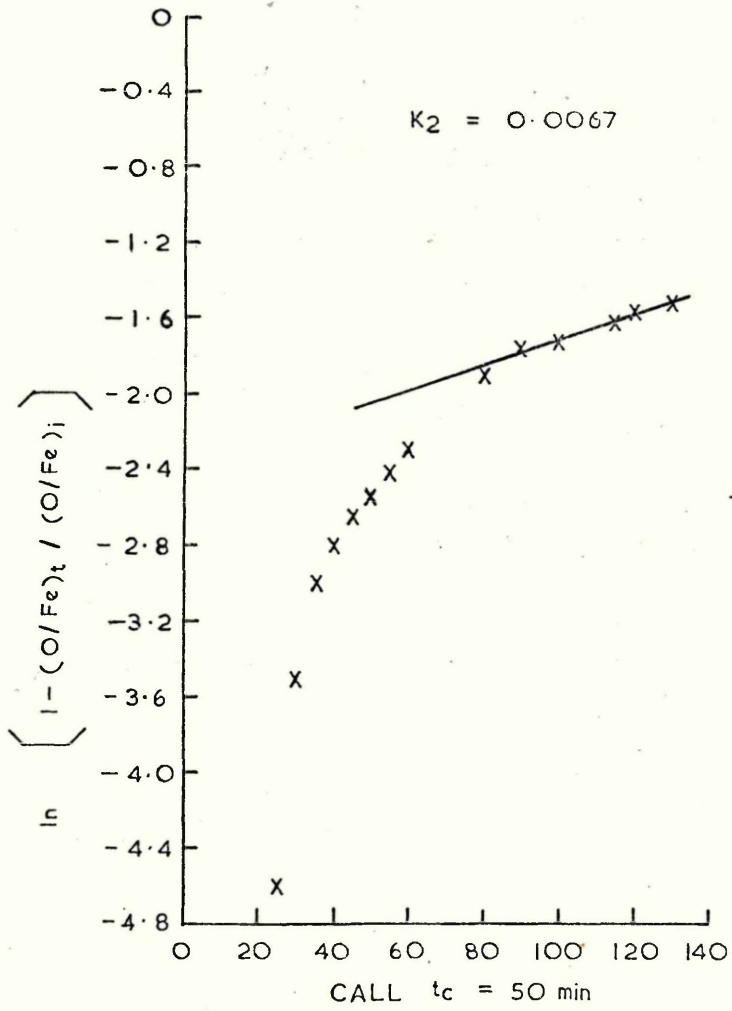


FIG. 129a

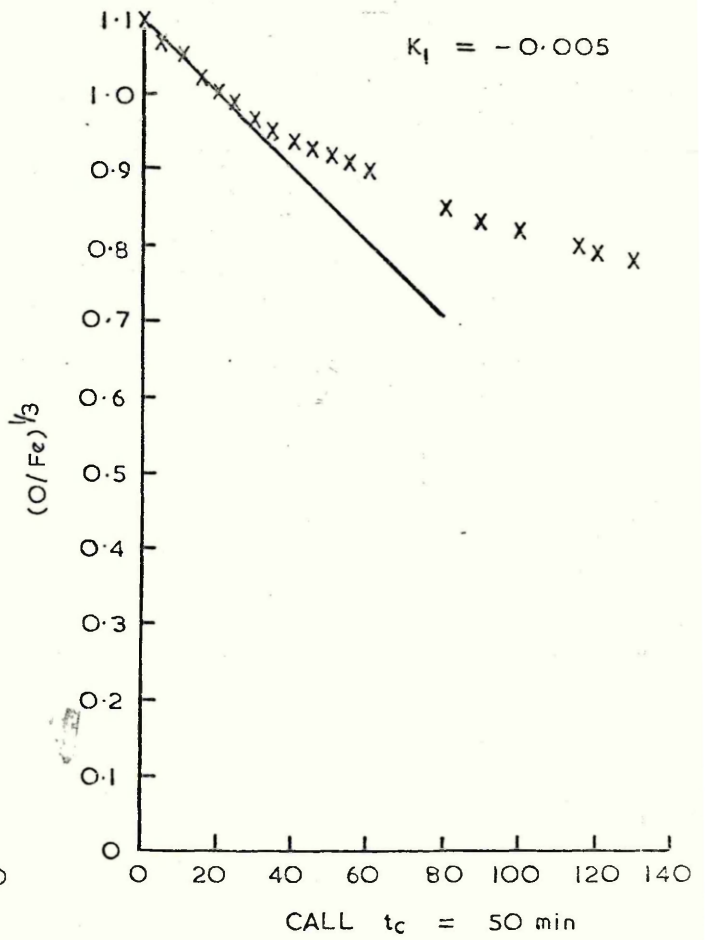


FIG. 129b

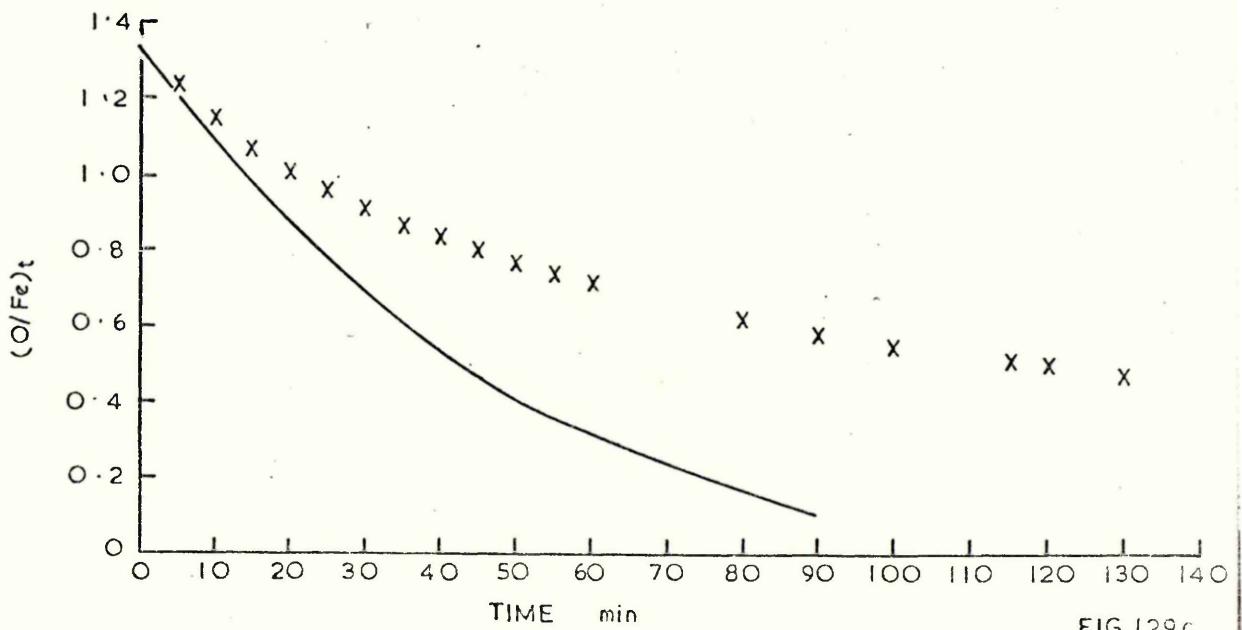


FIG. 129c

SERIES 2 (STANTON)

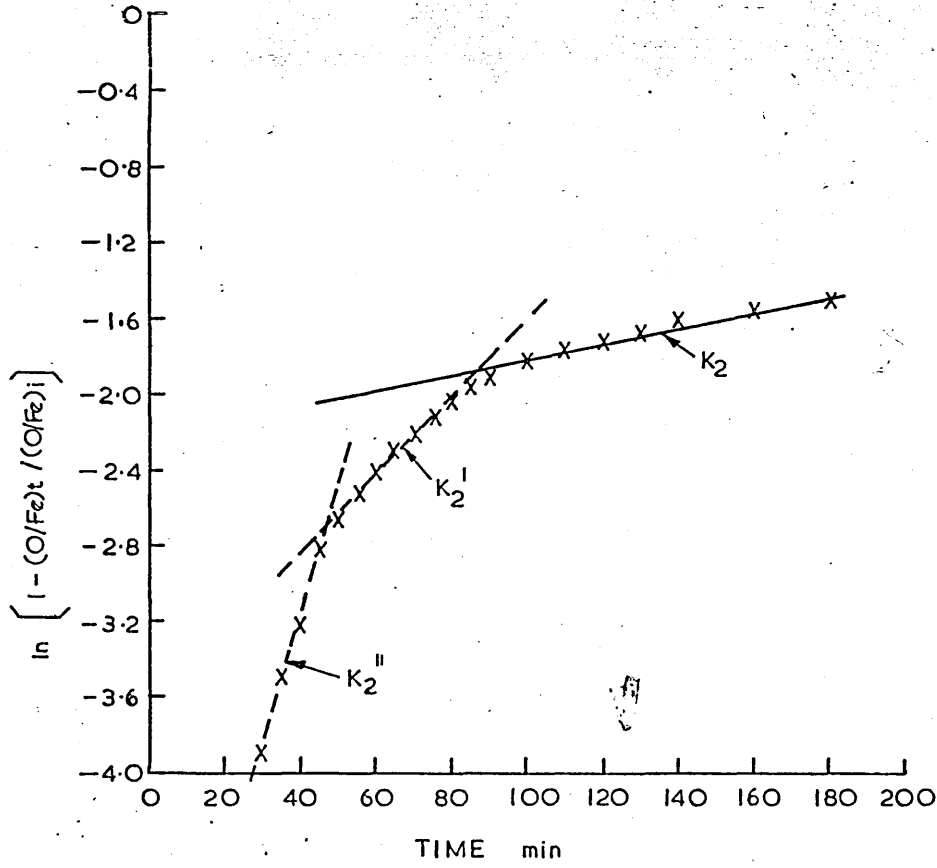


FIG. 130a

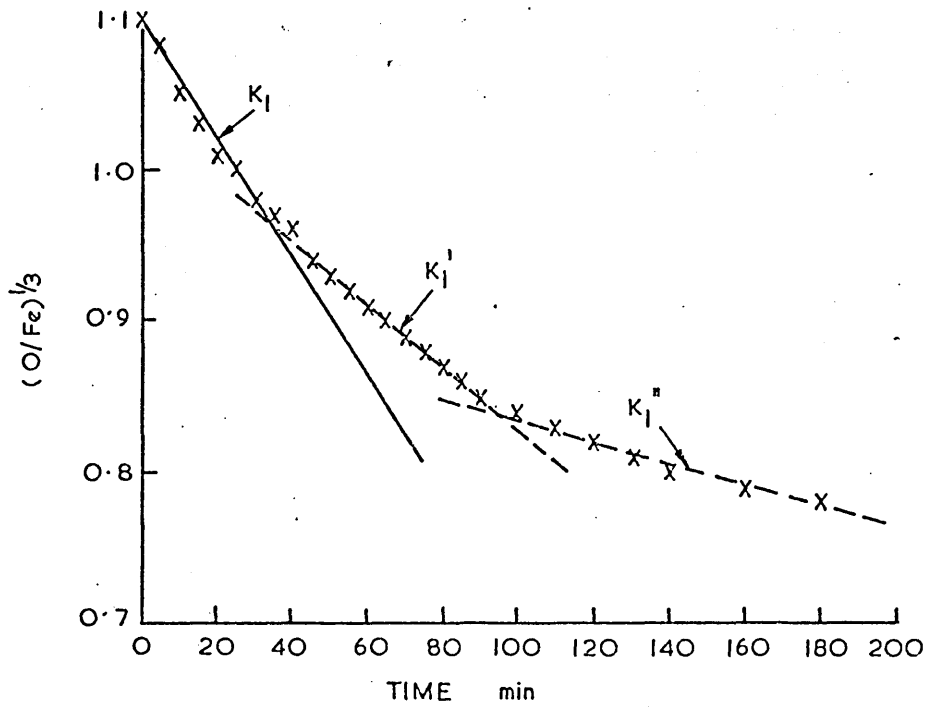


FIG. 130b

KIRUNA MAGNETITE REDUCED H₂ 650°C
 SERIES I (SPRING) INDIVIDUAL LAW PLOTS

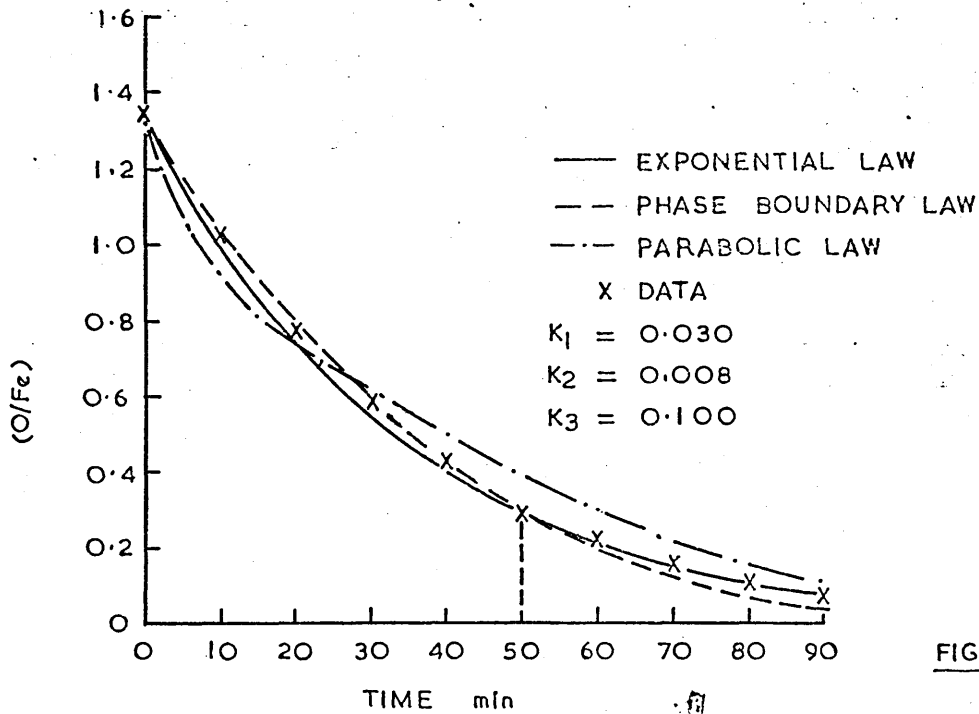


FIG. 131 a

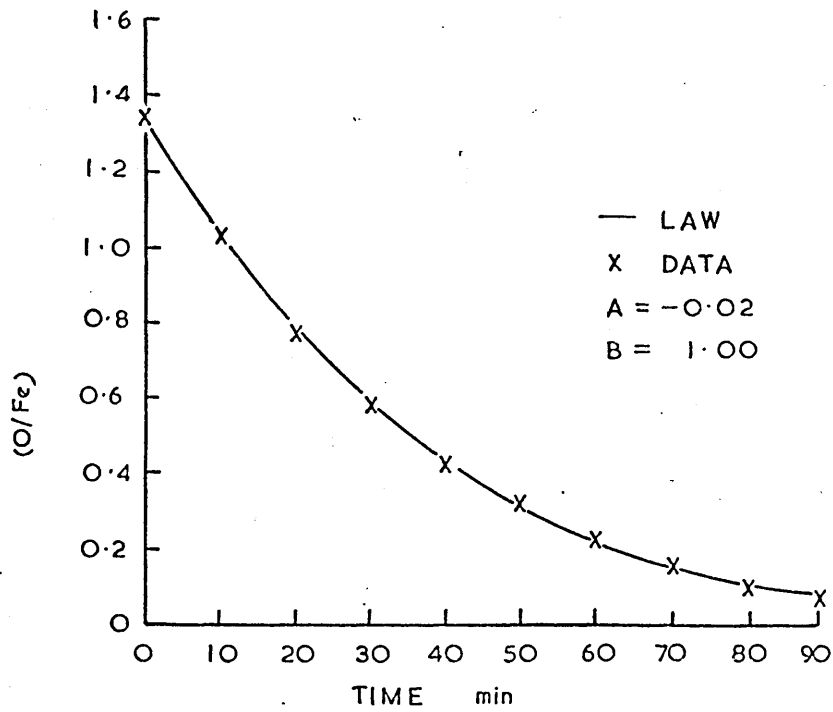


FIG. 131 b

SERIES I (SPRING) INDIVIDUAL LAW PLOTS

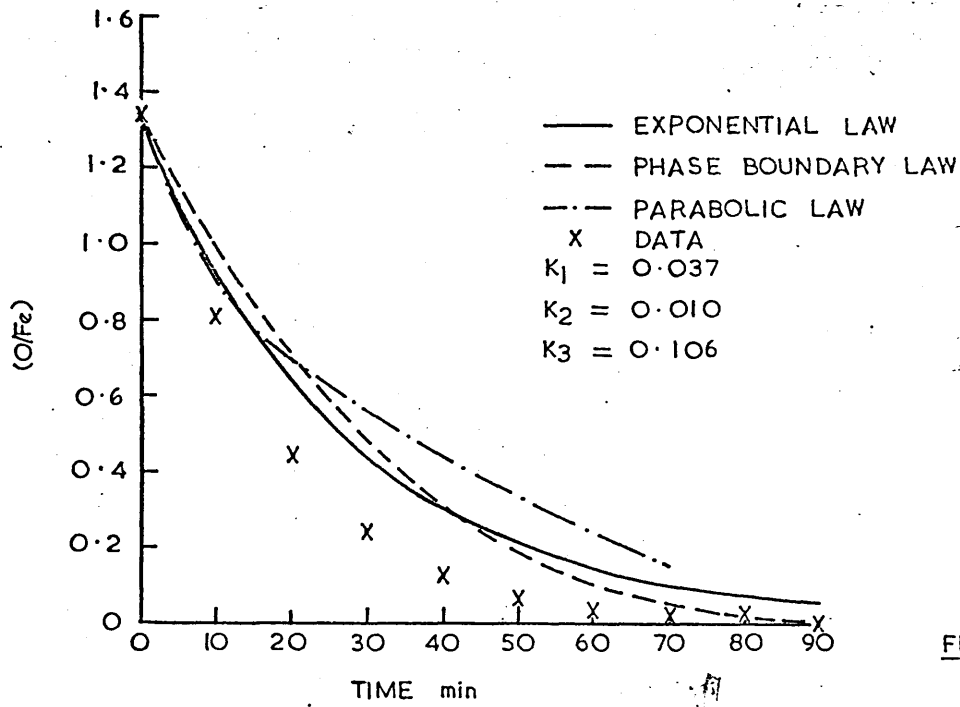


FIG. 132a

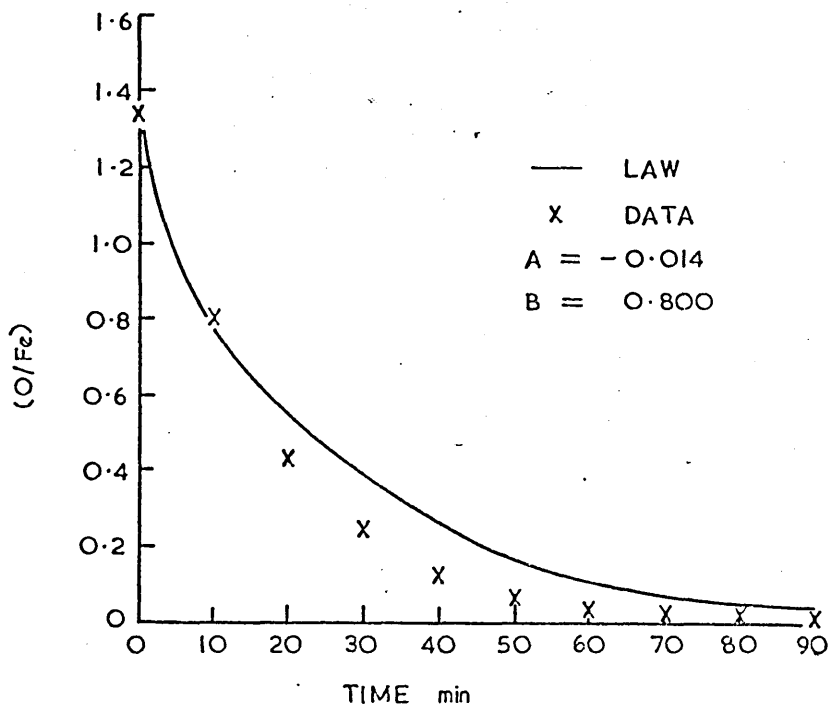
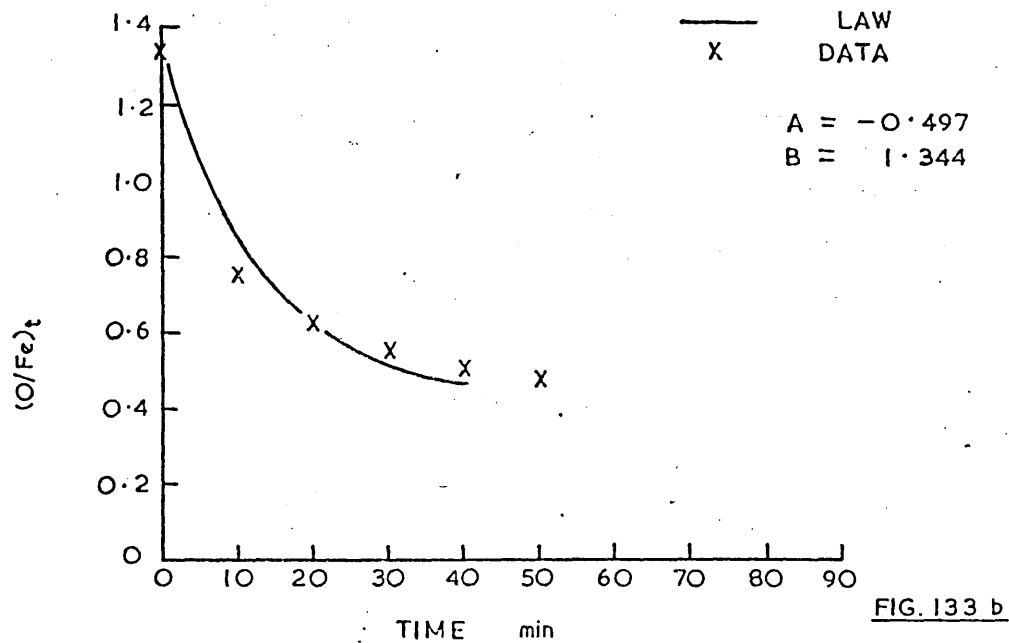
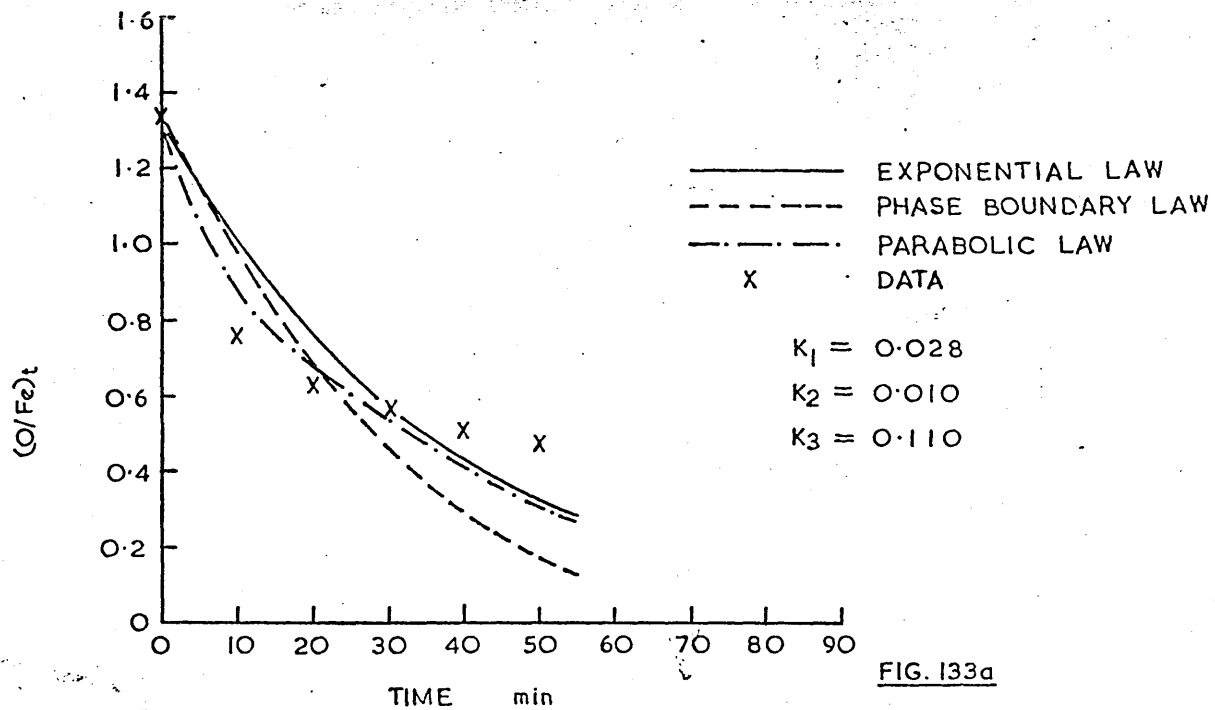


FIG. 132b

SERIES I (SPRING) COMPUTED INDIVIDUAL

LAW PLOTS



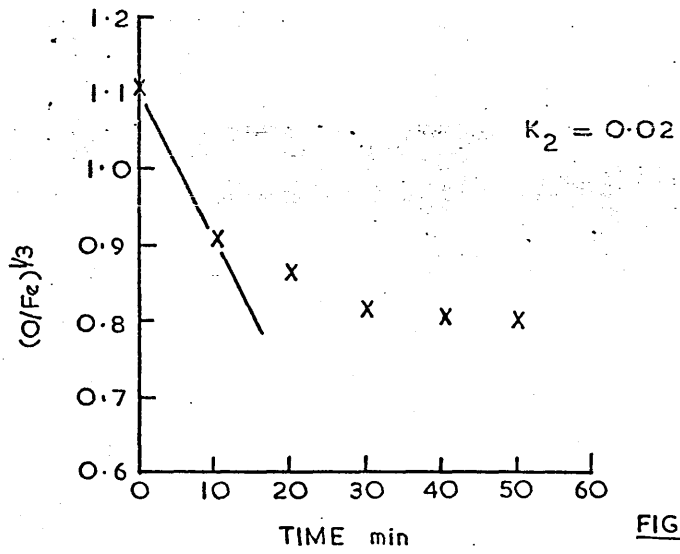


FIG. 134 a

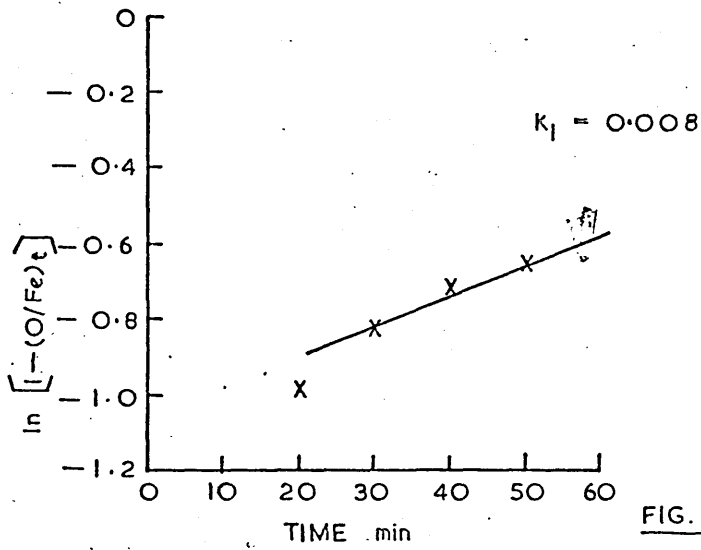


FIG. 134 b

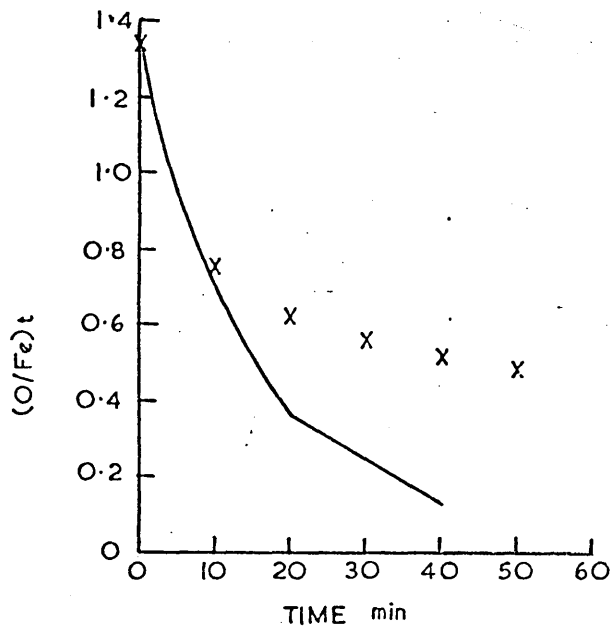
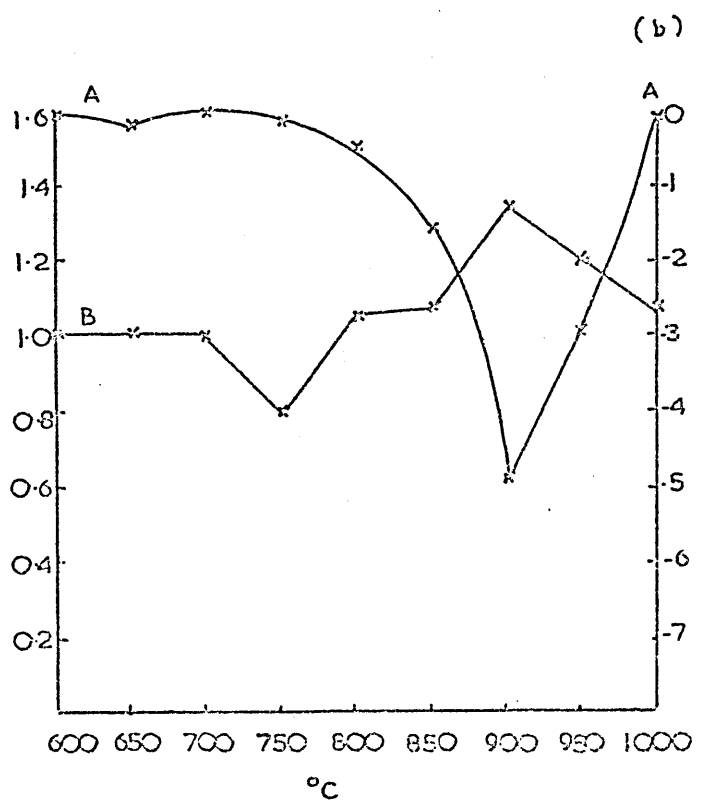
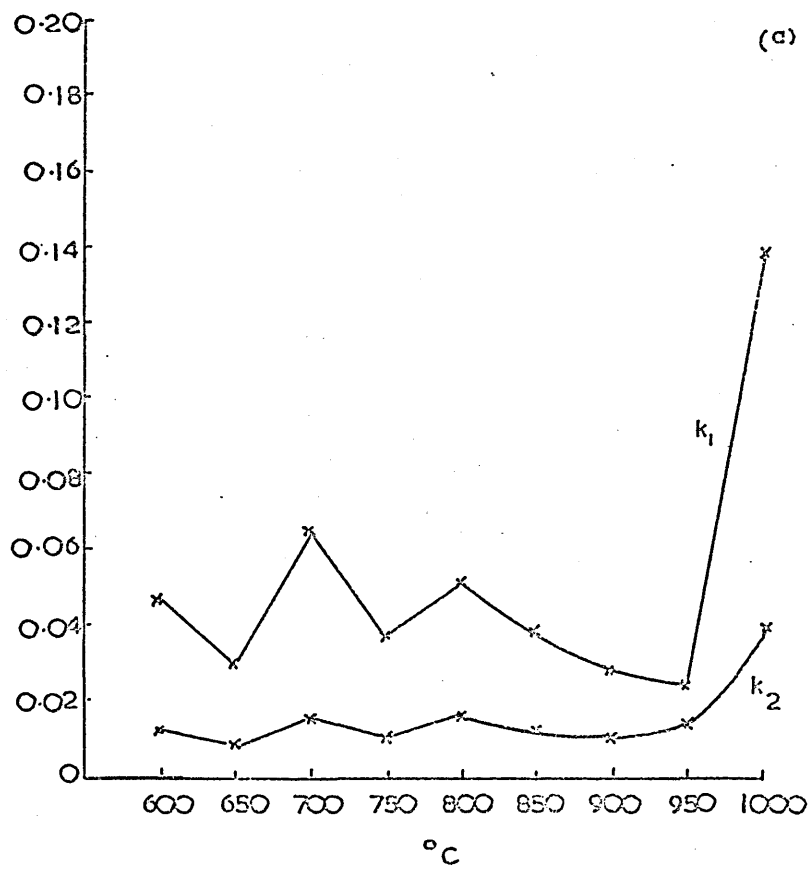
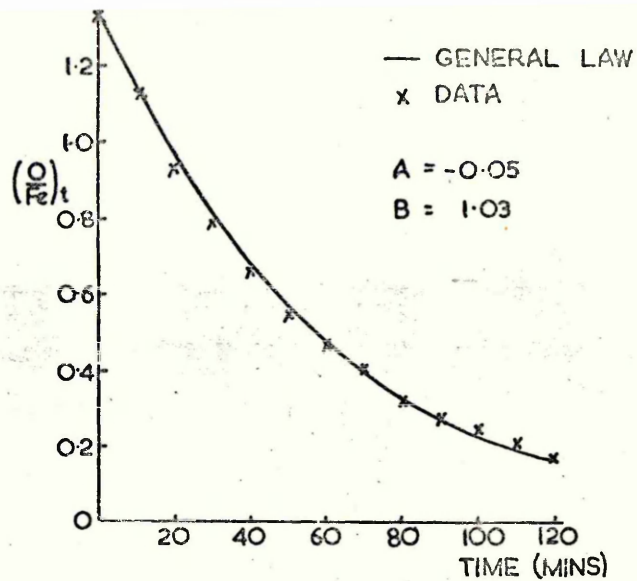
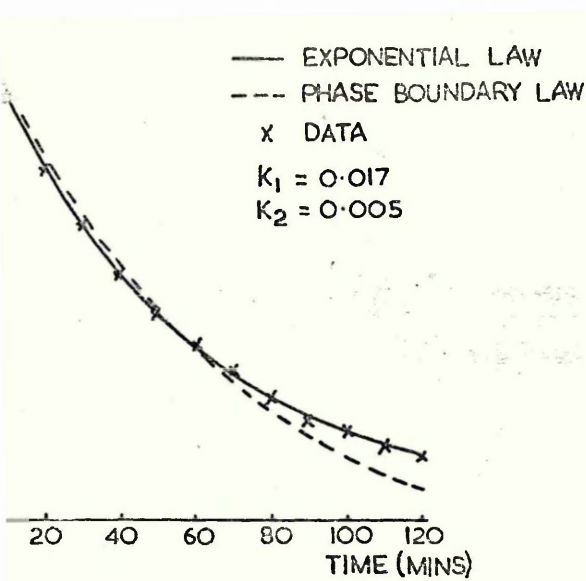


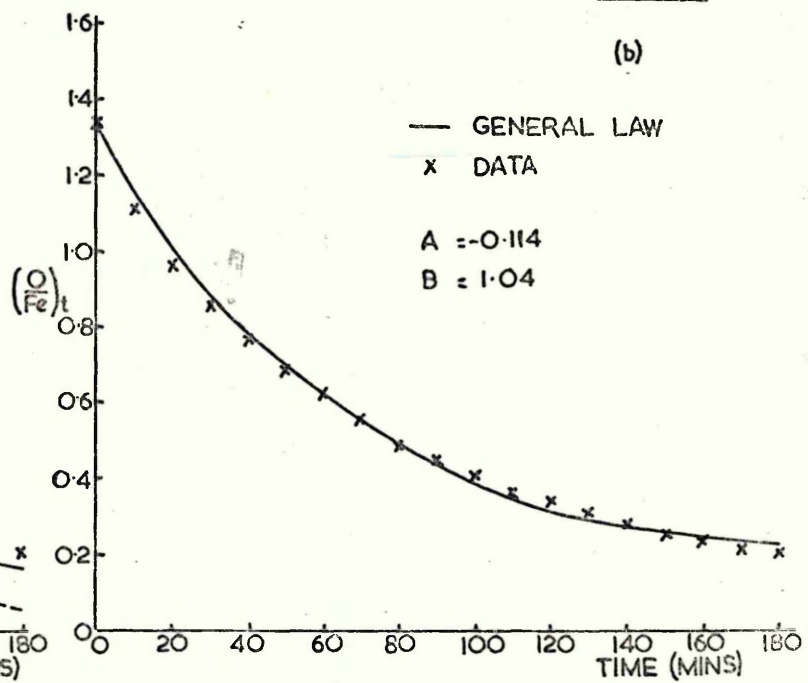
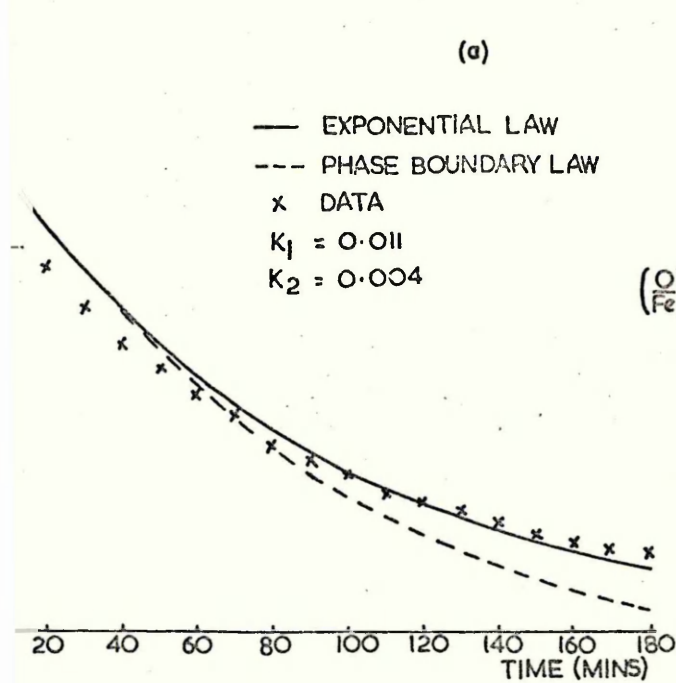
FIG. 134 c

FIG. 135 KIRUNA MAGNETITE SERIES I (SPRING)
RATE CONSTANT PLOTS

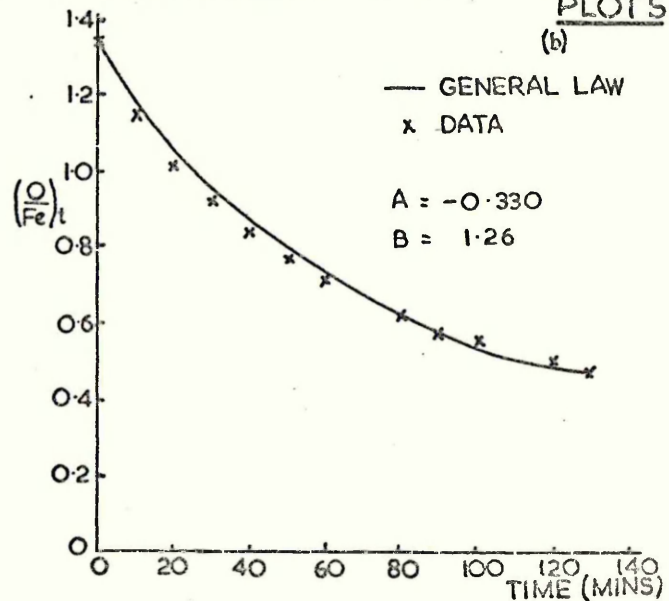
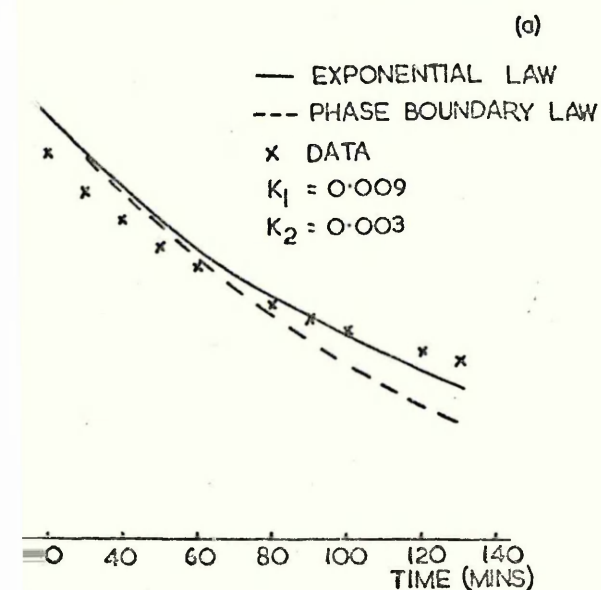


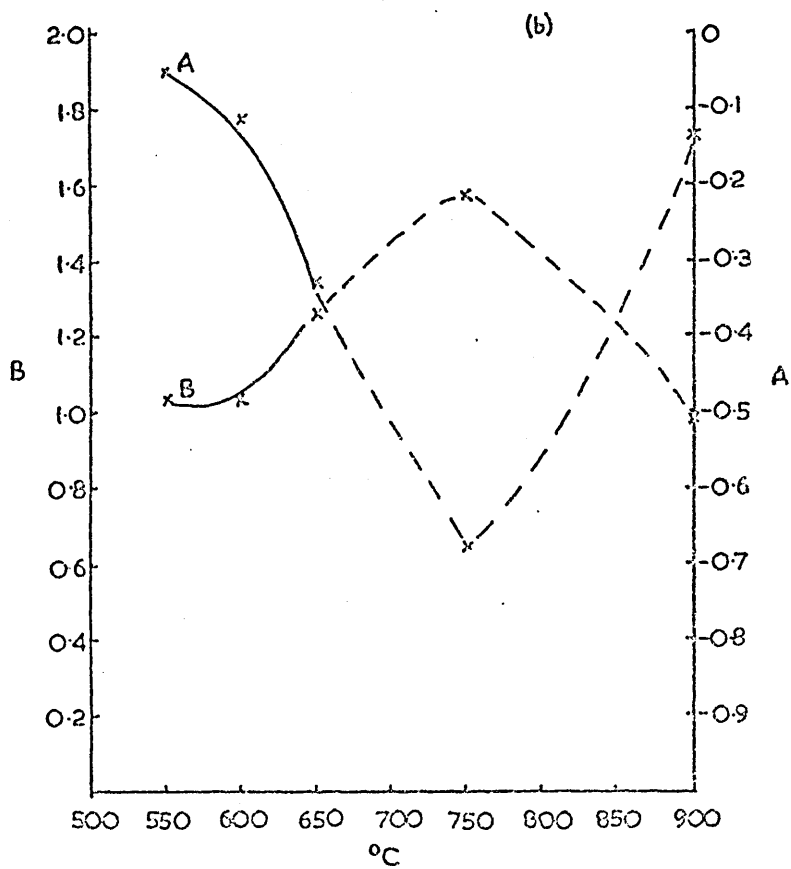
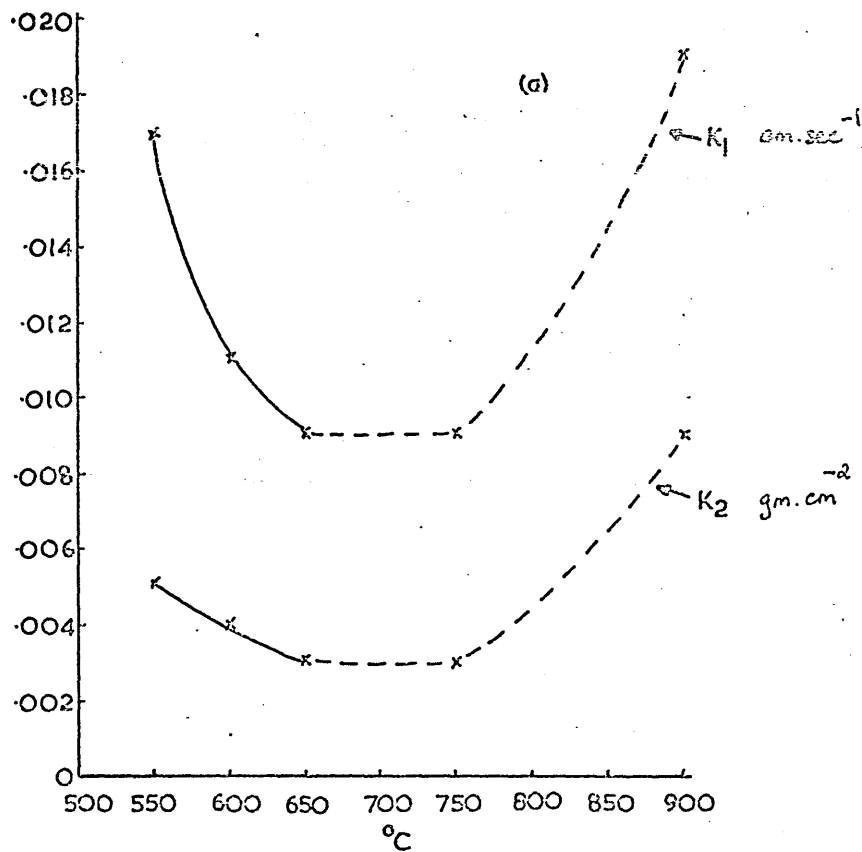


7. SERIES 2 (SPRING), KIRUNA MAGNETITE : RED H₂ 600°C. INDIVIDUAL LAW PLOTS



8. SERIES 2 (SPRING), KIRUNA MAGNETITE : RED H₂ 650°C. INDIVIDUAL LAW PLOTS





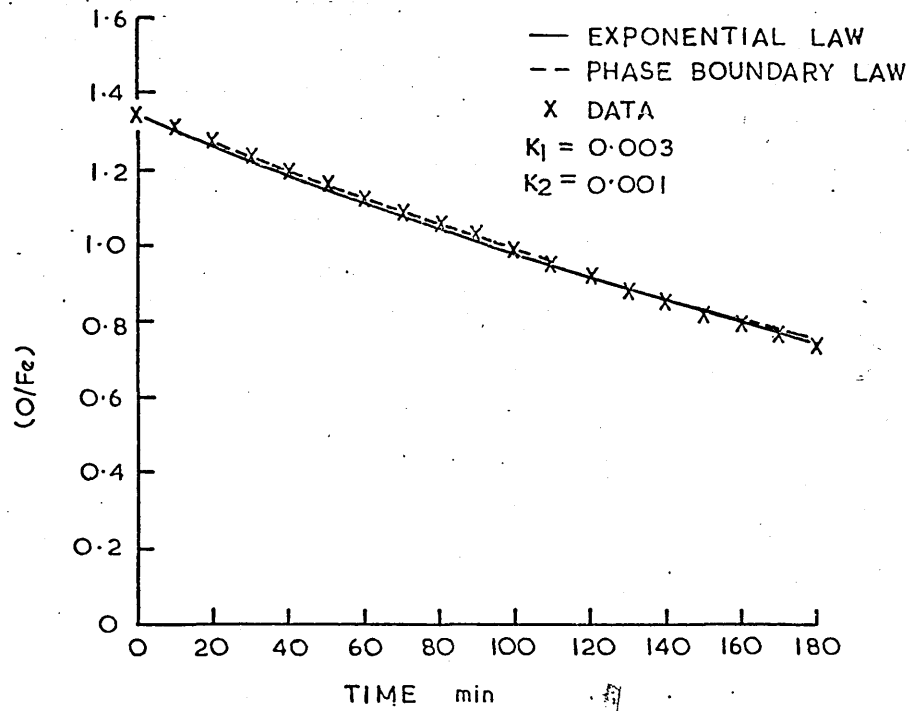


FIG. 140 a

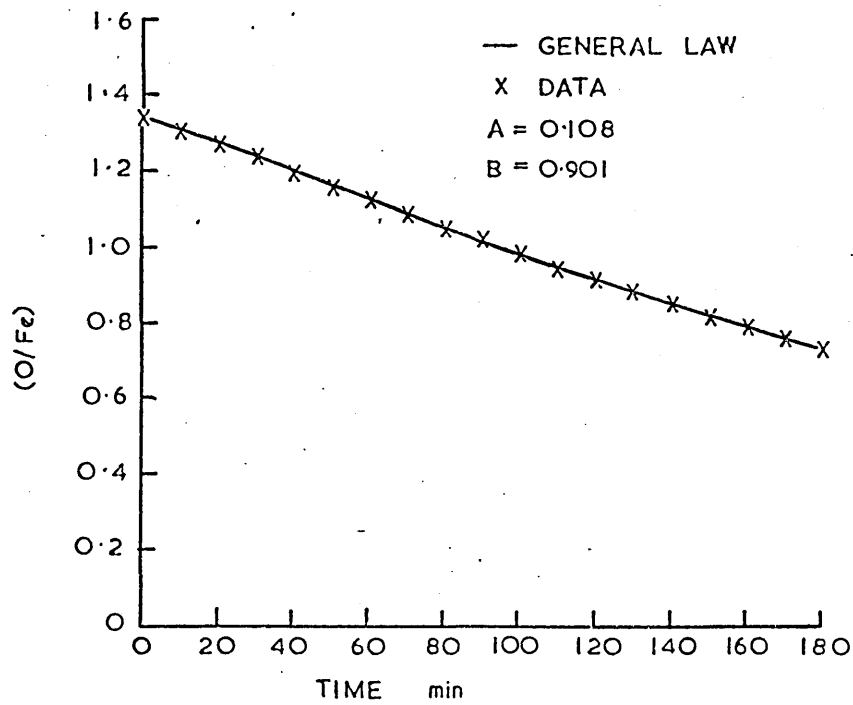


FIG. 140 b

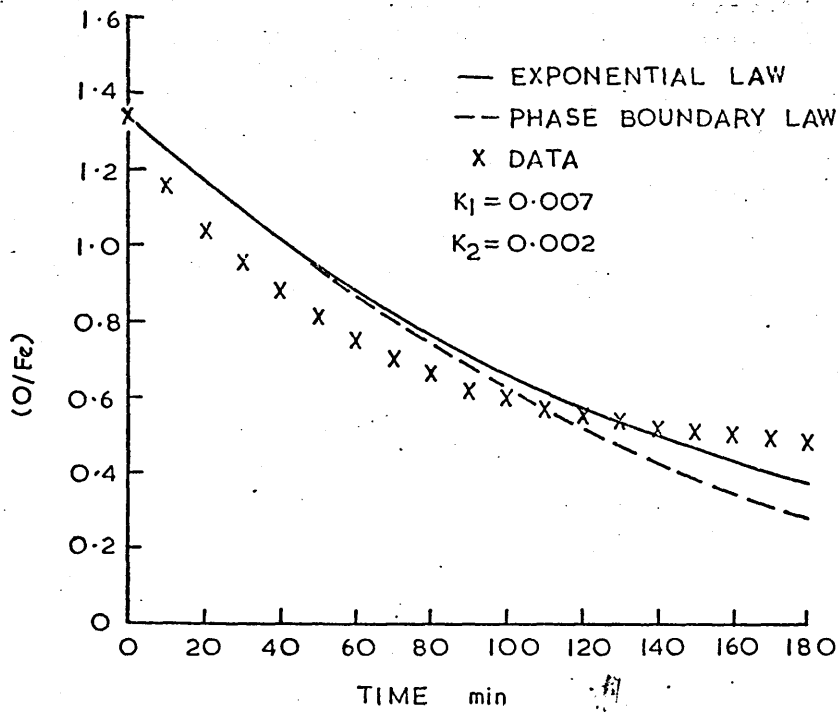


FIG. 141a

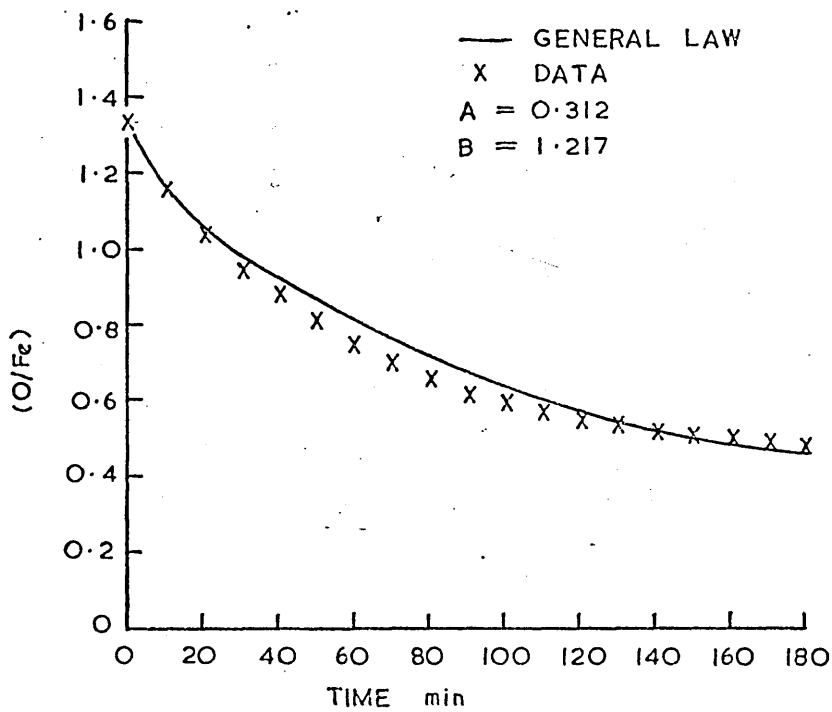
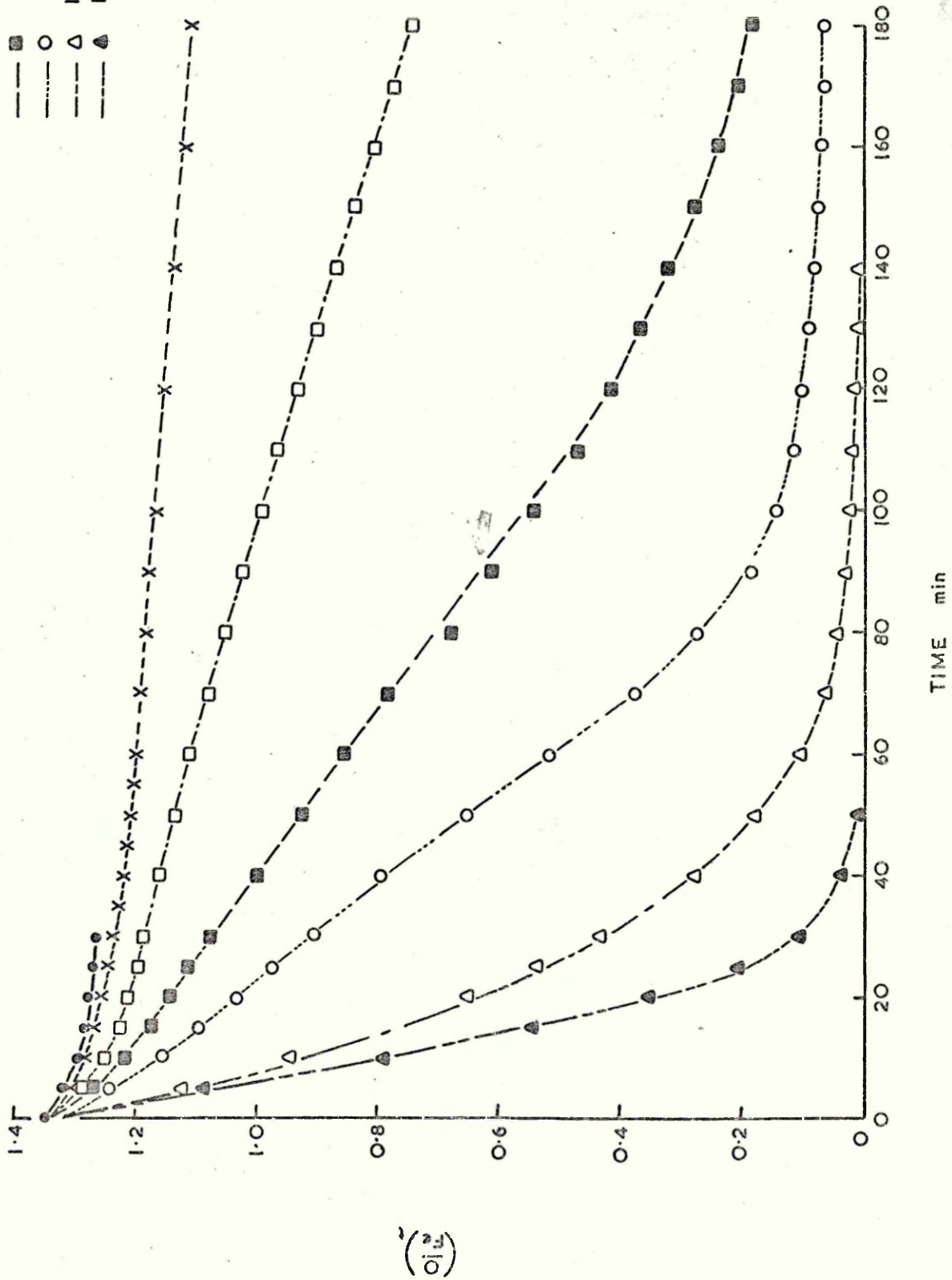


FIG. 141b

AF. SINTER PELLETS REDUCED H₂ 700°C — 1100°C

- 700°C
- 800°C
- 840°C
- 870°C
- 900°C
- 1000°C
- 1100°C

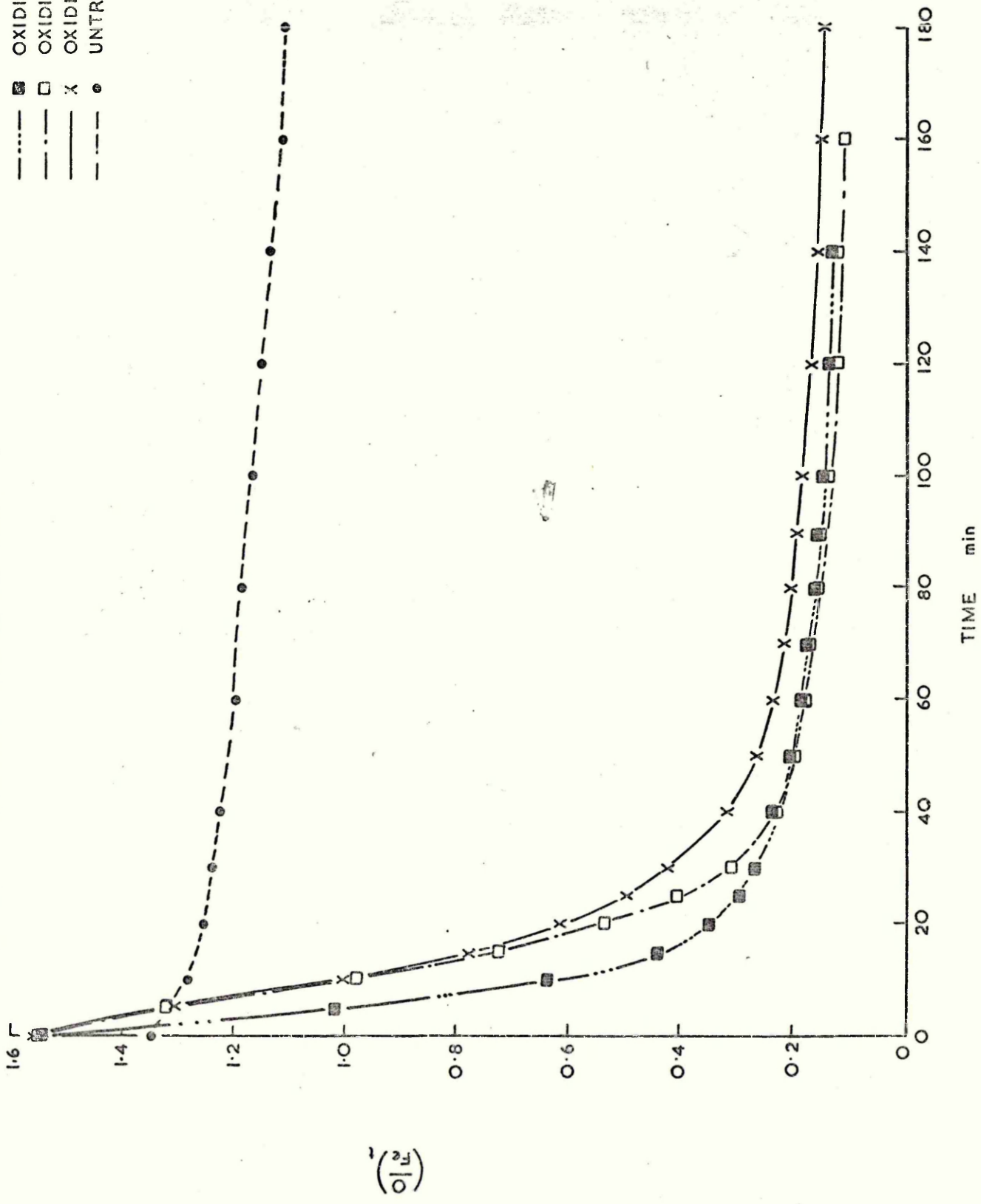
-
- X
-
-
-
- △
- ▲



TIME min

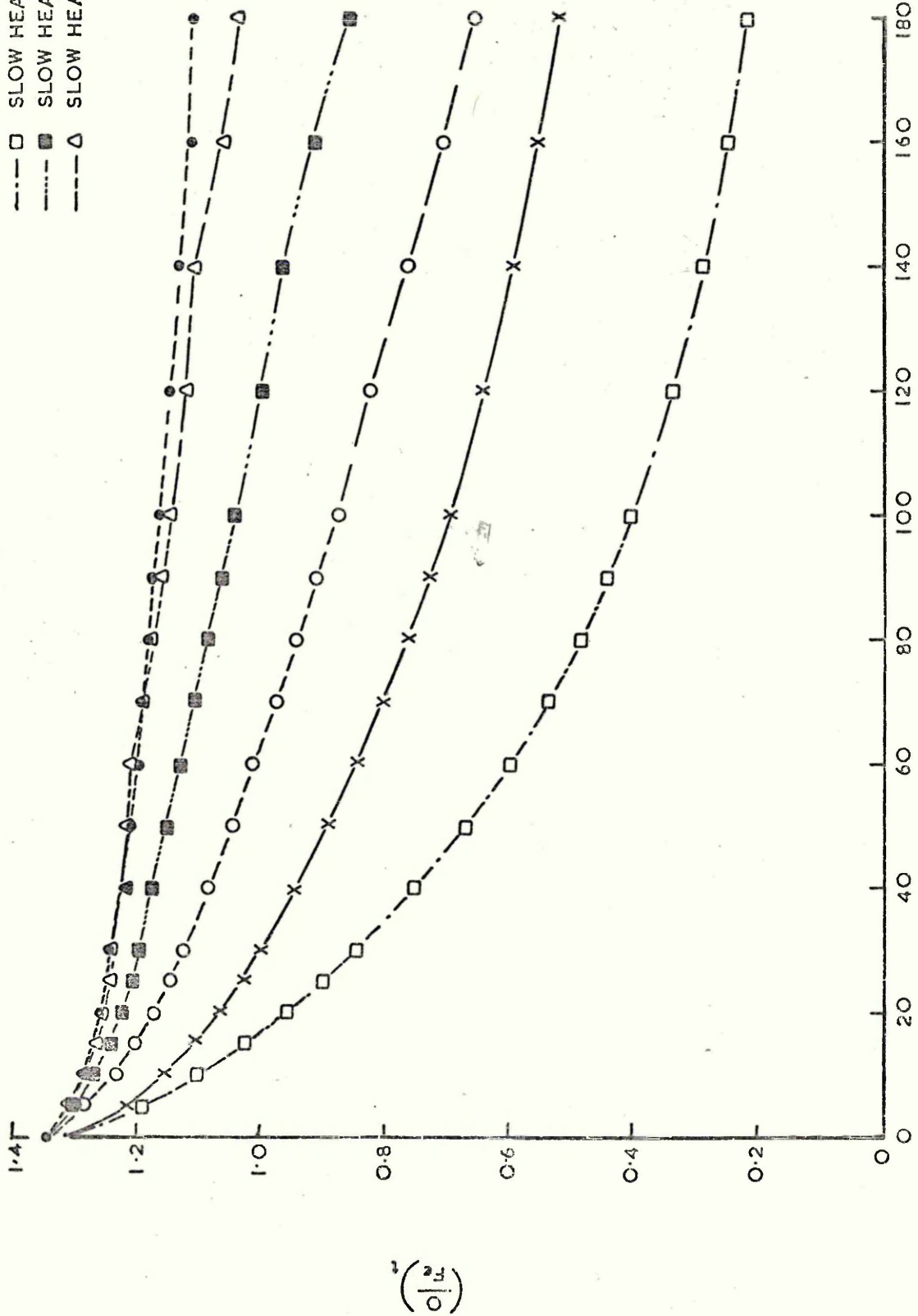
AF. SINTER PELLETS FULLY OXIDISED REDUCED H₂ 800°C

- OXIDISED 500°C
- OXIDISED 750°C
- X— OXIDISED 1000°C
- UNTREATED



AF. SINTER PELLETS THERMALLY TREATED REDUCED H₂ 800°C

- UNTOUCHED
- X--- SLOW HEAT --- SLOW COOL 1000
- O--- SLOW HEAT --- SLOW COOL 850
- SLOW HEAT --- SLOW COOL 750
- SLOW HEAT --- SLOW COOL 650
- △--- SLOW HEAT --- SLOW COOL 500



TIME min

$$\left(\frac{2}{0.12}\right)^2$$

AF. SINTER PELLETS THERMALLY TREATED 750°C REDUCED H₂ 800°C

- ○ --- UNTREATED
- X --- SLOW HEAT — SLOW COOL
- O --- FAST HEAT — FAST COOL
- □ --- SLOW HEAT — FAST COOL
- ■ --- FAST HEAT — SLOW COOL

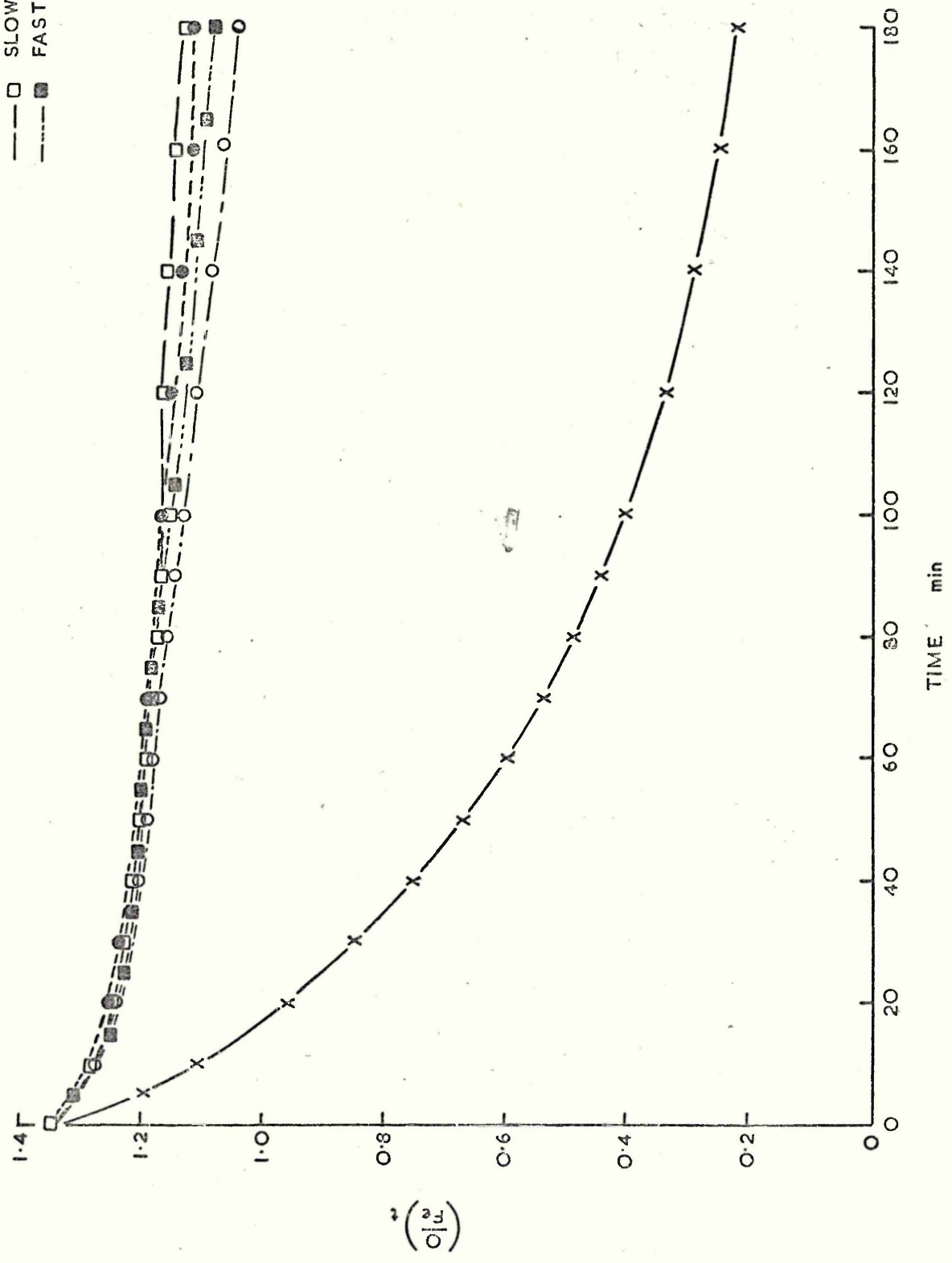


Fig. 146

Appleby-Frodingham Sinter Pellet. Reconstituted

Unreduced

63x

Fig. 147

Appleby-Frodingham Sinter Pellet. Reconstituted

Unreduced

160x

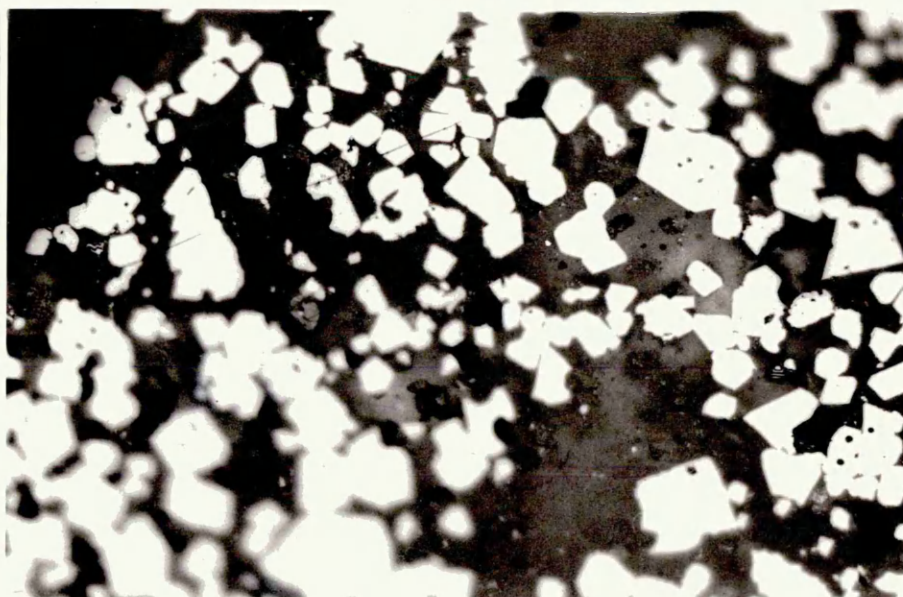
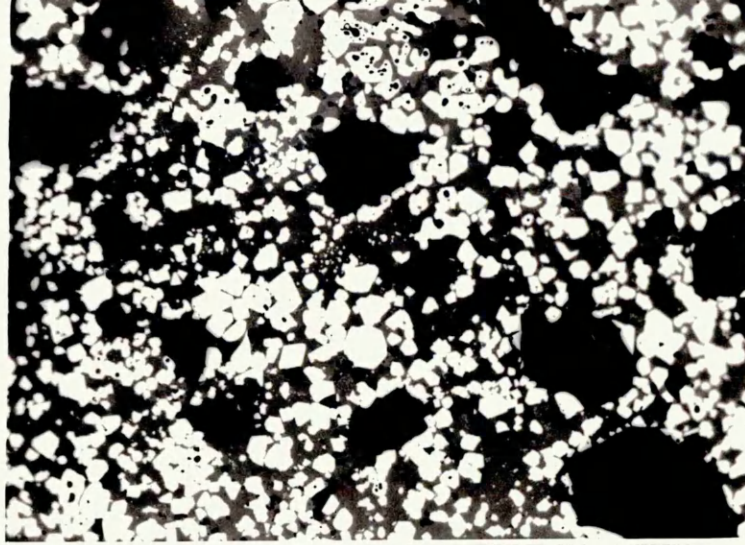


Fig. 148

A.F. Sinter Pellet
Reduced H₂ 700°C
16x

Fig. 149

A.P. Sinter Pellet
Reduced H₂ 700°C
400x (oil immersion)

Fig. 150

A.F. Sinter Pellet
Reduced H₂ 700°C
400x (oil immersion)

Fig. 151

A.P. Sinter Pellet
Reduced H₂ 700°C
400x (oil immersion)

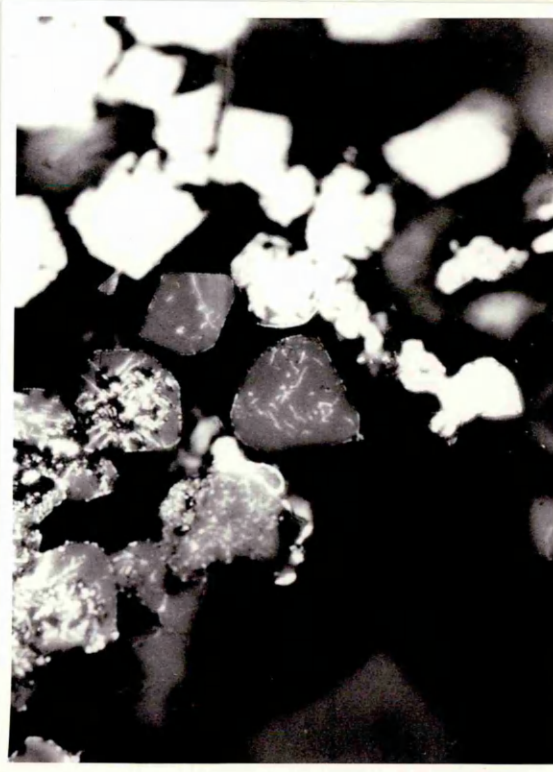
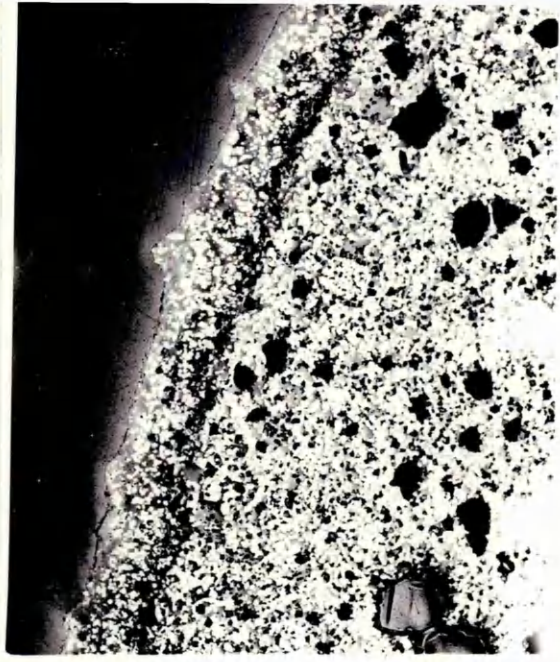


Fig. 152 A.F. Sinter Pellet. Reduced H₂ 800°C 32x

Fig. 153 A.F. Sinter Pellet. Reduced H₂ 800°C 160x

Fig. 154 A.F. Sinter Pellet. Reduced H₂ 800°C 400x
(oil immersion)

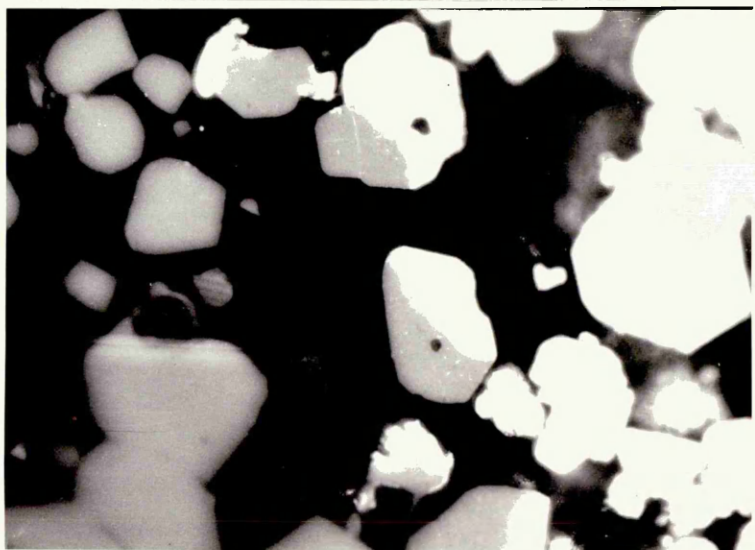
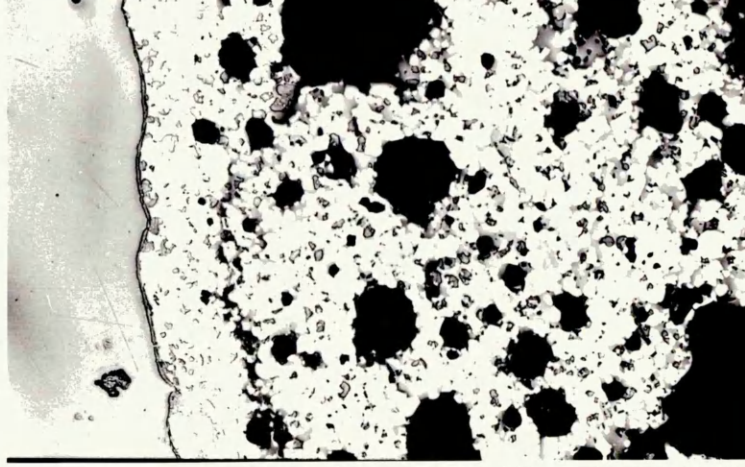


Fig. 155 A.F. Sinter Pellets Reduced H_2 $800^\circ C$ 400x (oil immersion)

Fig. 156 A.F. Sinter Pellet. Reduced H_2 $800^\circ C$ 400x (oil immersion)

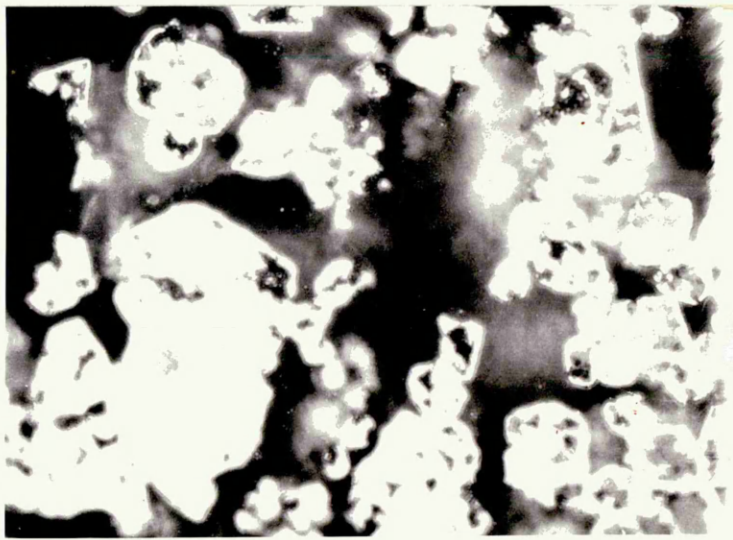


Fig. 157

A.F. Sinter Pellet. Reduced H₂ 840°C

32x

Fig. 158

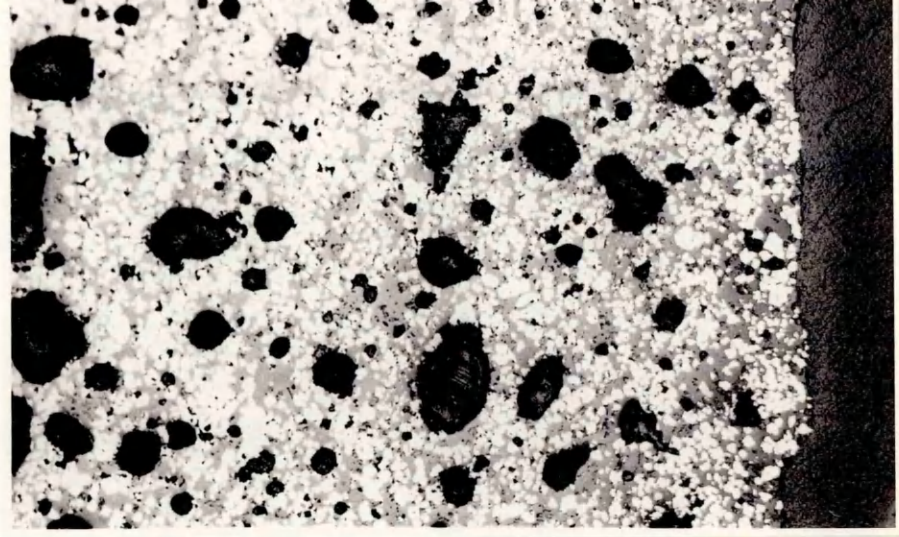
A.F. Sinter Pellet. Reduced H₂ 840°C
mid-radius

400x oil
immersion

Fig. 159

A.F. Sinter Pellet Reduced H₂ 840°C edge

400x oil
immersion



157



158



159

Fig. 160 A.F. Sinter Pellets. Reduced H_2 $870^{\circ}C$ 32x

Fig. 161 A.F. Sinter Pellets. Reduced H_2 $870^{\circ}C$ 160x

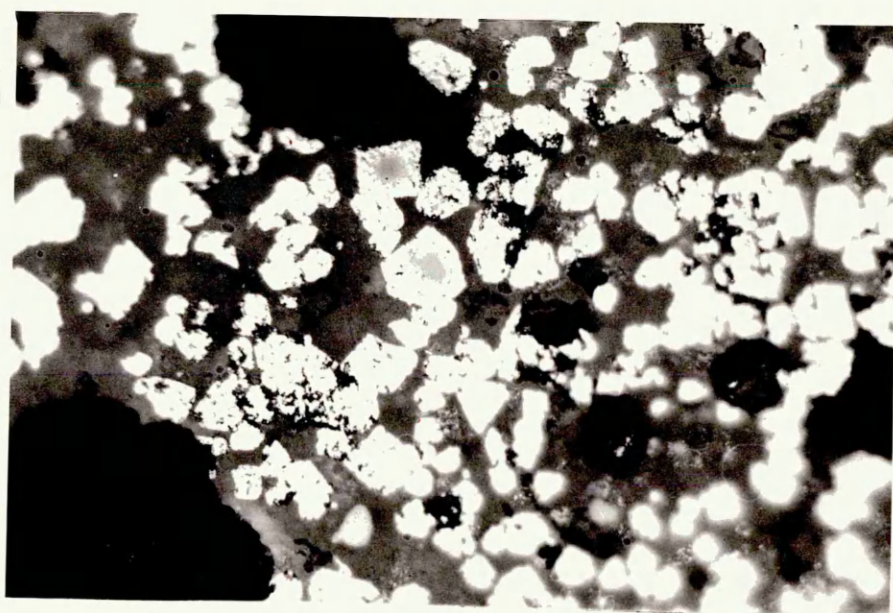
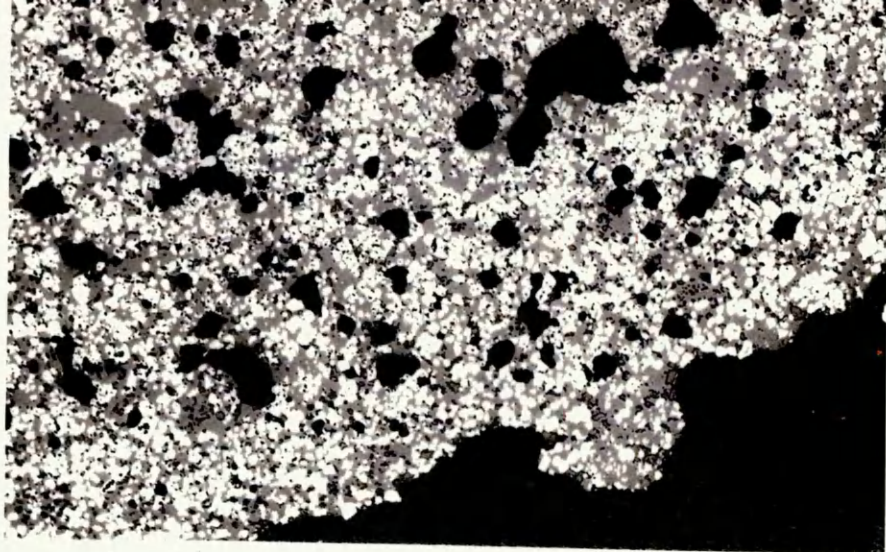


Fig. 162

A.F. Sinter Pellet. Reduced H_2 $900^{\circ}C$ 400x
oil
immersion

Fig. 163

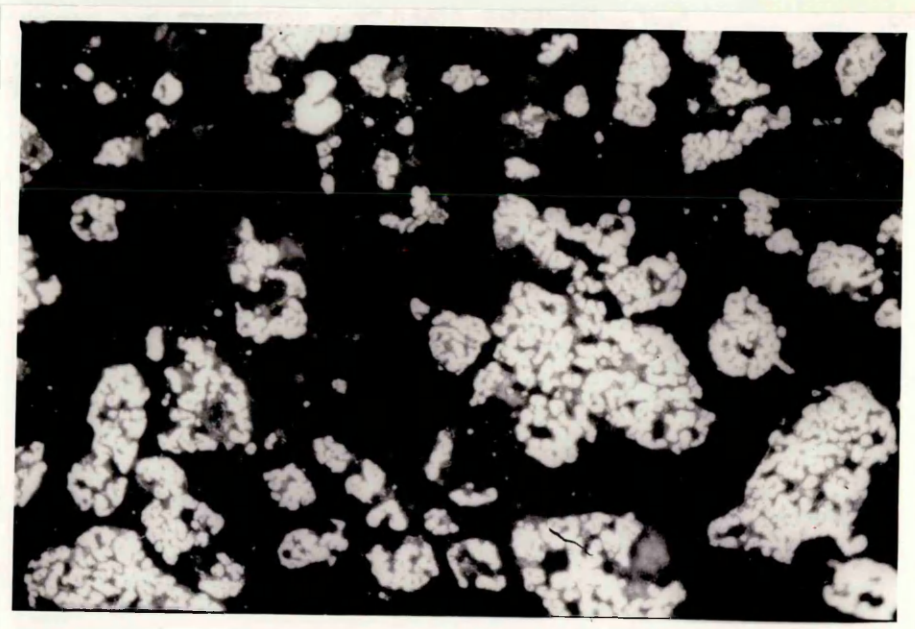
A.F. Sinter Pellet. Reduced H_2 $1000^{\circ}C$ 400x
oil
immersion

Fig. 164

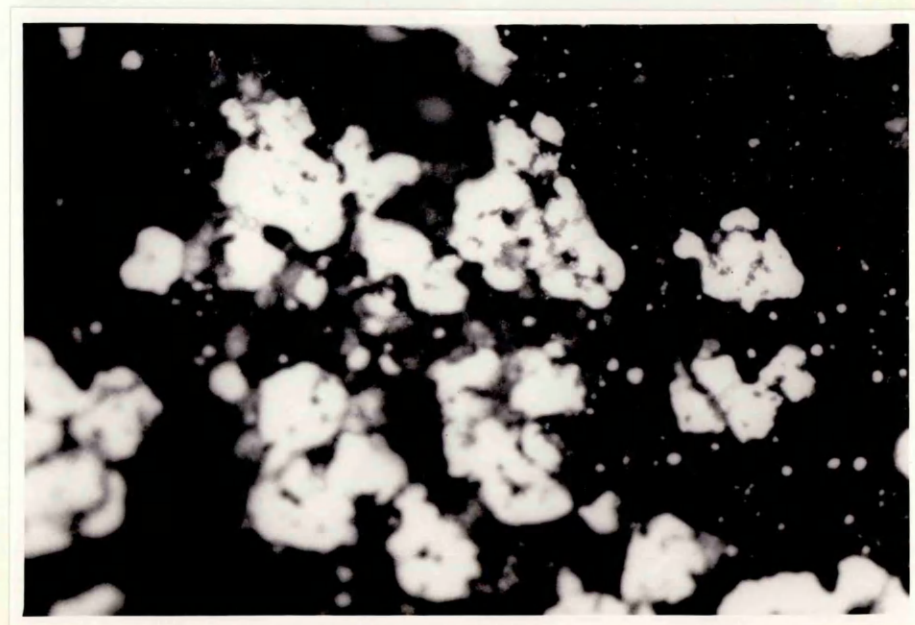
A.F. Sinter Pellet. Reduced H_2 $1100^{\circ}C$ 400x
oil
immersion



12



13



14

Fig. 165 (a) A.F. Sinter Pellet. Oxidised 1000^oC 400x

Fig. 165 (b) A.F. Sinter Pellet. Oxidised 1000^oC 400x
Reduced H₂ 800^oC

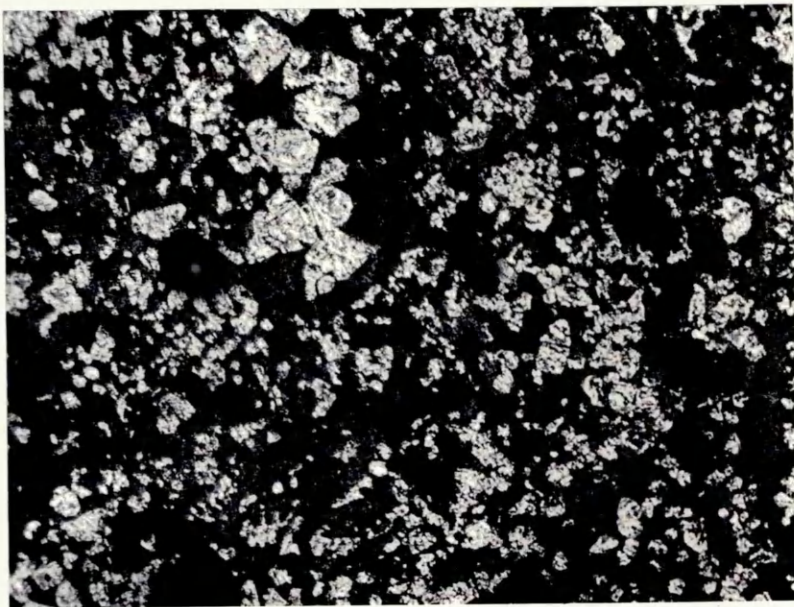


Fig. 166

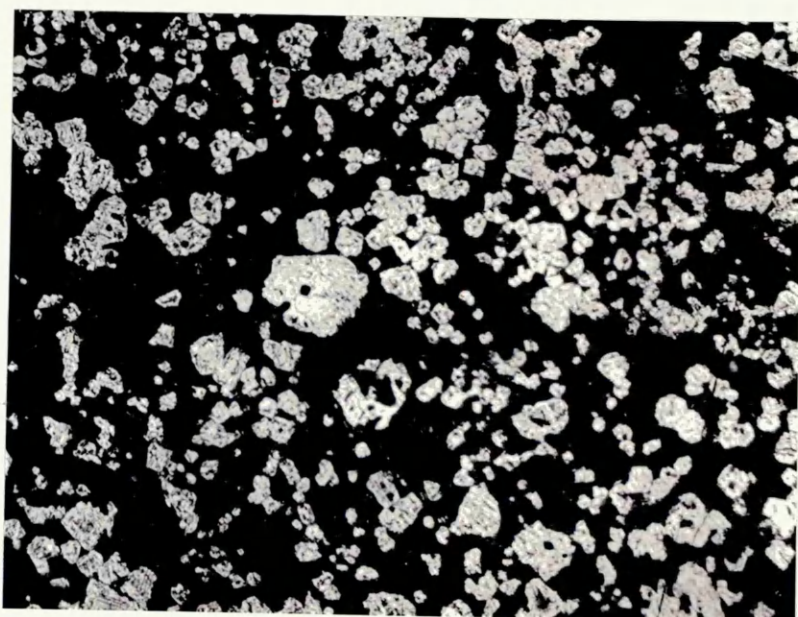
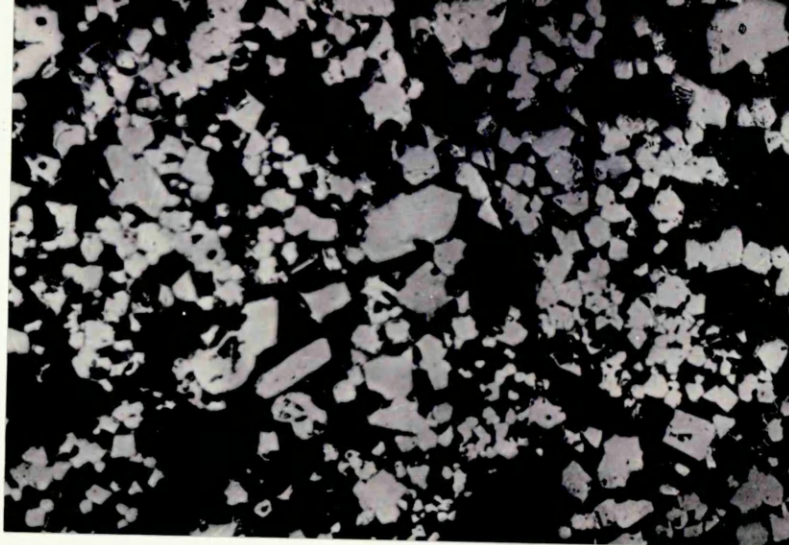
A.F. Sinter Pellet. Oxidised 500°C

400x

Fig. 167

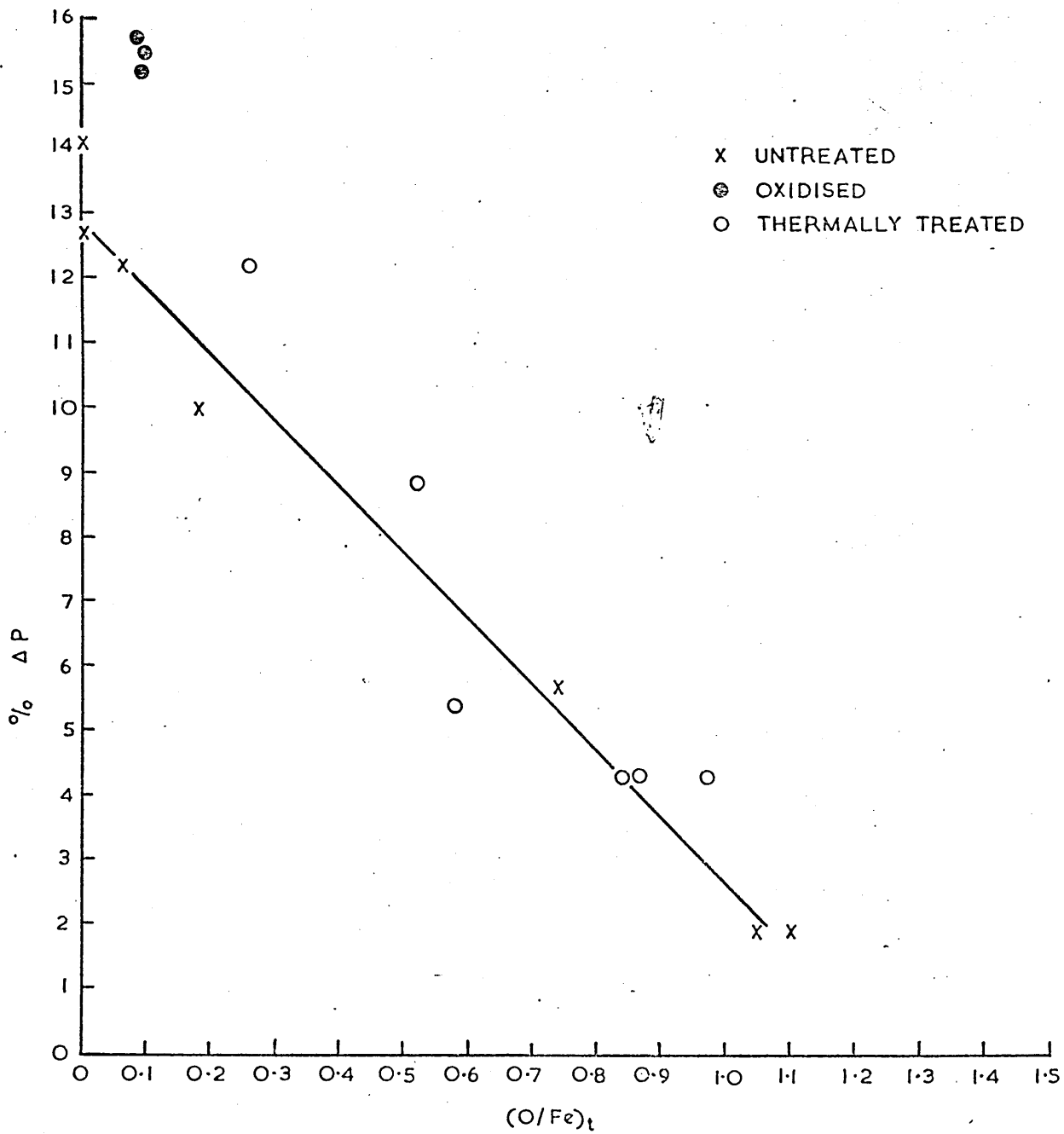
A.F. Sinter Pellet. Oxidised 500°C
Reduced H₂ 800°C

400x



CHANGE IN POROSITY OF SINTER PELLETS

% ΔP VS. $(O/Fe)_t$



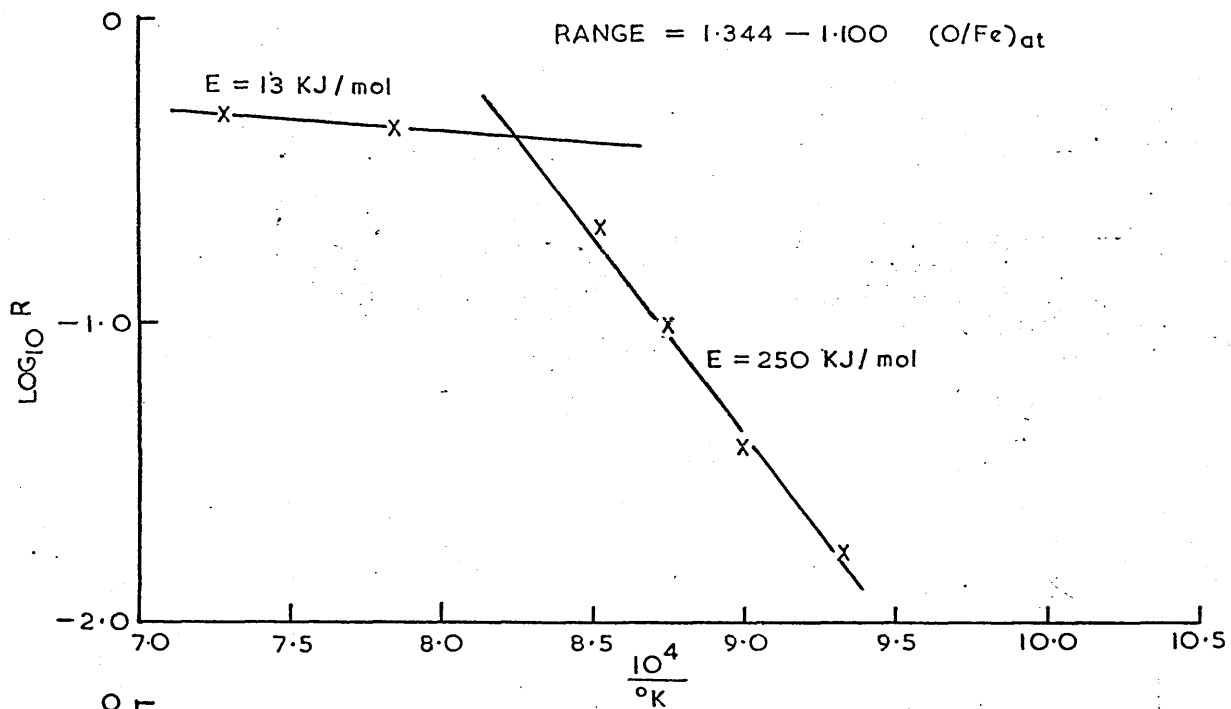


FIG. 169

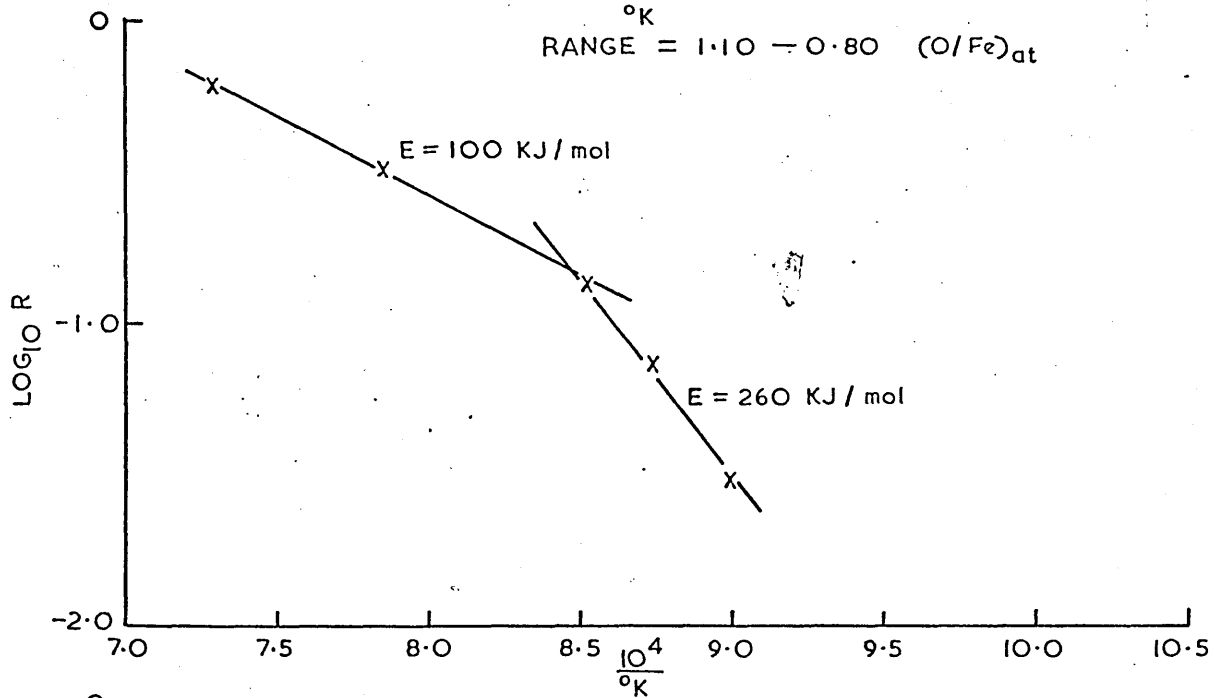


FIG. 170

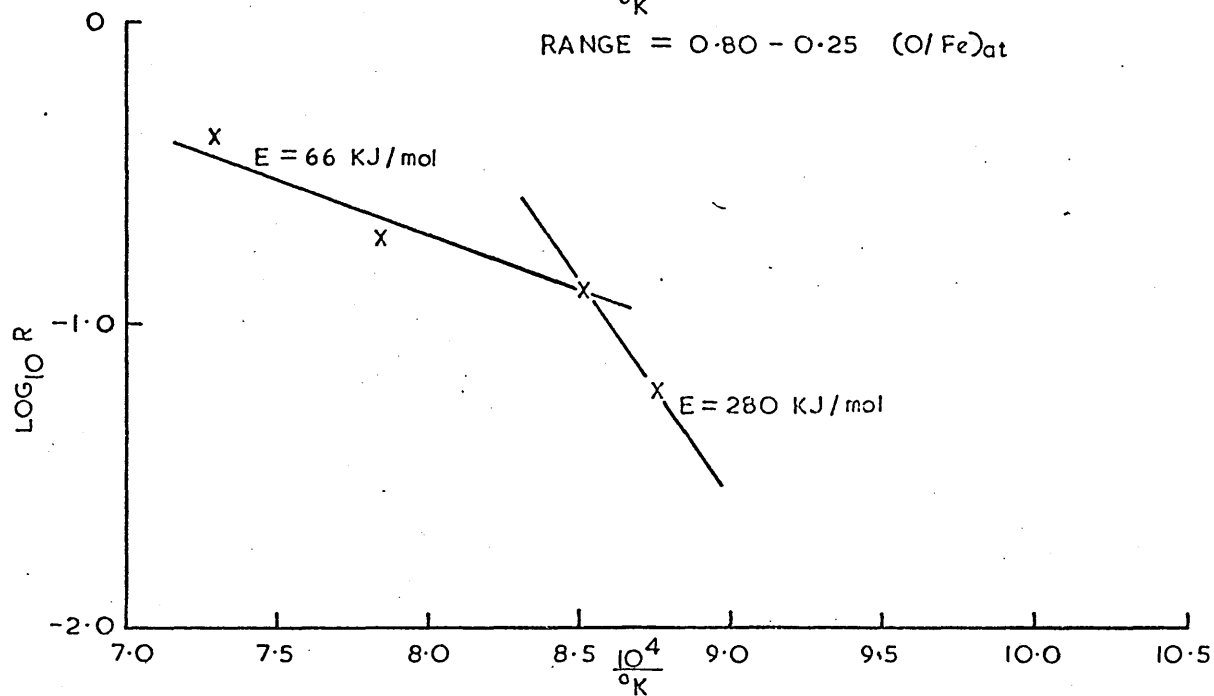


FIG. 171

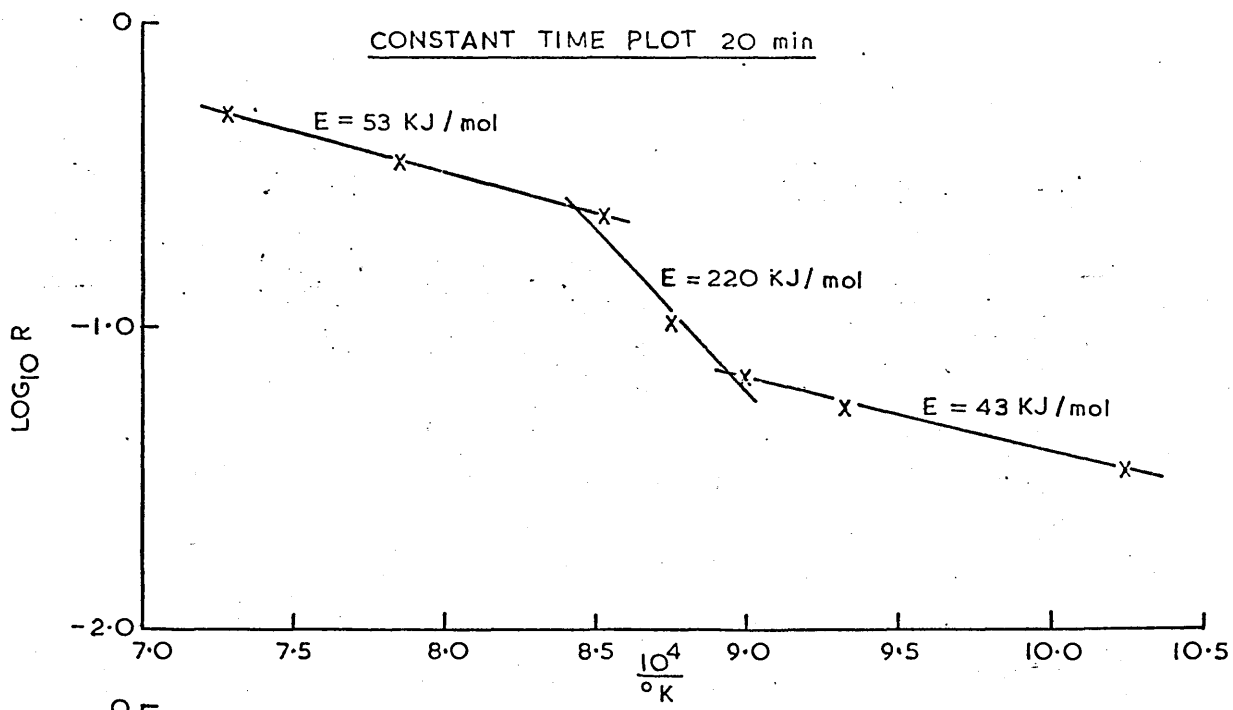


FIG. 172

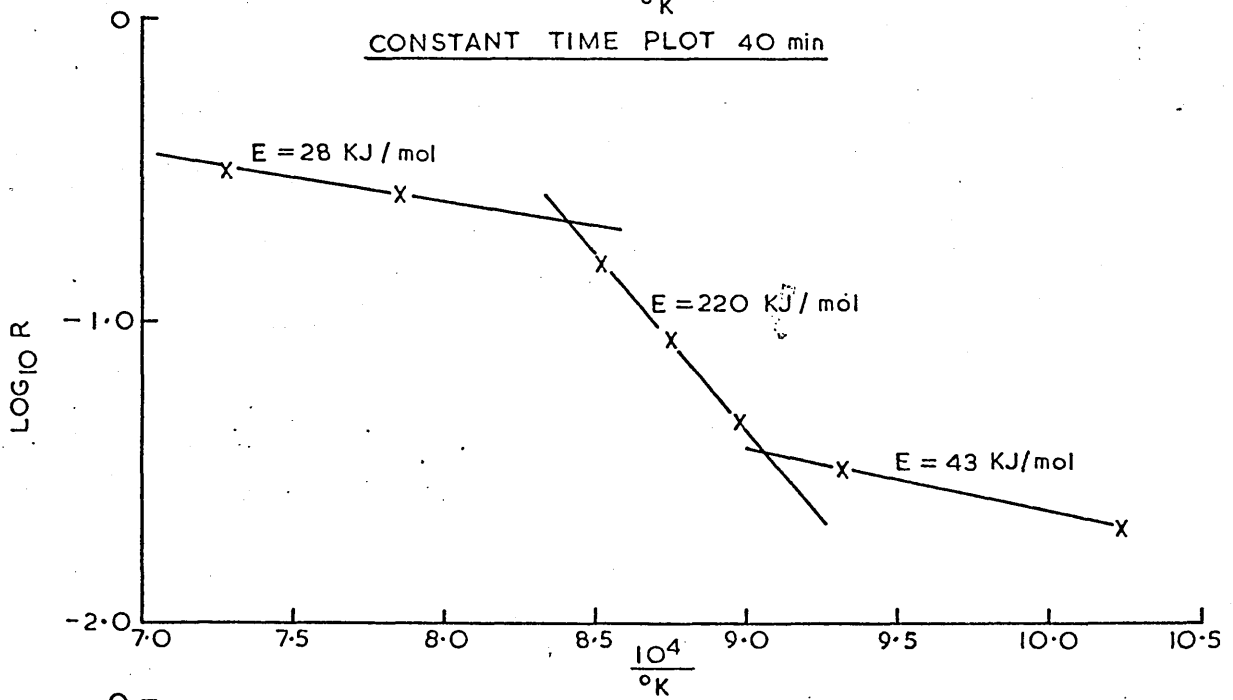


FIG. 173

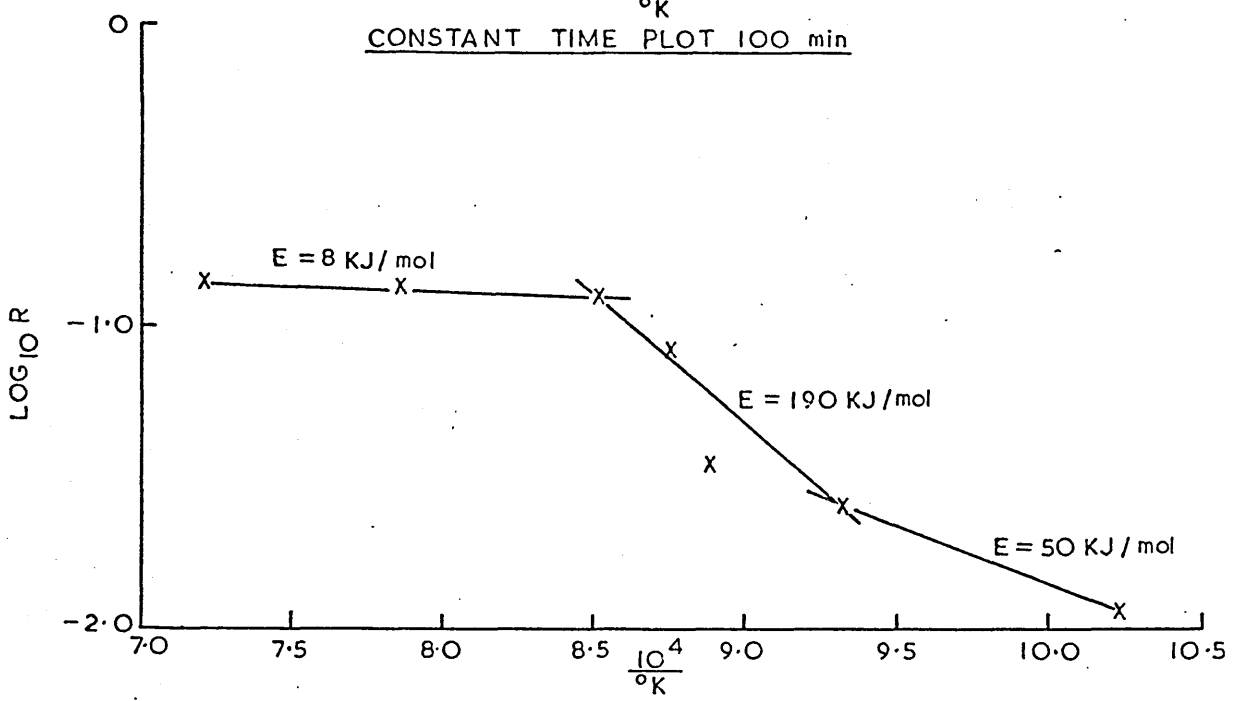


FIG. 174

INDIVIDUAL RATE LAW PLOTS

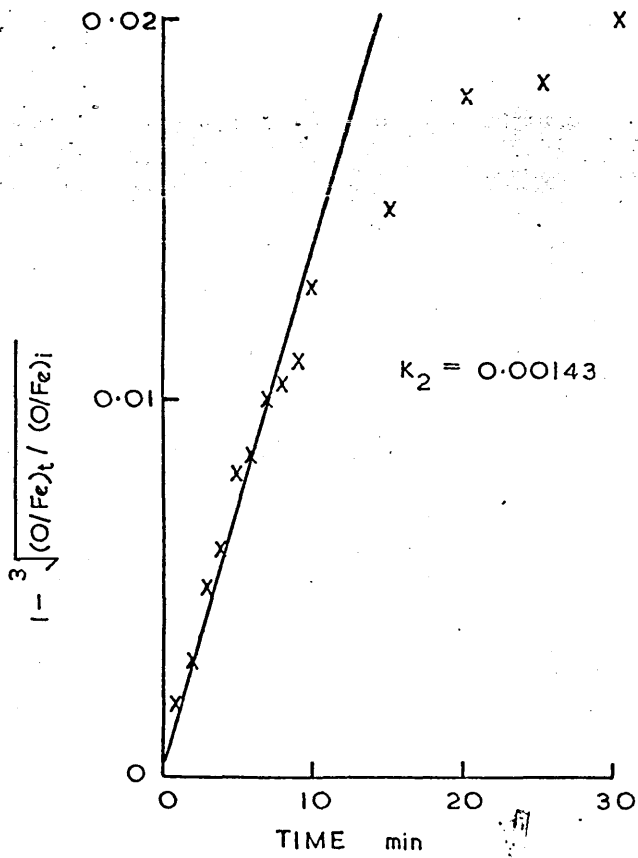


FIG. 175 a

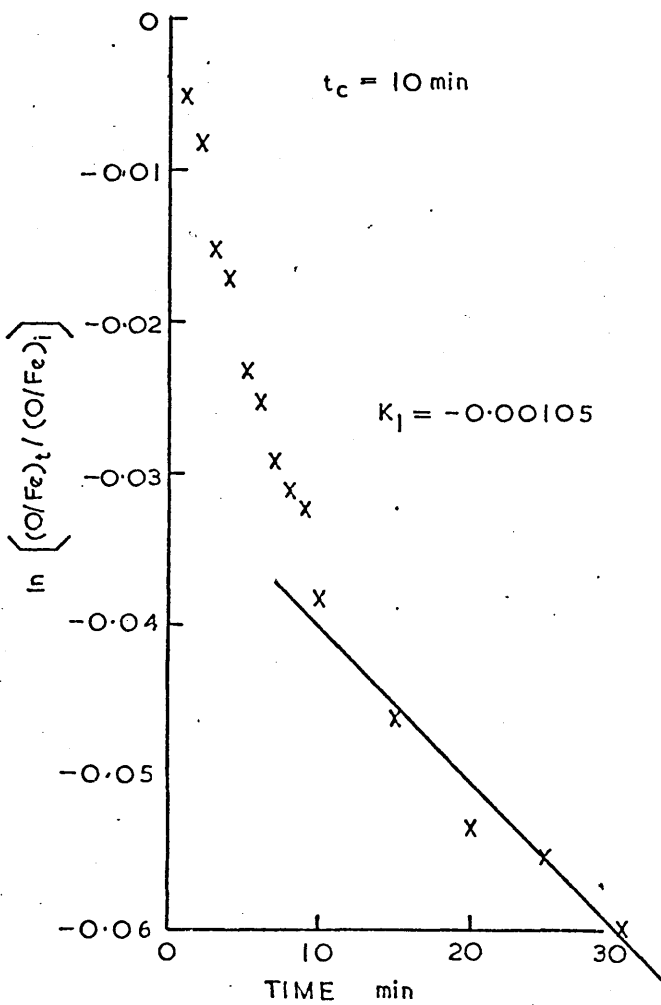


FIG. 175 b

FIG. 175 a & 175 b

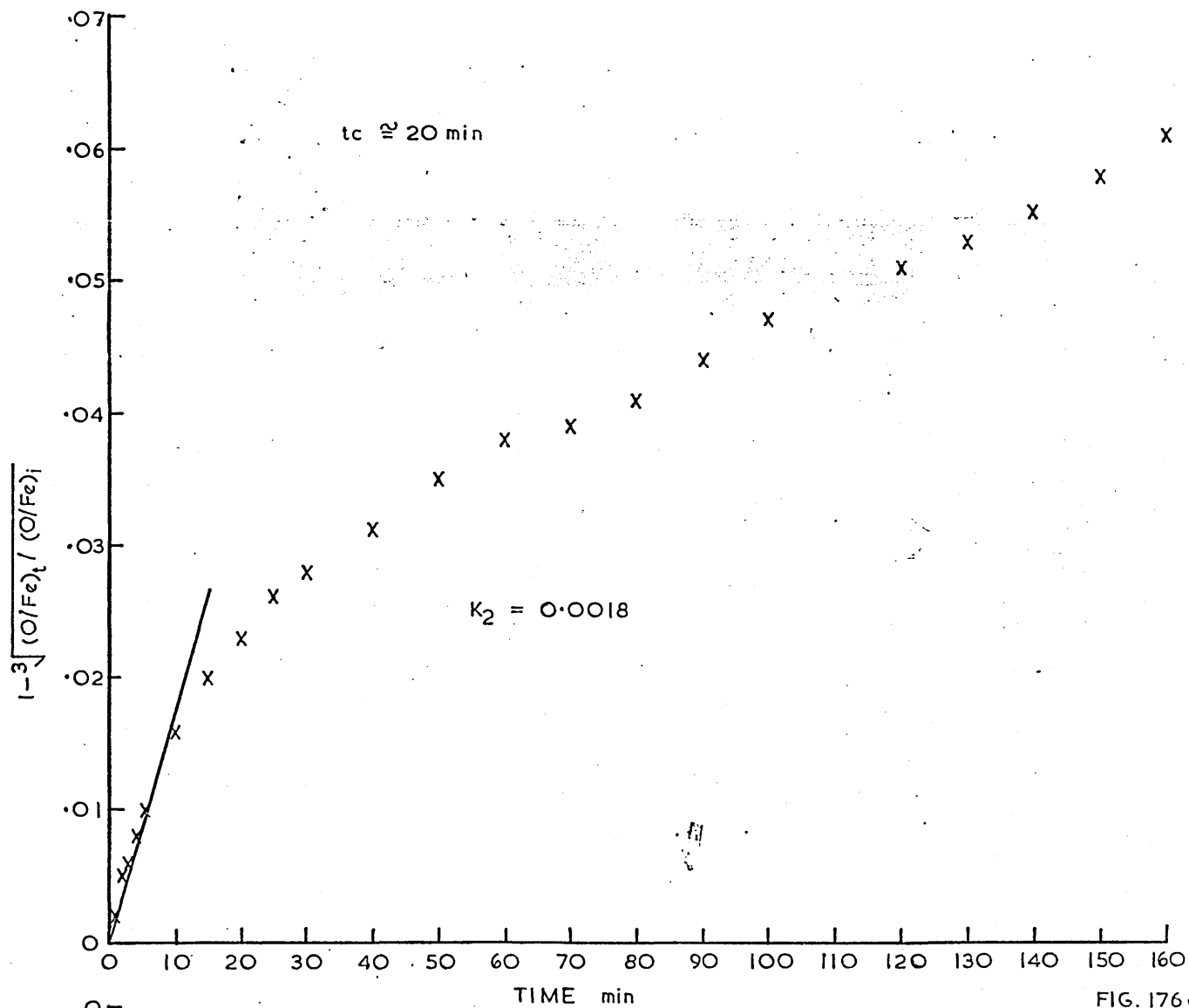


FIG. 176a

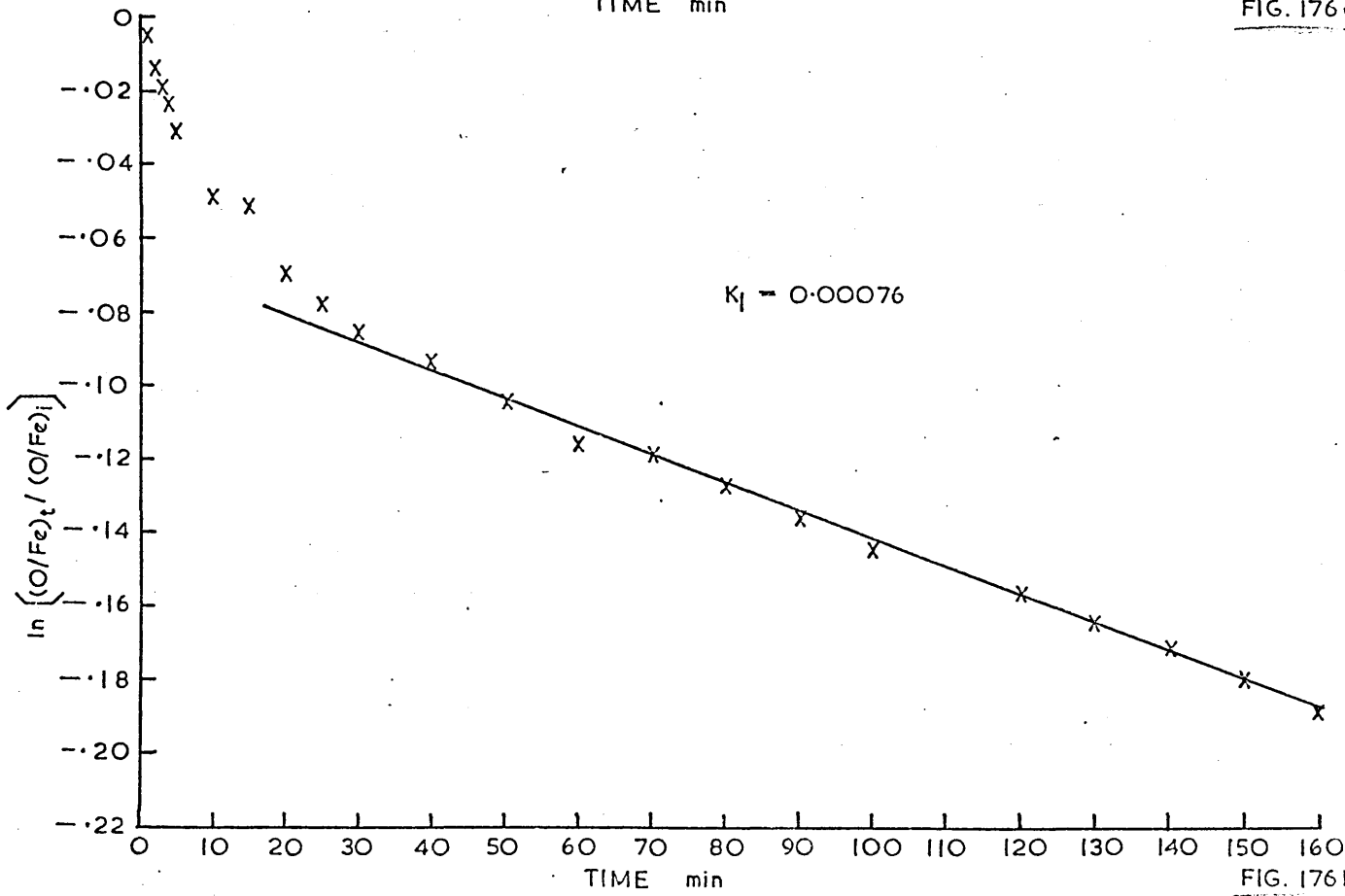


FIG. 176b

FIG. 176a & 176b

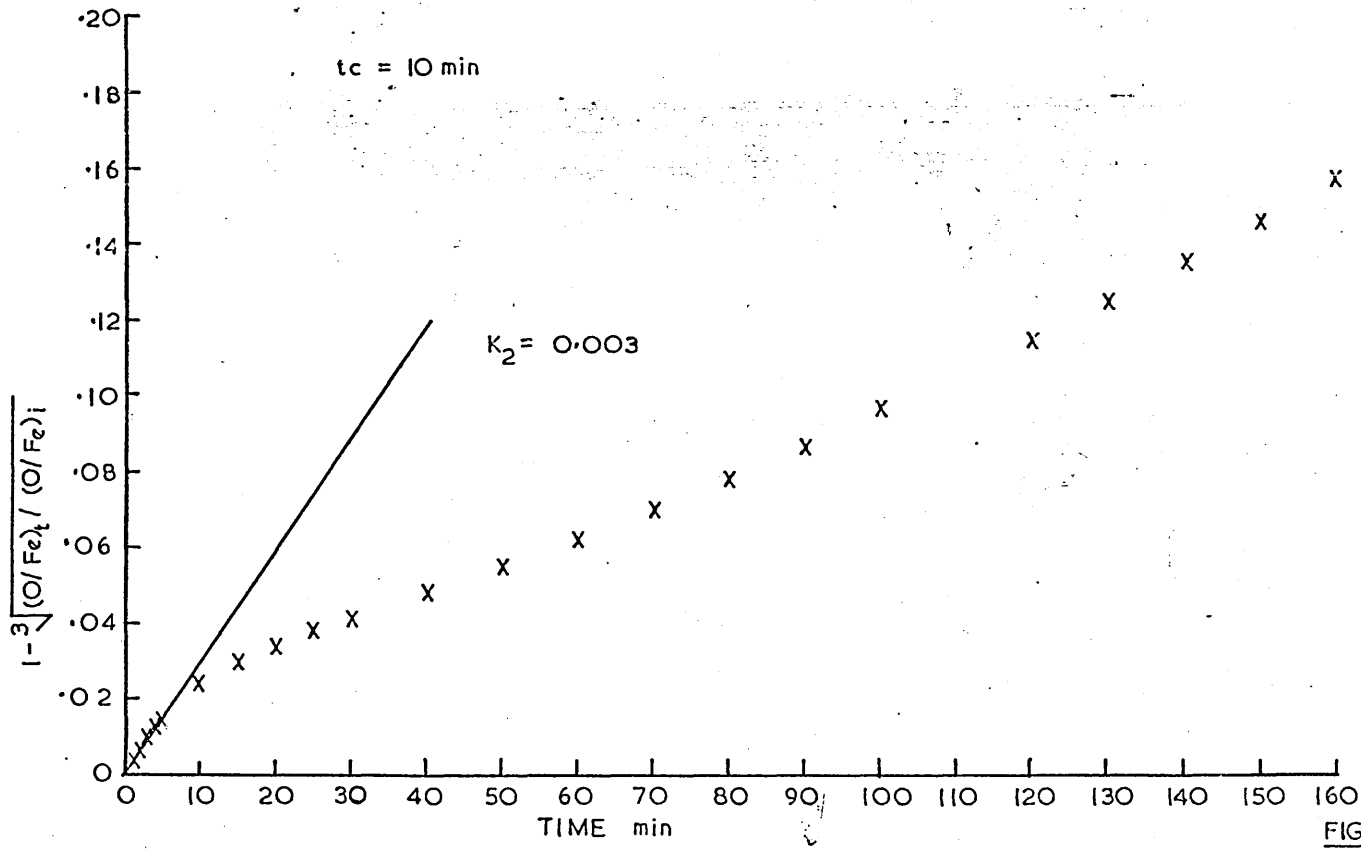


FIG. 177a

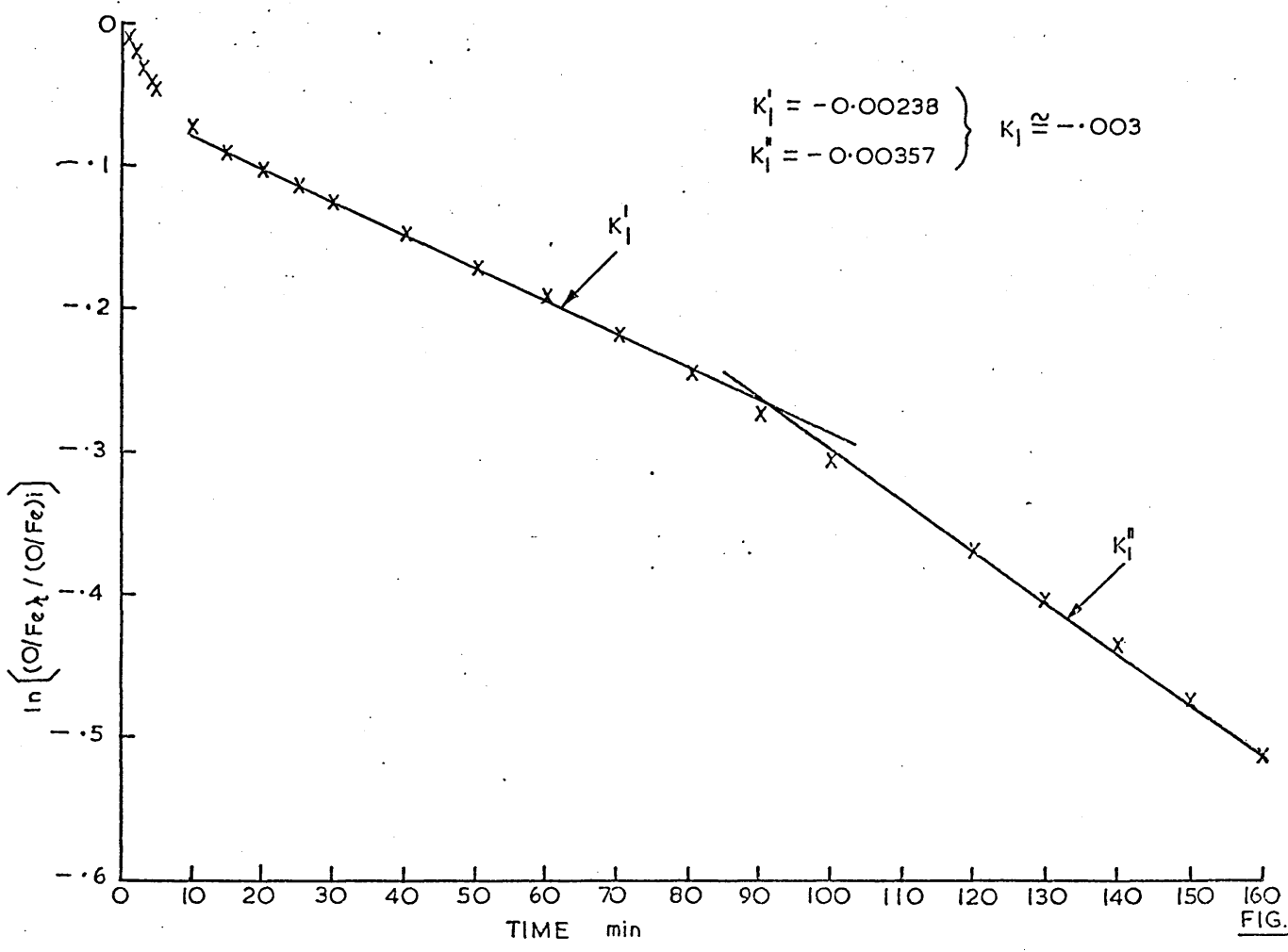


FIG. 177b

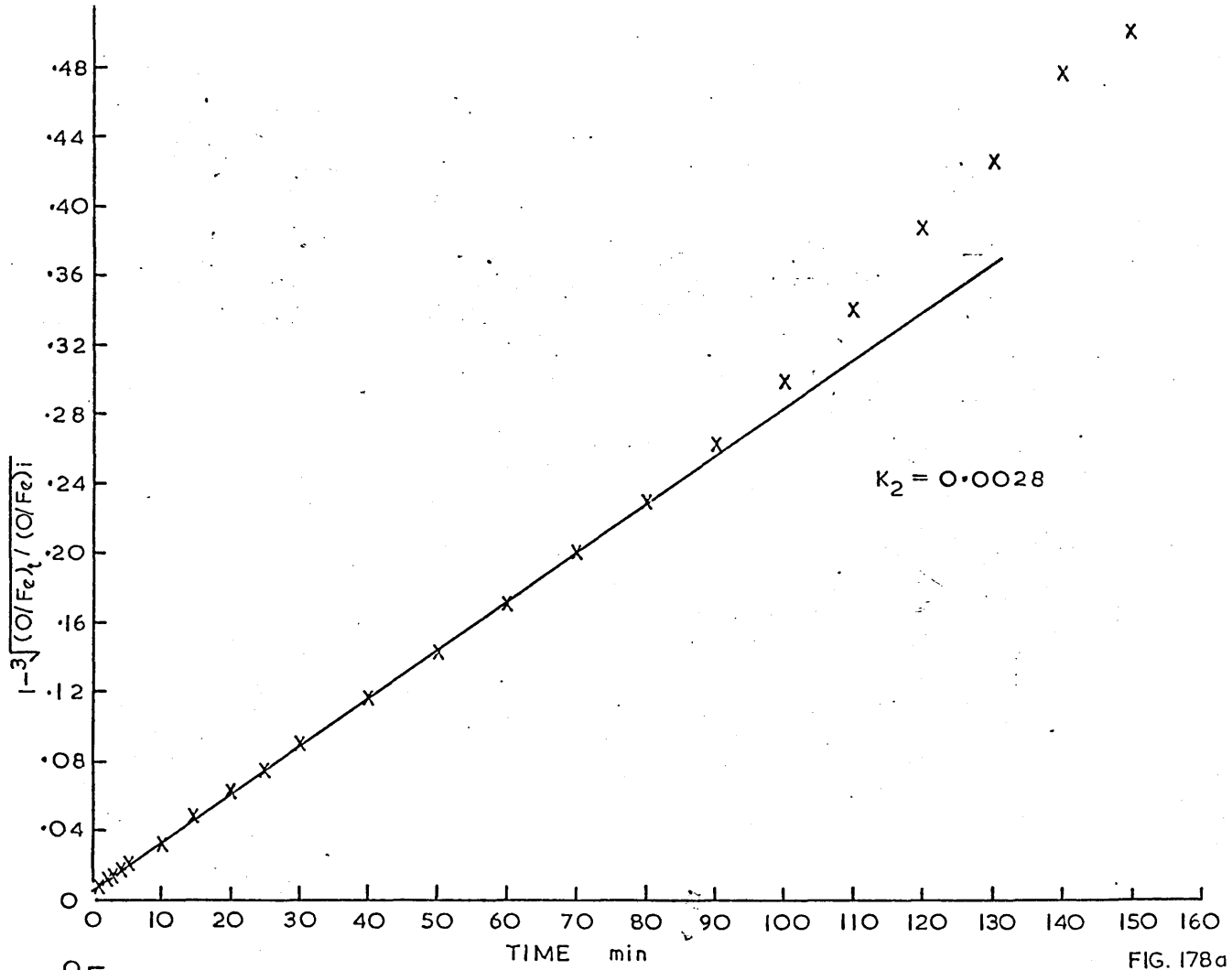


FIG. 178a

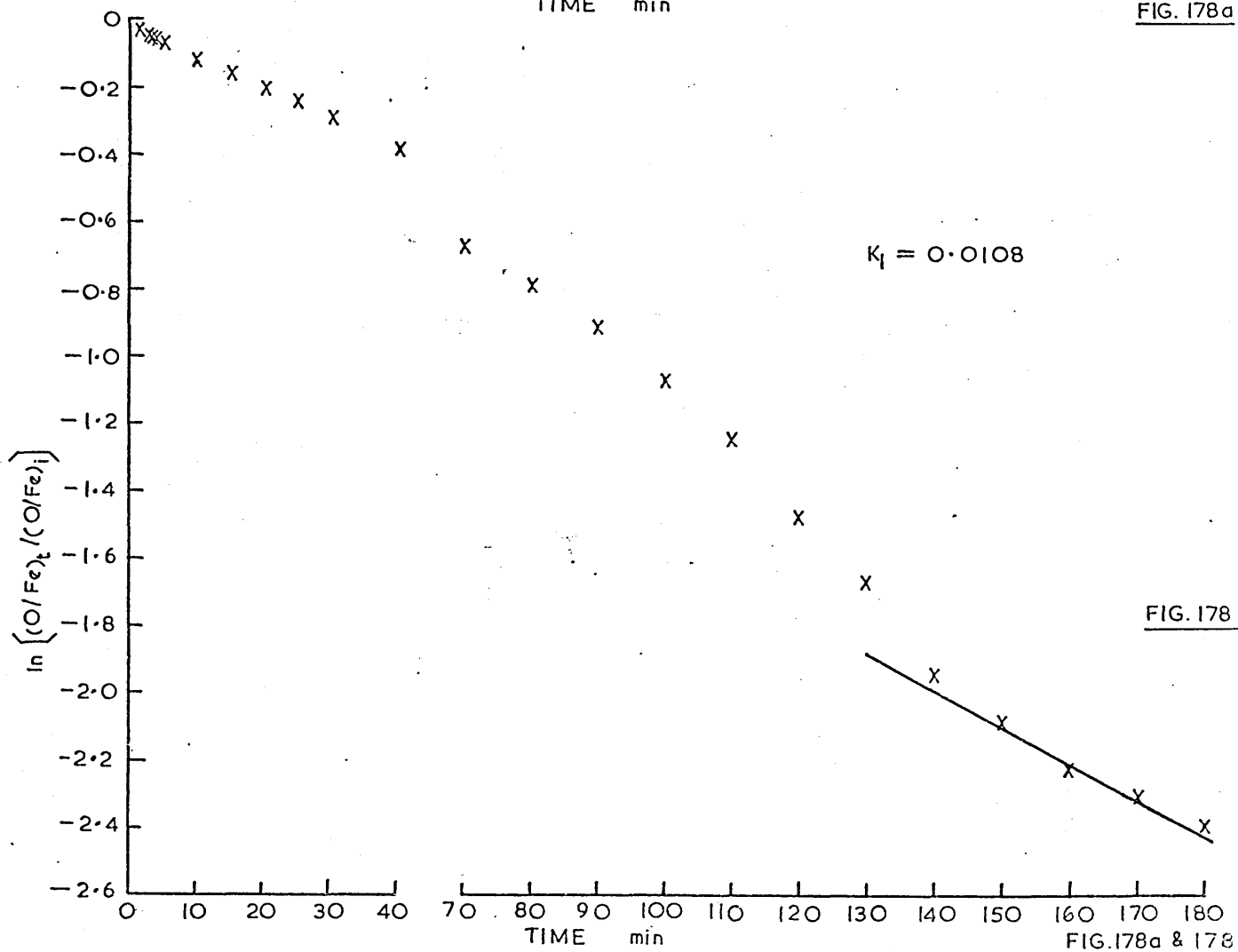


FIG. 178b

FIG. 178a & 178b

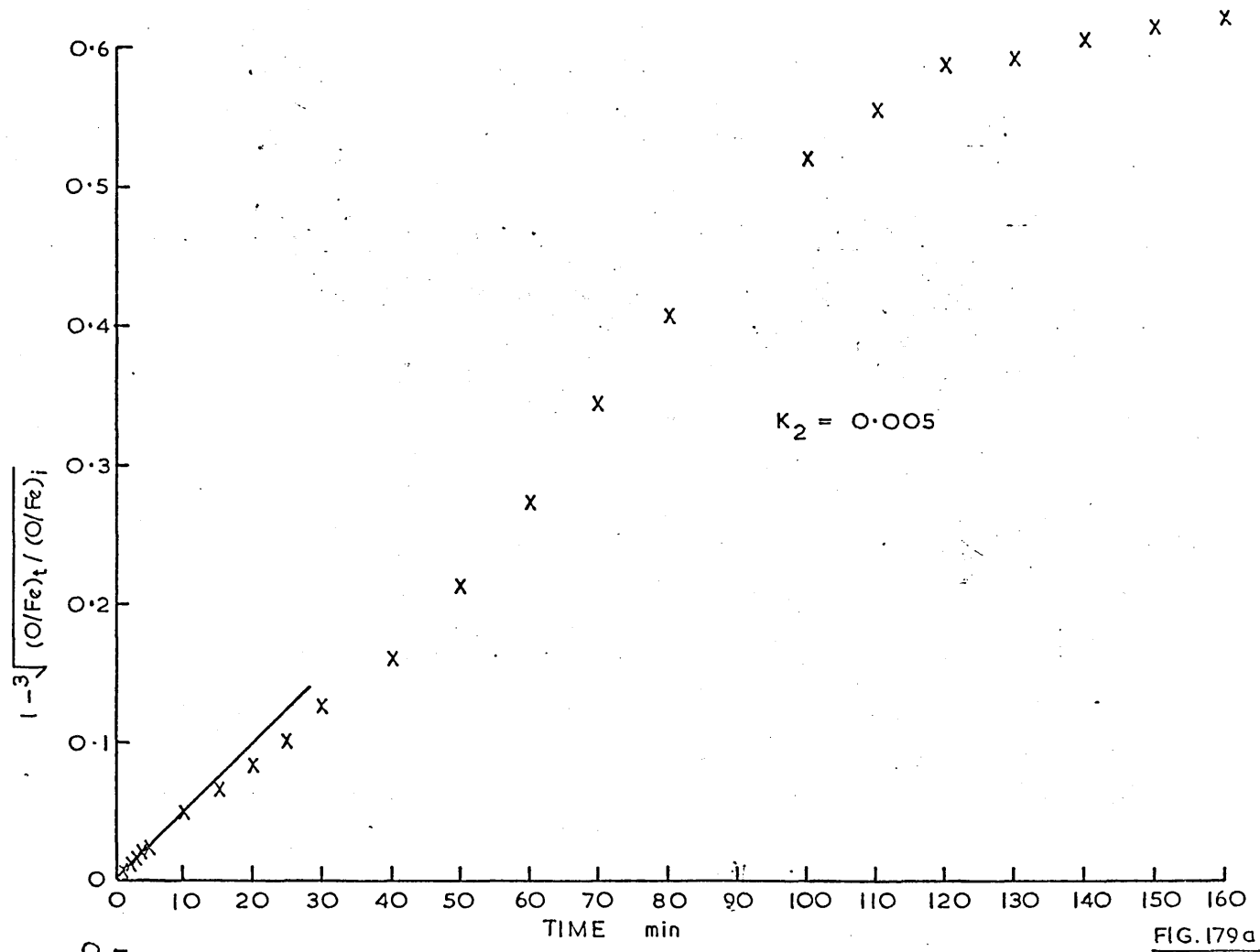


FIG. 179a

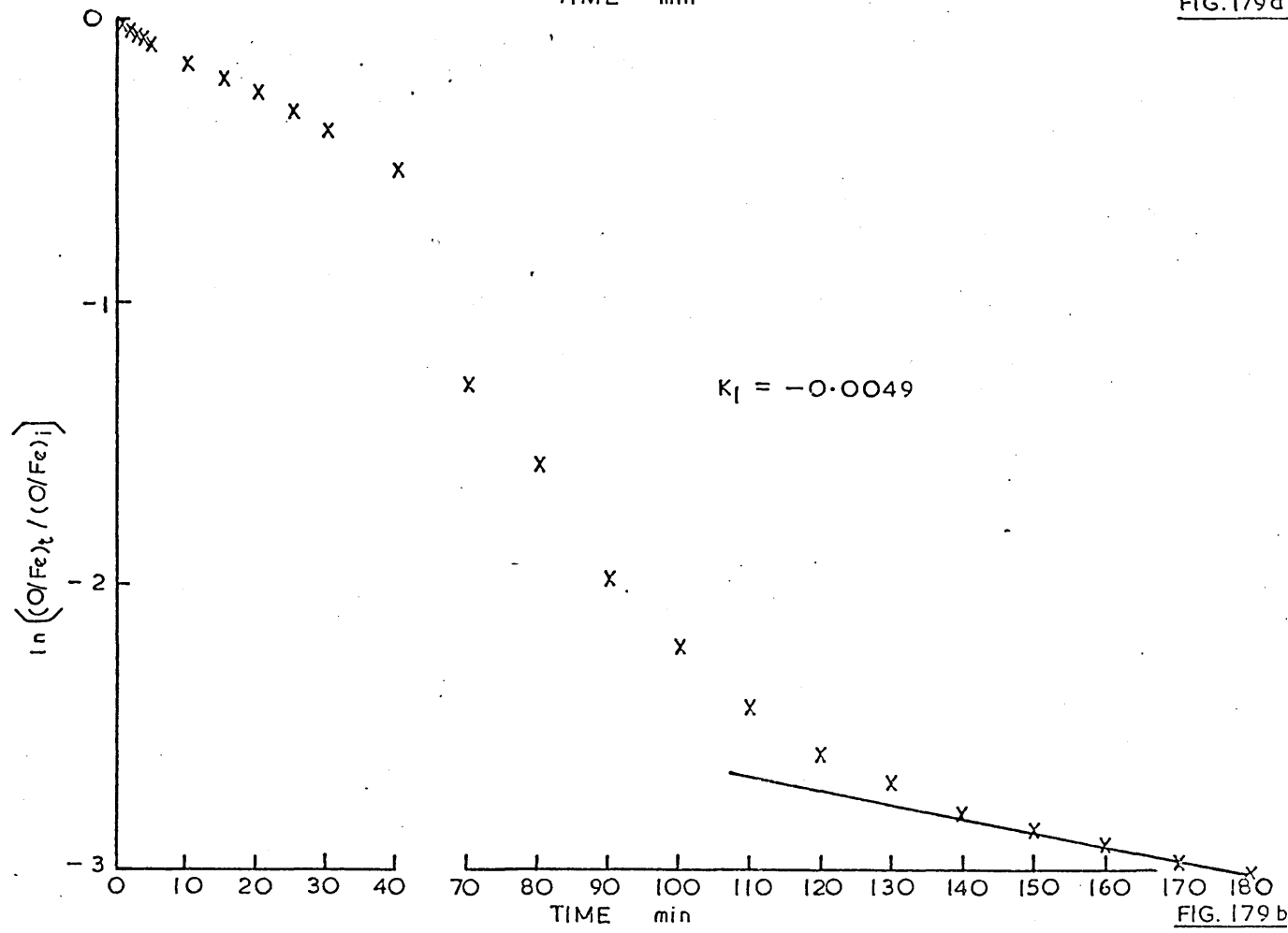


FIG. 179b

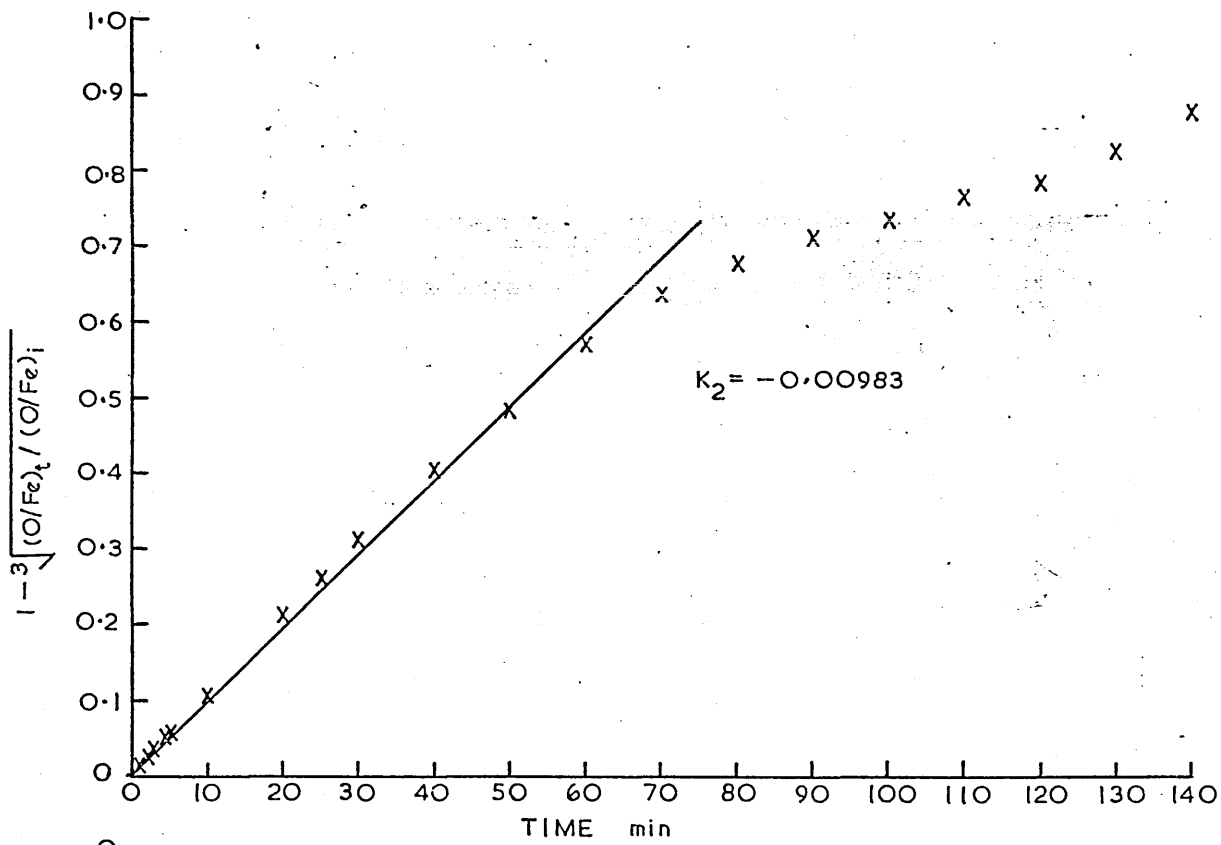


FIG. 180a

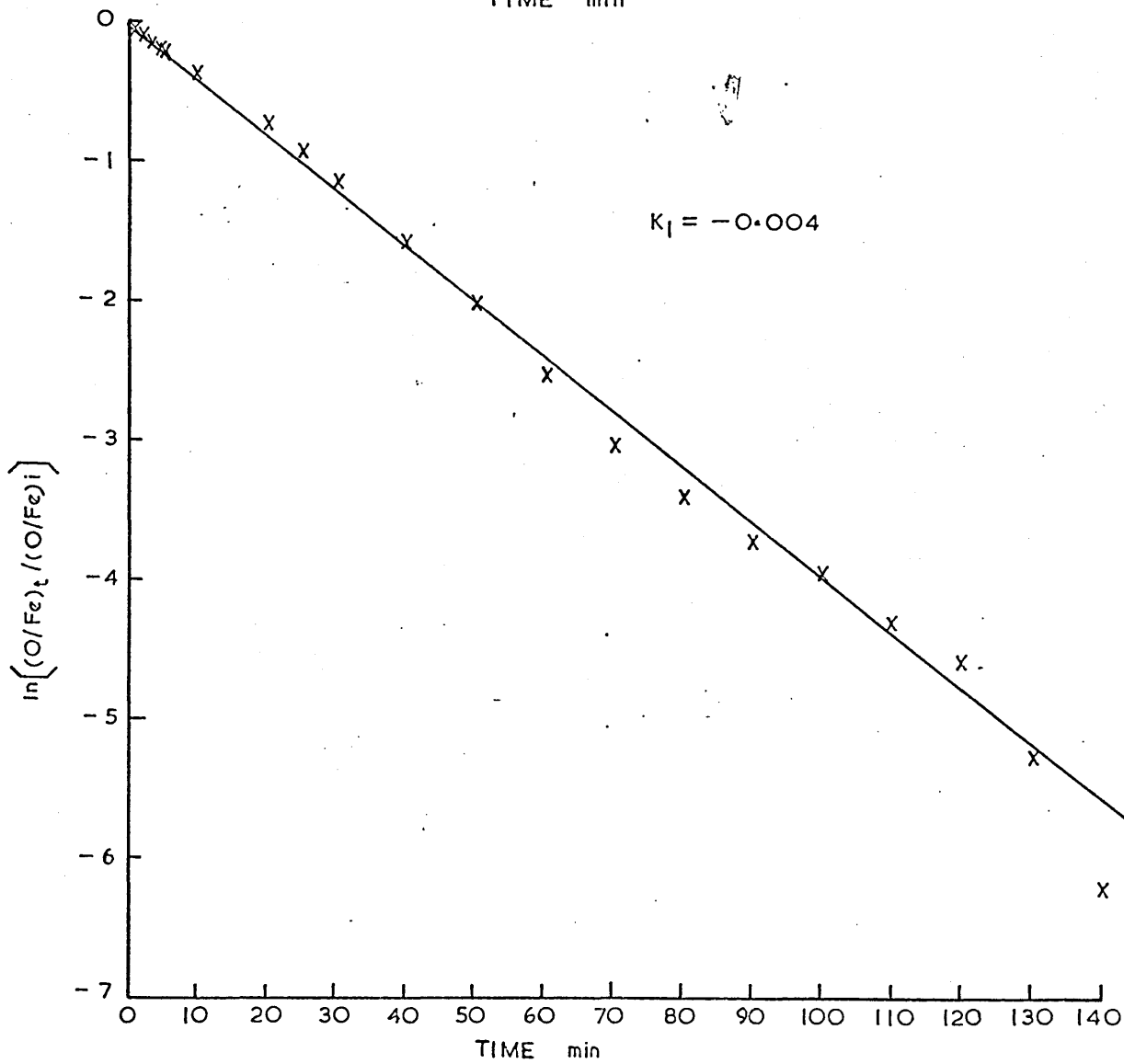


FIG. 180 b

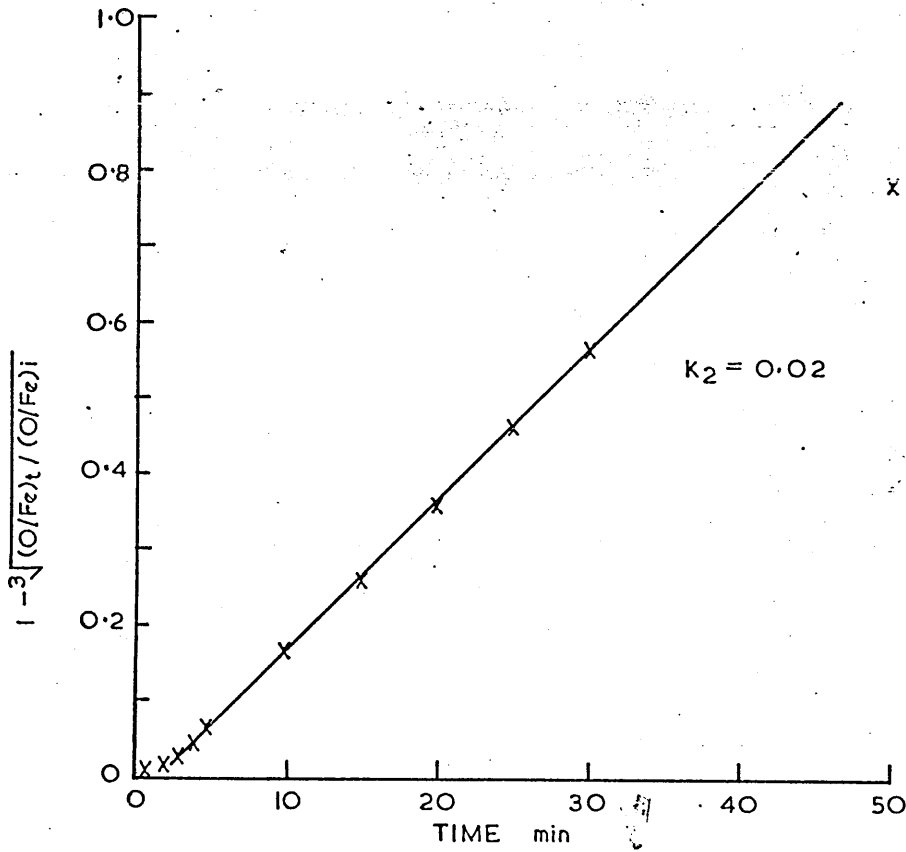


FIG. 181a

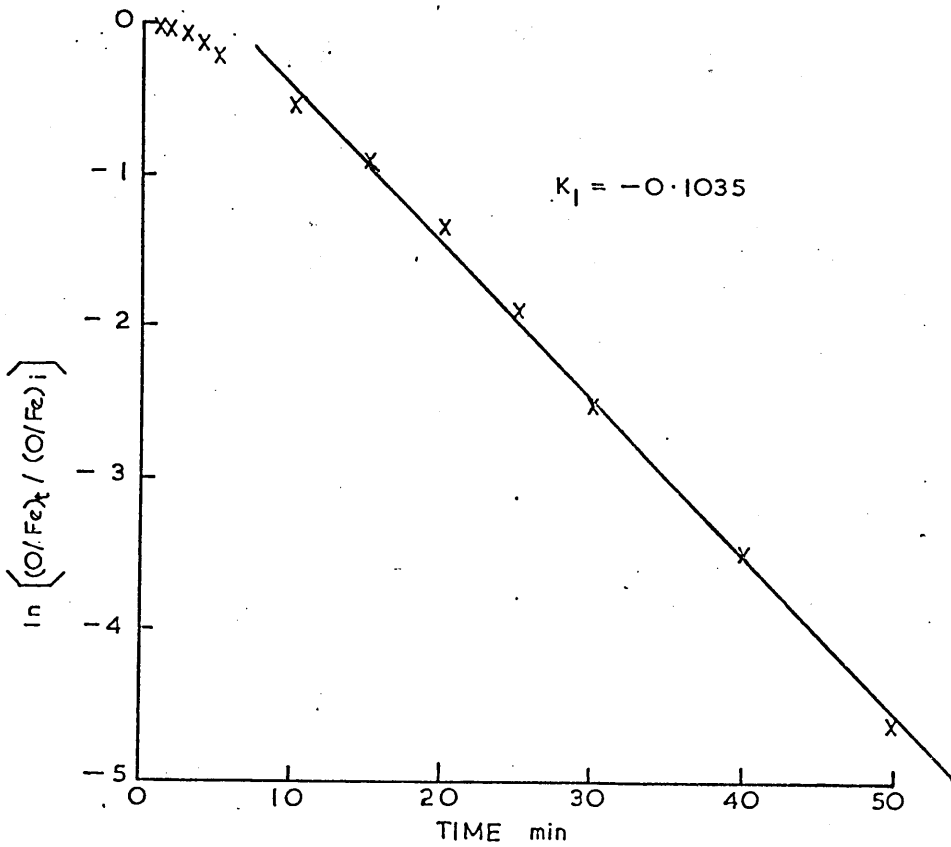
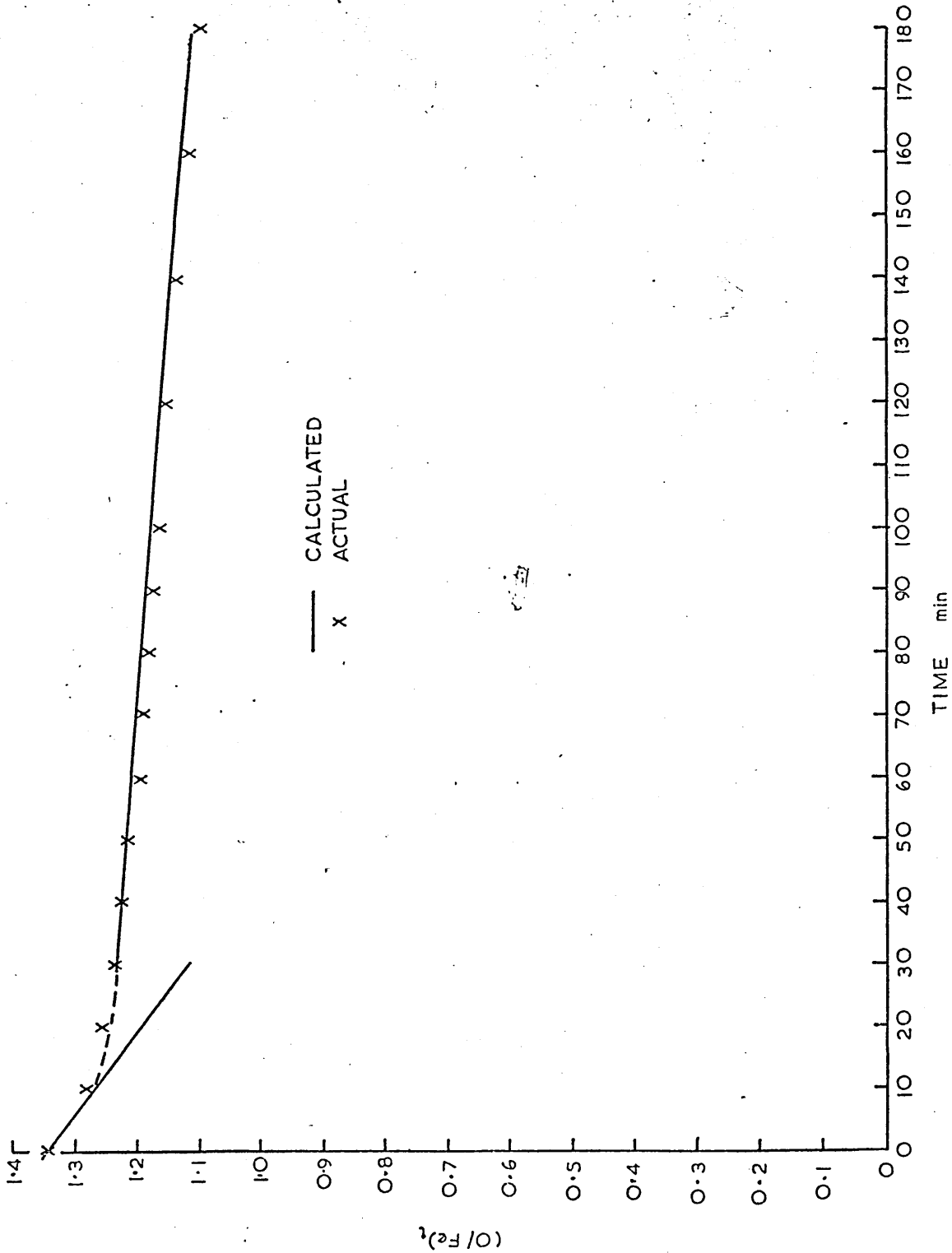


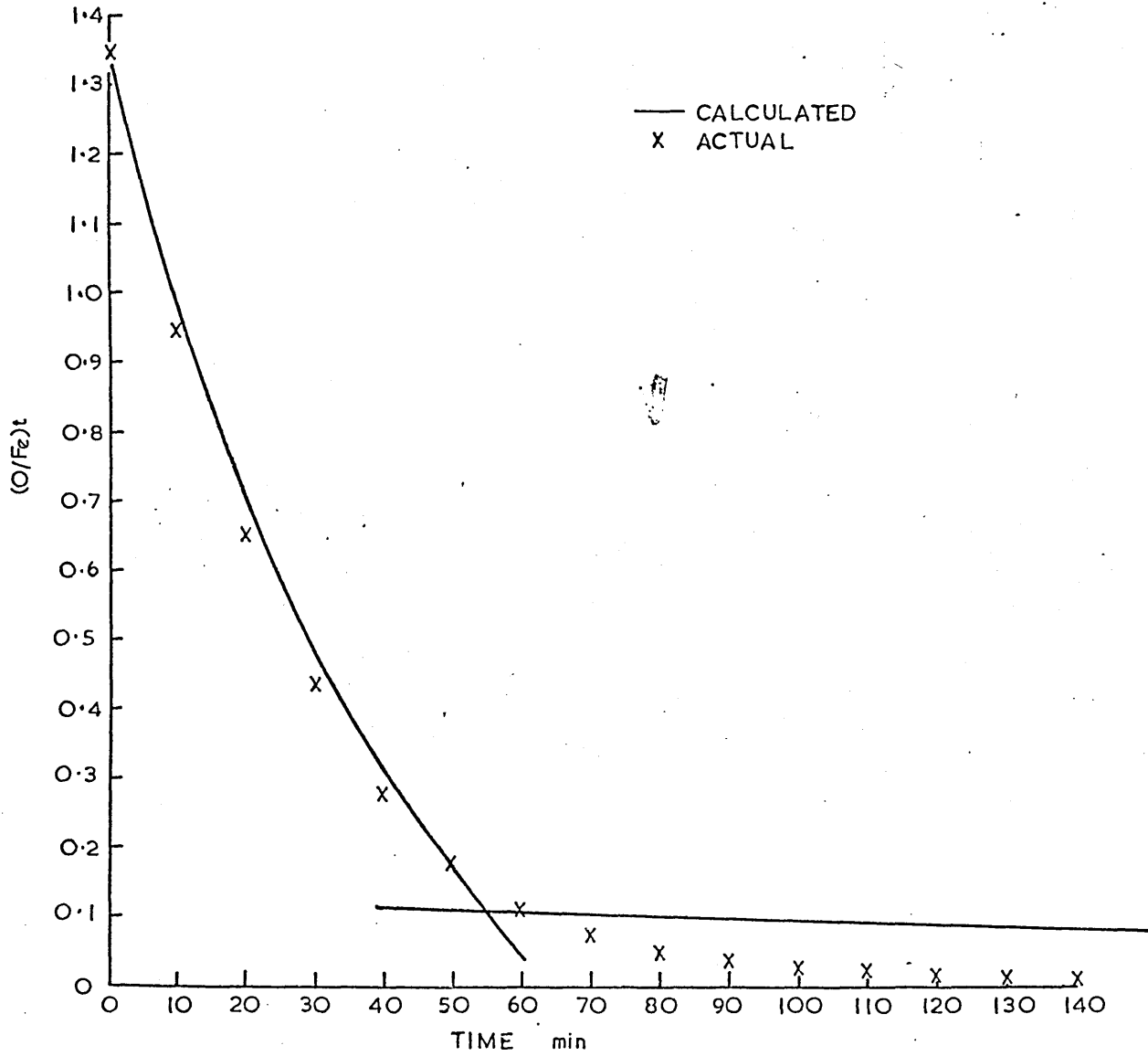
FIG. 181b

MANUAL GENERAL LAW PLOTS



A/F SINTER PELLETS 1000°C

MANUAL GENERAL LAW PLOTS



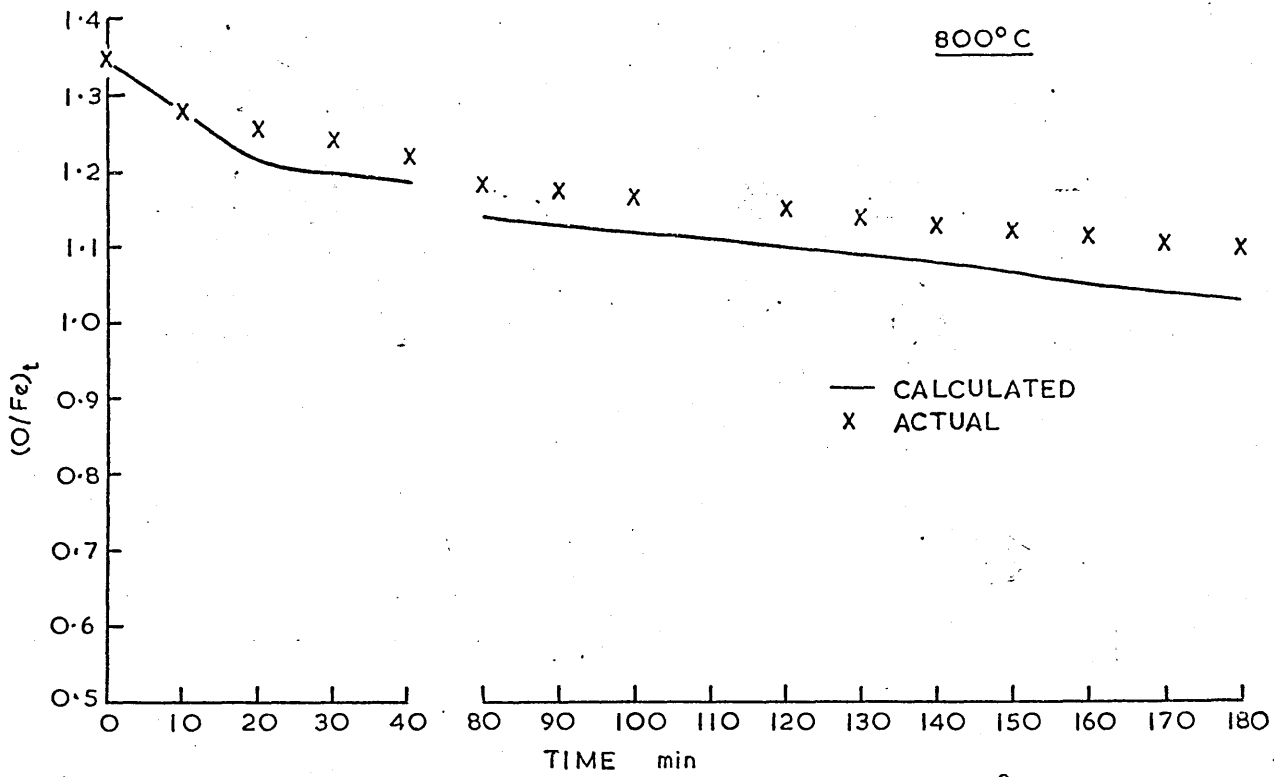


FIG. 184a

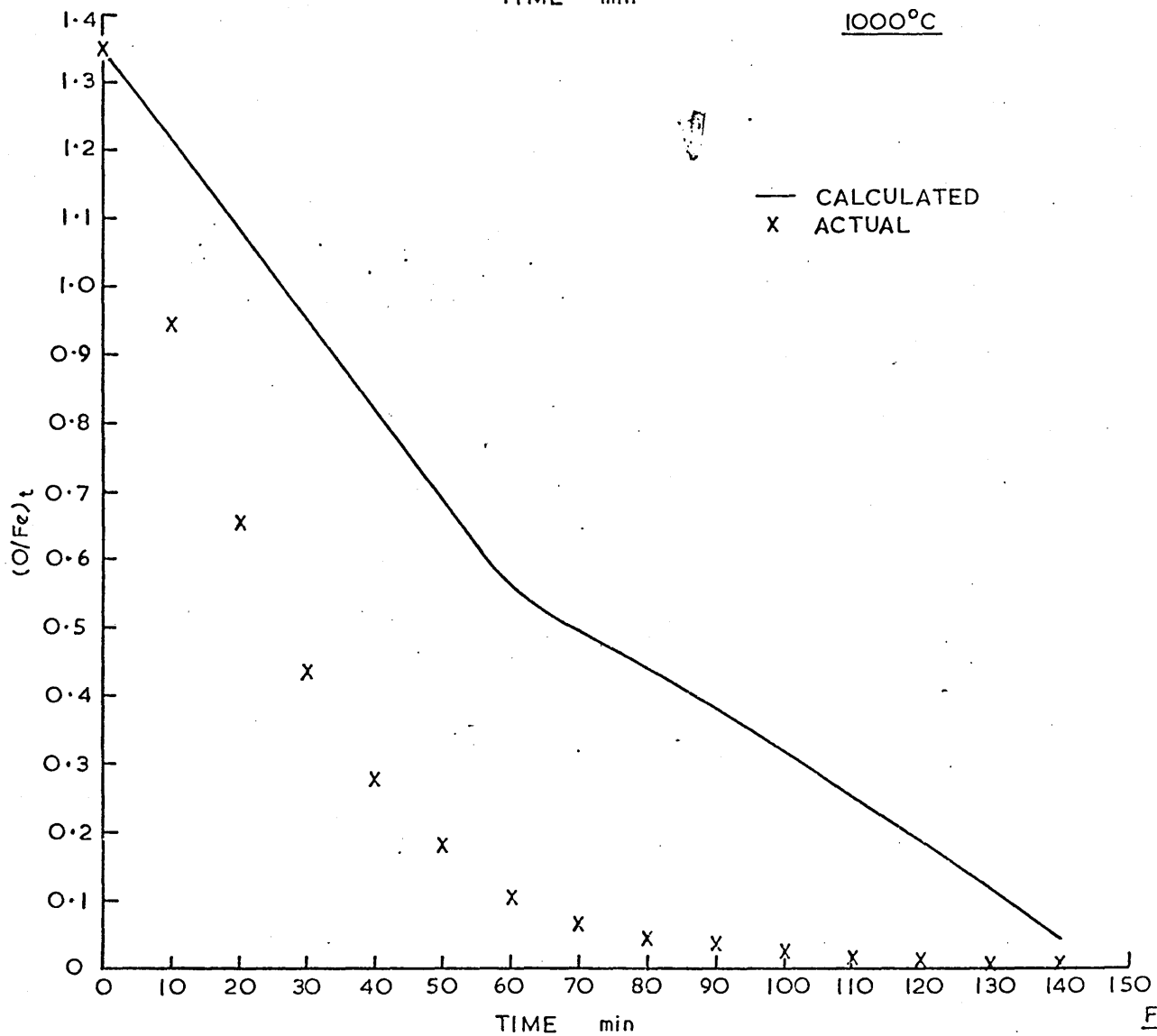


FIG. 184b

COMPUTER INDIVIDUAL AND GENERAL LAW PLOTS

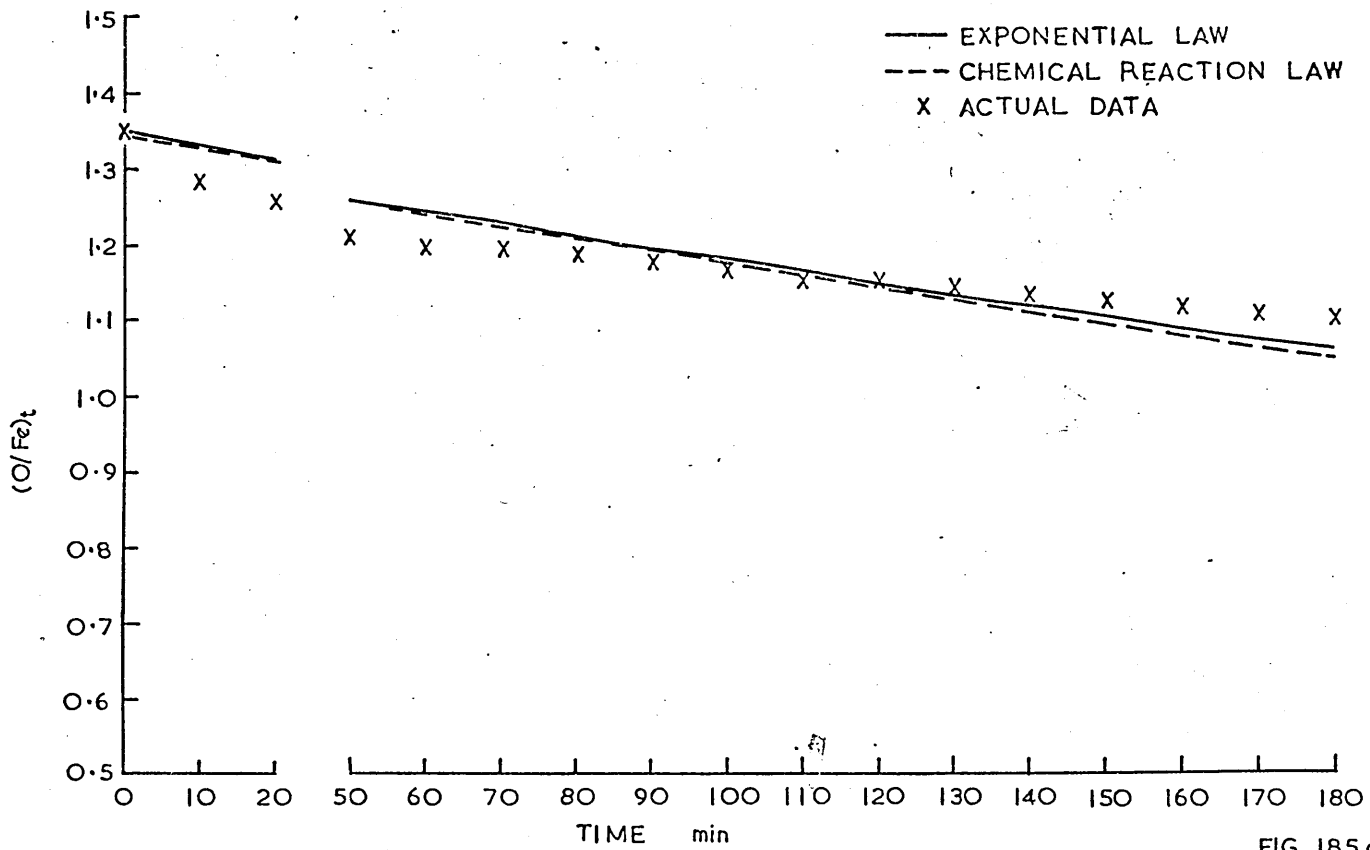


FIG. 185 a

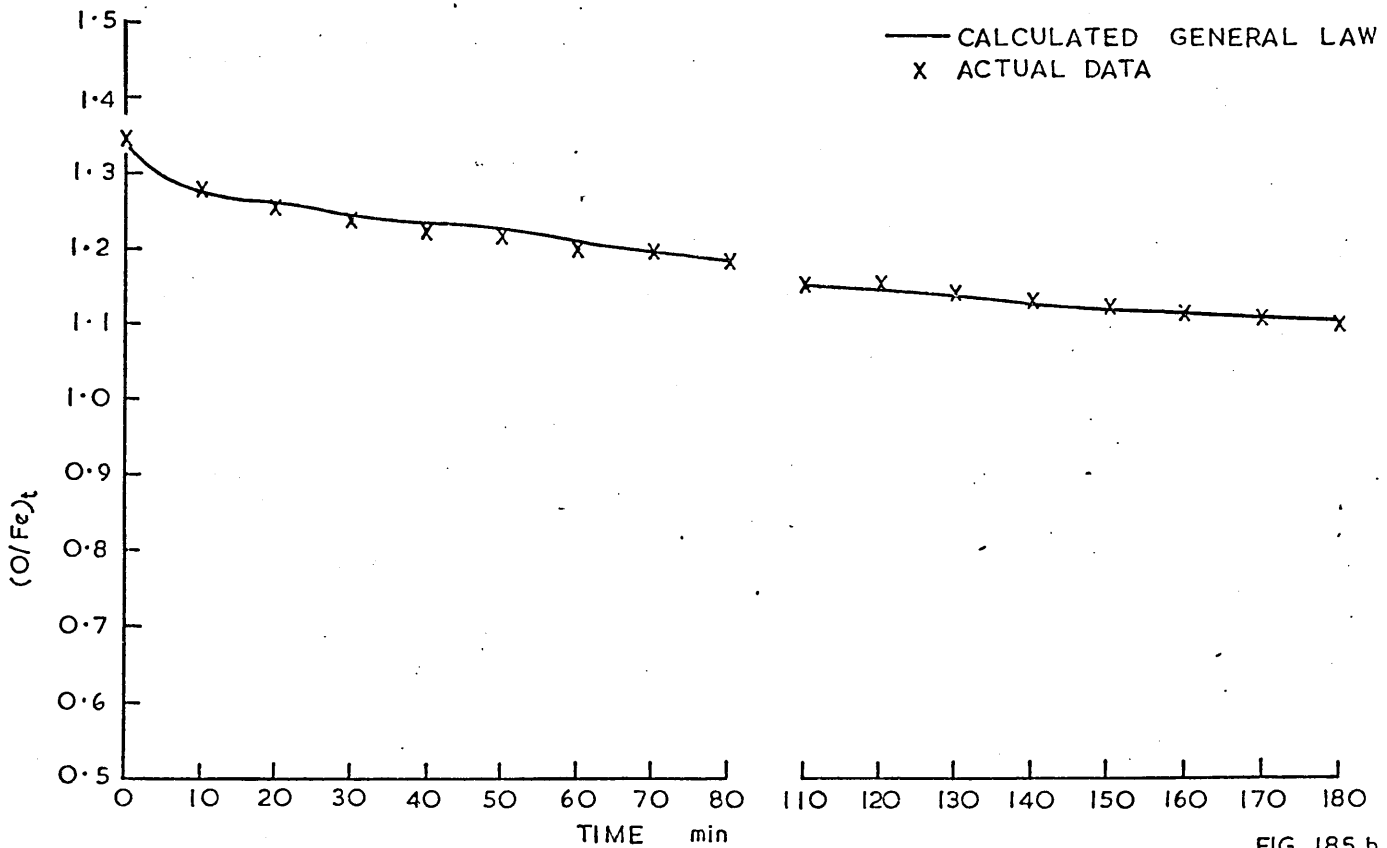


FIG. 185 b

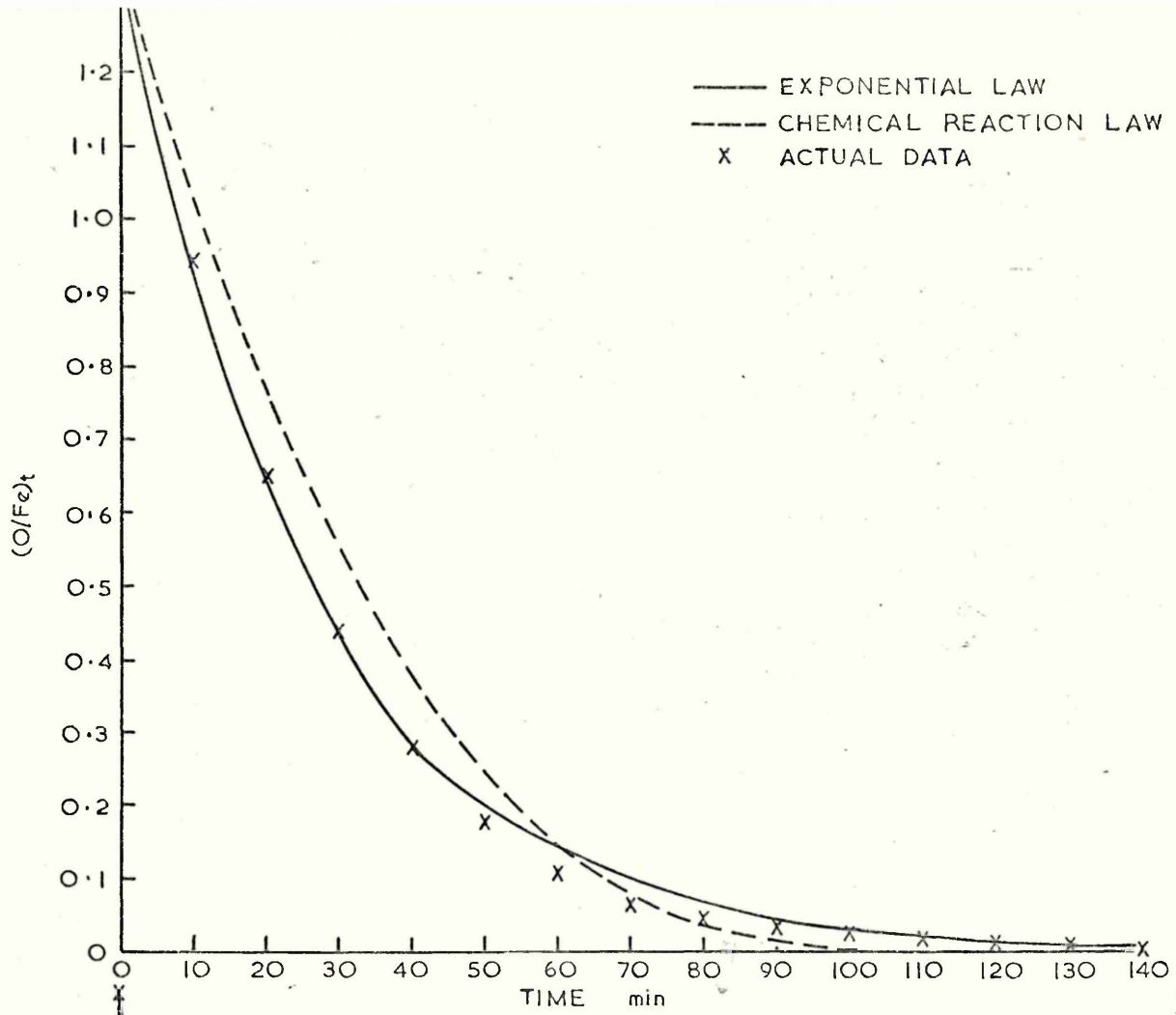


FIG. 186a

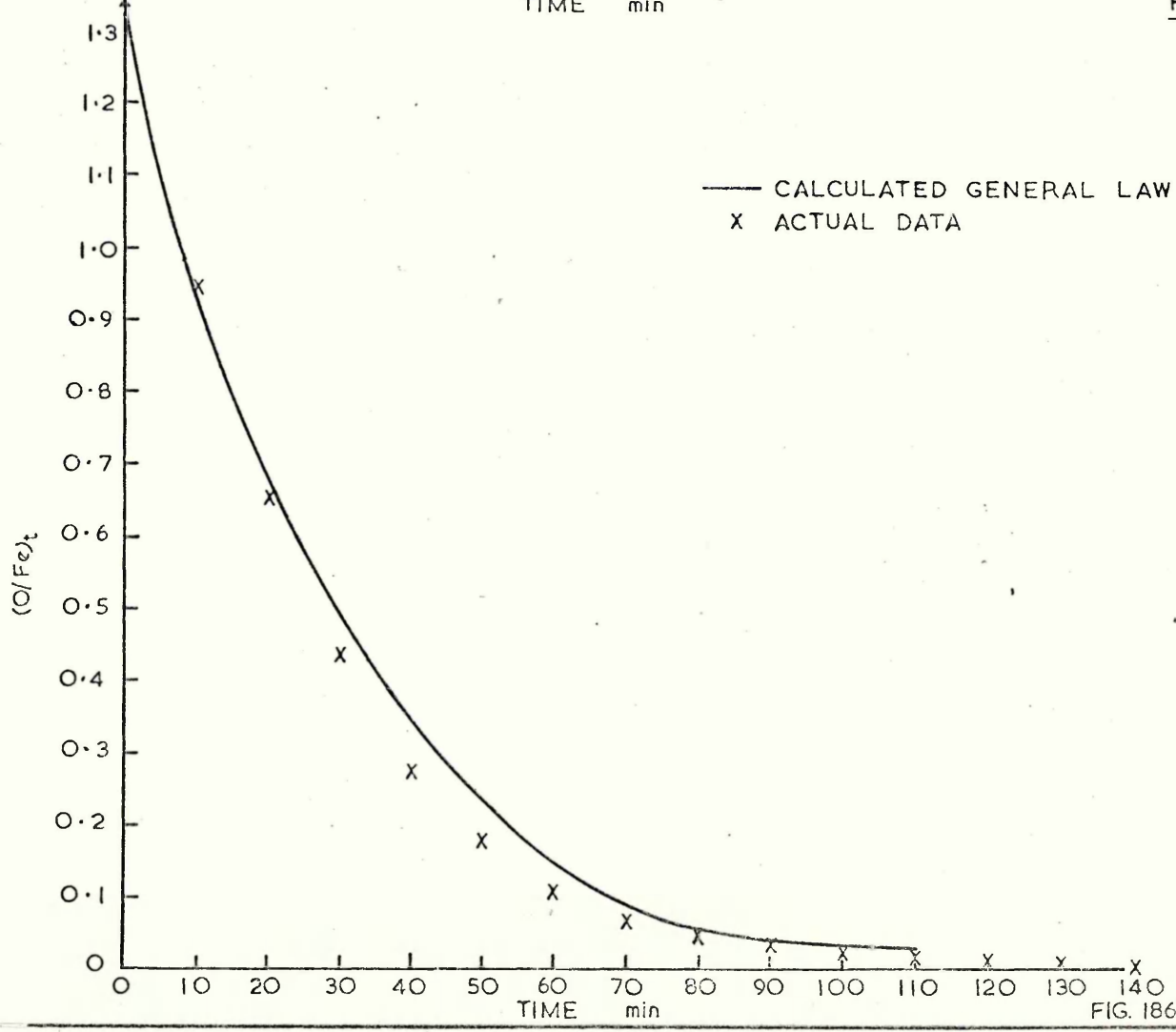


FIG. 186 b

FIG. 186a & 186 b

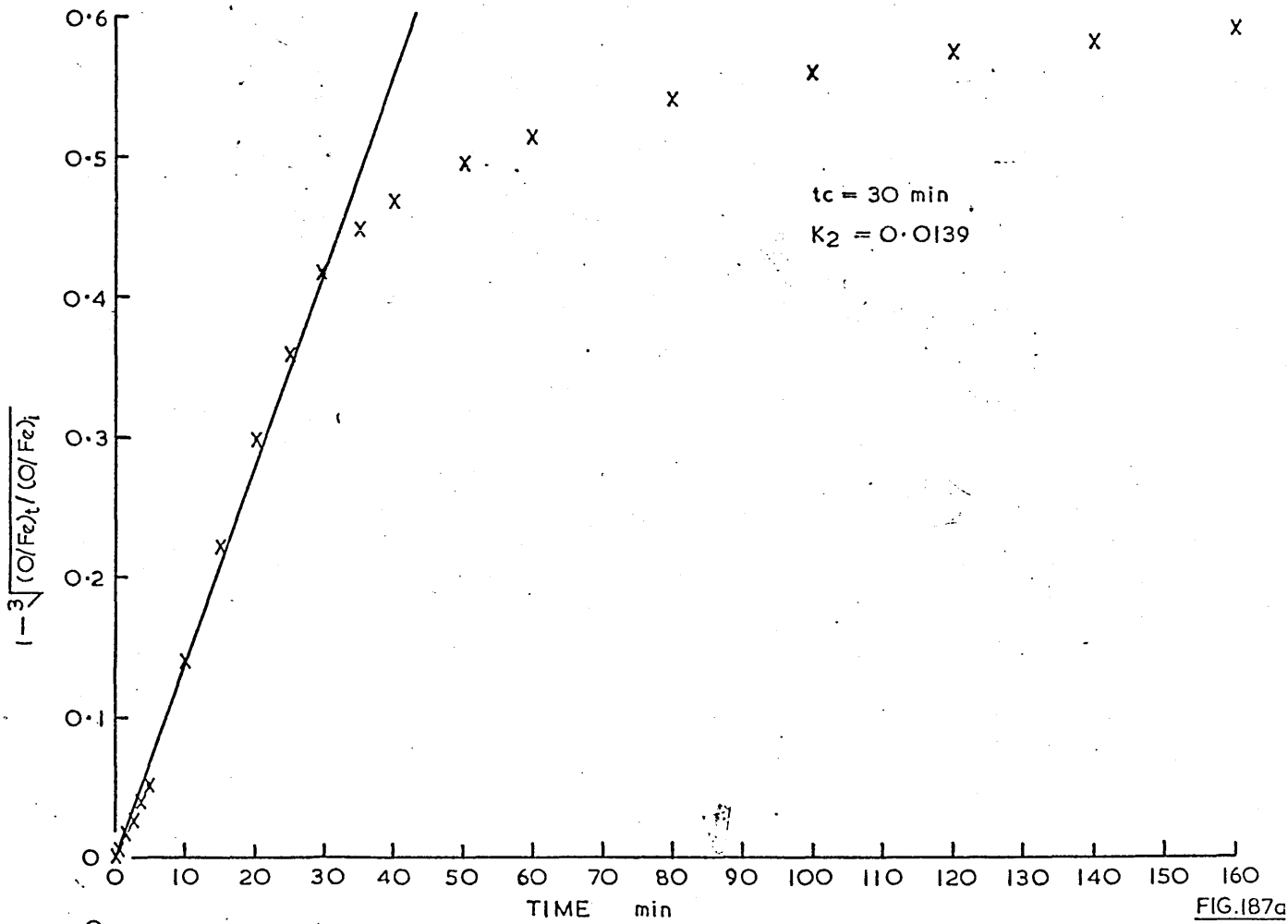


FIG. 187a

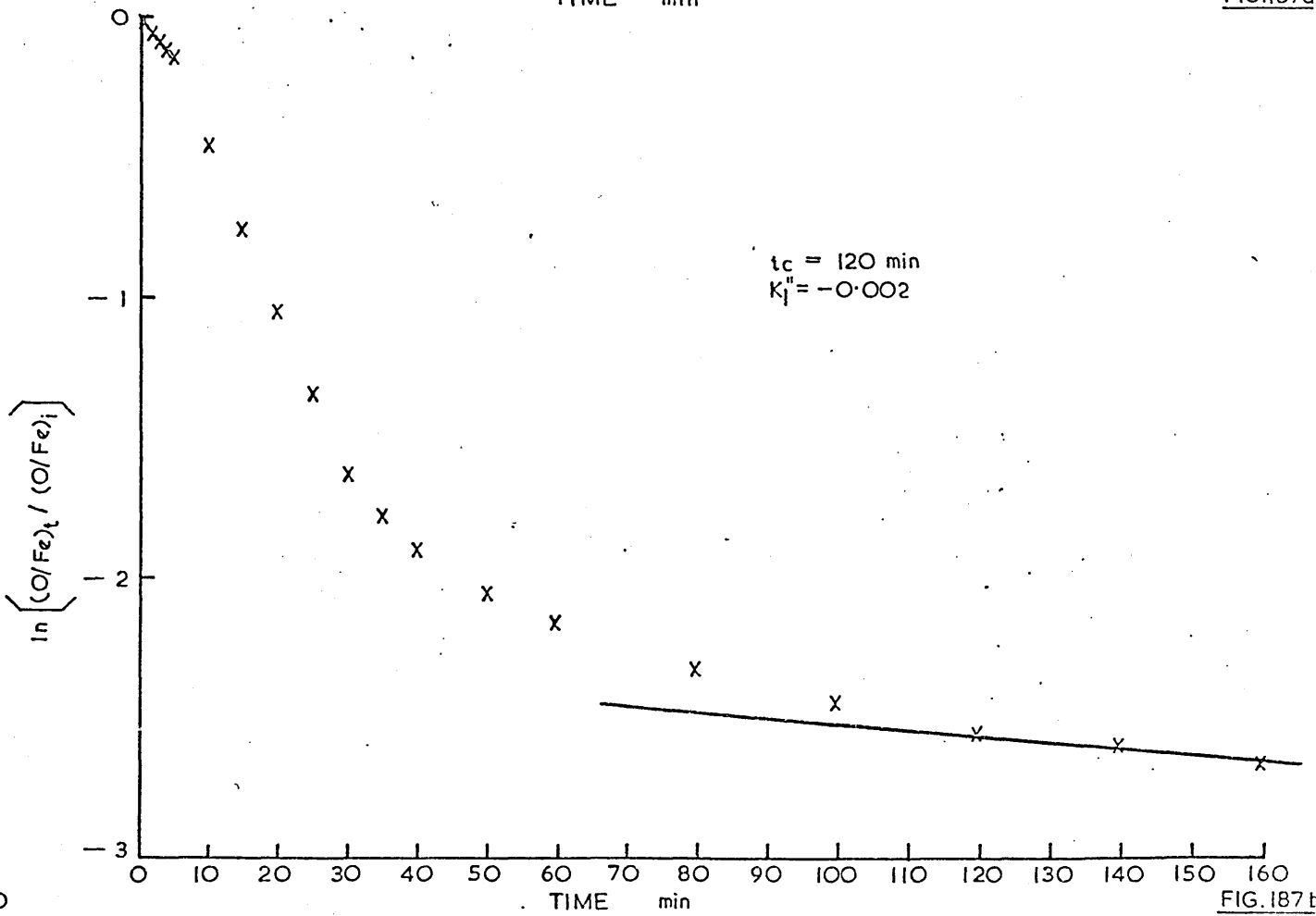
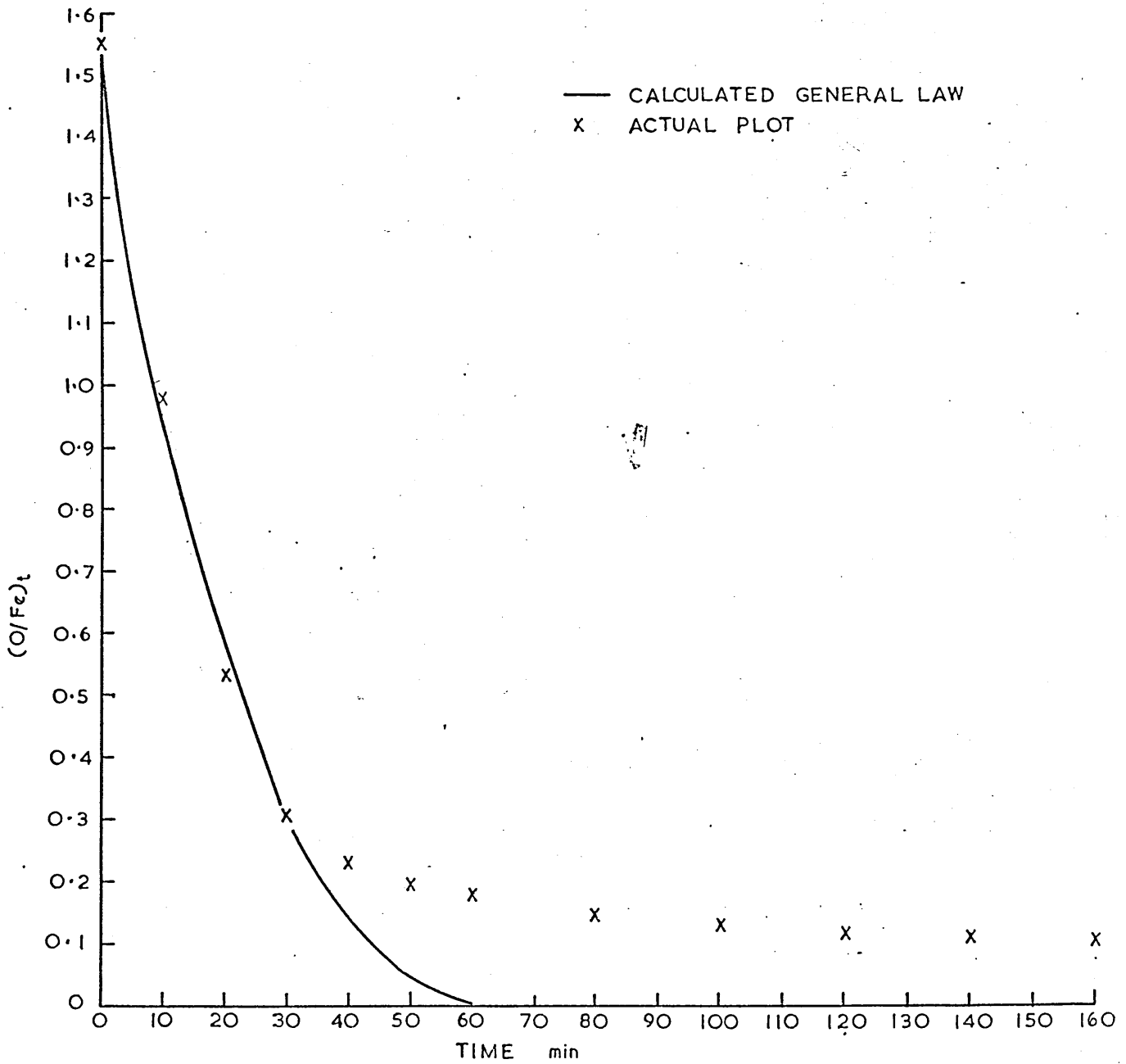


FIG. 187b

FIG. 187a & 187b

MANUAL GENERAL LAW PLOTS



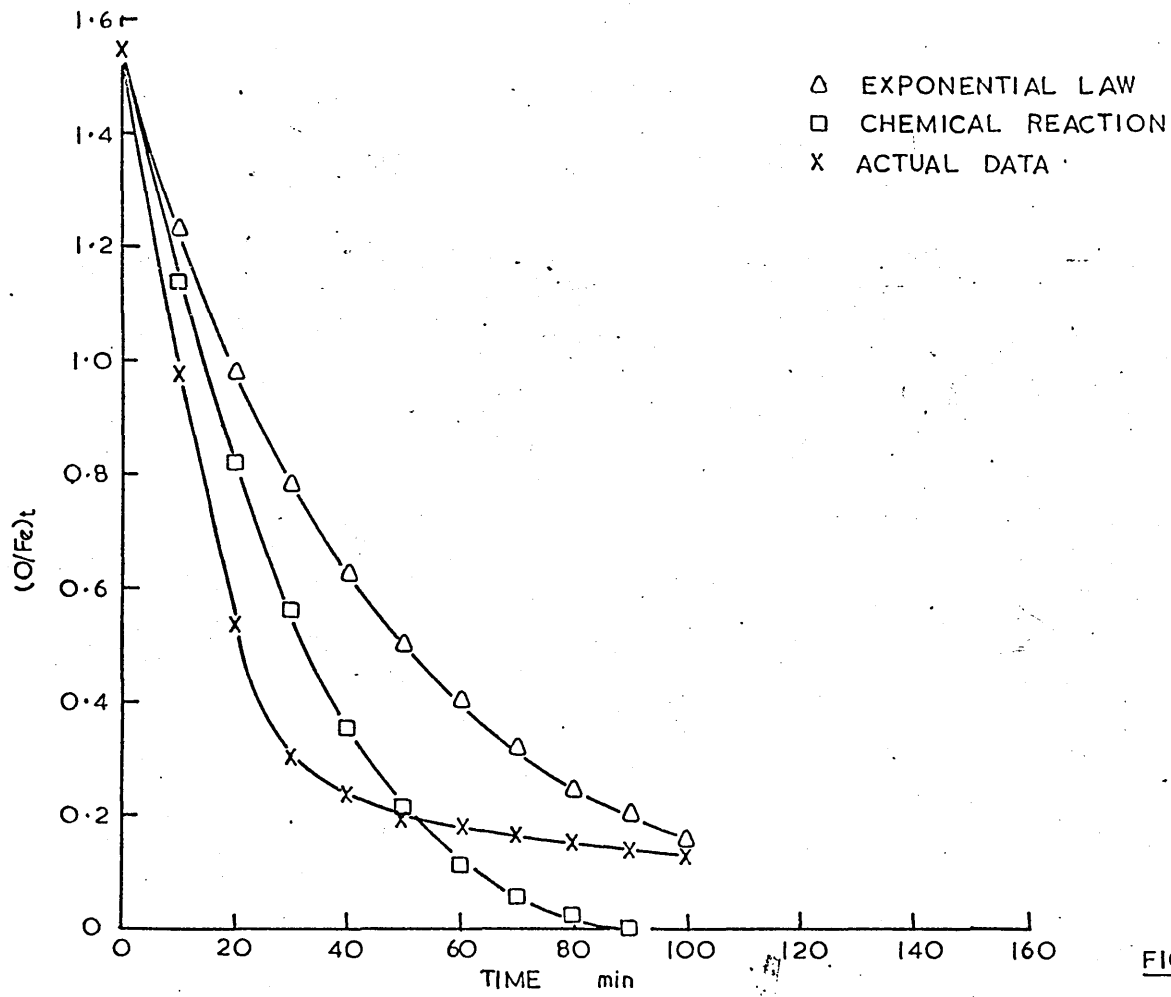


FIG. 189

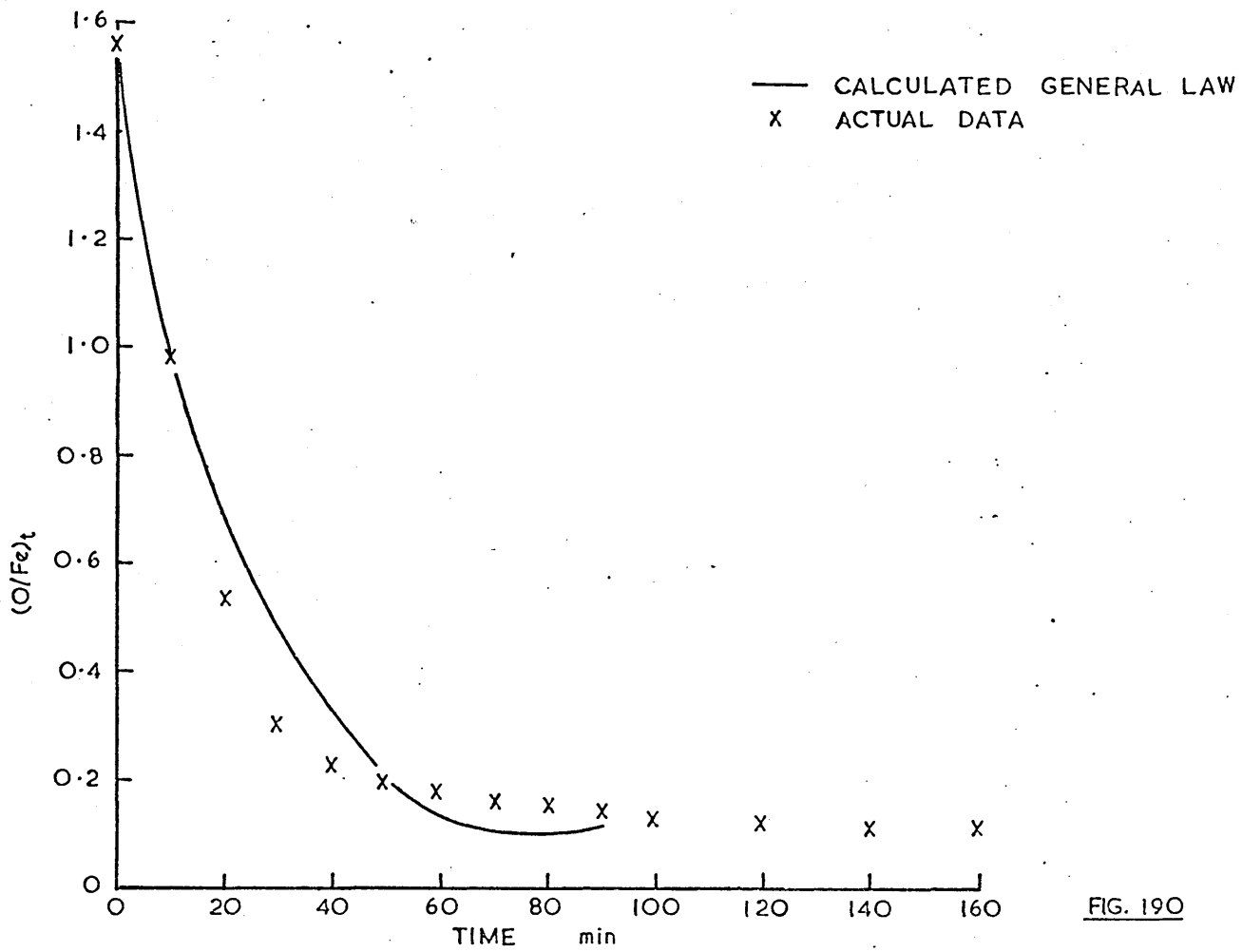


FIG. 190

FIG. 189 & 190

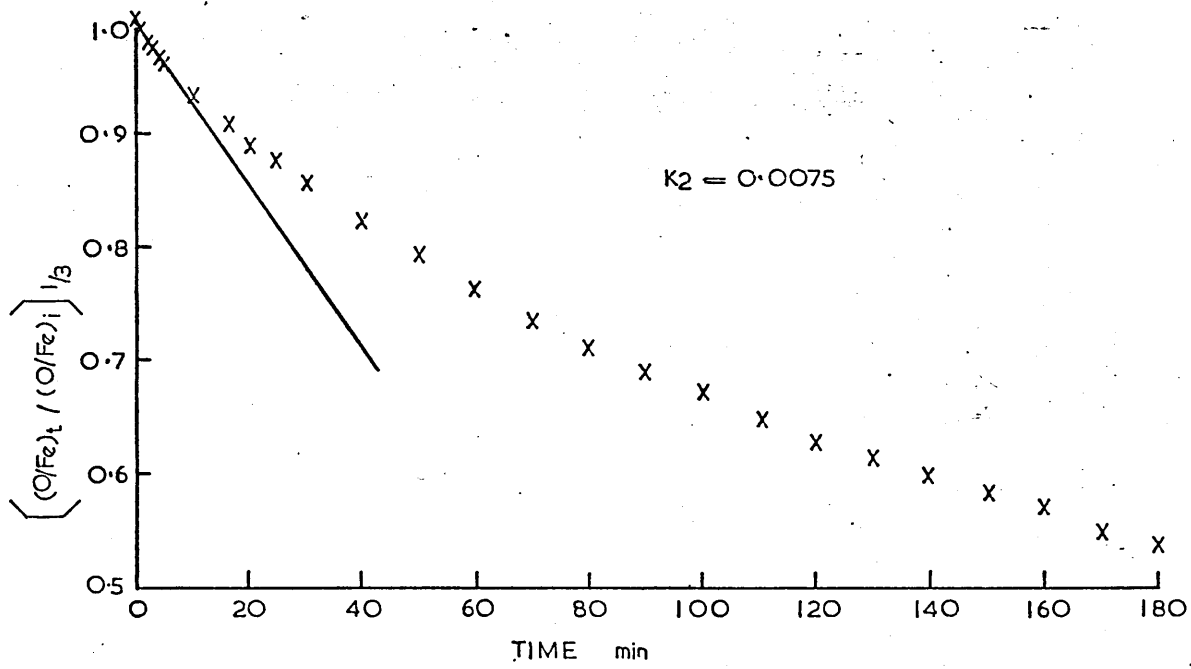


FIG. 191 a

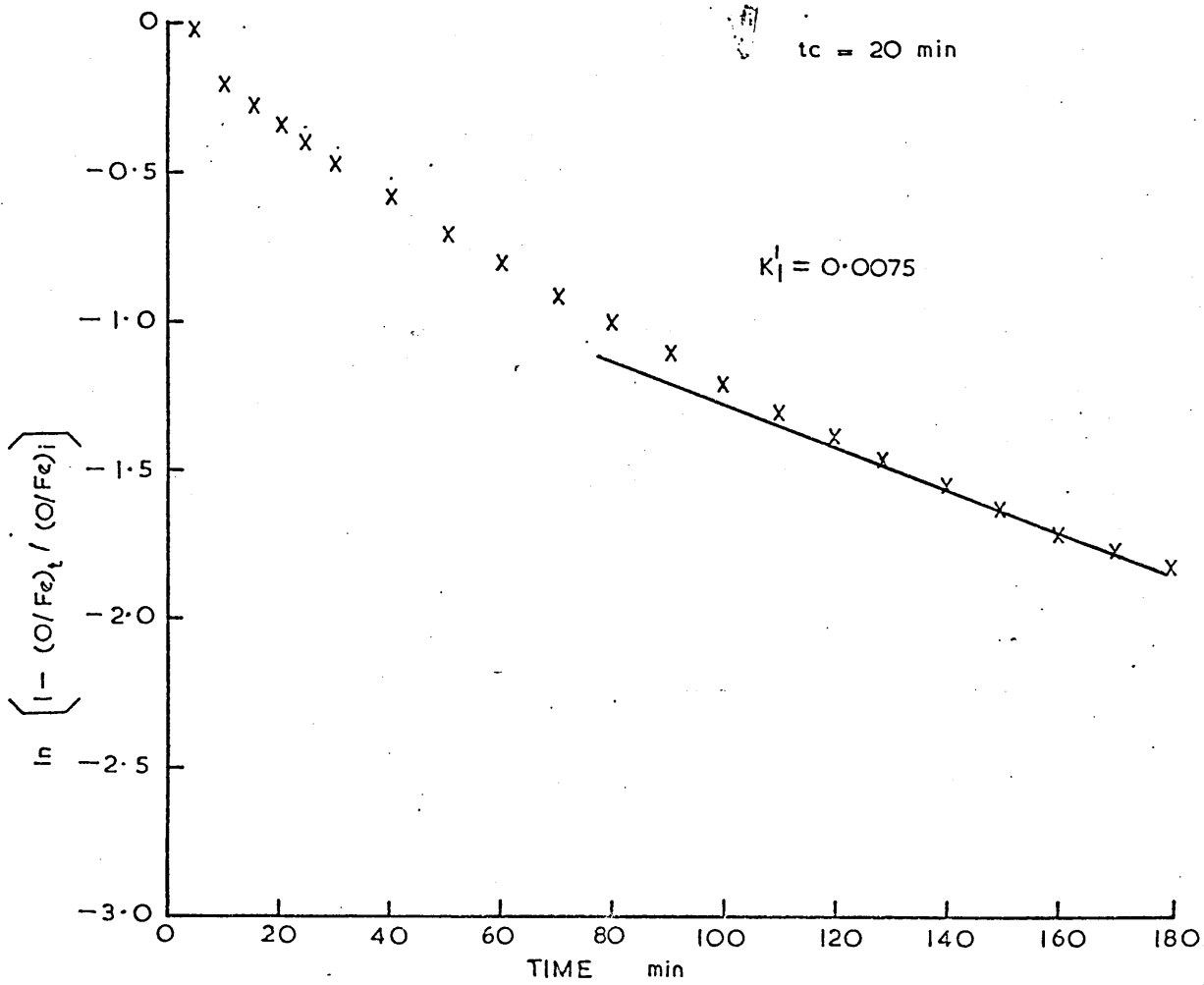
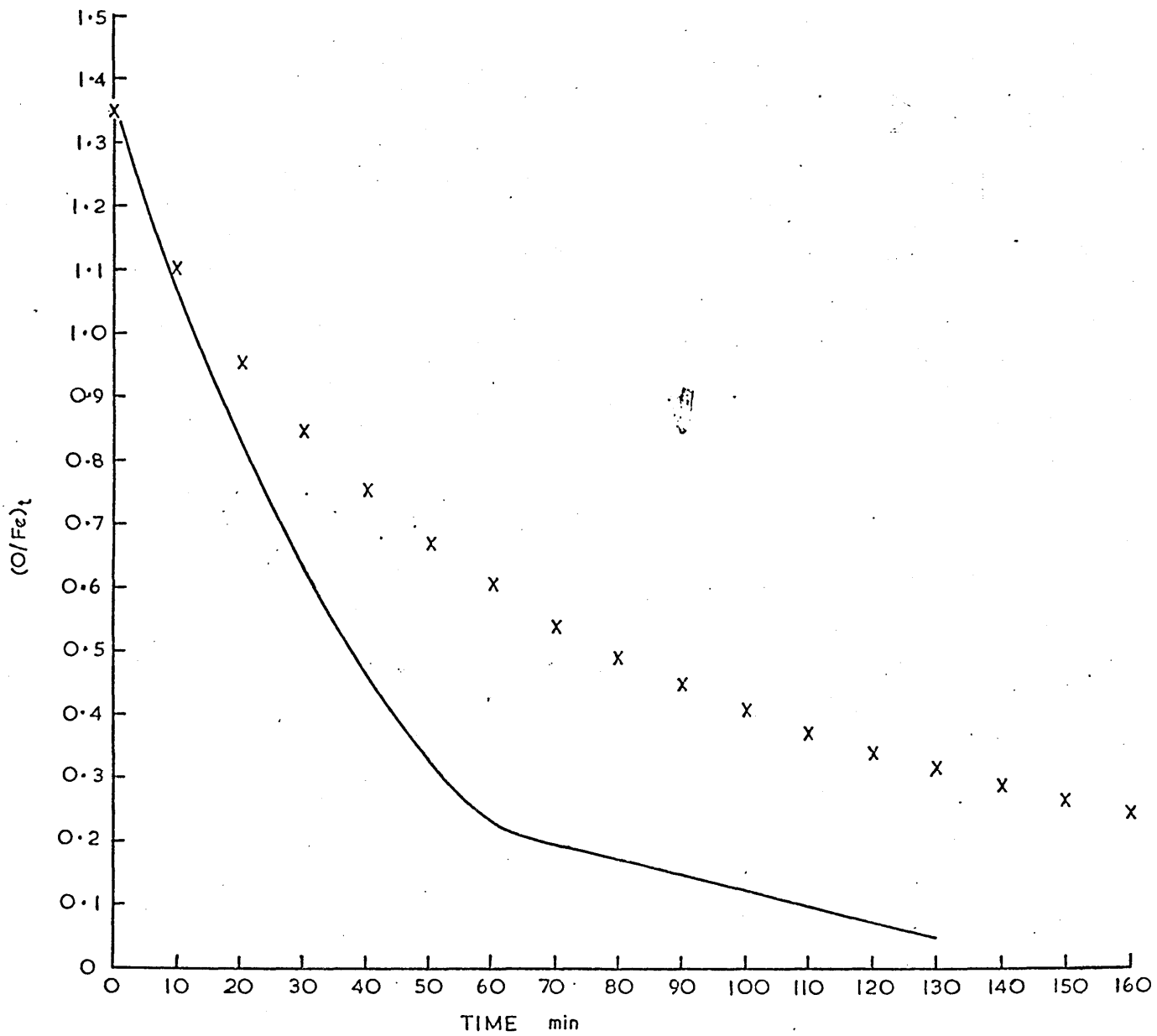


FIG. 191 b

MANUAL GENERAL FIT



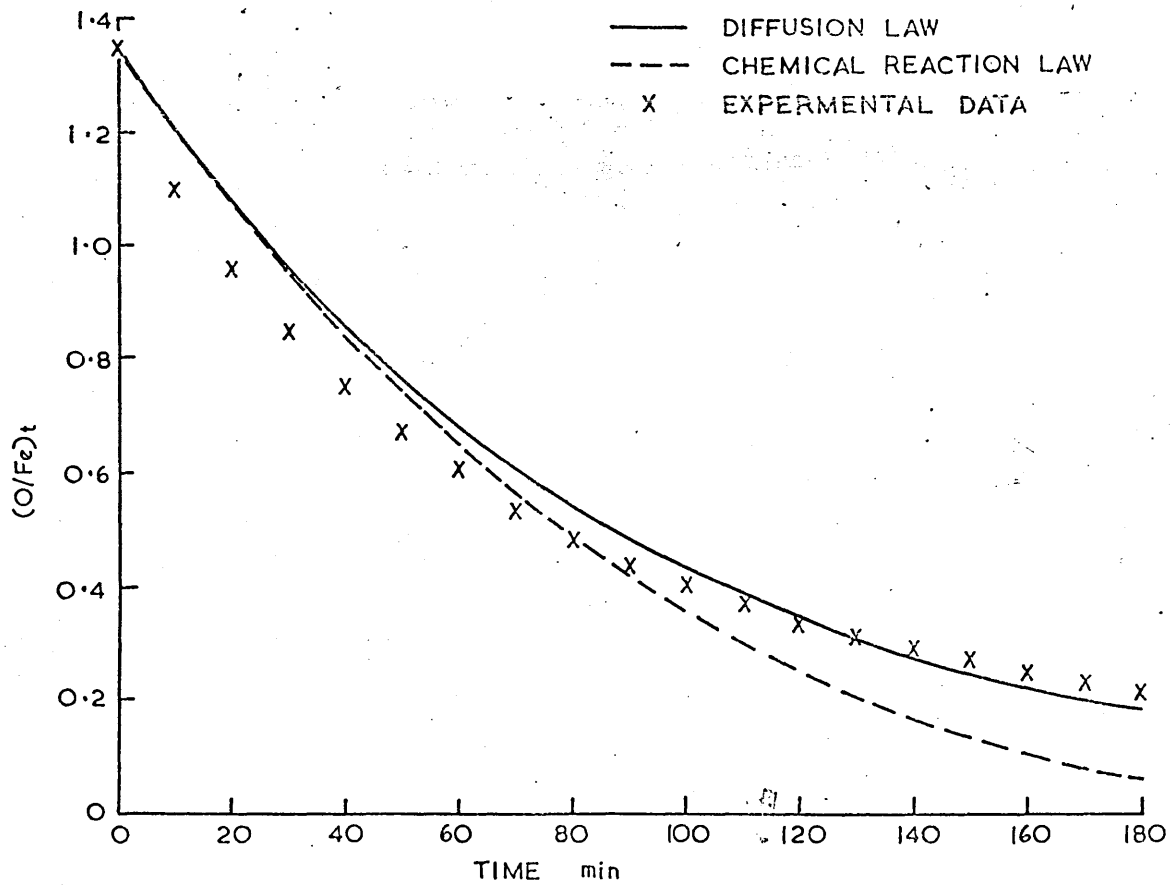


FIG. 193 a

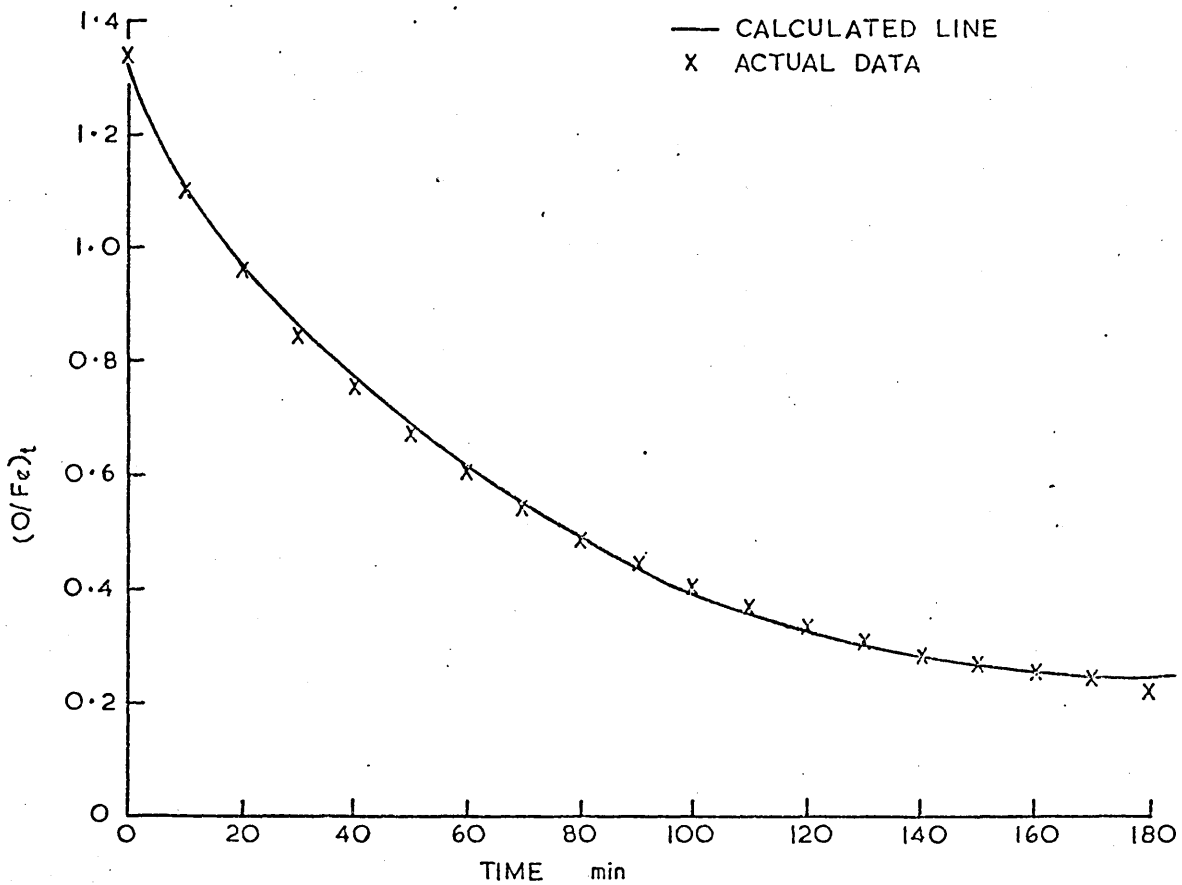


FIG. 193 b